Global Common Conversion Point Stacking and its Applications

Lucas Sawade

Thesis for the Degree
Master of Science in Geodynamics

Department of Earth Sciences
University of Bergen
June 1, 2018

Abstract

Imaging of globally varying subsurface structures is traditionally done by using seismic tomography to map large volumetric anomalies. Methods that image sharp discontinuities in seismic impedance have been restricted to regional or local studies. A global, three-dimensional method is developed that stacks converted earthquake waves originating in such discontinuities, as a function of their conversion points. The method relies on the database GLImER, which contains a global dataset of earthquake recordings that were processed into records of seismic impedance contrasts, namely receiver functions. The implementation of the method follows four steps that are (1) tracing the theoretical conversion points of the receiver functions, (2) creating a global bin grid, (3) binning the receiver functions as a function of their theoretical conversion points, and (4) traveltime-correcting and stacking the binned receiver functions. The stacks are computed with phase-weights to efficiently attenuate incoherencies in the signal. Furthermore, our method takes advantage of the crustal multiples to further enhance the stacks. We test our developed method on both synthetic data created with RAYSUM and real data of the Cascadia subduction zone with the conclusion that dipping discontinuities of up to 20° can be smoothly imaged. Furthermore, the subducting slab was shown to have a 4° southwards dip orthogonal to the convergence of the Juan de Fuca and the North American plate. Following the tests, the method is applied to the East African continent to create two almost continuous cross sections from the Afar Region to Cape Town. The cross sections are used to survey both the topography of the Mohorovičić (Moho) discontinuity and the mantle transition zone (MTZ) discontinuities at ∼410 and ∼660 km. Our images show that (1) the Moho is predominantly affected by Africa's tectonic history, showing jumps at nearly every tectonic boundary with shallowing from northern Kenya towards the Afar region, and that (2) the MVZ is generally thinning from South Africa to the Afar region with an abrupt thickening towards the Arabian Peninsula. Both the shallowing of the Moho and the thinning of the MTZ are attributed to the mantle upwelling previously imaged by seismic tomography. The abrupt thickening of the MTZ in the north-east of the Afar region is attributed to a change in mantle flow direction which manifests in a steep, negative temperature gradient towards the Arabian peninsula in consistency with geodynamically modelled mantle flow.

Acknowledgements

First of all, I would like to express my gratitude to my supervisor Stéphane Rondenay. His assistance in writing style and technique is the reason for a readable text as well as my improved understanding of the English language. Furthermore, his intrinsic excitement for every bit of Earth science and his socratic way of leading a discussion have not only helped me solve the scientific problems I encountered but also inspired me to follow the academic path in Earth sciences.

Also, I would like to thank my co-supervisor, Lars Ottemöller, for his excellent remarks and critique on the text as well as technical discussions.

I would like to thank my Peter Makus for both his constructive feedback on the text and functionalities he added to my plotting codes.

Moreover, I would like to thank Lars André Fardal Refsland and Øyvind Kongshaug for simply for being the best roommates one could wish for during the process of writing a thesis; not to forget insightful discussions on Matlab, LaTeX formatting and seismology in general.

Likewise, I would like to thank Mi Vu for being — safe to say — the biggest support during my Masters. By my side, she had to endure my physical presence but mind-absence when codes were not working, or listen to me complaining about it. But most of all, I would like to thank her for being the reason to disconnect from writing and coding. Otherwise, I would probably have lost all my hair by now.

Last, but definitely not least, I would like to thank my parents, Petra and Burkhard. Without them supporting my endeavour of studying abroad, I would not have pursued a Bachelors degree at the University of Bergen, nor would I have taken part in the Masters progam here.

Contents

Chapter 1

Introduction

Seismology has been used to reveal the Earth's interior for over a century now. Knowledge of the Earth's internal structure is key to understanding its evolution and dynamics. Traditionally, seismic tomography has been the method of choice to map subsurface structures within the crust and the upper mantle that vary at global scale by investigating large volumetric anomalies. Methods that are sensitive to sharp discontinuities, however, have been restricted to local or regional studies and have never been applied at a global scale. This thesis attempts to address this shortcoming by implementing a new framework for globally imaging these sharp discontinuities using converted earthquake waves that will be stacked according to their conversion points (Dueker and Sheehan, 1997). This framework relies on the recently established database of the project GLImER (**G**lobal **L**ithospheric **Im**aging using **E**arthquake **R**ecordings). The aim of GLImER was to automatically process earthquake recordings into records of seismic impedance contrasts, also referred to as receiver functions (Rondenay et al., 2017). These seismic impedance contrasts are introduced by sharp discontinuities in mineral composition, phase, temperature and/or pressure.

The motivation for the development of our new imaging method originates in the need to map lateral changes in topography of three sharp discontinuities of the crust and upper mantle: the Mohorovičić discontinuity and the two mantle transition zone discontinuities at approximately 410 and 660 km depth. Globally imaging these discontinuities can provide constraints on variations in temperature, pressure and seismic velocities of the crust and upper mantle and hence, information concerning the past, present and future evolution of the Earth's interior and exterior.

In the specific case of East Africa, methods using converted earthquake waves have been used to image the crust and the upper mantle in three separate regions and have provided significant results (Cornwell et al., 2011; Dugda, 2005; Julià et al., 2005; Last et al., 1997; Nair et al., 2006; Nguuri et al., 2001; Niu et al., 2004; Owens et al., 2000). What these studies lack, however, is a composite view of these regions to robustly make an assumption of the lateral changes in velocity and temperature between the different tectonic regions at continental scale. The method developed here is used to create a general overview of the crustal and mantle structure of the East-African continent from Cape Town to the Afar region in northern Ethiopia. Especially intriguing are changes in topography of the Moho discontinuity and the thickness of the mantle transition zone. A cross section spanning from southern South Africa to Ethiopia crosses two cratons and several regions with known rift activity (Saria et al., 2014). This rifting has been attributed to mantle upwellings, which are pushing upwards from the mantle (Begg et al., 2009; Hansen et al., 2012). The increase in temperature in the upper mantle from South Africa towards Ethiopia caused by this upwelling should, therefore, show a thinning of the lithospheric crust and the mantle transition zone (Bina and Helffrich, 1994; Helffrich and Bina, 1994).

Outline

Following the introduction, the motivation for the development of the method will be further developed by providing a brief review of Earth's internal structure and dynamic processes in Chapter 2. Afterwards, the methodological background will be given in Chapter 3. With the methodological background of receiver function imaging in mind, Chapter 4 will present the receiver function data and the implementation of the common conversion point method on a global grid. The developed method will then be tested using synthetic receiver function data, which is created with the code RAYSUM (Frederiksen and Bostock, 2000), in the last section of Chapter 4. Subsequently, Chapters 5 and 6 are dedicated to the application of the method in two notably different tectonic areas: The Cascadia subduction zone and the East-African continent. The Cascadia subduction zone has already been imaged by numerous seismic investigations (e.g. Bostock et al., 2002; Cheng et al., 2017; Rondenay et al., 2001; Tauzin et al., 2016). A recent study conducted by Tauzin et al. (2016) has provided a unique view of the Cascadia subduction zone at North America's west coast using the common conversion point stacking

method with an extremely dense network. The aim of Chapter 5 is to test the method developed in Chapter 4 on real data by comparing our results to those of Tauzin et al. (2016). In Chapter 6, the method will be applied to East Africa with the expectations to provide some new constraints on crustal and upper mantle structure in the region. Chapter 7 is dedicated to briefly discuss the advantages and disadvantages of the method in view of the results obtained in the preceding two application chapters. Lastly, Chapter 8 will provide a conclusion as well as a possible future outlook for the method as a part of project GLImER.

Chapter 2

Earth's Structure and Dynamics

The Earth is a heterogeneous body with elastic properties that vary from atomic to global scale. At global scale the Earth is made up of layers categorised by either their petrological makeup (i.e., the chemical composition) or their rheology (i.e., rigidity). There are five main layers distinguished by their composition (see Figure 2.1). The uppermost layer is the crust with a thickness ranging between 7 and 70 km. The second layer is the upper mantle which starts just below the crust and reaches depths of up to 700 km. The third layer, the lower mantle, extents from the bottom of the upper mantle to approximately 2,900 km where the outer core begins. Below the mantle, the outer core stretches from 2,900 to 5,100 km and the inner core from 5,100 km to Earth's centre at 6,371 km. The rocks in these layers are categorised by their ratio in silica to magnesium and iron content. Felsic rocks contain large amounts of silica, while intermediate, mafic and ultramafic rocks are described by decreasing silica content and an increasing iron and magnesium content, respectively. The mantle mostly comprises ultramafic rock while the crust is generally more felsic, i.e., containing more silicate. The boundary between the two is called the Mohorovičić discontinuity (Moho), see Figure 2.1. The core is made up of an iron-nickel alloy and believed to not contain any lighter elements due to its density (Marshak, 2015).

The division of the Earth's layers by their rheology results in a different set of discontinuities, including in particular the lithosphere-asthenosphere boundary (LAB). The lithosphere (see Figure 2.1) consists of both the crust and the uppermost, rigid part of the mantle. The layer below the lithosphere is called asthenosphere. Here, rocks become so hot that they are ductile. This happens approximately at the isotherm of 1300° C and at circa 100-150 km depth and results in a viscous flow of the ductile rocks in the asthenosphere.

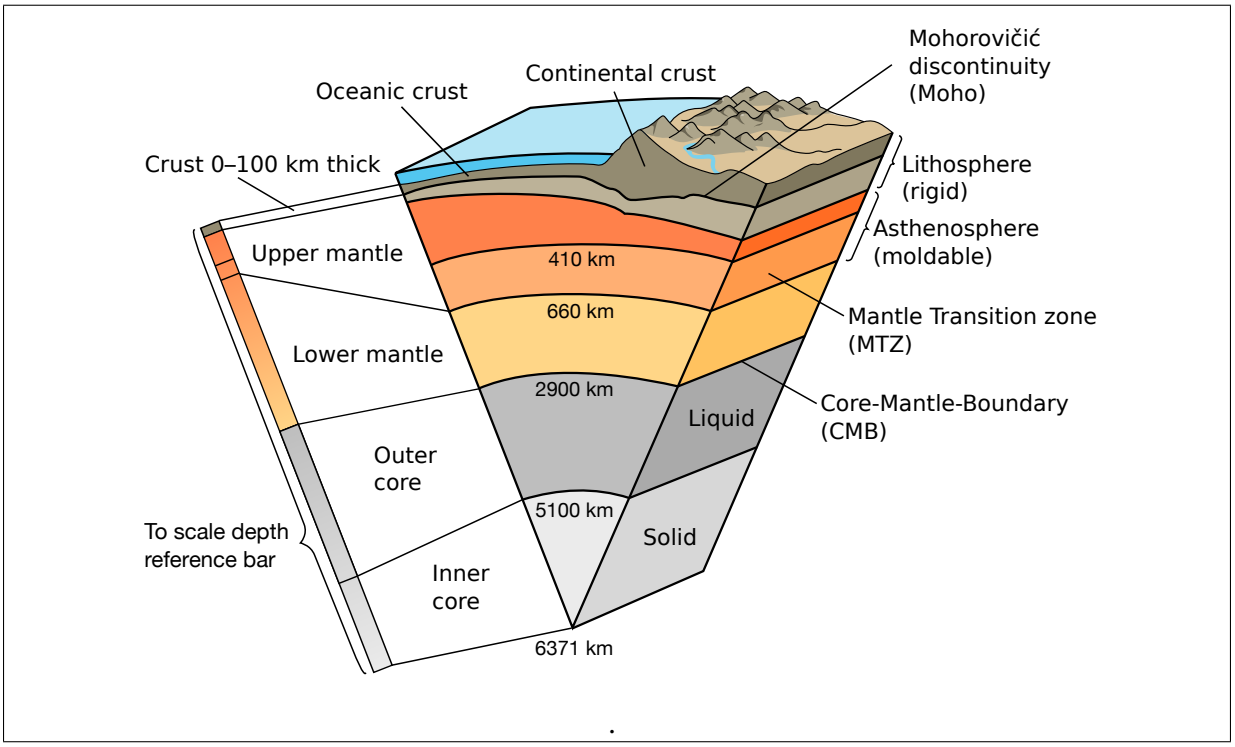

Figure 2.1: A schematic cutaway of the Earth with a to-scale reference bar on the left. The surface is at 0 km depth and the centre of the Earth at 6371 km. The figure describes the different locations and thicknesses of the Earth's layers by both composition and rheology. The crust is divided into two parts: dense, mafic oceanic crust and less dense, felsic continental crust. Both are underlain by the rigid part of the ultramafic upper mantle which is thicker below the continents. The Mohorovičić discontinuity (Moho) marks their boundary and together they form the lithosphere. Below the lithosphere, the asthenosphere starts; it is the ductile part of the upper mantle and contains the mantle transition zone (MTZ) which inhibits a series of olivine's phase transitions. The lower mantle starts below the 660km discontinuity and reaches down to the core-mantle-boundary (CMB) at around 2900km. The core consist predominantly of iron and nickel; the outer core is liquid, while the inner core is solid (Marshak, 2015) [figure modified and taken from `https://pubs.usgs.gov/gip/dynamic/inside.html` (March,2018)]

Although the rigidity of the upper mantle changes at the LAB due to the increase in temperature and pressure, the minerals' alignment does not (Marshak, 2015).

Rocks cannot only be compared by their composition and rheology but also by their chemical phases. That is, the bonds between atoms making up crystalline structures become unstable and cause the atoms to realign into new, stable formations when they are subject to a certain change in temperature and/or pressure. This realignment results in a change of the physical properties, such as the density (Marshak, 2015). The mantle transition zone (MTZ) is one of the areas affected by phase changes (see Figure 2.1). Until $\sim$410 km depth, the upper mantle consists primarily of peridotite, a coarse-grained, ultramafic, igneous rock which is uncommon to the Earth's surface as a consequence of its reactivity with water at surface temperatures (Helffrich and Wood, 2001). At mantle depths, peridotite's main components are olivine, $(Mg,Fe)_2SiO_4$, and pyroxenes, but the increasing pressure and temperature at $\sim$410 km cause olivine to become unstable. Thus, olivine undergoes transformation into the stable β-spinel, also called wadsleyite (Bina and Helffrich, 1994). Note that the composition is not changing during this transformation. At $\sim$520 km, wadsleyite again transforms to the γ-spinel ringwoodite. Then ringwoodite decomposes into perovskite, $(Mg,Fe)SiO_3$, and magnesiowüstite, $(Mg,Fe)O$, at around $\sim$660 km (Bina and Helffrich, 1994). These three discontinuities (from now referred to as the 410, 520 and 660 according to their global, average depths) make up another example of how the Earth can be viewed as a static, spherically-symmetric, layered medium (Marshak, 2015). However, it does not behave like one (Marshak, 2015).

The Earth is a dynamical, constantly evolving system. The lithosphere is broken up into tectonic plates that are drifting on top of the asthenospheric mantle. Due to the mantle's viscosity and convective behaviour, the lithosphere is formed and destroyed at the tectonic boundaries as shown in Figure 2.2 (Marshak, 2015). At mid ocean ridges, high temperature mantle rocks are brought up to the sea-bottom, cooled and oceanic lithosphere is created. The upwelling of the mantle creates the 'Ridge-Push' force pushing the adjacent tectonic plates outwards. The other driving force of plate movement is the 'Slab-Pull' force which is a result of the gravitational force on subducted lithosphere. Oceanic lithosphere has a higher mean density than continental lithosphere (i.e. $3.3 g/cm^3$ as opposed to $2.7 g/cm^3$, respectively) since it is made up of dense mafic mantle rocks. Consequently, when oceanic lithosphere is pushed against continental lithosphere, the oceanic lithosphere is subducted underneath continental

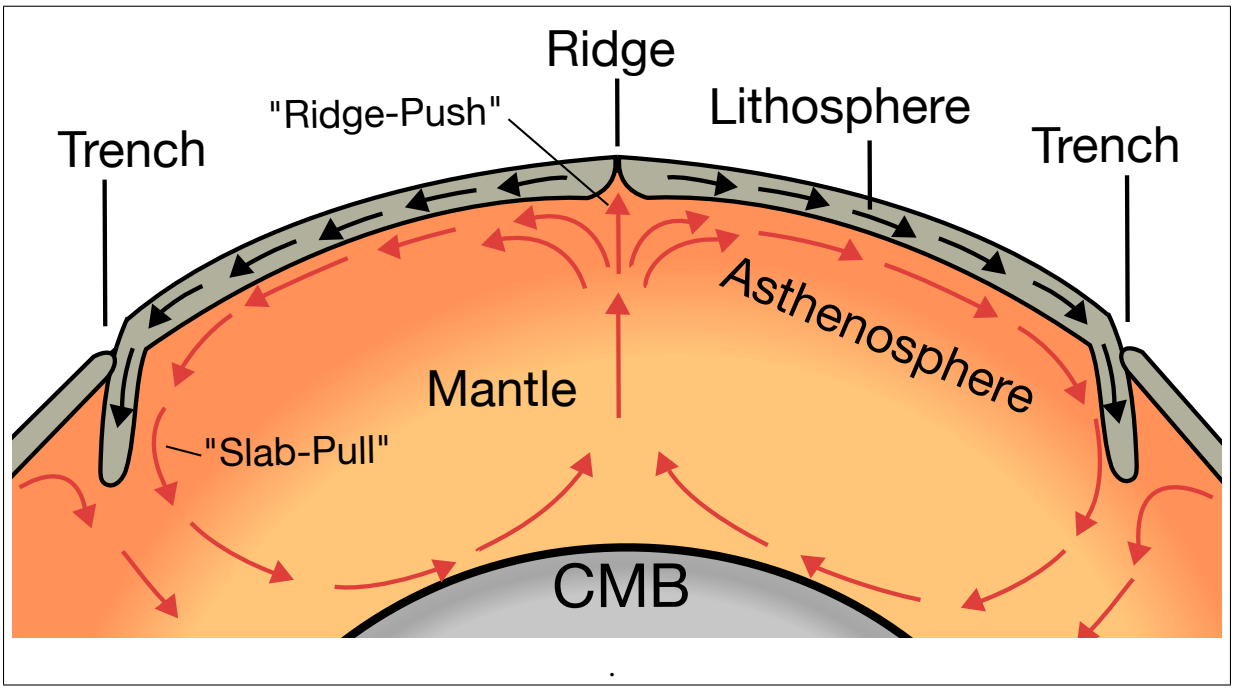

Figure 2.2: Schematic figure of mantle convection, tectonic plate movement and their driving forces. A mantle upwelling transports molten, high temperature rocks to a ridge creating a pushing force. When the rocks are cooled they solidify and attach to the adjacent plates creating new lithosphere. On the other sides of the lithosphere, subduction is pulling down the formed plate via slab-pull forces. How large the impact of each of the forces is remains a matter of active debate in the Earth Science community (Marshak, 2015). [Figure taken from `https://upload.wikimedia.org/wikipedia/commons/2/27/Oceanic_spreading.svg` and originally created by 'Surachit'. Modified and distributed under a CC BY-SA 3.0 license.]

lithosphere. Since the density of the slab is higher than that of the ambient mantle (Ganguly et al., 2009), the subduction process creates a pulling force dragging not only the subducted slab but also the attached oceanic lithosphere. When two continental plates collide, neither is subducted. Instead, they build up mass in their zone of collision, thicken and, hence, create mountains with deep crustal roots. As a result of these dynamic processes, the topography of lithospheric discontinuities varies locally, regionally and globally. Furthermore, changes in the temperature gradient in areas of subduction and mantle upwelling influence the depth of thermally affected boundaries varies from region to region.

Geophysical probing has long been used to map lateral variations in topography of the Moho and the MTZ discontinuities. The Moho's depth is mostly affected by the different tectonic environments (Marshak, 2015; Rondenay, 2009; Stein and Wysession, 2003) while the MTZ's topography is primarily affected by olivine's phase transitions at different depths due to varying temperature gradients (Bina and Helffrich, 1994; Helffrich and Bina, 1994; Helffrich

and Wood, 2001). The Moho is generally deeper below the felsic, continental crust due to the continental crust's thickness and lower density. An exception are areas of subduction where the oceanic crust is overridden by the continental crust and hence, the oceanic Moho lies below the continental one. The Moho is deepest where continents have recently collided because the overburden from mountain building forces the crust-mantle boundary downwards (e.g. Himalaya). Over long periods of erosion (millions of years), the mass above the lithospheric mantle diminishes and the Moho will become shallower again because of isostatic rebound (Mussett and Khan, 2000). Other regions in which the Moho becomes shallow are regions of continental rifts. Mantle upwelling of hot molten rock causes crustal break up by melting the lithosphere from below. In this case, the Moho does not only become shallower, but since crustal and mantle rocks become one mass, the sharp contrast in composition between crust and mantle often completely dissappears (Marshak, 2015). Consequently, mapping of the Moho can have major implications on the tectonic environment of the investigated regions. In the MTZ the temperature dependent phase transitions are also heavily influenced by the dynamic processes of mantle convection. When subducted plates have been dragged down far enough into the upper mantle, the MTZ is cooled down by the low temperatures of the subducted slab. As a consequence, phase transitions in the MTZ appear at significantly different depths than in areas with mantle upwelling (see Figure 2.3). Low temperatures in the MTZ will shallow olivine's phase transition to wadsleyite (410) and the transition from wadsleyite to ringwoodite (520), while they deepen the transition from ringwoodite to perovskite+magnesiowüstite (660). A mantle upwelling, on the other hand, heats up the mantle and moves the pressure gradient of olivine's phase transition to higher temperatures. The resulting depth of olivine's phase transition to wadsleyite is considerably deeper and the transition from wadsleyite to ringwoodite is skipped entirely by direct decomposition from wadsleyite to perovskite and magnesiowüstite at a shallower depth. In summary, the mapping of the MTZ can be used as a powerful tool for the deduction of mantle temperatures, i.e., be a 'mantle thermometer' (Owens et al., 2000). Consequentially, variations in topography can have implications for continental evolution.

Understanding the large-scale topography of the Earth's subsurface discontinuities cannot only help understand past tectonic processes and Earth's present state but also the Earth's future development at the surface. The investigation of the processes of continental creation and destruction is essential in understanding where seismic hazards are likely to

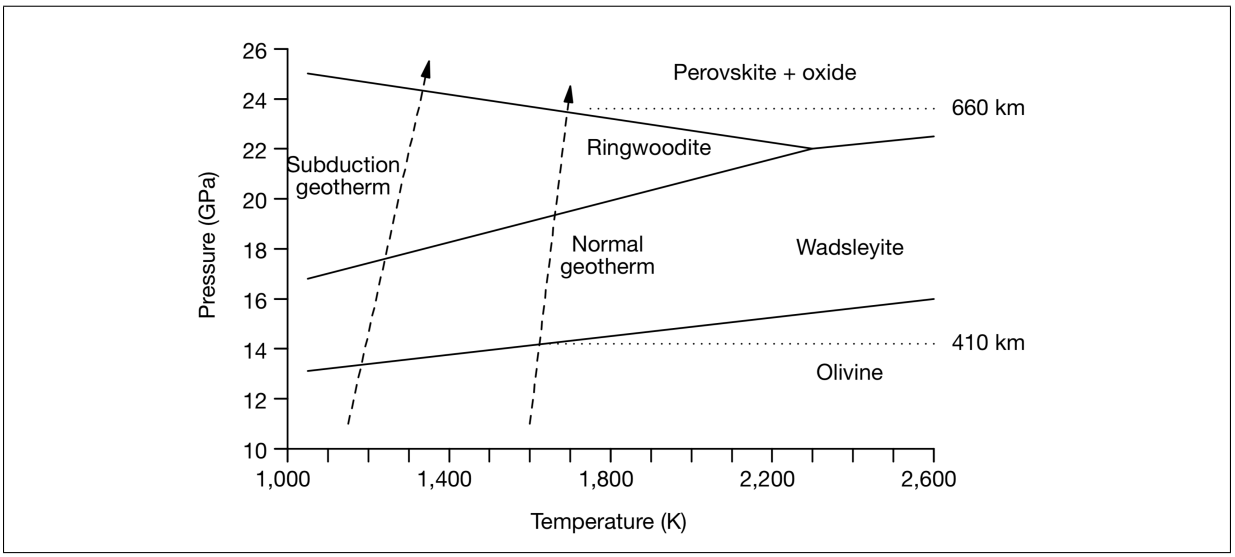

Figure 2.3: Descriptive phase-diagram of pure Mg_2Si0_4 olivine in mantle peridotite. The phase stability regions for olivine, wadsleyite, ringwoodite and perovskite+magnesiowüstite are divided by the solid lines. The dashed lines in the cooler part shows the approximate pressure-dependent temperature gradient common for subduction zones whereas the right dashed line shows a normal geothermal gradient. Warmer temperatures move the phase transitions to deeper (olivine $\rightarrow$ wadsleyite) or shallower depths (ringwoodite $\rightarrow$ perovskite+magnesiowüstite) (figure from Helffrich and Wood, 2001).

occur, for example, the origin of volcanoes, earthquakes and other hazards related to the movement of tectonic plates (Mussett and Khan, 2000; Stein and Wysession, 2003). Mountains, which have considerable effects on the climate, flora and fauna at local, regional and even continental scale, are originating in the movement and collision of tectonic plates (Marshak, 2015). There is even economic interest in the investigation of the Earth's dynamic processes. The development of continents is the basis for all petroleum exploration and mining. From the burial of ancient biological mass, which is transformed to oil and gas over millions of years, to the origin of volcanic pipes, which carry diamonds to the surface, all are dependent on subsurface processes and plate tectonics (Marshak, 2015; Mussett and Khan, 2000). Thus, understanding the plates' movement and evolution is key to finding occurrences of gems and resources. These are a few reasons in an endless catalogue of motivations to investigate the subsurface and especially sharp discontinuities. The difficulty is that the subsurface cannot simply be looked into. A certain set of tools is necessary to investigate the subsurface successfully.

Seismology has proven itself a powerful tool to map sharp discontinuities in the crust and upper mantle (Langston, 1979; Vinnik, 1977). Other methods, such as gravity measurements, electromagnetic measurements or simple drilling, do not penetrate the Earth deep enough or do

not provide the same resolution as seismological methods (Mussett and Khan, 2000; Stein and Wysession, 2003). Hence, seismology is the best choice for the mapping the crust and the upper mantle, and our tool of choice in this thesis to investigate the topography of both the Moho and the MTZ.

Chapter 3

Methodological Background

This chapter provides a review on converted waves and the origin of the receiver function method in Section 3.1. Then, the theoretical background on how to process earthquake recordings into receiver functions will be explained in Section 3.2. The last subsection of this chapter, Section 3.4, will present the idea of common conversion point stacking of receiver functions along with a few concepts before implemented the method globally in Chapter 4.

3.1 The Converted Wave

Seismology is the study of waves propagating through elastic media. There are two types of seismic waves defined by their particle motion relative to the direction of propagation: the faster P wave, which is a compressional wave, and the slower S wave, which is a shear wave. The P wave's particle motion is parallel to the direction of propagation, while the S wave's particle motions are normal to the direction of propagation in vertical as well as horizontal direction. Thus, the S wave has two components, SV and SH, respectively. Both P and S waves travel at distinct velocities depending on the medium they propagate through (v_P and v_S, respectively). One source of such seismic waves are earthquakes which can be recorded by nearby and distant seismic stations. These stations can be deployed as single stations or station arrays to densely cover an area and accurately survey regional subsurface variations (Stein and Wysession, 2003). This thesis focuses on seismic waves generated by earthquakes and recorded by seismometers scattered on Earth's continents (Rondenay et al., 2017).

When seismic waves travel through media of varying seismic properties (i.e. v_P, v_S and the density of the media), they are reflected, refracted and converted at the boundaries between two media. Seismic waves cannot only be described by their wavefronts, but also by their rays perpendicular to the wavefront in homogeneous media. In particular, Fermat's principle states that there exists a ray corresponding to a path of stationary minimum (or maximum) traveltime describing the travel path and time of the wave between source point A and receiver point B (Stein and Wysession, 2003). This path can be a direct path, or a combination of reflections and refractions. Along this path, the wave or ray is affected by changes in media, especially when it encounters the interface of two media that vary in seismic properties. For example, when a P wave obliquely hits the boundary between two seismically varying, isotropic media, it splits into both reflected and converted P and SV waves; that is, the direction of the particle motions, the polarisation, changes. The incident and outgoing angles are expressed by Snell's law (Mussett and Khan, 2000):

$$\frac{sin(i_1)}{v_1} = \frac{sin(i_2)}{v_2}, \tag{3.1}$$

where i_1 and v_1 are the incident angle and velocity, and i_2 and v_2 outgoing angle and velocity (see Figure 3.1 (a)). Not only does the wave split into the two types of particle motions P and SV, the energy of the incident wave is also distributed between the four outgoing particle motions (reflected P and SV, refracted P and SV). This behaviour is expressed by the Zoeppritz equations, which solve the partitioning of energy dependent on the incidence angle by applying conditions to the boundary between the two media (Aki and Richards, 2002). The difference or contrast in seismic properties between two media is referred to as the contrast in impedance I. In introductory seismology textbooks (Mussett and Khan, 2000), this is often exemplified by the acoustic impedance I which is only concerned with the vertical reflection and transmission.

$$I = \rho v,$$

where v is the velocity of the P wave and ρ the density. In the case of P to S converted waves however, the impedance contrasts of interest contains information of both P and S wave energy. Connolly (1999) resolved this issue by introducing the concept of elastic impedance[1], which

[1]Elastic Impedance, EI, introduced by Connolly (1999) where $K = v_S/v_p$:

$$EI = v_P \left(v_P^{\tan^2\theta} v_S^{-8K\sin^2\theta} \rho^{1-4K\sin^2\theta} \right)$$

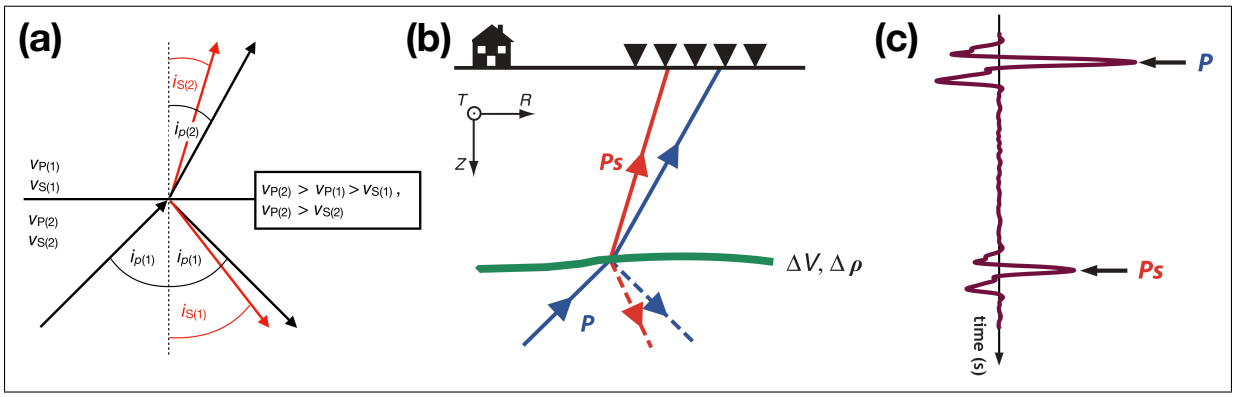

Figure 3.1: **(a)** Schematic image of behaviour of a P wave ray (black arrows) hitting a horizontal boundary from below. It reflects a P wave with the same angle and an S wave (red arrows) with a smaller angle. The refracted waves have both smaller angles because of the generally lower velocity in a shallower layer. **(b)** An earthquake's P wave (blue) hitting a sub-horizontal boundary with a seismic impedance contrast (green) from below. The wave will be partitioned by reflection (dashed) and transmission of the incident wave. Both P and S (red) reflected waves will travel downwards and the transmitted P and converted S waves, basis of the receiver function technique, will travel to the surface. **(c)** The resulting seismogram showing the direct P wave's pulse and the P to S converted wave's pulse with a time delay in the P wave coda. The ratio and sign of amplitudes between the incident and the converted wave is indicative of the magnitude and type of contrast. A positive *Ps* pulse, like the one shown, indicates an increase in seismic impedance, a negative pulse a decrease. (Figures (b) & (c) from Rondenay et al., 2017)

describes the seismic impedance as a function of incidence angle, both P and S velocity, and density. Discontinuities with a significant contrast in seismic impedance are the Moho and the discontinuities affiliated with the MTZ, which can be sampled and mapped by earthquake waves.

When an earthquake releases seismic energy at source A, it is affected by variations in seismic properties along the path it takes to the seismometer at point B. Particularly, when an incoming P wave is transmitted and converted into P and S waves at a horizontal discontinuity below the recording station B (see Figure 3.1 (b)), the first P arrival is observed to be followed by a delayed, similar looking, secondary arrival in the seismogram recorded at station B (see Figure 3.1 (c)). This delay is a consequence of the P to S converted wave travelling with the slower S wave velocity. The difference in arrival time can then be used to give an estimate about the depth of the discontinuity (Rondenay, 2009). The strength and polarity of the amplitude relative to the first arrival's amplitude indicates magnitude and type of discontinuity. A positive pulse with respect to the initial arriving P pulse describes an increase in acoustic impedance downward. A negative pulse marks a decrease. As the pulse on the recording increases, so does the contrast between the two media (Rondenay, 2009). This theory can not only be used

for incoming P waves but also for incoming S waves and other phases, e.g., an incoming S wave that is converted into a P wave. In the latter case, the seismograms have to be flipped in time since the incident direct S wave is arriving later than the converted P wave. These converted waves can be used to map the subsurface by isolating the seismic impedance contrast information carried in the recorded converted wave (Rondenay, 2009).

3.2 Receiver Functions

Approximately 40 years ago, Vinnik (1977) and Langston (1979) developed methods to directly image the contrasts at which earthquake waves are converted. The central aim of these methods is to isolate the converted signals and remove the influence that the earthquake's source-time function has on these signals. The latter step is necessary because the shape, size and polarisation of waves emitted by earthquakes vary depending on the mechanism, location and magnitude of the earthquake. This results in differences in the recorded seismograms, although the same discontinuities below seismic stations are sampled by incoming waves. Consequently, the traces must be freed from effects of the source signature. An earthquake recording that is free from effects of the earthquake's source signature and, ideally, only contains energy originating in the conversion of the incoming wave is called receiver function (RF) (Langston, 1979). To successfully extract and image these contrasts, suitable data have to be selected followed by a few necessary processing steps, which are both explained in the following sections.

3.2.1 The Incident P-Wave

Not all earthquake recordings are equally amenable to the calculation of receiver functions. In general, only seismic waves in the range from ca. 30 to 98° epicentral distance are suitable for receiver function analysis because of arrival complications introduced by raypaths outside of this range (Rondenay, 2009). Teleseismic waves (>30° epicentral distance) and their conversions arrive earlier than primary phases (e.g. PP, PPP, PkP, PcP, etc.) and are thus isolated from these (Rondenay, 2009). Additionally, triplications from the mantle transition zone are avoided when only teleseismic arrivals are taken into account (Stein and Wysession, 2003). Another advantage of considering exclusively teleseismic waves is that the arriving

wavefronts can be assumed to be planar across arrays of several hundred kilometers (Rondenay, 2009). The assumption of an incoming planar wave is convenient for the development of imaging methods, as will be seen in Section 3.3. Furthermore, local and regional ($<30°$ epicentral distance) recordings' ray parameter and polarisation direction tend to be more affected by location errors (Rondenay, 2009). On the other end of the range, earthquake waves originating from $>98°$ epicentral distance are diffracted at the core mantle boundary (CMB) and are therefore neglected in the calculation of receiver functions to avoid misinterpretations of the signal (Stein and Wysession, 2003). In theory, receiver functions can be computed from any type of incident wave (direct S and P, multiples pP, PP, SS, or even scattered wave energy). However, incident P waves arriving from teleseismic distances ($>30°$epicentral distance) are the simplest to interpret and process (Rondenay, 2009). Additionally, phases other than the direct P-wave are subject to scattered wave energy from previously arriving phases. Hence, signal to noise ratio is often too low to successfully interpret the receiver function (Rondenay, 2009). This thesis solely focuses on receiver functions computed from incident, direct P waves.

3.2.2 Partitioning of the Signal

To isolate the energy originating in conversions of incident P wave, the converted wave's energy needs to be separated from the energy of the incident wave field. Seismometers are generally not oriented parallel to the incoming wave, but record seismic energy along three Cartesian axes in the North-South, East-West and upwards vertical directions. The energies recorded from both incident and converted wave are therefore distributed on all three components of the seismometer. To isolate the particle motions of the P and S waves, a new set of axes can be matched with the direction of the particle motions by simple algebraic rotation (Rondenay, 2009). The first of two rotation steps is to rotate the horizontal axes of the recorded seismogram from North-South (N) and East-West (E) into radial (R) and transverse (T) axes so that the RZ-plane is parallel to the horizontal direction of the incoming P Wave (see Figure 3.2 (a)). In a horizontally-layered, isotropic medium, this rotation by the back azimuth from North to earthquake location limits the P and SV particle motions to the RZ plane (see Figure 3.3 (b)).

This rotation is expressed as follows:

$$\begin{pmatrix} \mathrm{R} \\ T \\ Z \end{pmatrix} = \begin{pmatrix} -\cos\gamma & -\sin\gamma & 0 \\ \sin\gamma & -\cos\gamma & 0 \\ 0 & 0 & 1 \end{pmatrix} \begin{pmatrix} N \\ E \\ Z \end{pmatrix}, \tag{3.2}$$

where N, E and Z are time samples from the recorded seismogram, γ the back azimuth and R,T and Z the time samples of the rotated seismograms (Rondenay, 2009). The transverse component ideally results in a zero trace (in a horizontally layered, isotropic medium) as seen in Figure 3.3 (b). A nonzero-transverse component is an indicator of anisotropy and/or a dipping layer. This rotation has little to no effect on the vertical component and is only efficient as long as the incoming wave is near-vertical. Since this is not always the case and most incidence angles lie approximately between 10° and 30°, another rotation can be performed (Rondenay, 2009).

To further isolate the P and SV wave energy motion, R and Z axes are projected into L and Q components. This is done by rotation of the R-Z plane around the transverse axis by the incidence angle of the P wave so that the L axis matches the particle motion of the P wave as visualised in Figure 3.2 (c). The incidence angle to the vertical, which is also the angle of rotation, can be found with the help of the surface P velocity α and the theoretical ray parameter p, which can be estimated via the tau-p tables for 1-D global models (Crotwell et al., 1999). Then, the RTZ components can be projected into the new coordinate system using

$$\begin{pmatrix} L \\ Q \\ T \end{pmatrix} = \begin{pmatrix} \cos i_\alpha & \sin i_\alpha & 0 \\ -\sin i_\alpha & \cos i_\alpha & 0 \\ 0 & 0 & 1 \end{pmatrix} \begin{pmatrix} Z \\ R \\ T \end{pmatrix}, \tag{3.3}$$

where Z, R and T are time samples, $i_\alpha = \sin^{-1}(p\alpha)$ is the incidence angle and L, Q and T are the rotated time samples (Rondenay, 2009; Vinnik, 1977). After this rotation, the P wave energy is almost completely isolated with some minor leakage from the shear SV particle motion (see

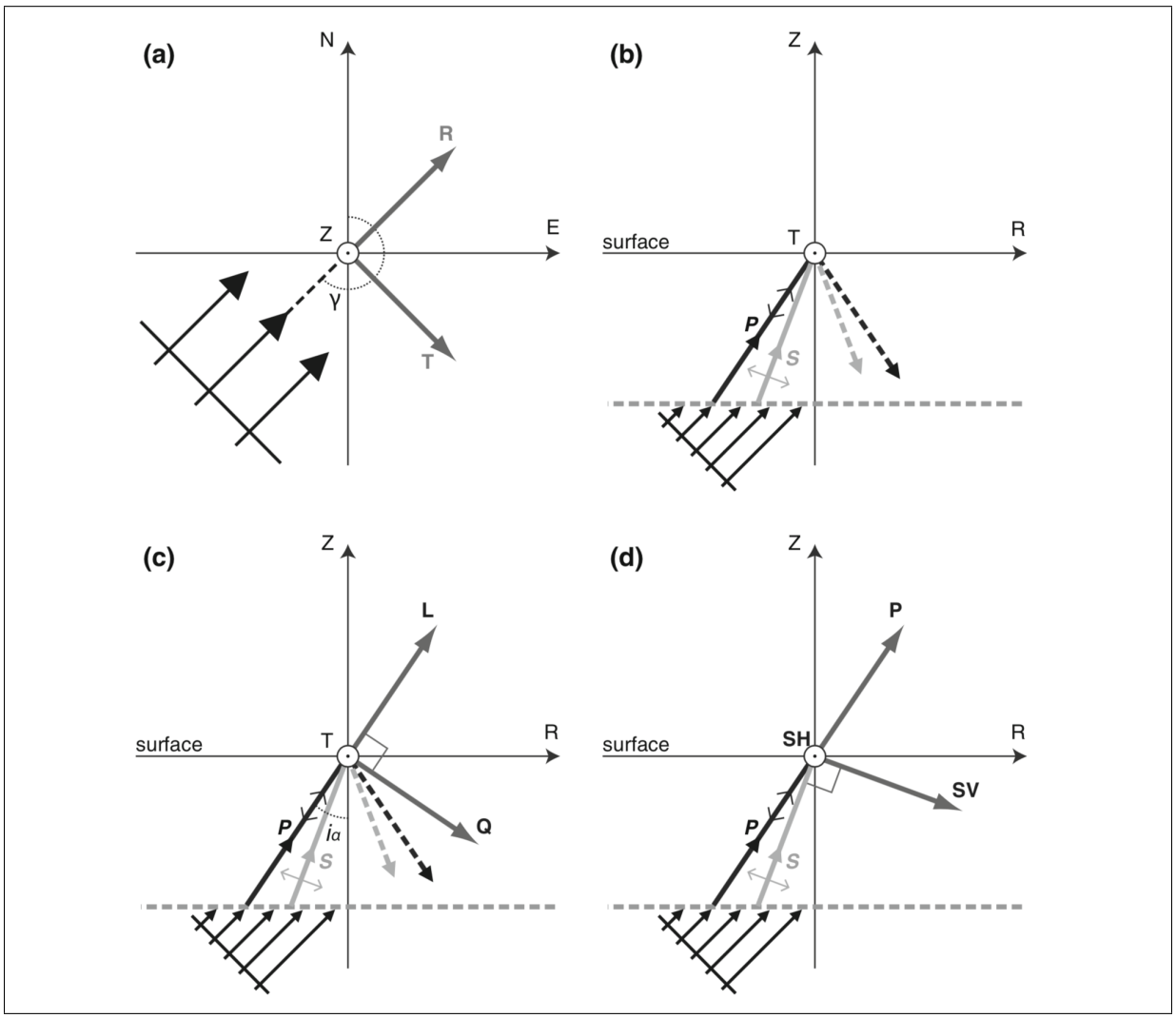

Figure 3.2: Schematic overview of the projection/rotation steps necessary for isolating the converted signal. **(a)** Algebraic projection of the 3 component seismogram from NEZ to RTZ by the back azimuth γ. The R axis then coincides with the horizontal direction of the incoming P wave. **(b)** Cross section of the situation after the first rotation in (a). The horizontal dashed line describes a boundary at which a planar incident P wave is converted. The propagation direction of the converted P wave is shown in solid black and the converted S wave's one in solid grey. The polarization is indicated by the open arrows and the surface reflections are shown as dashed arrows. **(c)** The second rotation from RTZ to LQT by the incidence angle i_α. After this rotation the L axis is parallel to the P wave's polarization direction. **(d)** Alternative rotation from RTZ to P-SV-SH that isolates the particle motions entirely. Figure 3.3 shows the effect of the rotation on the data. (Figure from Rondenay, 2009)

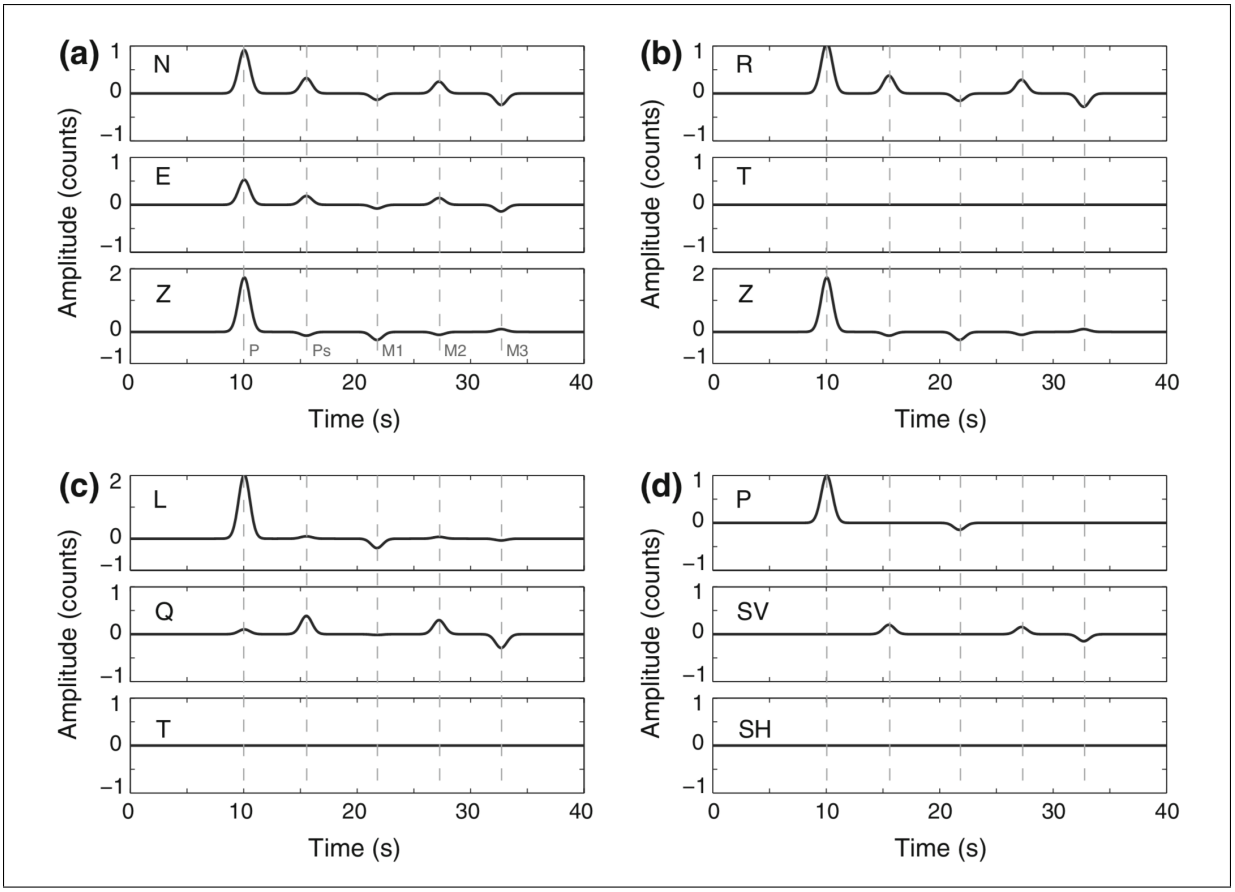

Figure 3.3: Isolation of the converted signal by projection of a recorded earthquake signal, as shown in Figure 3.2. The synthetic data is created with the RAYSUM software package (Frederiksen and Bostock, 2000) for an incident P-wave with back azimuth $\gamma = 210°$ and a ray parameter $p = 0.08s/km$, recorded at a single station. The incident P wave samples an isotropic model with 40 km-thick horizontal layer ($\alpha_0 = 6.0km/s$, $\beta_0 = 3.4km/s$, $\rho_0 = 2,600kg/m^3$) over a half-space ($\alpha_1 = 8.1km/s$, $\beta_1 = 4.5km/s$, $\rho_1 = 3,500kg/m^3$). **(a)** N–E–Z. The phases that can be observed are: the direct P arrival, the converted Ps arrival, and the surface multiples M1, M2 and M3. **(b)** R-T-Z. **(c)** L-Q-T. **(d)** P-SV-SH. (Figure from Rondenay, 2009)

Figure 3.3 (c)). This leakage is caused by the minor difference in ray parameter of the incident P and the converted S wave (Rondenay, 2009).

A different approach to the second rotation, which designed to eliminate leakage in the signal on the instruments between P and SV particle motions, is the rotation of the RTZ components into the P, SV and SH components by using a method based on the free-surface transfer matrix (Bostock and Rondenay, 1999; Kennett, 1991). The free-surface transfer matrix is used to take both incidence angles of P and SV/SH waves into account and projects the axes so that they match the particle motion (Rondenay, 2009). Additionally, it attempts to eliminate effects of the free-surface, i.e. down-going waves (see Figure 3.2 (d)). This rotation is expressed as

$$\begin{pmatrix} P \\ SV \\ SH \end{pmatrix} = \begin{pmatrix} \frac{\beta^2 p^2 - 1/2}{\alpha q_\alpha} & \frac{p\beta^2}{\alpha} & 0 \\ p\beta & \frac{1/2 - \beta^2 p^2}{\beta q_\beta} & 0 \\ 0 & 0 & 1/2 \end{pmatrix} \begin{pmatrix} Z \\ \mathrm{R} \\ T \end{pmatrix} \tag{3.4}$$

where R, T and Z are defined as above, P, SV and SH axes contain the isolated P, SV and SH particle motions respectively, α and β are the P and S velocities at the near-surface, and $q_\alpha = \sqrt{1/\alpha^2 - p^2}$ and $q_\beta = \sqrt{(1/\beta^2 - p^2)}$ are the respective vertical slownesses. In theory, the latter rotation isolates the P and the converted SV particle motion completely (see Figure 3.3 (d)) and should be a vast improvement to the previous two methods. In practice, teleseismic imaging is not carried out under perfect conditions. The above transformations are all based on the assumption of a one-dimensional, horizontally-layered, isotropic Earth. Seismic anisotropy in the subsurface, dipping layers and wave-scatterers are common and will cause leakage between all axes. Furthermore, near-surface velocity estimation errors will result in an error in the transformation matrix (note that this also affects the rotation from RTZ to LQT). These are a few reasons why the difference between the last two transformations is often negligible (Rondenay, 2009). After the isolation of the particle motions, the recordings are still heavily influenced by the shape of the pulse recorded from the earthquake.

3.2.3 Deconvolution

The goal of the deconvolution is to separate seismic impedance contrasts, commonly referred to as the ground's impulse response, which carries information about the subsurface below a

station, from the effects of the source and the seismometer's impulse response. In addition to the earthquake's effect on the recording, the type of seismometer used to record earthquakes around the world differs vastly and affects the seismograms in various ways (Havskov and Ottemoller, 2010). In general, seismograms can be viewed as a convolution of the earthquake's source-time function, which is the displacement as a function of time at the earthquake location, the ground's impulse response, and the impulse response of the seismometer (Langston, 1979). This can be expressed by the following set of equations:

$$D_P(t) = S(t) * I(t) * E_P(t), \tag{3.5}$$

$$D_{SV}(t) = S(t) * I(t) * E_{SV}(t), \tag{3.6}$$

$$D_{SH}(t) = S(t) * I(t) * E_{SH}(t), \tag{3.7}$$

where $*$ denotes the convolution operator, D is the recorded signal data in projected form on the P, SV and SH components, S the earthquake's source-time function, I seismometer's impulse response and E Earth's impulse response containing the seismic impedance contrasts. Since the real source-time function of the earthquake generally differs from an inverted one, it is assumed that the incoming direct arriving P wave is unaffected by seismic impedance contrasts in the subsurface (Langston, 1979; Vinnik, 1977). That is, Equation 3.5 reduces to

$$D_P(t) \simeq S(t) * I(t). \tag{3.8}$$

Consequently, the signal and instrument's response can be seperated from the Earth's impulse response on the seismometer's other two components by deconvolution.

The simplest and most straightforward method to perform the deconvolution is spectral division (Rondenay, 2009). Theoretically, the traces have to be transformed from time into frequency domain where SH and SV are then simply divided by the P component (Langston, 1979):

$$E_{SV}(\omega) = \frac{D_{SV}(\omega)}{S(\omega)I(\omega)} = \simeq \frac{D_{SV}(\omega)}{D_P(\omega)}, \tag{3.9}$$

where ω is the frequency. In reality, this division is unstable. Noise in the recording and $D_P(\omega)$ approaching zero cause Equation 3.9 to be numerically unstable. A solution to this problem is to regularise the equation. The approach stabilises the equation by multiplying the complex conjugate of the incident signal with both nominator and denominator of Equation 3.9 and

adding a regularisation parameter to the denominator afterwards (Langston, 1979; Owens et al., 1984). This prohibits the denominator from approaching zero:

$$\hat{r}(\omega) = E'_{SV}(\omega) = \frac{D_{SV}(\omega)D_P^*(\omega)}{D_P(\omega)D_P^*(\omega) + \varepsilon} \tag{3.10}$$

where $'$ denotes the regularised solution, $\hat{}$ indicates the Fourier transform, the superscript * marks the complex conjugate and ε is the damping factor (Rondenay, 2009). If the deconvolution is successful, the *SV* trace is free from effects of both instrument and source pulse, and performing the inverse Fourier transform on $\hat{r}(\omega)$ results in the radial receiver function $r(t)$. Exchanging D_{SV} with D_{SH} in Equation 3.10 would result in a transverse receiver function which is beyond the scope of this thesis. Note that deconvolving the P from the P component results in a single peak on the trace around the arrival time of the P wave—in an ideal case (and $\varepsilon = 0$).

As a consequence of the rough assumption of the P trace being the source signal, noise in the recordings and often inaccurate velocity estimates in previous steps, the deconvolution is not performed under perfect conditions either. Therefore, the quality of the results may vary considerably (Rondenay, 2009). After the deconvolution, recordings from different earthquakes can easily be compared since they only contain the seismic impedance contrasts. In principle, one should be able to create images from individual receiver functions. This is seldom possible in practice because the signal to noise ratio is too low. The signal to noise ratio can, however, be improved by stacking the traces.

3.3 Traveltime Correction and Stacking

To be able to stack the receiver functions and enhance the imaging quality, it is essential that the receiver functions are traveltime-corrected prior to the stacking. Teleseismic waves are attenuated in a series of ways. Travelling from an earthquake to a station they are subject to scattering, geometrical spreading, intrinsic attenuation etc. (Stein and Wysession, 2003). Stacking the traces results in a constructive sum of the signal and a destructive sum of the noise. The simplest form of receiver function stacking is based on the assumption of a horizontally-layered, isotropic medium and an incoming planar wave shown in Figure 3.4 (Rondenay, 2009). The traveltimes of receiver functions depend on the ray parameter of the incoming wave as seen in Figure 3.4 (b). To stack receiver functions originating from different earthquakes coherently,

the traces must be move-out corrected, i.e., time-corrected for their varying incident angles (Rondenay, 2009).

To calculate the move-out correction and stack receiver function coherently, the traveltimes to conversion depth h have to be found. Since direct P and converted Ps are both propagating from the discontinuity to the surface, the traveltimes of the receiver functions are equal to the difference in traveltime of the delayed, converted Ps wave and the incident P wave, to the discontinuity. This differential traveltime, henceforth referred to as receiver function traveltime, can be expressed by the equation

$$T_{P_s}(p,h) = \int_{z=0}^{z=h} (\sqrt{1/\beta^2(z) - p^2} - \sqrt{1/\alpha^2(z) - p^2})dz \tag{3.11}$$

where z is the depth (positive in downward direction), p is the ray parameter, α and β the P and S velocities (Gurrola et al., 1994; Rondenay, 2009). In Equation 3.11, it is assumed that the ray parameter of both incoming P and converted S waves are the same, i.e., $p_P = p_{Ps}$. The assumption of the ray parameters being equal is an approximation and only sufficiently accurate for arrivals from teleseismic distances, which are converted in the upper mantle (Rondenay, 2009). Equation 3.11 can be discretised into a sum by assuming a model of finite isotropic layers:

$$T_{P_S}(p,h) = \sum_{i=0}^{i=n(h)} \left(\sqrt{1/\beta^2(z_i) - p^2} - \sqrt{1/\alpha^2(z_i) - p^2}) \right) \Delta z_i, \tag{3.12}$$

where z_i is the thickness of each layer i (Rondenay, 2009).

The travel times of the receiver functions are corrected by calculating the move-out time for each receiver function's ray parameter and depth. The move-out is found by computing the difference between the receiver function's traveltimes and the traveltimes of an arbitrary reference ray parameter p_0 (Rondenay, 2009):

$$\Delta T_{Ps}(p,h) = T_{Ps}(p,h) - T_{Ps}\,(p_0,h) \tag{3.13}$$

This means that the travel time difference $\Delta T_{Ps}(p,h_j)$ for each time-sample t_j in a receiver function $r(t_j)$ at hypothetical depth h_j is computed since the move-out varies with depth. Then, this traveltime difference is applied to the timing of every sample. The time-correction is easiest to perform in the frequency domain and followed by a linear stack in the time domain. A stacked

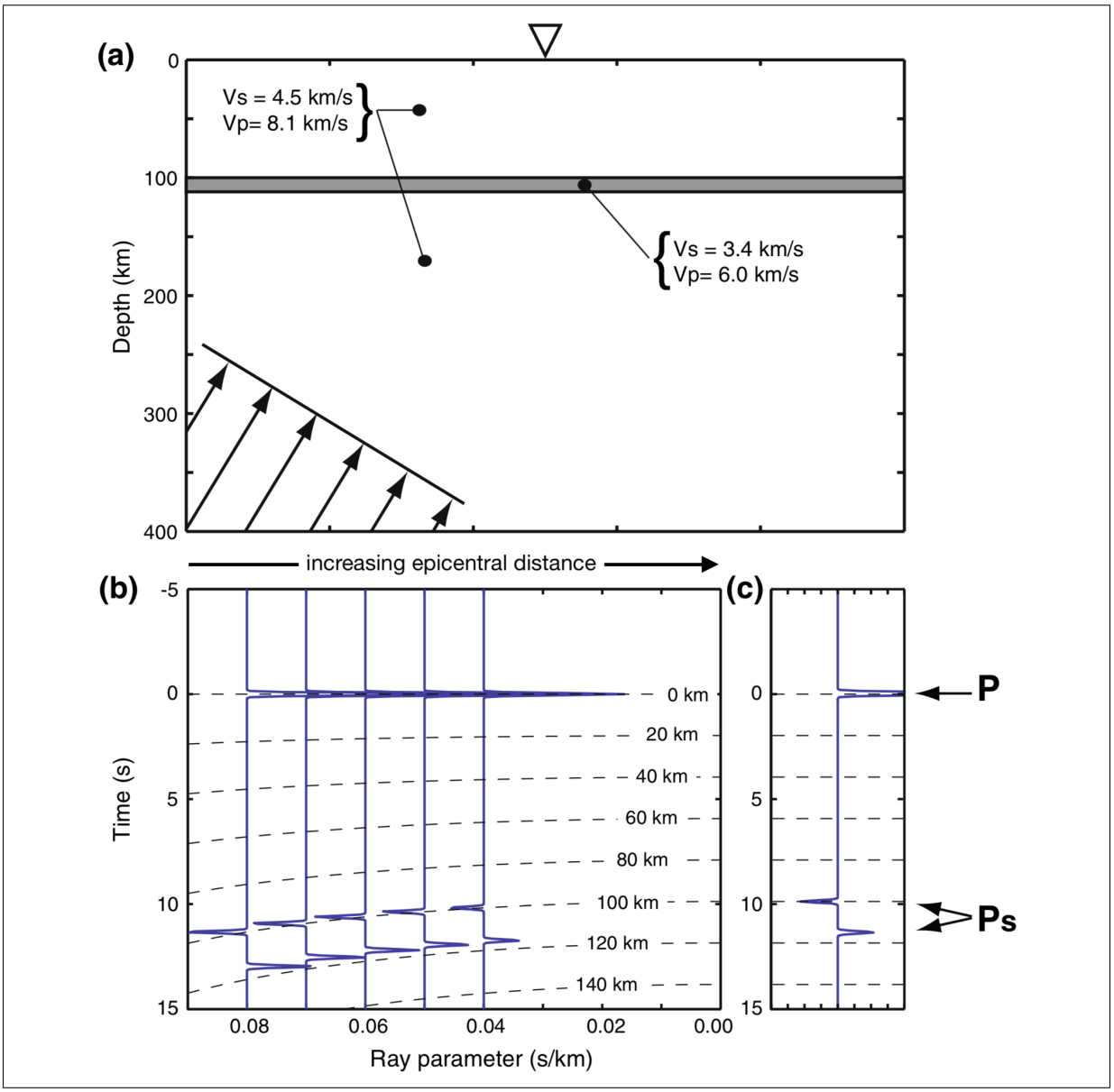

Figure 3.4: Traveltime correction and single station stacking for P to S converted waves. **(a)** Model used to calculate receiver functions from incident P waves of a range of incident angles with recording station as upside-down triangle. The velocity model is isotropic and consisting of a horizontal low-velocity layer (100–112 km depth) enveloped by half-space. The line normal to the arrows marks an incoming planar wave. **(b)** Receiver functions plotted side by side as a function of ray parameter with incident P arrival at $0s$. The dashed lines mark the theoretical arrival times for Ps converted waves for a given depth. The $Ps-P$ differential time is increasing with decreasing epicentral distance. **(c)** Stacked receiver function. The stacked receiver function is calculated by summing receiver functions of varying incident ray parameters along the dashed traveltime curves in (b) and projecting it for a reference ray parameter ($p_0 = 0s/km$). (Figure modified from Rondenay, 2009)

receiver function of N traces can be expressed by

$$R(t) = R(h(t)) = \text{IFT}\left[\sum_{k=1}^{N} \hat{r}_k(\omega) e^{i\omega\Delta T_{Ps}(p_k,h(t))}\right], \tag{3.14}$$

where IFT is the inverse-Fourier-transform (Rondenay, 2009). The move-out corrected stack of receiver functions calculated with Equation 3.14 may be plotted as a function of time or depth as seen in Figure 3.4 (c). Array data, i.e., receiver functions that were computed as a part of an array of seismic stations, can be plotted in pseudo 2D profiles depending on the separation of neighbouring stations (Rondenay, 2009).

Creating pseudo 2D profiles by plotting single station stacks side-by-side provides the clearest images of the subsurface as long as the station separation is larger than the receiver function aperture at the depth of investigation (see Figure 3.5 (b)). The disadvantage of single station stacking, however, is the spatial averaging that is introduced by summing receiver functions with a variety of incidence angles (see Figure 3.5 (a), Rondenay (2009)). At 410km and 660km depth, for example, the receiver function aperture of incoming rays can be as wide as 320km and 570km, respectively. In the likely case of a dipping converter along the aperture, the stacks sum destructively when the receiver functions are stacked at a single over all azimuths and distances. Thus, it can neither reproduce dips nor sudden jumps in arrival time introduced by structures such as tectonic boundaries (Rondenay, 2009). Disregarding the spatial averaging, juxtaposing single station receiver function stacks can provide a great overview of regional variations in subsurface structure; especially in regions where the density of seismic stations is not high enough to use other methods requiring a high station density (Havskov and Ottemoller, 2010).

3.4 Common Conversion Point Stacking

A station separation that is smaller than the receiver function aperture at the depth of investigation opens the possibility of stacking receiver functions according to their conversion points (see Figure 3.5 (c)). This method, which was introduced by Dueker and Sheehan (1997), originates in the theory of common midpoint gathers (CMP) used in reflection seismology, and provides an improved lateral resolution compared to the single station stacks (Rondenay, 2009). The receiver functions are grouped into equally spaced bins at either one

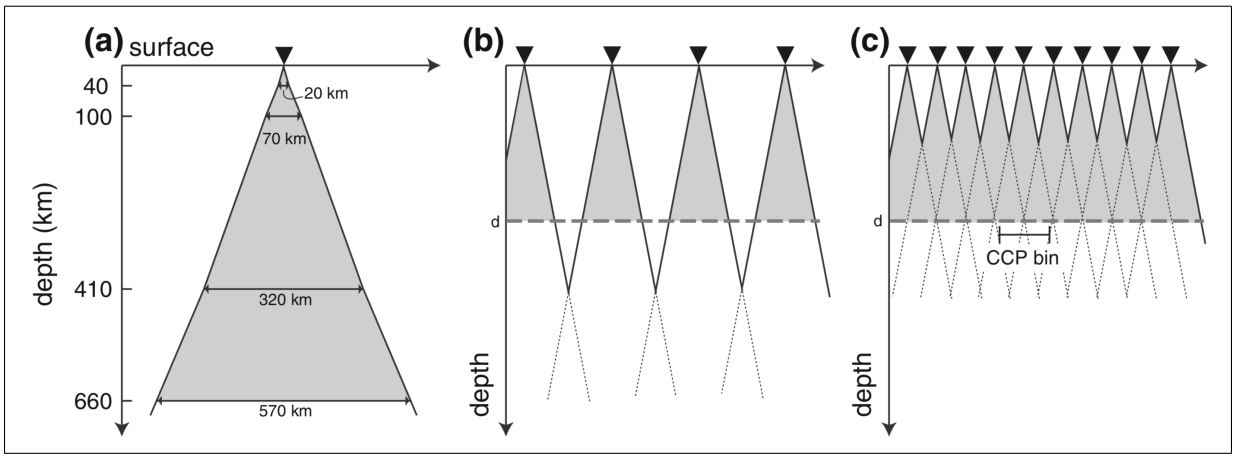

Figure 3.5: **(a)** Schematic image of the receiver function aperture. Due to the different angles the earthquake recordings taken at a single station cover a certain area or aperture; i.e., the P wave can be converted to an S wave on a diameter below a station that becomes larger with depth. This image gives an overview of the largest apertures of Ps conversions at the depths of the Moho, 100 km, 410 km and 660 km. **(b)** A pseudo 2D profile can be constructed by juxtaposing single station receiver function stacks. However, summing of recordings of the aperture causes spatial averaging. **(c)** When the station separation is small enough, earthquake recordings of different stations overlap and can be stacked in bins corresponding to the receiver functions conversion points. (Figure from Rondenay, 2009)

depth or over a range of depths and then stacked accordingly. The conceptual procedure is shown in Figure 3.6. First, the theoretical travel paths of the *Ps* converted waves are calculated from their conversion point at depth h to the surface, using a background velocity model, e.g. IASP91 (Kennett and Engdahl, 1991). This provides an approximation of both the location of the theoretical conversion point and the receiver function traveltime from the surface to the hypothetical depth h (a method for the three-dimensional case will be presented in Section 4.2.2). In Figure 3.6, the conversion points are denoted as piercing points since they pierce depth h at location x along the surface. The receiver functions are then grouped into bins according to their conversion points. Some bins might not be pierced by receiver functions' travel paths, while others are pierced by several recordings, see empty bin in Figure 3.6. After grouping the receiver functions, they are time-corrected using Equation 3.13. In other words, the receiver function traveltime to depth h is calculated for a vertical incidence ($p = 0$) through the same velocity model. Note that this traveltime must be shorter than any other receiver function traveltime to depth h. After shifting the receiver functions according to their difference in traveltime to the vertical theoretical traveltime, they are stacked and the signal is enhanced for depth h. Bins are then juxtaposed, again, to provide a pseudo 2D cross section of

the subsurface. When this is done for a series of successive depths, the image is focused over the entire depth range (Rondenay, 2009).

The disadvantage of common conversion point stacking is the underlying assumption of a horizontally-layered, isotropic Earth. When the subsurface under investigation contains dipping layers, for example, this method introduces imaging errors. Another receiver function method is based on an inverse scattering approach to recover perturbations of the elastic properties in the lithosphere (Bostock et al., 2001). This can be done using any type of heterogeneous model since the incident wave energy is back-propagated to its origin (Rondenay, 2009). Although migration can, in theory, be done using any type of seismic model, the background velocity model must be more accurate and the station density must be significantly higher than the one necessary for the calculation of common conversion point stacks (Rondenay, 2009). Variations in a discontinuity's topography make single station stacking ineffective due to the destructive spatial averaging associated with the method. For migration, on the other hand, not only is a dense seismic network necessary but so is an accurate velocity model; both of which are not present in the case of the large East-African continent. In conclusion, the currently most efficient method to image sharp discontinuities below the African continent using receiver functions is the common conversion point stacking method.

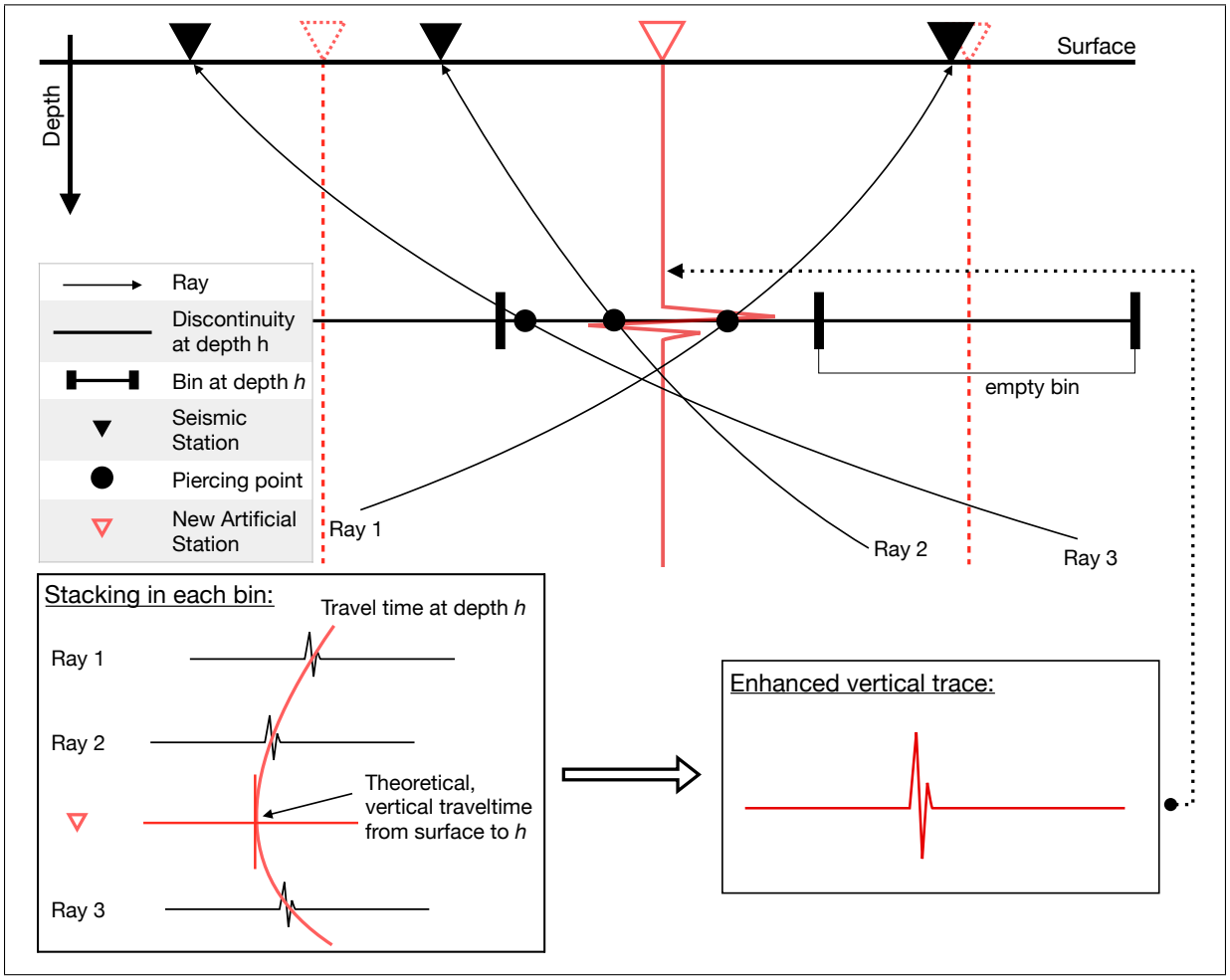

Figure 3.6: Schematic figure describing the common conversion point stacking procedure. A description of the elements in the figure can be found in the legend on the left of the figure's centre. **(Top)** Receiver function travel paths recorded at three different stations (Rays 1, 2 and 3) sample and pierce the same discontinuity at depth h at approximately the same horizontal location. The discontinuity at depth h is divided into equally spaced bins. The red trace shows the stacked trace. The red, dashed artificial stacking locations describe empty bins; i.e. bins that are not pierced by any receiver functions at depth h. **Box, bottom left:** The receiver functions piercing one bin are collected and shifted in time to match the theoretical, vertical traveltime from the surface to depth h of the bin. **Box, bottom right:** After shifting the traces. they are stacked coherently. As a result, the signal is enhanced.

Traditionally, the common conversion point (from now on also CCP) technique has been used at to map local and regional variations in topography of the Moho and the MTZ discontinuities (Dueker and Sheehan, 1997; Niu et al., 2004). However, these discontinuities vary in topography at continental and even global scale, which calls for a global implementation of the common conversion point stacking method. Only recently has worldwide seismic station coverage become dense enough to raise the interest in global common conversion point stacking. In 2017, a global receiver function database was published through project GLImER. GLImER established an automated workflow to calculate receiver functions from publicly available seismic data and build a global database with an ever-expanding catalogue of receiver functions. The GLImER database opened up the possibility to focus on a range of global applications of receiver functions; among them a harmonic decomposition method to infer anisotropy in the lithosphere (Farestveit, 2017) and an automated inversion for seismic velocities in the crust (Drottning, 2017). Common conversion point stacking of receiver functions is a great addition to further expand the catalogue of methods exploiting this database. It facilitates the worldwide investigation of lateral variations in crustal thickness and topographical variations of the MTZ discontinuities.

Chapter 4

Data and Method

This chapter serves two purposes: First, it will present the receiver function data of project GLImER (Rondenay et al., 2017) used later in this thesis to survey the Cascadia subduction zone and the East-African continent. Without a global data set of receiver functions no attempt could have been made at creating a global common conversion point stacking method. Secondly, a three-dimensional common conversion point stacking method is developed by expanding the two-dimensional common conversion point stacking method presented in Section 3.4 to the third dimension. The method implements the common conversion point stacking method for a global, three-dimensional grid of common conversion bins to group and stack receiver functions of the GLImER database. The new implementation of the common conversion point method will be elaborated in three steps. First the grid is created, then, the travel paths are calculated and finally receiver functions are binned and stacked. Afterwards, the inclusion of crustal reverberations to improve stacking results will be discussed. At the end of the Chapter, the method will undergo synthetic testing before being applied on real data in the following Chapters 5 and 6.

4.1 Data

Until recently, a global common conversion method would have been fruitless. Global coverage of seismometers was scarse (Rondenay et al., 2017) and the density of data was not high enough to produce decent results with a global three-dimensional stacking method. Stacking bins would have contained an insufficient number of receiver functions and would not

have provided better results than single station stacking. However, in the past two to three decades seismologists have been reaching the most remote places on Earth with their seismographs. This surge in the deployment of seismometers and the creation of public data-bases (e.g. the Incorporated Research Institutions for Seismology [IRIS-DMC], Observatories & Research Facilities for European Seismology [ORFEUS]), which collect recorded data systematically, has provided an unprecedented density and volume of global seismic data. Project GLImER downloads the earthquake data from these databases and uses it to create its own database of receiver functions in an automated process.

A previous project, the EarthScope Automated Receiver Survey by the Incorporated Research Institutions for Seismology (Crotwell and Owens, 2005), was also concerned with the automated calculation of receiver functions. The aim of the IRIS-EARS project is to globally compute receiver functions, estimate Moho depths and crustal v_P/v_S ratios by H-K stacking (Zhu and Kanamori, 2000). In contrast to the IRIS-EARS project, the goal of GLImER is to efficiently automate receiver function calculation using different approaches to deconvolution and data from several public data centres and publish the computed data for anyone to use (Rondenay et al., 2017). The main difference is that receiver function data can directly be used to create images of the subsurface, as opposed to solely producing values for Moho depth and v_p/v_s ratio (Rondenay et al., 2017). In the following paragraphs, project GLImER's automated process is explained in detail to clarify the origin of the data used in this thesis.

The raw earthquake data used in project GLImER is downloaded by automated web service requests from different public data centres and seismic networks. Until now, the data has been collected from three different institutions: the IRIS Data Management Center (IRIS-DMC), Observatories & Research Facilities for European Seismology (ORFEUS) and the Norwegian National Seismic Network (see Figure 4.1 for an overview of seismic stations used. Rondenay et al., 2017). For each station, only earthquakes with an epicentral distance between 29° and 98° (the reasons that these limits are chosen are explained in Section 3.2.1), and with a body wave magnitude $m_b \geq 5.5$ are eligible for further processing. Earthquakes with a magnitude < 5.5 normally have too low of a signal to noise ratio to give adequate results in the receiver function calculation. The traces are downloaded with a time window of 150 seconds, in which the theoretical P-wave arrival is set to 30 seconds. Both broadband

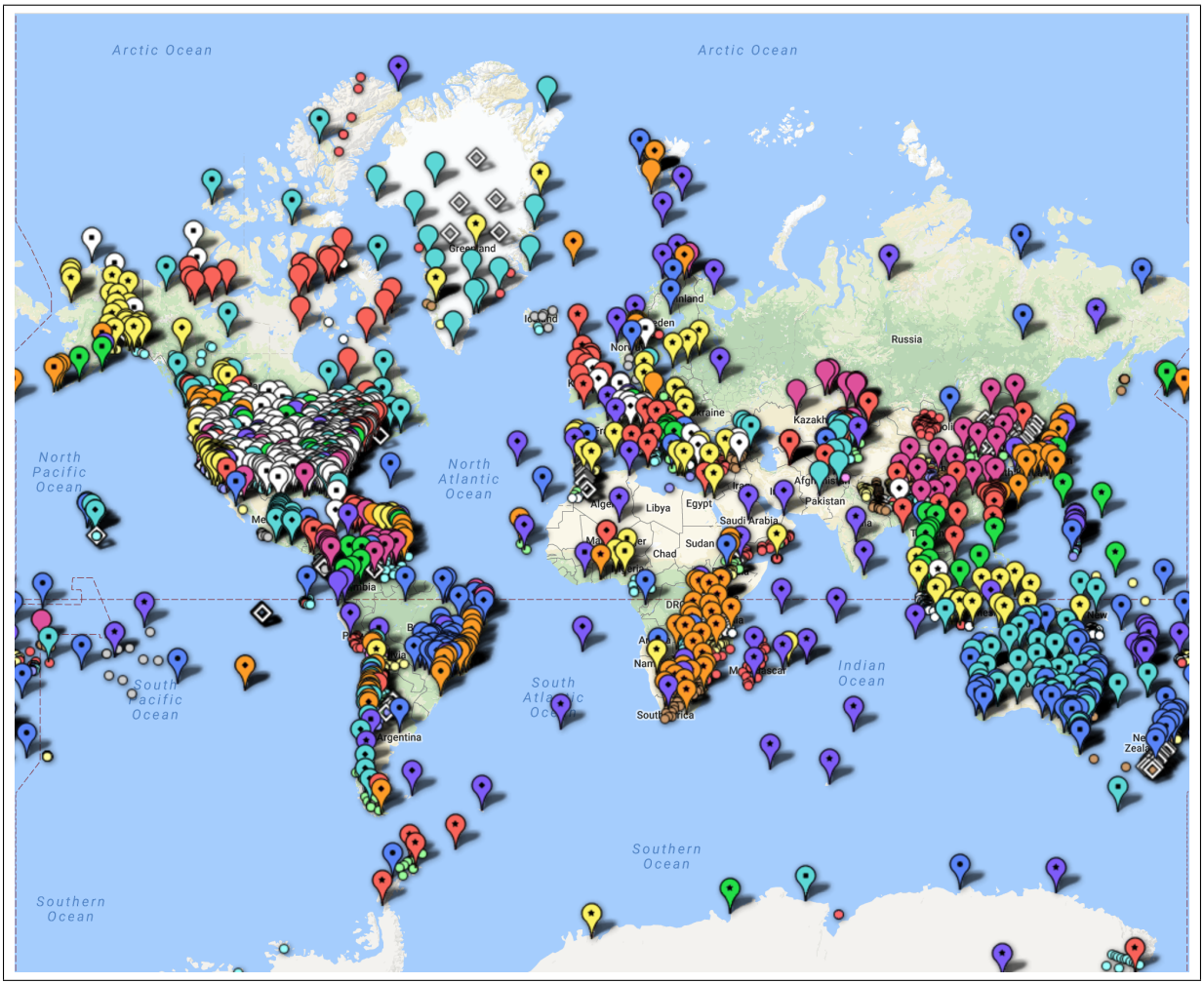

Figure 4.1: An overview of the permanent and temporary stations used for receiver function calculation in project GLImER. Permanent networks are marked by the large pins, whereas temporary networks are marked by smaller circles or diamond-shaped markers. The network TA, for example, which includes all stations of the transportable USArray (Trabant et al., 2012) is indicated by the white pins with a black square.

(BH) and high broadband (HH) data are gathered. After the earthquake data have been downloaded, they are pre-processed.

The pre-processing is divided into three steps. First, all raw traces are tapered using a Hamming taper of 7.5 seconds on each end of the traces. Then, a Butterworth filter from 0.03 to 4.9 Hz is applied to prevent aliasing when downsampling to 10 samples per second. Thirdly, the data is projected to isolate the particle motions. The traces undergo the first rotation from the seismometers N-E-Z into the R-T-Z coordinate system (see Section 3.2.2). Not all traces are equally well suited for further receiver function analysis due to the very high noise levels of some traces.

After being pre-processed, the traces are carefully selected by two separate quality control procedures involving the signal to noise ratio. To find a trace's signal to noise ratio (SNR), the pre-arrival noise from 7.5 to 25 seconds is compared with the P-wave arrival signal from 30 to 37.5 seconds. Traces with a SNR larger than or equal to 8.75 and 10 dB on the R and Z components, respectively, are the only ones to be kept. Additionally, the traces must have a net decay > 0 dB between the arrival signal and the signal contained in the P-coda from 45 to 52.5 seconds (i.e. 15 to 22.5 seconds after the arrival of the direct P wave). This process is repeated for different frequency bands (0.03-1.5Hz, 0.1-1.5Hz, 0.5-1.5Hz). After quality control has been performed, the traces can be analysed.

The receiver functions are computed in a series of steps as a part of the analysis. The polarisation direction of the incident wave is found by performing singular value decomposition on R and T components of the incident wave and used to find the average P-velocity. Afterwards, the R-T-Z components are rotated into the L-Q-T coordinate system (see Section 3.2.2) using the obtained velocity. Following the rotation, the L component is deconvolved from the Q and T components using regularised spectral division with the damping factor based on pre-signal noise (see Section 3.2.3). This deconvolution results in a radial receiver function (deconvolved Q component) and a transverse one (deconvolved T component) as seen in Section 3.2.3.

Now, the receiver functions could be plotted as a function of conversion time or depth, but to obtain the best results, they are band-pass-filtered once again according to the investigation depth. To image the Moho, the receiver functions are filtered with a band-pass-filter (BPF) 0.03-1.5 Hz (P to S converted). Due to the shallow depths of investigation, higher frequencies are necessary in order to image the subsurface at a higher resolution. To image the MTZ, however, the receiver functions are filtered with a BPF 0.03-0.3 Hz since all recorded high frequency data stems from the near-surface and has higher amplitudes than conversions originating at mantle depth (Stein and Wysession, 2003). Furthermore, the contrasts of the MTZ discontinuities are of lesser magnitude (Bina and Helffrich, 1994). Afterwards, they can be plotted as single station stacks (see Figure 4.2), pseudo 2D profiles or 3D volumes (Rondenay et al., 2017). The global common conversion point method developed in the following section takes advantage of this database by collecting all its receiver functions and binning them according to their points of conversion.

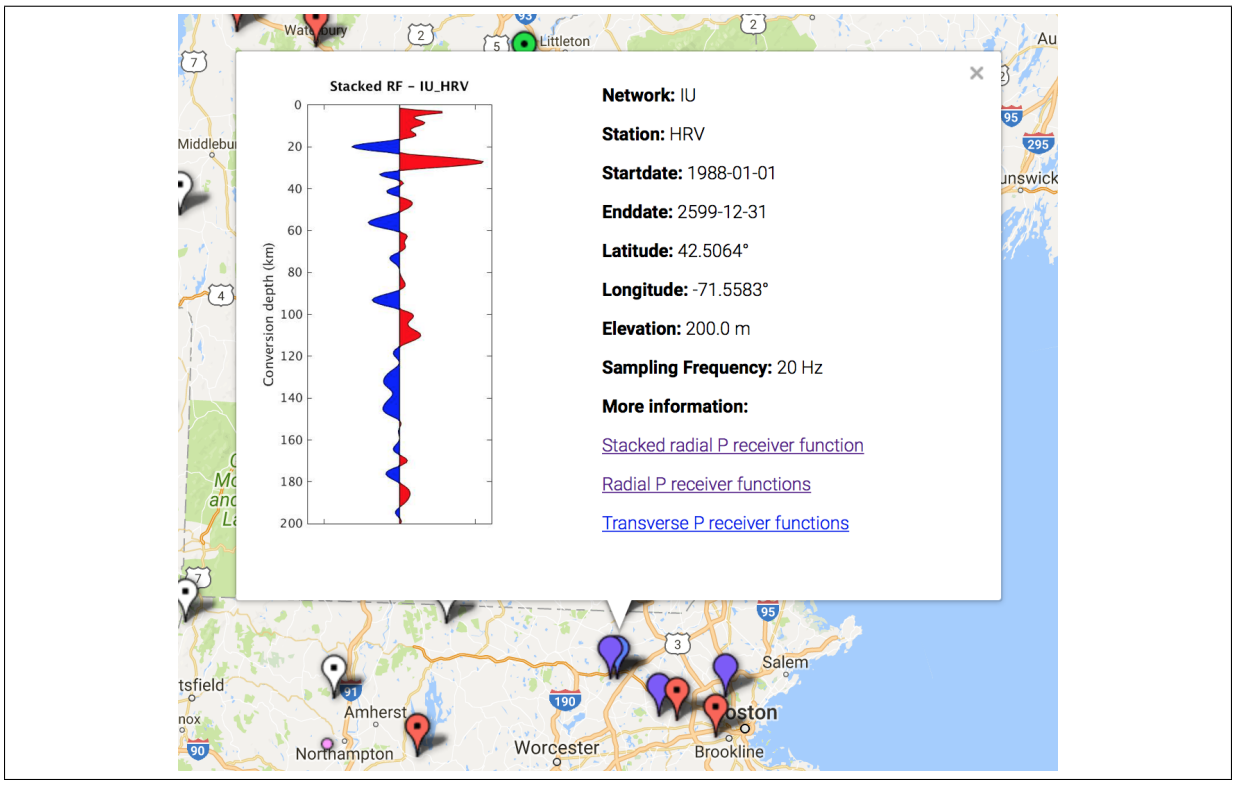

Figure 4.2: The station IU-HRV with station properties next to a single station P receiver function stack as a function of conversion depth approximated by the IASP91 velocity model. In red, positive pulses showing an increase of seismic impulse response with increase of depth and, in blue, negative pulses showing a decrease of impulse response with increasing depth.

4.2 Method

Earthquake recordings are not constricted to a two-dimensional plane as seen in Figure 3.6. Earthquake waves propagate in three dimensions through the Earth and can be described as rays that extent from one point, A, to another point, B, as discussed in Section 3.1. Furthermore, the incident waves are converted in three dimensions. To stack receiver functions globally as a function of conversion points, a new method for common conversion point binning and stacking is introduced by (1) creating a three dimensional global grid of common conversion bins, (2) tracing the receiver functions' travelpaths in three dimensions to their points of conversion, (3) binning the receiver functions as a function of conversion bin and depth, and (4) correcting for traveltime and stacking the receiver functions in their bins. This stacking procedure facilitates the investigation of subsurface discontinuities, such as the Moho and the boundaries of the MTZ, at global scale in three dimensions with greatly improved lateral resolution. To further enhance the stacking results at lithospheric depth, the procedure will be modified to include

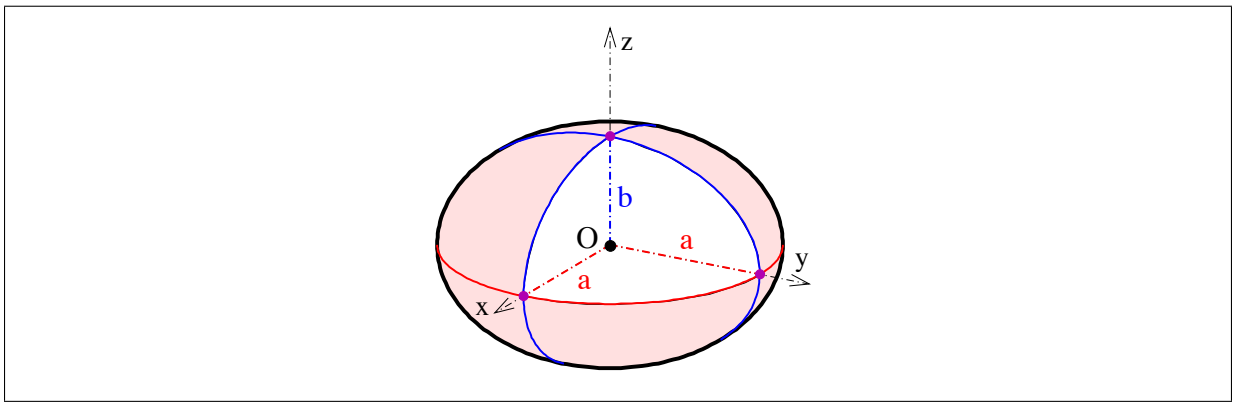

Figure 4.3: Schematic figure of an oblate spheroid similar to the shape of the Earth. *O* is the origin (centre of the Earth) and *x*, *y* and *z* are the Cartesian coordinate axes. *a* denotes the radius of the major axis (distance from the equator to Earth's centre) and *b* the radius of the minor axis (distance from the poles to Earth's centre). (Created by 'Ag2gaeh' and distributed under a CC BY-SA 4.0 license.)

multiples for an improved mapping of the Moho. This will be tested with synthetic data at the end of this section.

4.2.1 Common Conversion Bin Grid

The first hurdle in achieving a working common conversion point stacking code is that the stacking grid must be divided into equally sized common conversion bins to impartially distribute receiver functions between the bins. This can be done in various ways. If the area of investigation is relatively small (few hundred kilometres in diameter and up to 200km deep), all geographical locations can be projected into a local, tangential, Cartesian coordinate plane with its centre in the middle of the array. Afterwards, it can be divided into equally sized rectangles to ensure even binning of all receiver function piercing points. Especially in shallow 2D-surveys imaging the Moho, e.g. (Tauzin et al., 2016), this practice is sufficiently accurate. For larger study areas, projections of the geographical locations into a tangential 2D-plane are not accurate enough. A projection would introduce approximation errors as a result of the variation in metric length of 1° longitude as a function of latitude (see Figure 4.3 and table 4.1). Niu et al. (2004) tackled the issue with the use of circular common conversion bins along a line. In this thesis, a different approach is used.

The grid developed here is based on geographical locations which define a set of equally sized rectangles on the surface of the Earth. The grids origin coincides with the intersection of prime meridian and equator. To make sure that the rectangles are equally sized, the rectangles'

Latitude in [°]	Latitude in [$km/°$]	Longitude in [$km/°$]
0°	110.574	111.320
15°	110.649	107.551
30°	110.852	96.486
45°	111.132	78.847
60°	111.412	55.800
75°	111.618	28.902
90°	111.694	0.000

Table 4.1: List over variations in metric length of a 1° latitude and longitude due to Earth's ellipticity. Calculated with equations from Osborne (2013, Chapter 5) and in respect to the WGS84.

corner points need to be calculated with respect to the changing metric length of 1° longitude as a function of latitude. Approximately equally-sized bins can be calculated by using the kilometre per longitude relation dependent on latitude for an ellipse (see table 4.1). This relation stems from the Mercator spheroid projection equations (Osborne, 2013):

$$\Delta_{long}(\phi) = \frac{\pi a \cos\phi}{180^\circ \sqrt{1 - e^2 \sin^2\phi}} \tag{4.1}$$

where ϕ is the latitude and e eccentricity defined by the major and minor axes a and b, respectively, and the relation $e^2 = (a^2 - b^2)/a^2$ (see Figure 4.3). For the calculations, a and b are defined as $a = 6378.137km$ and $b = 6356.752km$ and are taken from the 1984 World Geodetic System (WGS84). In this approximation of the Earth, the metric length of 1° latitude varies as a function of latitude as well. However, the variations are so negligible that a relation of $1^\circ \ latitude \hat{=} 1^\circ \cdot 2\pi \cdot R_E/360^\circ = 1^\circ \cdot 2\pi \cdot 6371km/360^\circ = 111.195km$ is assumed (see Table 4.1).

The resulting common conversion point grid can be seen in Figure 4.4. This is an example of a rough grid with average bin size of $310,000km^2$, which would introduce heavy spatial averaging. In reality, the grid size is customisable; i.e. the bin's or gridcell's square sizes can be changed. A great advantage comes with customisable grid size. If the area of study is densely populated with stations and recorded data, the gridcell size can be decreased to allow for a higher resolution (see Chapter 5.2 for an example). If the area of study is large and station

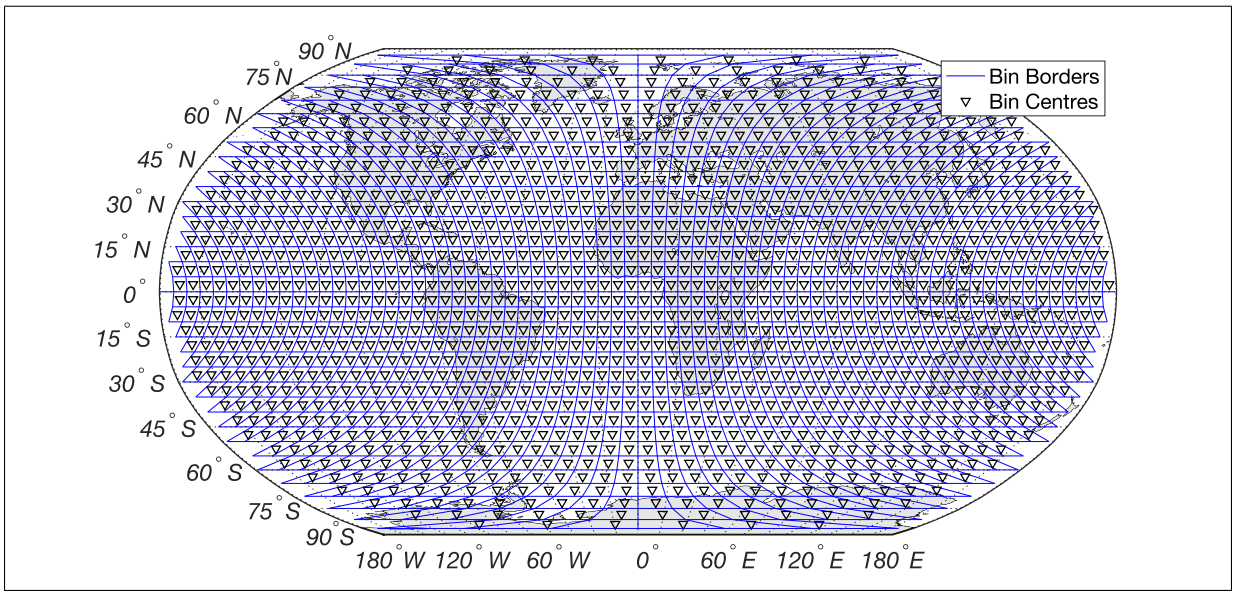

Figure 4.4: Example of a CCP grid with a bin size of 5° by 5°. The downwards pointing triangles are the bin's centres while the blue lines show the CCP grid's borders.

and data coverage is not as dense, on the other hand, lateral resolution can be sacrificed for a better regional or continental scale view of the subsurface (see Section 6.2). Vertically, the grid follows its geographical corner points. This is theoretically not ideal since the bins become smaller with depth. However, a depth dependent common conversion point grid is difficult to implement in a spherical Earth and the gridcell area at 800km depth is merely 24% smaller than the gridcell area at the surface. For a gridcell size of $(1°)^2$:

$$\begin{aligned}\frac{A_{z=800km}}{A_{\text{Surface}}} &= \frac{(1° \cdot 2\pi(6371km - 800km)/360°)}{(1° \cdot 2\pi(6371km)/360°)^2} \\ &= \frac{(97.232km)^2}{(111.195km)^2} \\ &= \underline{\underline{76\%}}\end{aligned}$$

4.2.2 Ray Tracing

To stack the receiver functions in bins corresponding to their piercing points, their travelpaths have to be found first. Ray tracing is the calculation of a wavefront's travelpath from point A to point B along a line or path. To approximate the receiver function's travelpath from its conversion point to the surface, a backwards method is used here. Instead of tracing the earthquake's ray from the origin to the station, the origin is assumed to be the station which the

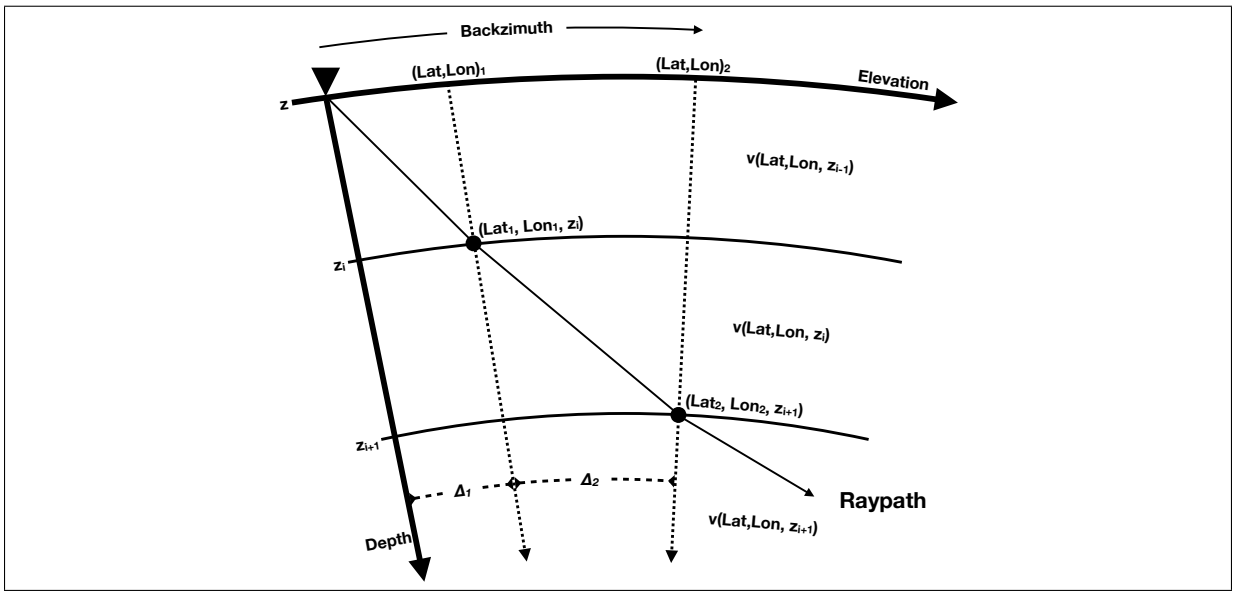

Figure 4.5: Schematic figure describing the raytracing procedure. The downwards pointing triangle is the station location with in (Latitude, Longitude, Elevation). Δ is the epicentral distance. $(\text{Lat,Lon})_i$ is the location of the piercing point at depth z_i where z_0 is the elevation. The raypaths are calculated one-dimensionally in the great-circle plane defined by station location and origin of the earthquake from the station along the back azimuth as denoted at the top of the figure. v denotes both discrete P and S velocity dependent on Latitude, Longitude and depth. See text for further detail.

ray is traced back from. The ray is 'shot' backwards as an approximation for the travelpath. This is done in a one-dimensional manner using a three-dimensional velocity model. That is, a spherically-layered, isotropic earth is assumed, but velocities along the raypath are taken from a three-dimensional model. This is the standard procedure in CCP stacking. Full three-dimensional ray tracing would likely improve the results. However, given the one dimensional assumption of horizontal layers in CCP stacking, which already introduces an error, the improvement might not be worth the computational time; further investigation would be necessary but is beyond the scope of this thesis. First, the tau-p tables (Crotwell et al., 1999) provide the ray parameter as a function of epicentral distance collected from the GLImER database. These are calculated using the one-dimensional velocity model IASP91 (Kennett and Engdahl, 1991). The back azimuth is the direction of propagation and calculated from the earthquake origin versus station location. Then, the ray is 'shot' along the direction of the back azimuth. The complete procedure follows a series of steps explained below and is shown schematically in Figure 4.5.

The travelpaths are calculated within the great-circle plane which is defined by the station location, the origin of the earthquake and Earth's centre. To trace the rays, two sets of equations

are combined: The one-dimensional spherical ray tracing equations from Shearer (2009) and the receiver function traveltime equations from Rondenay (2009). The travelpath's piercing points are found by approximating their geographical location as a function of depth and epicentral distance. The piercing point's depths along the raypath are predefined by the discrete depth vector

$$\vec{z} = [z_0, z_1, z_2, ..., z_n],$$

where $z_0 = -10km$ and $z_n = 250km$ or $z_n = 750km$ depending on the depth of investigation; additionally, if $z_n = 250km$, then $\Delta z = 1km$; if $z_n = 750km$, then $\Delta z = 2km$. The station location is defined as (Lat_0, Lon_0, z) where z is the negative elevation of the station. From z, the ray is shot downwards to the next largest depth z_i in the predefined depth vector $\vec{z}$. The first piercing point is then defined as (Lat_1, Lon_1, z_i). To find the epicentral distance Δ_i between (Lat_i, Lon_i) and (Lat_{i+1}, Lon_{i+1}), a modified version of the following equation is used

$$\Delta\left(p_{\text{sph}}\right) = 2p_{\text{sph}} \int_{r_{\text{tp}}}^{r_e} \frac{1}{\left[(vr)^2 - p_{\text{sph}}^2\right]^{1/2}} \frac{dr}{r}, \tag{4.2}$$

where p_{sph} is the spherical ray parameter in $[s/rad]$, v the seismic velocity and r the radius (Shearer, 2009). To calculate the epicentral distance from one depth to the next, Equation 4.2 has to be discretised to calculate the epicentral distance between to points of conversion:

$$\Delta\left(p_{\text{sph}}, z_i, z_{i+1}\right) = p_{\text{sph}} \frac{1}{\left[(v(z_i) \cdot (z_{i+1} + zi)/2)^2 - p_{\text{sph}}^2\right]^{1/2}} \frac{z_{i+1} - zi}{(z_{i+1} + zi)/2}, \tag{4.3}$$

where r is exchanged with values in $\vec{z}$ to describe the depths. Since the focus lies on imaging the P to S converted wave, the S velocity is used to calculate the epicentral distances between conversion points. Note that the incident P wave is transmitted at a different point than the P wave is converted to an S wave. This difference, however, can only affect the velocities chosen for computing the traveltimes of the incident P wave, not the location of the conversion points of the P to S converted wave. Since this approximation is still an improvement to using a one dimensional model velocity, the calculation of the P wave's transmission points is omitted to save computational time. After the epicentral distance is found, the geographical location of the next piercing point can be calculated using the starting point $(Lat, Lon)_0$, back azimuth, and epicentral distance in radians as arclength. Then, this process is repeated for all z_i.

The traveltimes are computed using Equation 3.11. This equation assumes a horizontally-layered, isotropic medium which is not the case for a spherical Earth. To work around this, the Earth-flattening approximation is applied (Shearer, 2009), i.e.

$$e^{-z_f/a} = r/a \quad \text{or} \quad z_f = -a\ln(r/a), \tag{4.4}$$

where a is the radius of the Earth and r is the distance from the center of the Earth and z_f is the depth in the transformed horizontally-layered Earth. Note that $r = a - z_s$, where z_s is the depth in a spherical Earth. The velocity has to be transformed as well:

$$v_f\left(z_f\right) = (a/r)v(r), \tag{4.5}$$

where v is either the P or S velocity in a spherical Earth and v_f is the transformed velocity. These transformations are put into Equation 3.12 to calculate the receiver function traveltime to conversion depth z_i with the velocities collected above:

$$T_{Ps}(p, z_i) = \sum_{i=i(z)}^{i=i(z_i)} \left(\sqrt{1/\beta_f^2(z_{f(i)}) - p^2} - \sqrt{1/\alpha_f^2(z_{f(i)}) - p^2}\right) \Delta z_f(i), \tag{4.6}$$

where α_f and β_f are the transformed P velocity and S velocities, z the initial station depth/elevation, z_i is the conversion depth and $\Delta z_f(i) = z_f(i+1) - z_f(i)$ the transformed difference in depth between two conversion points. These equations are used in combination with the GyPSuM velocity model.

The GyPSuM velocity model is a three-dimensional, 1°-by-1°, tomographic velocity model for both P and S velocities. It was created by Simmons et al. (2010) and retrieved from the online database of velocity models at the IRIS-DMC (Trabant et al., 2012). This velocity model accounts for large, volumetric velocity changes in both P and S velocities. A comparison of traveltimes between the IASP91 velocity model and the GyPSuM velocity model is shown in Appendix A.2. At each depth the velocity in the model that is closest to the conversion point is taken to calculate the traveltime and epicentral distance to the next conversion point. As an example, the receiver functions' travelpaths of five different stations are calculated using the raytracing method explained above, and are shown in Figure 4.6. After the travelpaths and traveltimes of the receiver functions have been calculated, they can be binned and stacked according to their location of conversion.

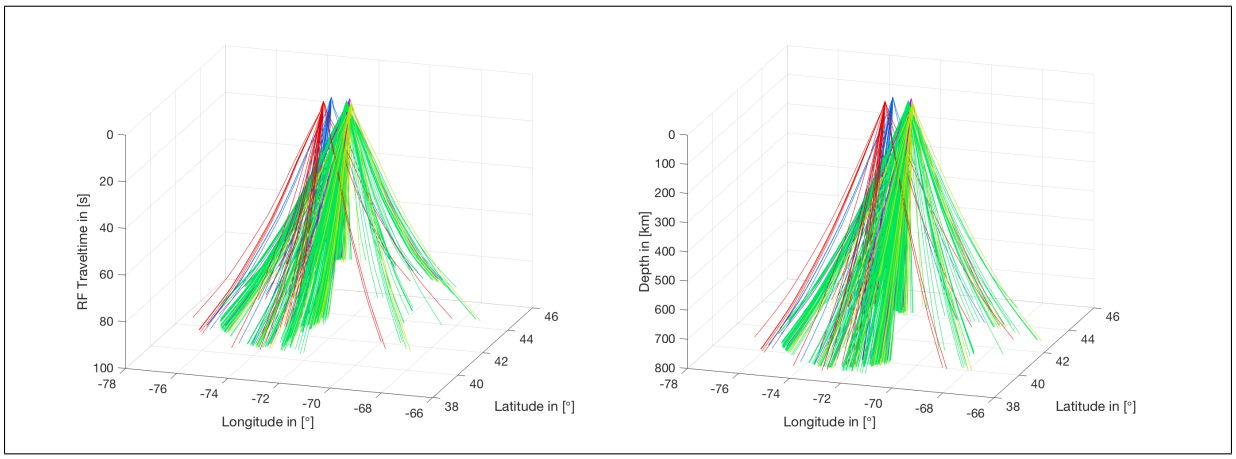

Figure 4.6: Raypaths calculated for five stations North-West of Boston. TA-K62A (blue), NE-QUA2 (red), TA-K63A (pink), IU-HRV (green) and NE-WES (yellow). **(a)** Shows the travelpath as a function of (lat,lon,traveltime). Note that certain paths are shorter than others because the smaller the incidence angle is, the shorter the traveltimes are and hence, the ray stops at an earlier time. **(b)** Shows the travelpaths as a function of (lat,lon,conversion depth).

4.2.3 Stacking

The actual stacking of the receiver functions as a function of their conversion points is done in four steps: (1) collecting the receiver functions that are converted in a certain bin at a certain depth; (2) calculating and correcting the receiver functions' traveltimes by their move-out; (3) stacking the receiver functions at each depth; (4) interpolation of the depth dependent stacks as a function of depth and time. This results in a vertical common conversion bin stack for each geographical bin location as seen in Figure 4.4.

The receiver functions are binned by checking whether their theoretical travelpath pierces a certain bin at a certain depth. This collection can either be restricted to one bin, or the receiver functions of adjacent bins can be included in the stacking of one bin. Since most areas on the globe are still sparsely covered in seismic stations, the volume of data used for the stacking in three dimensions is usually quite sparse, as well. While including receiver functions that pierce adjacent bins in the stacking introduces spatial averaging, which is not wished for usually, it can greatly improve the stacking results in areas with low data density. Although this can smoothen discontinuities with large jumps, it provides excellent results for subsurface structures that only slightly vary in their topography compared to the lateral extent (e.g. the 410-discontinuity and 660-discontinuity). In the spatial averaging approach, the receiver functions of all 8 adjacent bins are included, such that all adjacent bins overlap. A schematic of the two bin collection procedures for a given bin is shown in Figure 4.7.

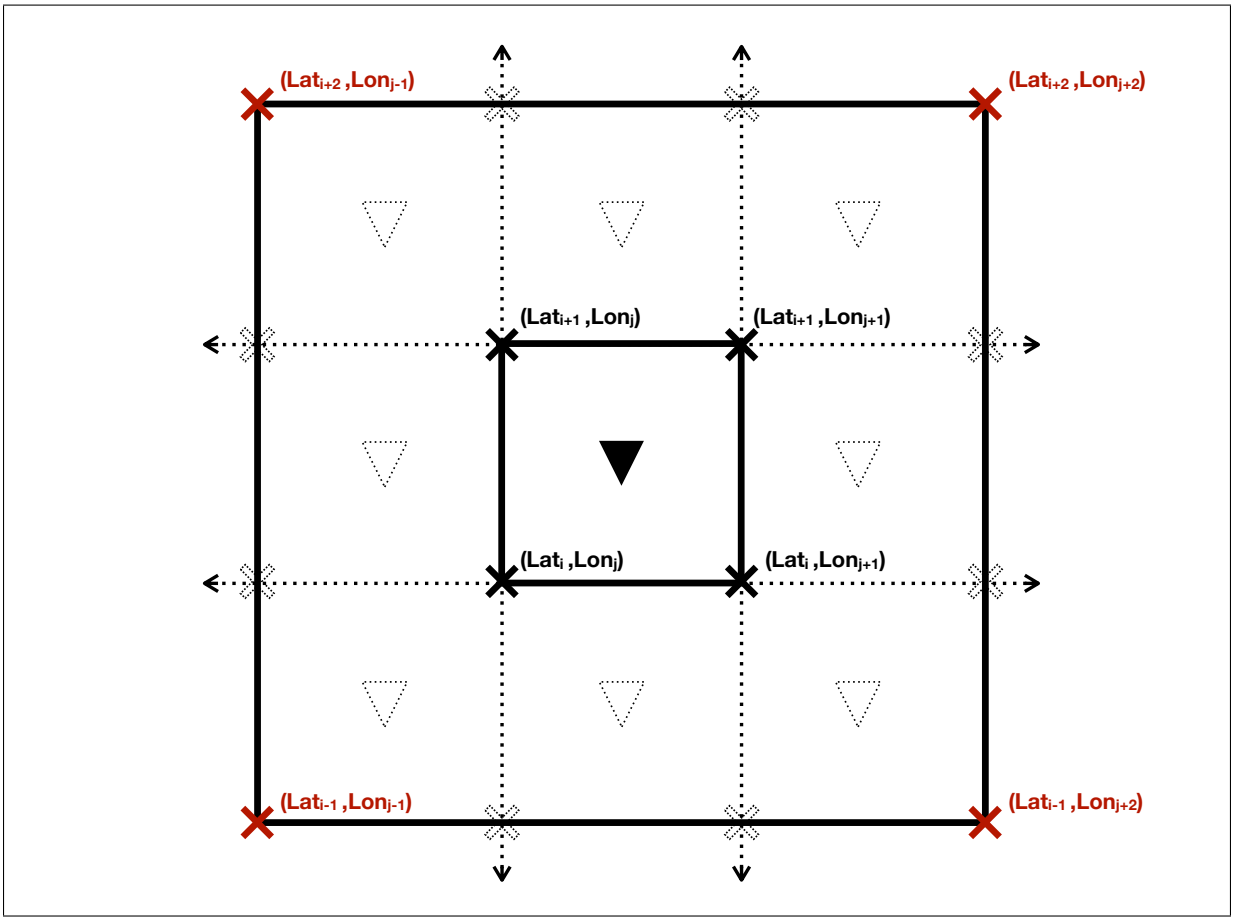

Figure 4.7: Schematic drawing of a common conversion bin describing the receiver function collection procedure. The upside done triangles are the bin centres, the solid triangle marks the bin used in this collection process and the outlined ones are other bin centres. The crosses mark the grid nodes. While the solid crosses mark the nodes for the collection of the current bin, the dashed crosses are used for a different bin. The black solid crosses and black (Lat,Lon) locations describe the nodes setting the boundary for standard CCP stacking without spatial averaging. The red solid crosses indicate the nodes defining the boundaries when spatial averaging is used. For each bin centre and depth, all receiver functions are found that were converted within either of these boundaries.

For each bin and depth, the receiver functions collected in the previous step are time corrected and then stacked. The traveltime correction is done using the same procedure as described at the end of Section 3.3 and seen in Figure 3.6. The receiver functions' traveltimes to the depth of conversion are found using the ray tracing developed in Section 4.2.2. Then, the traces are traveltime-corrected to the vertical, theoretical traveltime which is calculated with the closest vertical velocities in the three dimensional velocity model. After traveltime correction, the receiver functions can be stacked linearly at each depth (see Section 3.3) using

$$g(t_i) = \frac{1}{N}\sum_{j=1}^{N} s_j(t_i), \tag{4.7}$$

where g is the stack, s_j the $j-th$ trace and t_i the $i-th$ sample of trace s_j. Another, improved method of stacking is phase-weighted stacking. Phase-weighted stacking was introduced by Schimmel and Paulssen (1997) and first used for common conversion point stacking by Frassetto et al. (2010). Using the Hilbert transform (see Appendix A.1), the instantaneous phase of all traces is calculated, and depending on the similarity of the traces' phases $\Phi_j(t_i)$, each linear stack at time t_j is given a weight; the larger similarity, the larger the weight:

$$g(t_i) = \frac{1}{N}\sum_{j=1}^{N} s_j(t_i)\left|\frac{1}{N}\sum_{k=1}^{N}\exp\left[i\Phi_k(t_i)\right]\right|^{v}, \tag{4.8}$$

where the part of the equation that is outside of absolute value is the linear stack and the phase weight is calculated within the absolute value. v is the weight determining the magnitude of wanted similarity in instantaneous phase of the traces. If the weights are viewed as a filter, v would determine the filter's sharpness that increases with increasing v. Note that $v = 0$ results in a linear stack. After the stacking is done for every depth of a bin, the stacks need to be interpolated through depth and time.

The traces are interpolated through time and depth of the vertical, theoretical receiver function travelpath. This is done in a simple bilinear interpolation with one stacked trace in time for each stacking depth over an entire depth range. This is depicted and described with Figure 4.8. When this is done for several adjacent bins, they can be plotted in pseudo 2D cross sections and sliced 3D volumes. Although this procedure can be done considering direct conversions only, stacking multiples of the transmitted or converted wave can greatly improve stacking results.

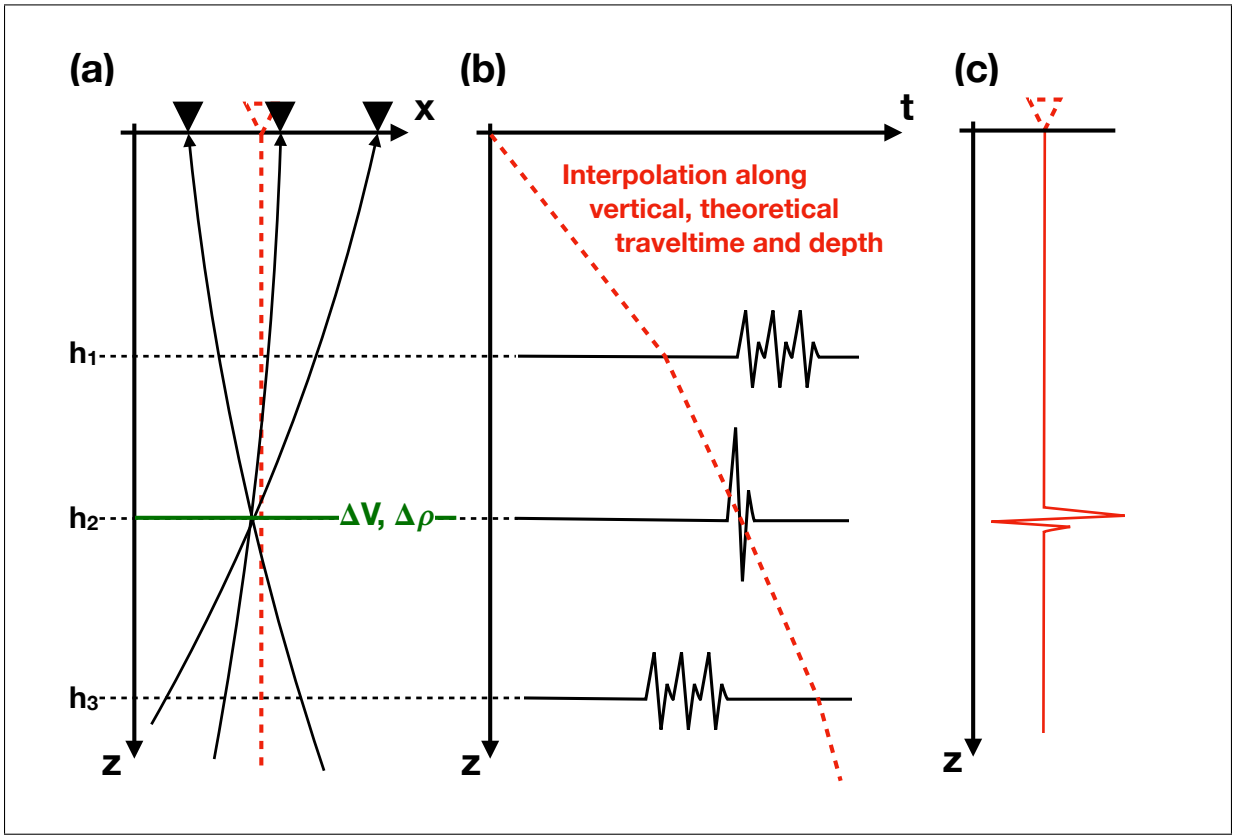

Figure 4.8: The interpolation procedure for common conversion point stacking over a range of depths h_i. **(a)** Geometry of the bin and incident waves sampling a perturbation in seismic properties (green). Note that this is in two dimension to simplify the schematic. The following steps ((b) & (c)) are the same for both two and three dimensions. **(b)** The traces are traveltime-corrected and stacked for each depth, as seen in Section 3.3 and Figure 3.6. Due to the different traveltimes to the conversion depth, this results in incoherent stacking of the traces at depths h_1 and h_3 and coherent stacking at depth h_2 which coincides with the perturbation. Afterwards, the traces are interpolated using the theoretical, vertical traveltimes and conversion depths along the dashed, red line. **(c)** The plot shows the stacked interpolated trace of the bin.

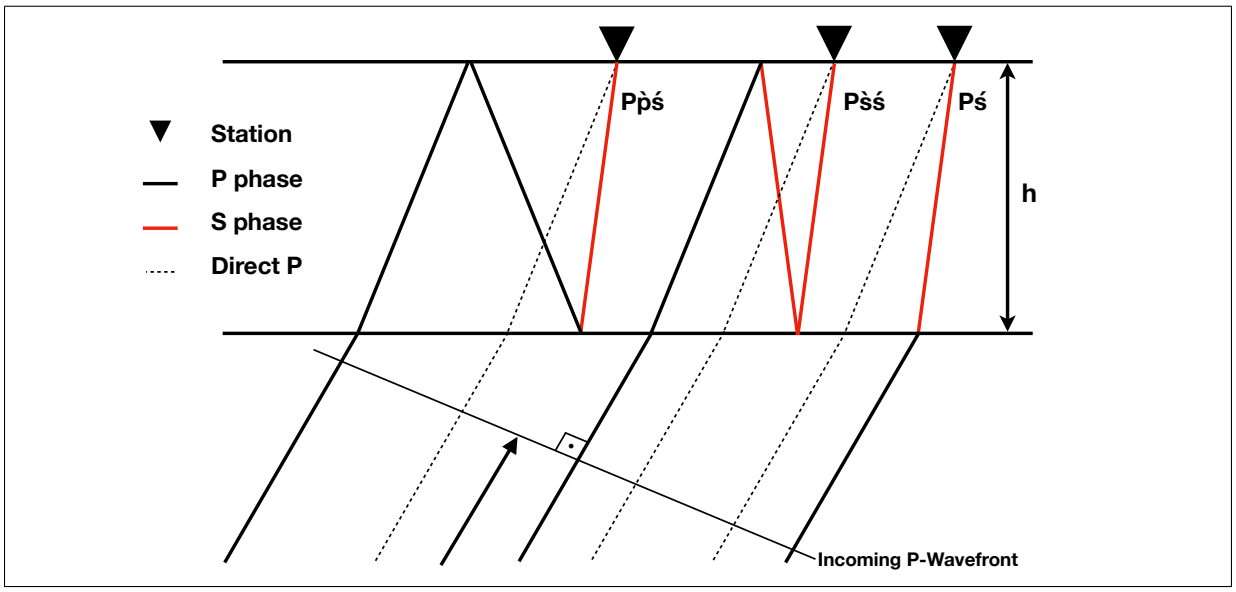

Figure 4.9: Schematic of the travelpath of the different modes

4.2.4 Multiples

After the incident wave is transmitted or converted at a discontinuity, it can be reflected by the free-surface and, again, be reflected or converted to an S wave at the same discontinuity before being recorded at the seismic station. These crustal reverberations and the direct P to S converted wave result in a series of wave modes which all sample the same discontinuity: The *Pś* (the normal P to SV converted) and the multiple modes *Pp̀ś* and *Ps̀ś*, where the capital letter is the incoming, up-going wave, the grave accent ` denotes a free-surface reflected and possibly converted, down-going wave and the acute accent ´ marks a reflected up-going wave. The schematic raypaths are shown in Figure 4.9 (Rondenay, 2009). Due to the reverberations longer travelpath, they are observed at a later time within the receiver function (Rondenay, 2009). Stacking all modes, each time-corrected according to its own traveltime, efficiently enhances the signal of the discontinuities, while it sums the incoherent contaminations destructively. For two reasons, the multi-mode stacking method is only used for lithospheric imaging: (1) The multiples' traveltime to deeper discontinuities would extent further than the records of the data used in this thesis and the arrivals would possibly interfere with arrivals of other, later arriving seismic phases; (2) The travelpath for multiples is much longer than for directly converted waves. Hence, multiples are often attenuated a lot more than direct arrivals. This attenuation is reasonable for lithospheric multiples, but multiples originating in discontinuities beyond the lithosphere will have a too low signal to noise ratio for them to provide any usable data (Havskov and Ottemoller, 2010; Stein and Wysession, 2003).

Traveltime correction has the effect of squeezing the traces, and the traveltime correction for multiples is larger than the traveltime correction for the direct converted *Pś* mode. Thus, the traveltime corrected multiples will have a smaller width of signal than the direct converted *Pś* mode. By filtering each of the modes with a high-cut filter (*Pś* – 1 Hz, *Pp̀ś* – 0.2 Hz, *Ps̀ś* – 0.2 Hz) prior to the traveltime correction, the traces are set to approximately equal signal width after the traveltime correction (Tauzin et al., 2016). Note that even though this widens the recorded signal, the filtering is necessary to ensure coherent stacking of the modes and is done in the computation of all multi-mode stacks for the purpose of the thesis.

The correction for the multiples' traveltimes is rather simple to implement. The traveltimes to conversion depth h are calculated using equations

$$T_{P\grave{p}\acute{s}}(p,h) = \int_{z=0}^{z=h} \left(\sqrt{1/\beta^2(z) - p^2} + \sqrt{1/\alpha^2(z) - p^2} \right) dz \tag{4.9}$$

$$T_{P\grave{s}\acute{s}}(p,h) = 2\int_{z=0}^{z=h} \left(\sqrt{1/\beta^2(z) - p^2} \right) dz. \tag{4.10}$$

Then, in an equal procedure as in Section 3.3, the traveltime differences to the theoretical vertical P to S converted traveltime are calculated for coherent stacking:

$$\Delta T_{P\grave{p}\acute{s}}(p,h) = T_{P\grave{p}\acute{s}}(p,h) - T_{P\acute{s}}(p_0,h) \tag{4.11}$$

$$\Delta T_{P\grave{s}\acute{s}}(p,h) = T_{P\grave{s}\acute{s}}(p,h) - T_{P\acute{s}}(p_0,h)\,. \tag{4.12}$$

After the traveltime correction, the three corrected traces can each be stacked using the stacking procedures described in Section 4.2.3. After each mode is stacked according to common conversion points, the three CCP stacks may be stacked as well. They can be stacked either linearly, phase-weighted (Tauzin et al., 2016) or they can be stacked using a Zhu and Kanamori (2000) inspired method giving a weight to each mode before summing them:

$$MM = w_1 \cdot P\acute{s} + w_2 P\grave{p}\acute{s}, -w_3 P\grave{s}\acute{s}, \tag{4.13}$$

where MM is the multi-mode stack and the weights are given as $w_1 = 0.7$, $w_2 = 0.2$ and $w_3 = 0.1$. Note that owing to seismic reflection's nature of reversing the polarity of the reflected wave, a negative summation with the *Ps̀ś* mode is necessary. When the images are linearly stacked or stacked with simple weights, the coherent discontinuities are constructively stacked,

while the incoherent signals are destructively stacked. Thus, the multiple energy that is seen in the *Pś* CCP stack will also be seen in the final stack, but with a much smaller amplitude; these small amplitude residuals are called echoes (Rondenay, 2009). With phase weighted stacking however, it is possible to remove the incoherent parts since they are not in phase (Schimmel and Paulssen, 1997; Tauzin et al., 2016). To verify the multi-mode stacking method and the phase-weighted stacking in a topographically complicated area, the following section is concerned with testing the method on synthetic data.

4.2.5 Synthetics

To test the method, synthetic data are created along a linear seismic array using the RAYSUM code by Frederiksen and Bostock (2000) and then processed using the method that was developed throughout this Chapter. This test is a quantitative comparison between the different options to calculate the common conversion point stacks. Meaning, data sets will be created and processed with the various binning and stacking procedures described in Sections 4.2.1 and 4.2.3, respectively. The stacks will be calculated by binning and stacking the receiver functions with spatial averaging and without spatial averaging and using simple linear stacking and phase-weighted stacking. Additionally, after calculating the common conversion point stacks for each mode a comparison between three different multi-mode stacking procedures is given.

RAYSUM creates synthetic P-SV-SH receiver functions (see Section 3.2.2) given a layered velocity model, receiver locations and parameters of the incoming wave which are ray parameter and back azimuth. The model is seen in Figure 4.10. The properties of the layers are found in Table 4.2. What is special about this model is the difference in elevation. It is set up to test the elevation dependent ray tracing described in Section 4.2.2. The rest of the model is constructed similar to Model-1 used in a common conversion point study by Tauzin et al. (2016). Note that the chosen model is strongly simplified and does not comply with the theory of isostacy (Mussett and Khan, 2000). However, for the purpose of testing the performance of the raytracing and stacking methods, the chosen model rather satisfies the needs than being an isostatically correct model. What makes the model appropriate are continuous horizontal and dipping discontinuities while being subject to a jump in elevation and, hence, traveltime. A change in crustal thickness would make it difficult to identify issues in the ray tracing and

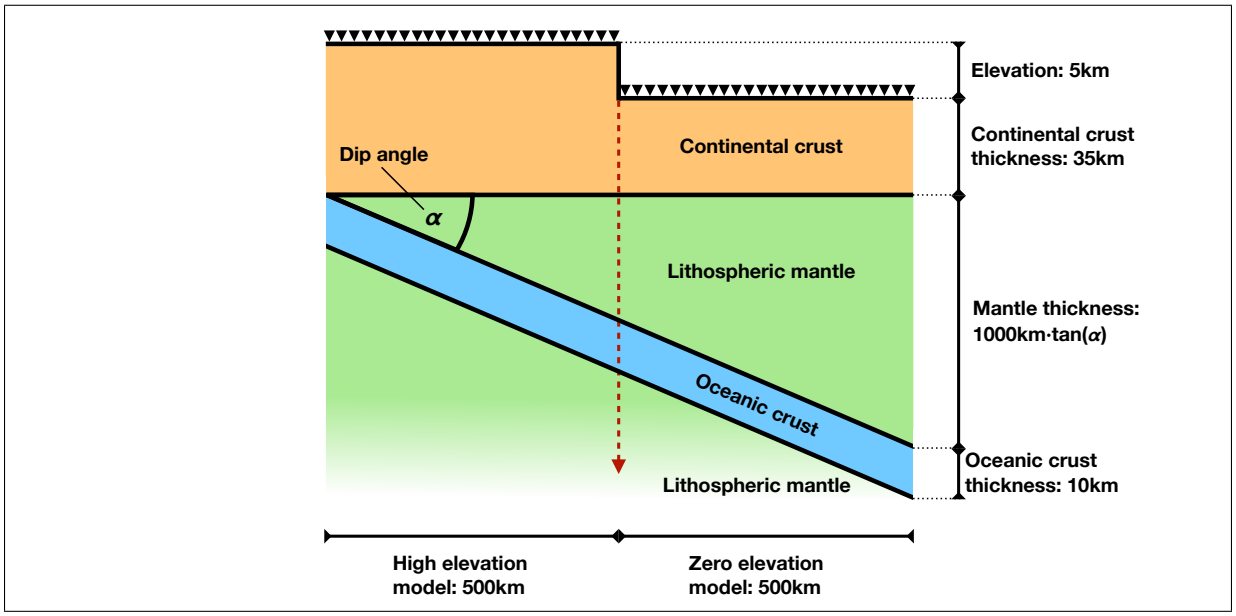

Figure 4.10: Schematic drawing of the model used to calculate the synthetic data. The model consists of two parts of continental crust which are together overriding a dipping oceanic crust. The first western 500km of the cross section is a plateau with an elevation of 5km and the eastern 500km have zero elevation. The first 35km below zero elevation is continental crust which is riding on top of the lithospheric mantle. The layer of oceanic crust starts right below the continental crust in the west and dips towards the east with an angle α. Below the oceanic crust, the model consist of a lithospheric mantle half-space with the same properties as the lithospheric mantle above the oceanic crust. The upside down triangles are seismic stations. The exact properties for each layer can be found in table 4.2. The velocity model for the calculation of the CCP stacks is indicated by the red, dashed arrow in the centre of the model.

Layers	**Density** ρ $[kg/m^3]$	**P-velocity** V_P $[km/s]$	**S-velocity** V_S $[km/s]$
Continental crust	2600	6.66	3.70
Oceanic crust	3500	6.12	3.40
Lithospheric mantle	3500	8.10	4.50

Table 4.2: Properties of the layers used to calculate the synthetic data. For the model geometry, see Figure 4.10.

traveltime correction. Using this model, receiver functions are calculated for each station at the surface of the model. The 201 stations have a separation of 5km along the surface as schematically seen in Figure 4.10. At each station, a total of 14 receiver functions are calculated from incident P waves of different parameters. The P waves' back azimuths are set parallel to the array, pointing towards either end of the line. Since the model is set to an East-West alignment these are $\gamma = [90°, 270°]$. For each back azimuth, seven incident P waves are calculated with the ray parameters $p \in [0.0500, 0.0740]$ in $[s/km]$ and $\Delta p = 0.004$ $[s/km]$, which sums to a total of 2814 receiver functions for each model with dipping angle $\alpha = [5°, 10°, 20°, 40°]$. In Figure 4.11, the data created for a dipping angle of 20° can be seen as a function of trace number and time sample, where $\Delta t = 0.1s$. The trace numbers follow location, then back azimuth and then rayparameter. Hence, the first fifteen traces T_i are $T_1[0km, \gamma_1, p_1]$, $T_2[0km, \gamma_1, p_2]$, $T_3[0km, \gamma_1, p_3]$ $\ldots T_8[0km, \gamma_2, p_1]$ $\ldots T_{15}[5km, \gamma_1, p_1]$. Note that, although the model and setup seen in Figure 4.10 are two dimensional, the receiver functions are processed using the same three dimensional method as developed in this chapter. Afterwards, a two dimensional cross section is extracted from the three dimensional data.

After receiver functions are created for all dipping angles, the data is stacked using a 2.2km-by-2.2km common conversion point grid along the line with 1km vertical spacing. The velocity model used for the ray tracing is a one dimensional model extracted from the centre of the model in Figure 4.10; it is indicated by the red, down-going and dashed arrow. For each angle, the modes are first CCP stacked using linear stacking of the single modes followed by the three multi-mode stacking procedures explained in Section 4.2.4. For an angle of 20°, the two steps are shown in Figure 4.12, which shows the single mode CCP stacks, and Figure 4.13, which shows the multi-mode stacks. The same procedure is done for phase-weighted stacks of

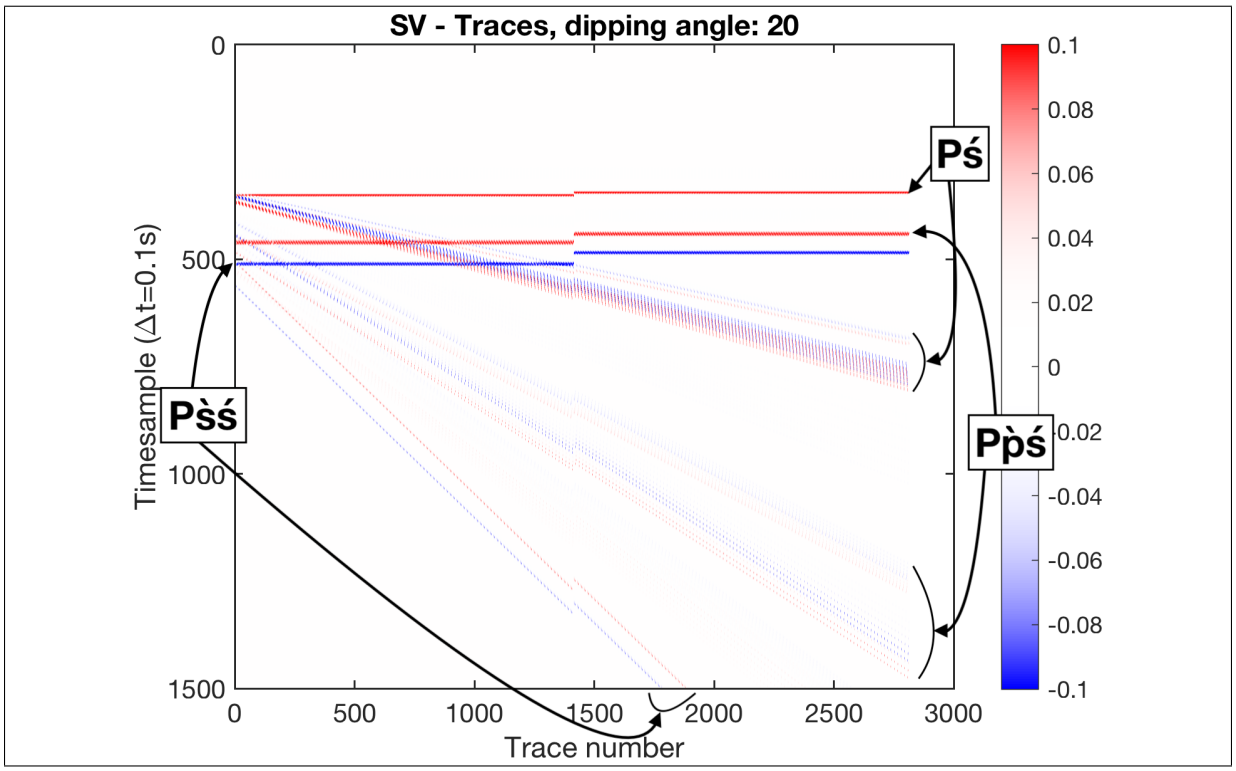

Figure 4.11: Receiver function data for a 20° dipping angle. Important here is the obvious jump in traveltime in the horizontal centre of the data. The jump is introduced by the change in elevation in the synthetic model. Arrows indicate the different modes.

the single modes (see Figures 4.14 and 4.15) and the other three angles. The full set of figures and test combinations is found in Appendix C.

The results of these tests show that the method is successfully imaging the discontinuities, but with certain limitations. The horizontal, continental Moho discontinuity is imaged clearly throughout all tests. This was to be expected since CCP stacking assumes a horizontally layered earth. However, since the velocity model is taken from the centre of each dipping model, arrivals from the western part of the dipping discontinuities are imaged deeper than they are and arrivals in the eastern part will be imaged at shallower depth as seen in Figure 4.12. In the western part, this error is not as apparent as in the eastern part because the traveltime correction induced error for a dipping discontinuity is increasing with increasing depth. This error is also smallest for the *Pś* mode and largest for *Pp̀ś* because of the larger traveltime correction. This is less of an issue at a dipping angle of 5° and 10° than it is for the higher angles, as seen in Appendix C.

The advantage of the phase weighted stacking can already be observed in Figure 4.14, top (compare with Figure 4.12, top). While both linear and phase-weighted stacking have issues with reproducing the dipping layer where the dipping layer crosses the two multiple recordings of *Pp̀ś* and *Pp̀ś*, the phase-weighted stack attenuates the multiples effectively.

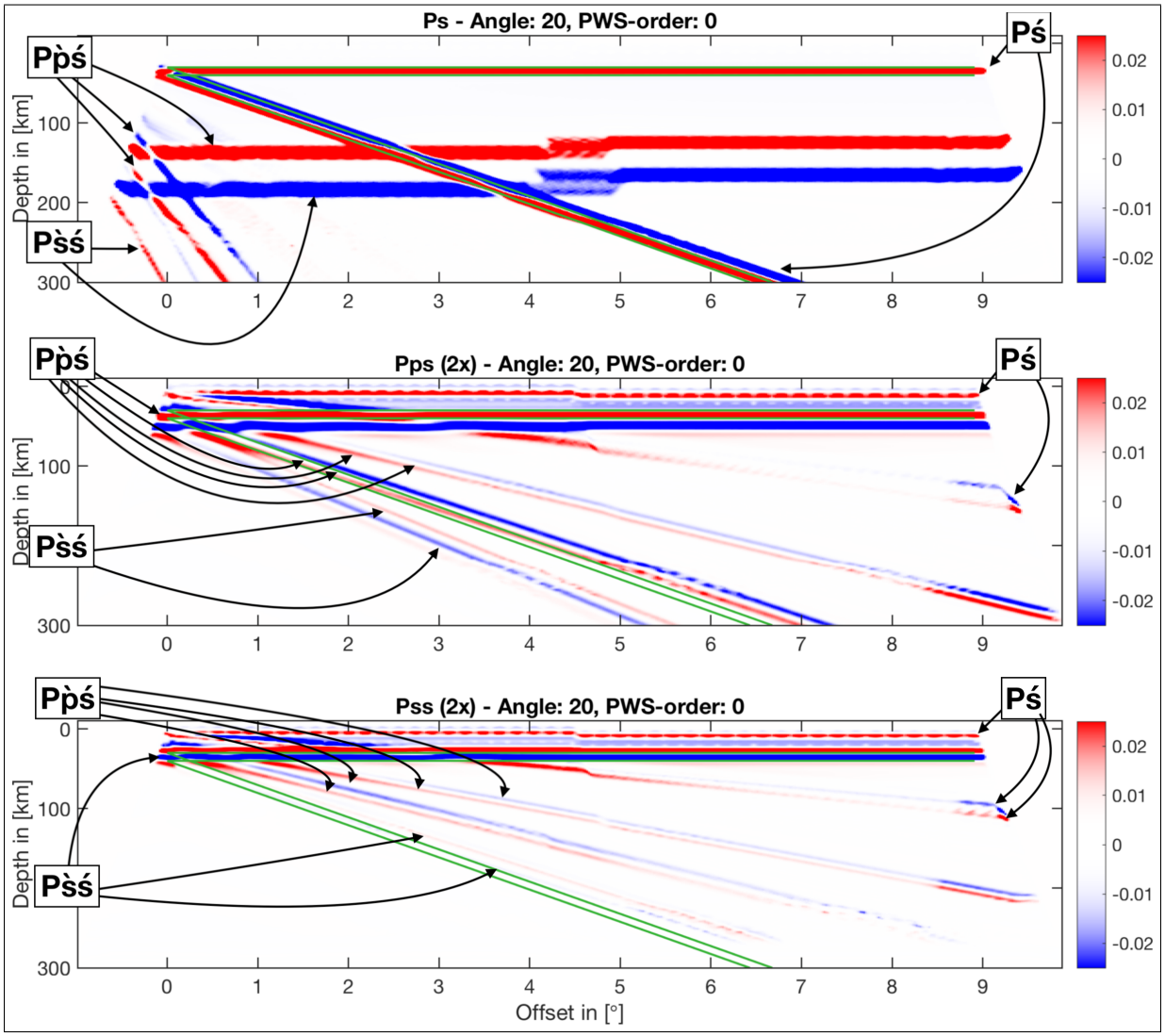

Figure 4.12: CCP stacked receiver functions of a dipping subducting oceanic crust with a dipping angle of 20°, traveltime corrected for the respective modes. Arrows indicate the different modes. Note that the *Pp̀ś* shows more arrows due to a backazimuth and rayparameter traveltime issue originating in the stacking assumption of horizontal layers. The green lines surround both the horizontal, continental Moho and the top of the oceanic crust with a boundary of 5km, so that the discontinuities lie in between those lines if they were imaged correctly. The CCP stacking is done using linear stacking. **Top** The *Pś* corrected. **Centre** The *Pp̀ś* corrected. **Bottom** *Ps̀ś* corrected.

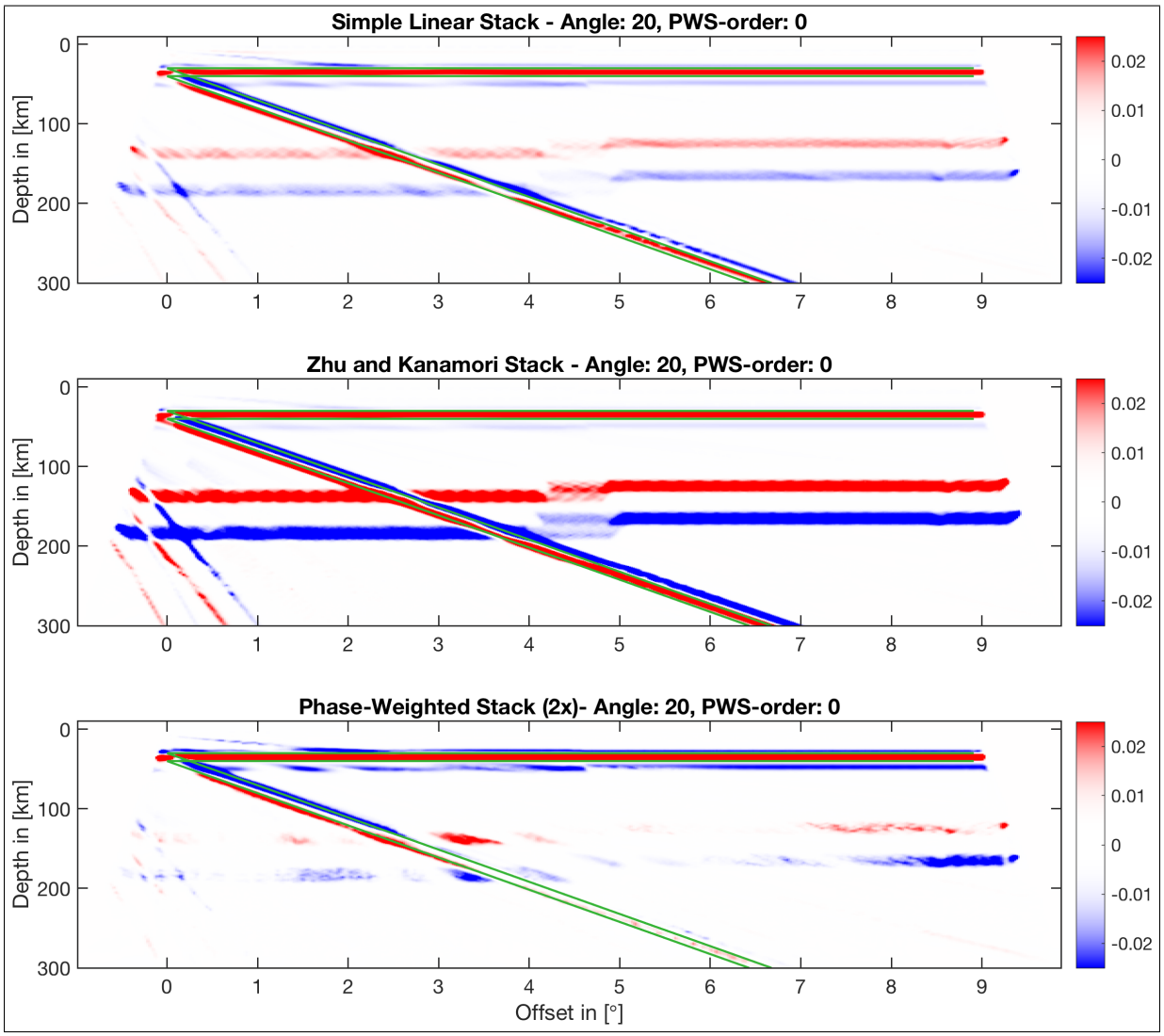

Figure 4.13: Multi-mode stacked CCP stacks of a dipping subducting oceanic crust with a dipping angle of 20°. The green lines surround both the horizontal, continental Moho and the top of the oceanic crust with a boundary of 5km, so that the discontinuities lie in between those lines if they were imaged correctly. The CCP stacking is done using linear stacking. **Top** The linear stack of the 3 modes. **Centre** The Zhu and Kanamori weighted stack. **Bottom** The phase-weighted stack with order of 2. Note that the PWS stack order in the title refers to the stacking of each mode, not the multi-mode stack. The phase-weighted multi-mode stack is always stacked with the order of 2.

Double phase-weighted stacking, i.e. a phase-weighted stack of the single modes and then a phase-weighted multi-mode stack, frees the records of almost all echoes for all models since the echoes are not in phase. In fact, the double phase-weighted stacking is the superior method for dips up to approximately 10°(Figure C.14, bottom) in this test. Almost all 'echoes' from the different modes are eliminated. For all angles of >20°, the single mode phase-weighted stacking combined with a simple linear stack of the modes efficiently lowers the amplitude incoherent signals (Figure C.23, top). Using a double phase-weighted stack for angles of this magnitude and higher does not only eliminate the incoherent echoes but also the coherent signals because the traveltime corrections to the dipping layer are erroneous for each mode. As Tauzin et al. (2016) have already experienced, the phase-weighted stacking does not reproduce any dipping discontinuity at 40° at all. Due to the large error in traveltime correction between the different modes, the modes are not in phase. The linear single mode stack combined with a linear stack of the modes (Figure C.30, top) seems to image the dipping layer at least slightly, but all energy seen originates from the single mode *Pś* CCP stack (Figure C.29, top). For a dip angle of such magnitude, a plain, single-mode *Pś* CCP stack provides the only interpretable results with the disadvantage of non-attenuated multiple amplitudes and a large error in imaging the angle of the dipping layer. The Zhu and Kanamori weighted stacking (Figures C.21, middle, & C.23, middle) provides worse results than simple linear stacking or phase-weighted stacking of the modes in any case.

If the common conversion point stacks are computed with spatial averaging over neighbouring bins, as proposed in Section 4.2.3, the signals of the discontinuities become generally smoother. As a result, the pulses originating from the discontinuities are not only thickened, as expected, but also gaps in the signal are filled especially at the larger depths (compare the non-spatially averaged stack in Figure C.23 and the spatially averaged stack in Figure C.27). It is evident, however, that almost all multi-mode stacking echoes disappear due to the high coherent to incoherent signal ratio in the horizontal layer as well as the dipping one. In contrast to the dipping discontinuity, the horizontal discontinuity is perfectly imaged (see Figure C.18).

Based on the synthetic tests, it is found that the imaging of the dipping layer underneath a structure that has a large jump in surface topography works especially well. When the traveltimes are corrected for one of the three modes, that mode's arrivals show almost no jump in the center of the cross section while the other two modes' arrivals show clear jumps

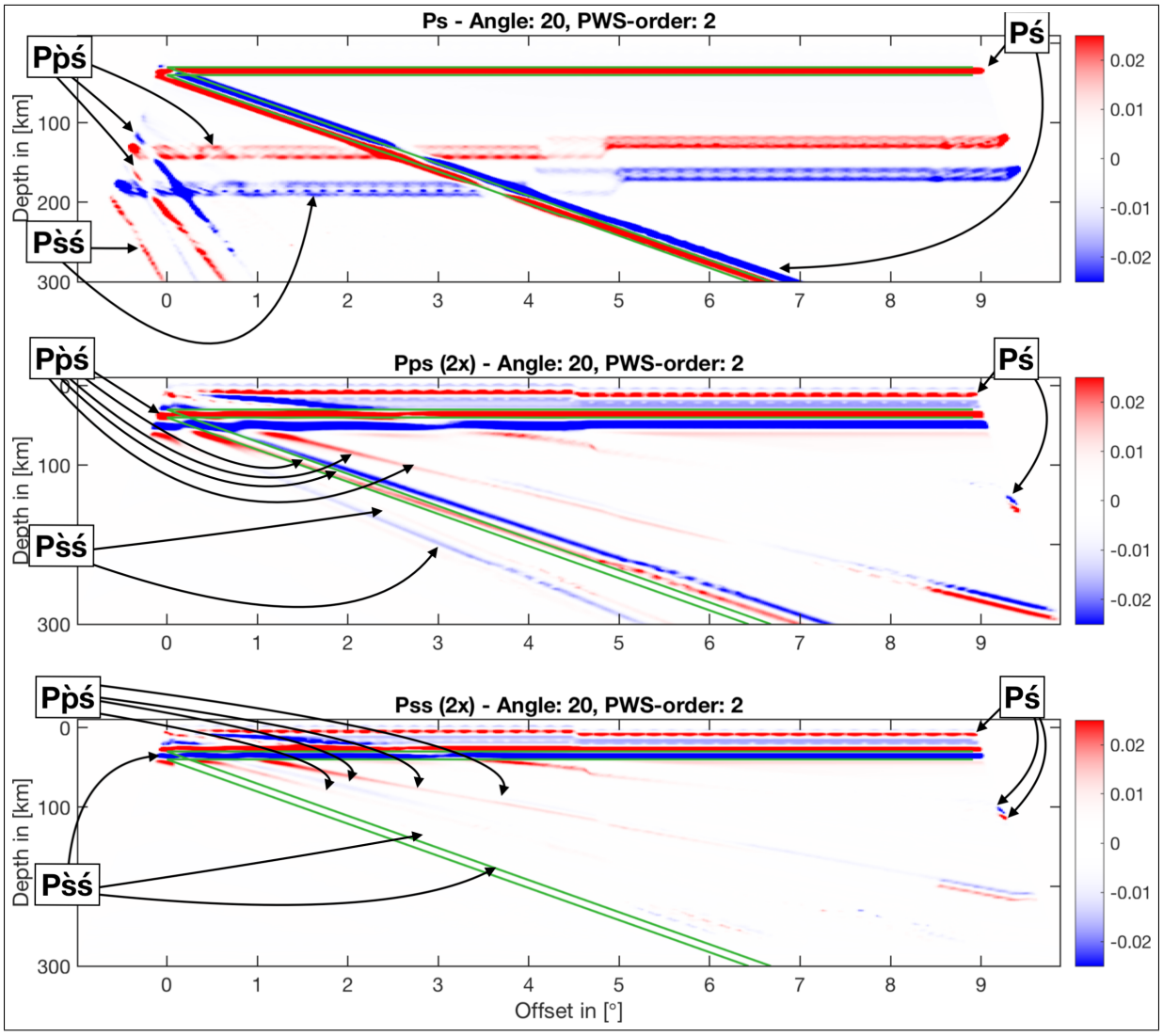

Figure 4.14: CCP stacked receiver functions of a dipping subducting oceanic crust with a dipping angle of 20°, traveltime corrected for the respective modes. Arrows indicate the different modes. The green lines surround both the horizontal, continental Moho and the top of the oceanic crust with a boundary of 5km, so that the discontinuities lie in between those lines if they were imaged correctly. The CCP stacking is done using phase-weighted-stacking with order 2. **Top** The *Pś* corrected, linear CCP stack. **Centre** The *Pp̀ś* corrected, linear CCP stack. **Bottom** *Ps̀ś* corrected, linear CCP stack.

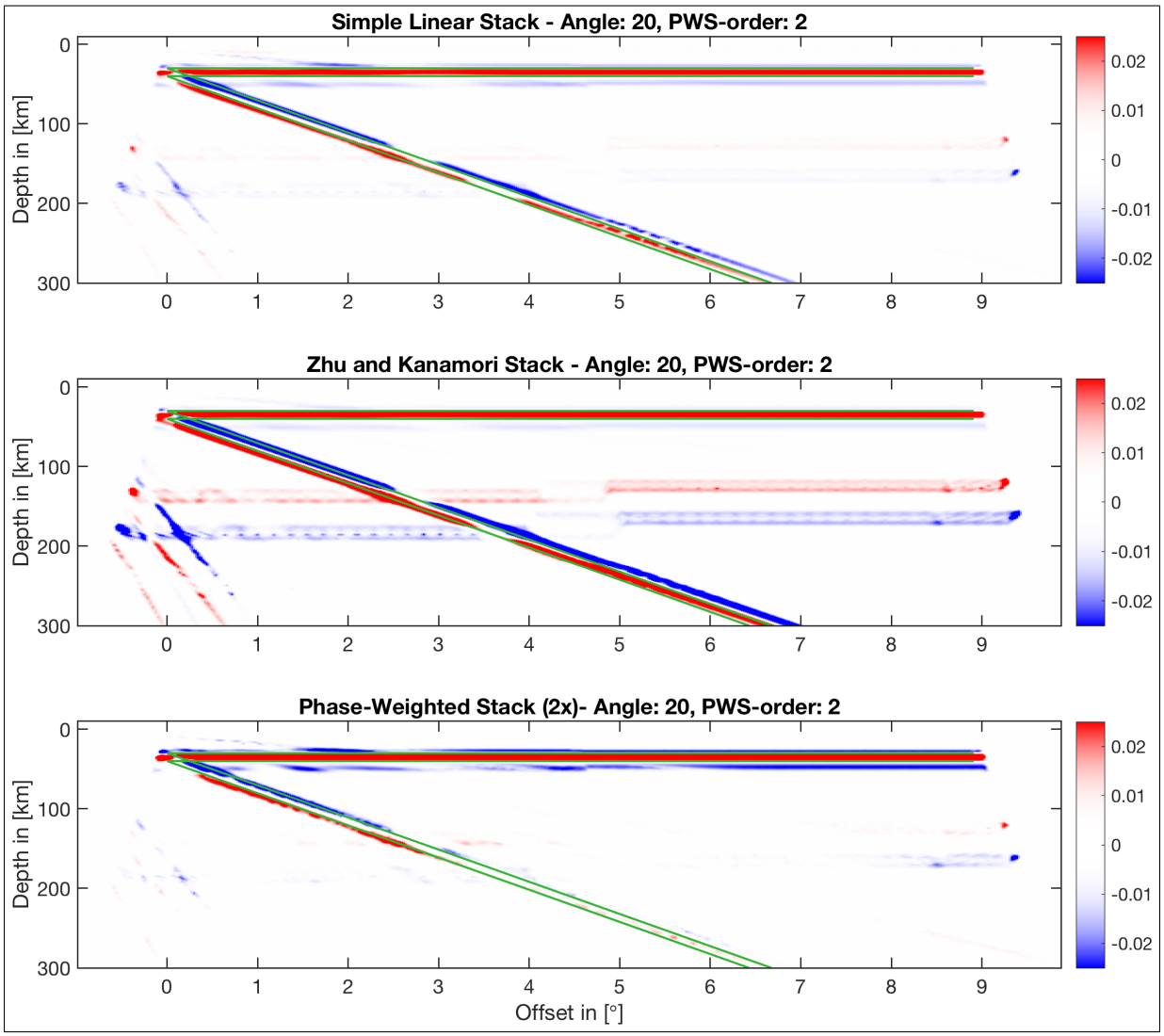

Figure 4.15: Phase-weighted stack of the single-mode CCP stacks of a dipping subducting oceanic crust with a dipping angle of 20°. The green lines surround both the horizontal, continental Moho and the top of the oceanic crust with a boundary of 5km, so that the discontinuities lie in between those lines if they were imaged correctly. The CCP stacking is done using phase-weighted-stacking with order 2. **Top** The linear stack of the 3 modes. **Centre** The Zhu and Kanamori weighted stack. **Bottom** The phase-weighted stack with order of 2. Note that the PWS stack order in the title refers to the stacking of each mode, not the multi-mode stack. The phase-weighted multi-mode stack is always stacked with the order of 2.

(compare the data in Figure 4.11 and the single mode CCP stacks in Figure 4.12). That the multiple modes, *Pp̀ś* and *Ps̀ś*, would have a small jump was expected. The traveltime correction for the multiple modes is more sensitive to changes in topography and the velocity model because of the large time-correction. However, the mapped jump is so small that it disappears in the multi-mode stack (see Figure C.23).

It can be concluded that, if the lithosphere to be imaged is unknown, a single mode, spatially averaged, phase-weighted stack (e.g. Frassetto et al., 2010) combined with a linear stack of the modes will provide the best universal results if the dipping angles in the subsurface do not exceed 20°. Spatial averaging should be used to fill some gaps in the data despite its disadvantage of thickening the signal. As long as that is kept in mind, it should produce superior results. For the following lithospheric studies investigating the Moho in the next two chapters, a single mode, spatially averaged, phase-weighted stacks will be used in combination with a linear multi-mode stack. For studies concerning the mantle transition zone in Africa, phase weighted *Pś* CCP stacks will be used in combination with spatial averaging.

Chapter 5

Application I. - Cascadia Subduction Zone

The Cascadia subduction zone beneath central Oregon is the result of the convergence of the Juan de Fuca micro-oceanic plate and the North American plate (Tauzin et al., 2016). Numerous studies have debated the depth, the general geometry of the subducting slab and the petrological nature of the subduction (Bostock et al., 2002; McCrory et al., 2012; Rondenay et al., 2001; Tauzin et al., 2016; Xue and Allen, 2007). A recent study was using a CCP method similar to the procedure developed in Chapter 4 (Tauzin et al., 2016). Tauzin et al. (2016) stacked CCP stacks of multiple receiver function modes using phase-weights in two dimensions to eliminate the multi-mode echoes mentioned in Section 4.2.4. This chapter is dedicated to testing the method developed in Chapter 4 on real data by comparing it to the results obtained by Tauzin et al. (2016). Since Tauzin et al. (2016) are projecting regional data into a two-dimensional plane, their method is technically advantageous in terms of data density. Consequently, their results serve as a great benchmark for the method developed in Chapter 4. To provide a well-founded comparison, the geological framework of the Cascadia subduction zone is provided in Section 5.1. Then, the obtained results are presented in Section 5.2 which is followed by a discussion of the results in Section 5.3.

5.1 Geological Background

The Cascadia subduction zone extends along the North America's West Coast from northern California to the south of British Columbia. While the subduction zone includes the subduction of the two micro-oceanic plates Juan de Fuca plate in the North and the Gorda plate in the

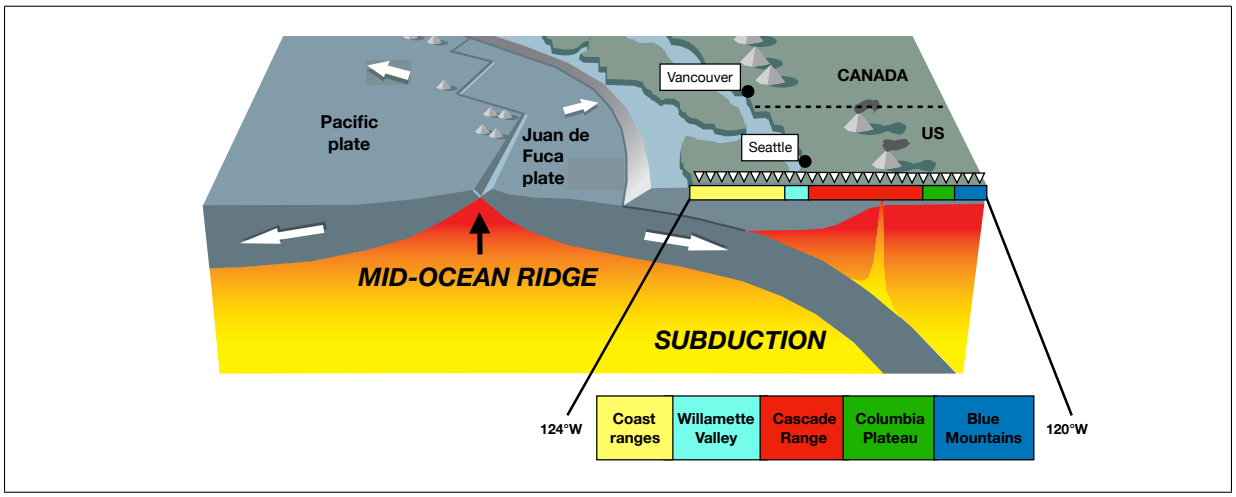

Figure 5.1: Schematic overview of the Cascadia subduction zone at 44.42°N. The stations of the CASC93 experiment are marked schematically by the triangles. The coloured bars show the major, geologically distinct areas below the array (also schematically). (modified from Begg et al. (2009))

South, the subduction of the Juan de Fuca plate beneath central Oregon is the focus of this study. The convergence velocity of the Juan de Fuca and the North American plate lies at $\sim$42 mm/yr in the direction of N69°E (Rondenay et al., 2001). A schematic overview of the tectonic framework is shown in Figure 5.1.

Recordings of the seismic stations in this area (seen in Figure 5.2) sample a series of accretionary events visible in the surface geology from the West Coast to the back-arc located in central Oregon (Rondenay et al., 2001). From coast to back-arc, the surface geology is composed of five geologically distinct regions: (1) the *Coast Ranges* (yellow bar in 5.1) consist of oceanic basalt terranes and sea mounts which accumulated on the North American plate during Paleocene to middle Eocene and were eventually covered by marine sediments of the fore arc. These marine sediments, known as the Siletz terrane, were uplifted in the late Eocene due to the continuous underthrusting of the Juan de Fuca plate (Rondenay et al., 2001); (2) the *Willamette Valley* (turqoise bar in 5.1), which is a structural trough inside the Siletz terrane, is covered by Tertiary and Quaternary sediment sequences of large thickness (Rondenay et al., 2001); (3) the *Cascade Range* (red bar in 5.1) is the consequence of volcanism in the continental arc, which, in turn, is a result of the subduction of the Juan de Fuca plate during the Tertiary and Quaternary, when the Western and the High Cascades formed, respectively (Rondenay et al., 2001); (4) the *Columbia back arc* (green bar in 5.1) is an area composed of various structural basins which are filled with volcanic and sedimentary layers from the Miocene to the Quaternary. High-elevation plateaus, such as the High Lava Plains and the Columbia Plateau,

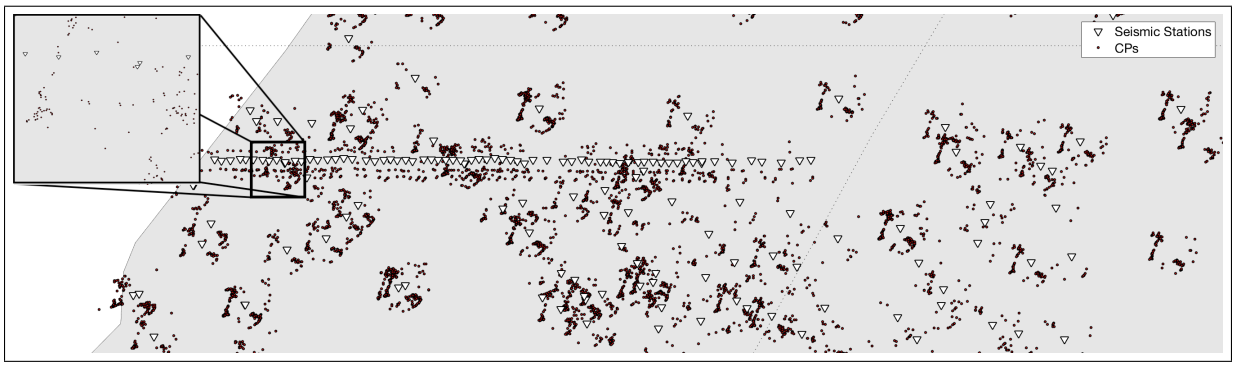

Figure 5.2: An overview of the receiver function piercing points at 50km depth. For orientation, the dense horizontal line of seismic stations is the CASC93 experiment at ca. 44.4°N just off central Oregon's west coast. The upside down white triangles are the seismic station, whereas the dots indicate the piercing points. **Top Left** Zoomed section of the piercing point overview.

were formed from these basins; they are seperated by (5) the *Blue Mountains* (blue bar in 5.1), which are terranes accreted in the Late Triassic to Early Cretaceous (Rondenay et al., 2001).

The subduction of the oceanic Juan de Fuca plate underneath the North American plate has been investigated by previous studies which do not all agree on the angle of the subducted slab. Tomographic images have shown a relatively steep subduction of $\sim 50°$ (Xue and Allen, 2007), while high-resolution receiver function studies have imaged the slab with an angle of $\sim 12°$ increasing to up to $\sim 27°$ below the arc (Rondenay et al., 2001). Methods that investigate the slab's geometry by locating the earthquakes on the slab's surface have imaged it as well with an eastwards, smoothly increasing dip angle (McCrory et al., 2012) as opposed to a steep subduction. The recent CCP stacking study by Tauzin et al. (2016) has found a subducting slab geometry in agreement with the studies conducted by Rondenay et al. (2001), Bostock et al. (2002) and McCrory et al. (2012).

Two interesting features in the subducting slab are found in the studies of Bostock et al. (2002) and Tauzin et al. (2016). First, the oceanic Juan de Fuca plate is characterised by a reduction in seismic S velocity from the overriding plate to the 10 km thick, subducting, basaltic crust. The velocity is lowered due to the hydration of the basalts in the oceanic crust (Rondenay et al., 2008). The high contrast observed between the overriding crust and the oceanic crust is possibly caused by frozen anisotropy in the subcrustal oceanic lithosphere (Audet, 2013). The second feature is a gap in contrast between the subducting slab and the continental Moho from $\sim 123°$W to $\sim$ 122.25°W at 30km depth. This gap is attributed to a serpentenised mantle fore-arc (Bostock et al., 2002). Water that is released from the subducted oceanic plate rises upwards into the mantle fore-arc and hydrates it. Depleted peridotite in the

mantle fore-arc stabilises hydrous minerals, such as serpentine. Owing to serpentine's low seismic velocities, the seismic impedance contrast between the serpentinised mantle fore-arc and the continental crust decreases drastically and results in a lack of contrast in the seismic images. It even reverses polarity in certain locations, suggesting lower velocities in the fore-arc than in the crust. Thus, the continental Moho seems to disappear above the mantle fore-arc (Bostock et al., 2002; Rondenay et al., 2008).

Eastwards, underneath the rest of the profile, the North American continental Moho is mapped fairly horizontal in both receiver function studies (Rondenay et al., 2001; Tauzin et al., 2016). The signal of the almost flat Moho is seen from $\sim$ 122.25°W at $\sim 40km$ depth and shallowing eastwards far into central Oregon to a depth of $\sim 35km$ (Tauzin et al., 2016).

The test of the method in the next two sections is an attempt to reproduce the features described above (the dipping oceanic plate, the flat North American Moho as well as the low velocity in the Juan de Fuca plate and the missing contrast between oceanic and continental Moho).

5.2 Results

The CCP stacks for Cascadia are calculated with a grid resolution of $0.05° - by - 0.05°$ and spatially averaged bins. The vertical distance between bins is set to 1 km. The piercing points are found by raytracing through the one dimensional IASP-91 seismic velocity model (Kennett and Engdahl, 1991). While this is far from the optimum in the case of a subduction zone, this chapter is designed to test this method and compare the results with the ones obtained by Tauzin et al. (2016) who used the IASP-91 model in their ray tracing. Furthermore, the single mode CCPs for all three modes will be computed, stacked with a phase-weight and then, the single-mode stacks will be linearly stacked to produce multi-mode stacks. Another condition that is applied in the stacking is that each bin at every piercing depth contains at least *ten* receiver functions. All other bins are left empty, i.e., they are set to a values of zero. This will result in white patches across the calculated volumes and cross sections.

Figure 5.2 shows the piercing points of the receiver functions at 50km depth. An investigation of the theoretically calculated piercing points helps to identify where the data density is the highest. Here, it can be observed that most piercing points are slightly south of

the CASC93 experiment. Hence, most of the cross sections shown in this section will be located south of the CASC93. Furthermore, the cross sections are often chosen to not be parallel to the CASC93 experiment to improve imaging of the subducting slab. While the subducting slab increases in depth eastwards, the horizontal distance from the conversions within slab to the stations increases. Another criteria for the orientation of the slices was simply the reproducibility of the subducting slab. Hence, the cross sections often are chosen to contain gaps in data because the slices were rotated to match the best image of the dipping oceanic crust.

Pś Mode Images

The results of stacking the *Pś* mode are shown in Figure 5.3. Particularly noticeable are the white patches on the cross section which are areas that have been pierced by less than ten receiver functions. The volume and both cross sections possess the same large, positive (red) signal at the near-surface in all regions with data coverage.

The latitude slice in Figure 5.3 (b) shows three distinct, positive signals. The first one is the flat positive signal at 40 km depth underneath central Oregon seen in (a) and (b) of Figure 5.3. On Figure 5.3 (b), this is indicated by the letter A. The positive signal extends from approximately 122°W to the end of the slice in the East. Between 120.5°W and ca. 119°W the slice is interrupted by a gap in the data. From 119°W to the eastern end of the profile, a shallower, positive and flat signal can be observed. In the same longitude range, between 100 and 150 km depth, a band of positive pulses can be followed. The band seems to dip ever so slightly in westward direction. At 123.5°W and 35 km depth in Figure 5.3 (a) and (b), a positive signal can be observed, which deepens eastwards and ends at approximately 122.2°W and 70 km depth (indicated by the letter B on Figure 5.3 (b)). This dipping signal is also surrounded by negative signals of lower amplitude. The dip angle increases from no apparent dip to 14° at 122.2°W. Another, apparently dipping, positive signal is seen at depths of approximately 100 to 150 km at the western end. This signal is dipping towards the East at 122.5°W and 200 km. Below this signal, a negative band is observed.

The longitude slice in Figure 5.3 (c) shows three distinct signals. At 50 km depth, the signal with the largest amplitude can be observed, which is indicated with the letter B since it refers to the same signal as seen in Figure 5.3 (b). The signal is dipping southwards from 50 km

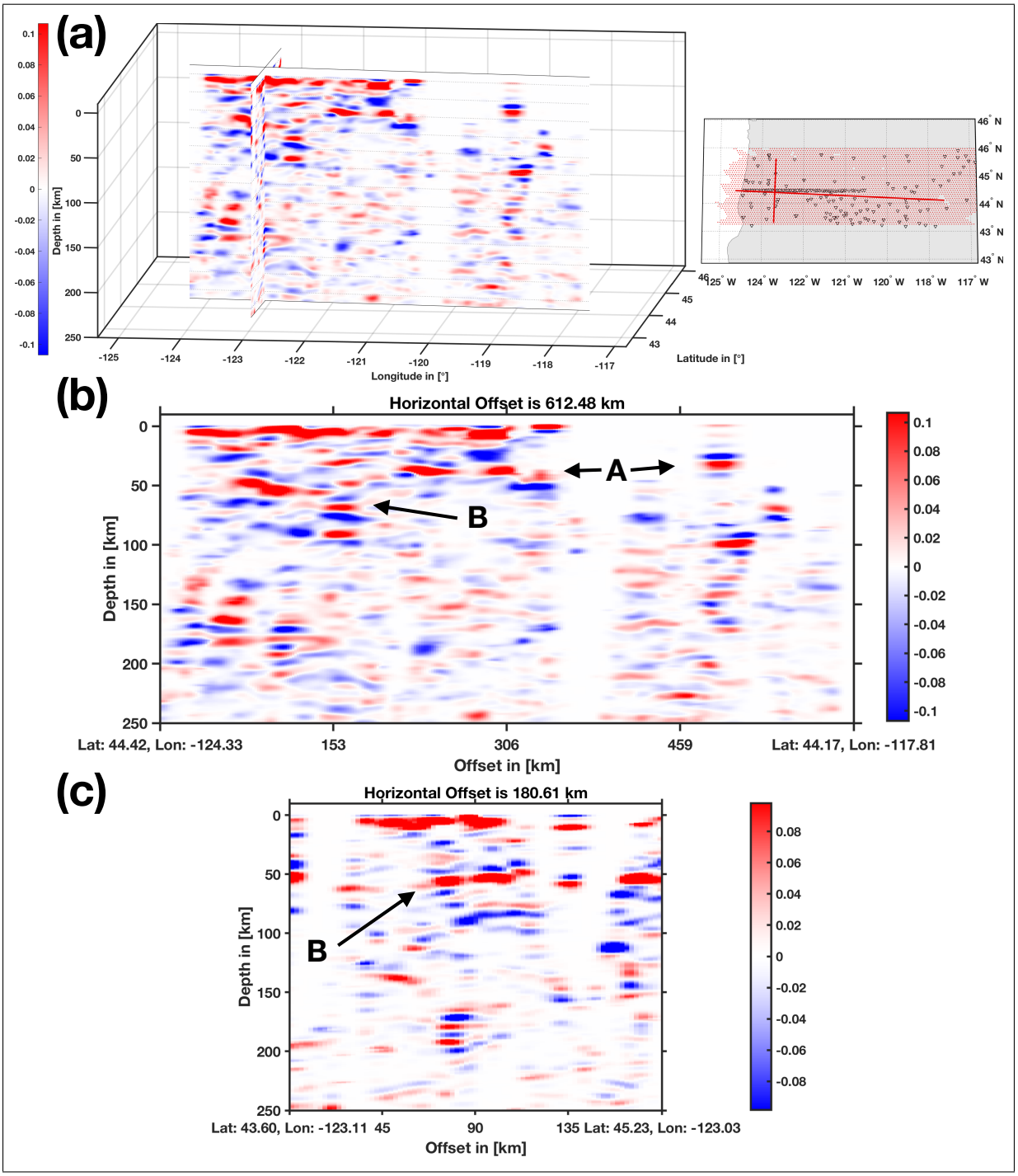

Figure 5.3: The volume and slices depicting the results of the *Pś* mode. The colourbars in all three figures indicate the amplitude. **(a)** The calculated volume is shown on the left and the slice locations are indicated on the map to the right. White triangles with black outline are seismic stations and red dots are CCP bin centres. **(b)** The latitude slice at a centre latitude of ca. 44.2°N. Location of the ending points indicated on the x-axis at the bottom on either end of the slice. **(c)** The longitude slice at a centre longitude of ca. 123°W. Location of the ending points indicated on the x-axis at the bottom on either end of the slice.

to approximately 55 to 60 km. It is preceded in depth by a negative signal and followed by one at approximately 70 km.

P̀ṕs Mode Images

The CCP stacking results of the *P̀ṕs* mode are shown in Figure 5.4. Again, just as for the *Ṕs* corrected mode, a positive signal at the near-surface can be observed throughout all images in Figure 5.4. It is, however, much thinner. On all images in Figure 5.4, an additional thin positive signal can be observed at approximately 10 km depth.

The latitude slice in Figure 5.4 (b) shows two distinct positive and two distinct negative signals. As Figure 5.3 (b), Figure 5.4 (b) shows a flat positive signal that stretches from 122.2°W to 121°W. Here however, the flat signal (A_1) is seen at 30 km depth. Furthermore, the positive signal is followed by a negative pulse (A_2). At 124.3°W and 30 km depth, a positive signal (B_1) dips with slightly increasing dip angle to a depth of 125 km at 120.5°W. Also this signal is followed by a negative pulse (B_2) which dips eastwards from 50 km depth to 135km depth.

The longitude slice in Figure 5.4 (c) shows one distinct positive signal and one distinct negative pulse. The positive signal (B_1) is dipping southwards from 45.2°N and 45 km depth to 43.9°N and 55 km depth. This signal is preceded by a large negative signal in the very centre of the slice and followed by a negative signal (B_2) with the same dip, but 10 km deeper.

P̀śs Mode Images

The results for the *P̀śs* seem very similar to the results that were obtained for the *P̀ṕs* mode in Section 5.2. Along the near-surface, a positive signal is seen in all parts with data coverage. A second signal, which was also seen in the results of the previous mode in Section 5.2, is the thin positive signal below the near-surface signal at depths of approximately 10 km seen in the volume as well as the two cross sections of the *P̀śs* mode.

In the latitude slice, there are three distinct positive/negative pairs (see Figure 5.5 (b)). Similar to the *P̀ṕs* mode, there are flat positive (A_1) and negative signals (A_2) at 25 and 35 km depth, respectively, from 122°W to 120.5°W. There, the two signal disappear due to a gap in the data. Another positive (B_1) and negative signal (B_2) pair is observed at 25 and 30 km depth, respectively, in the west of the study area at 124.2°W. From this location, both signals are

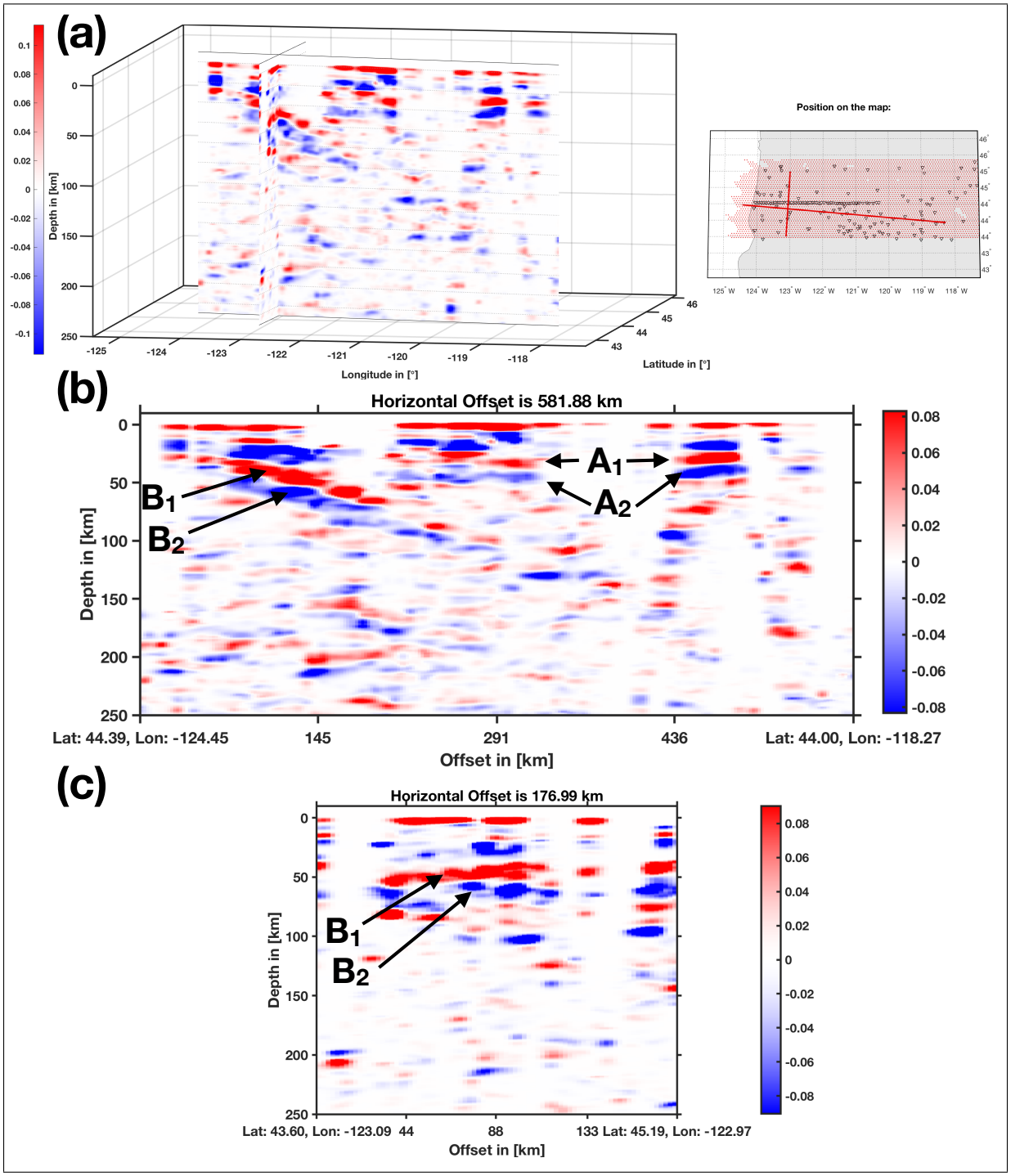

Figure 5.4: The volume and slices depicting the results of the *Pp̀ś* mode. The colourbars in all three figures indicate the amplitude. **(a)** The calculated volume is shown on the left and on the map to the right, the slice locations are indicated. White triangles with black outline are seismic stations and red dots are CCP bin centres. **(b)** The latitude slice at a centre latitude of ca. 44.2°N. Location of the ending points indicated on the x-axis at the bottom on either end of the slice. **(c)** The longitude slice at a centre longitude of ca. 123°W. Location of the ending points indicated on the x-axis at the bottom on either end of the slice.

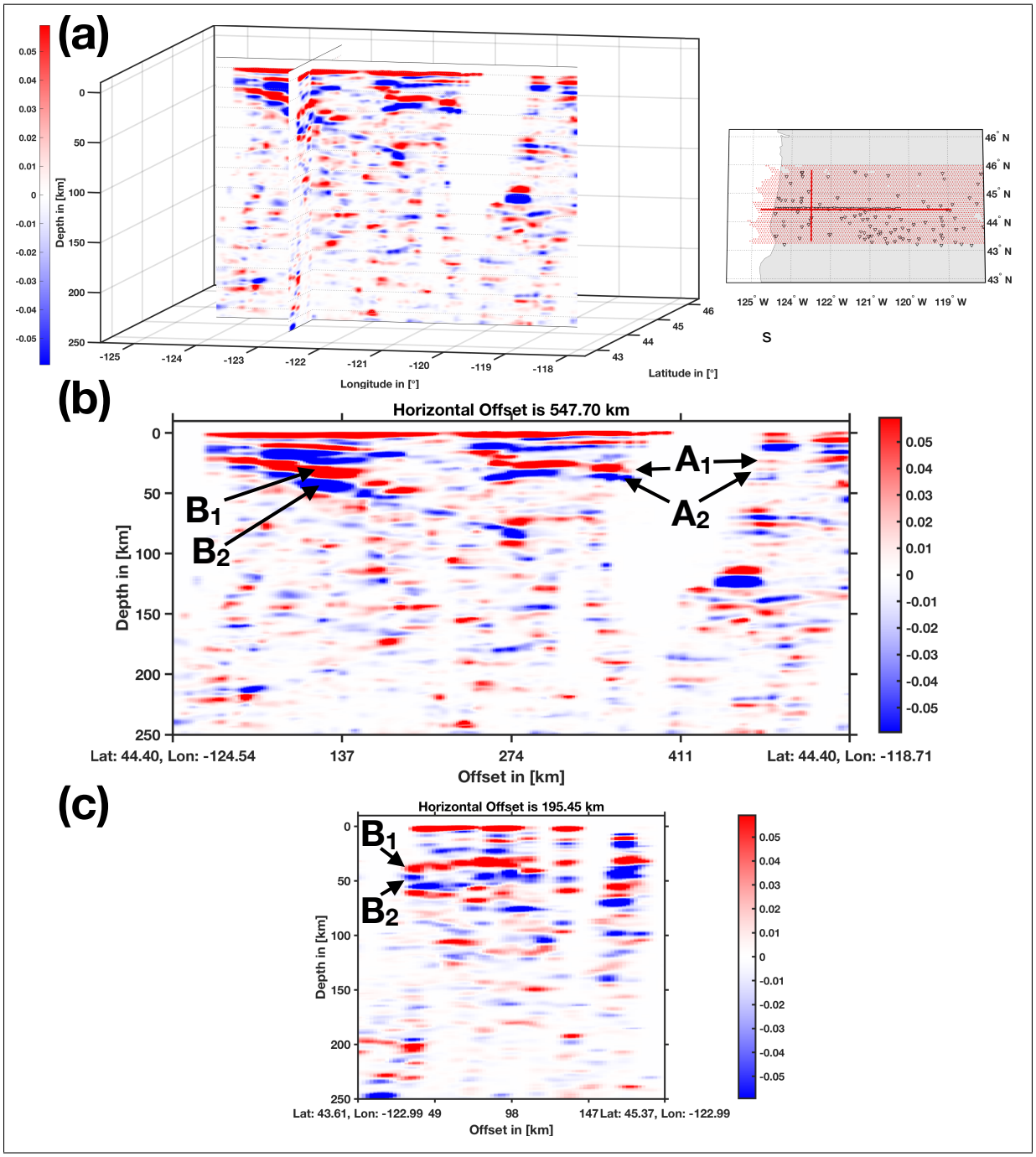

Figure 5.5: The volume and slices depicting the results of the *Pšś* mode. The colourbars in all three figures indicate the amplitude. **(a)** The calculated volume is shown on the left and on the map to the right, the slice locations are indicated. White triangles with black outline are seismic stations and red dots are CCP bin centres. **(b)** The latitude slice at a centre latitude of ca. 44.4°N. Location of the ending points indicated on the x-axis at the bottom on either end of the slice. **(c)** The longitude slice at a centre longitude of ca. 122.9°W. Location of the ending points indicated on the x-axis at the bottom on either end of the slice.

dipping with increasing angle to a depth of ca. 75 and 80 km, respectively, at 121.2°W. Up until 123°W, the signal pair is also preceded by a clear negative signal. The third distinct signal pair is located at 119.5°W and 115 and 123 km, respectively.

The longitude slice seen in Figure 5.5 (c) contains the same two positive (B_1) and negative signals (B_2) as the longitude slice of the *Pp̀ś* mode. Also here, they are separated by approximately 10 km. However, they appear 10 km shallower than in Figure 5.4 (c) at 35 and 45 km depth, respectively. Thus, the positive signal of Figure 5.4 (c) coincides in depth with the negative pulse seen in Figure 5.5 (c). In the southern part of data coverage, the positive signal is preceded by a negative signal.

Multi-Mode Stack Images

Figure 5.6 shows the linear multi-mode stack of the modes presented in Figures 5.3, 5.4 and 5.5. Note that the *Pś̀ś* mode is stacked negatively since its amplitude is inverted. Due to the *Pś* mode's high amplitude, it has the largest contribution to the stack. The one feature that both cross sections, (b) and (c) in Figure 5.6, have in common is the flat, positive near-surface signal. It extends from 0 to 10 km depth.

In the latitude slice in Figure 5.6 (b), four major, positive signals can be observed. A flat positive signal (A) can be observed here at 40 km depth. Its lateral extent stretches from 122.2°W to 120.8°W where there is a gap in data. After the gap in eastward direction, a flat, positive signal (A) is observed and shallowing from 40 km at 119.8°W to 35 km depth at 118.5°W. Below this signal at 100 km depth, a similar dipping, positive signal (C) can be observed. On the other end of the cross section, from 50 km depth and 123.5°W to 60 km depth and 122.8°W, a dipping positive signal (B) is observed with a very strong pulse. A band of weaker, positive pulses (D) is dipping at a harsher angle in the same longitude range from 100 to 150 km in the West to 175 to 225 km.

The longitude slice seen in Figure 5.6 (c) contains one distinct signal. This positive signal dips southwards from 50 km depth at 45.4°N to 60 km at 44.1°N.

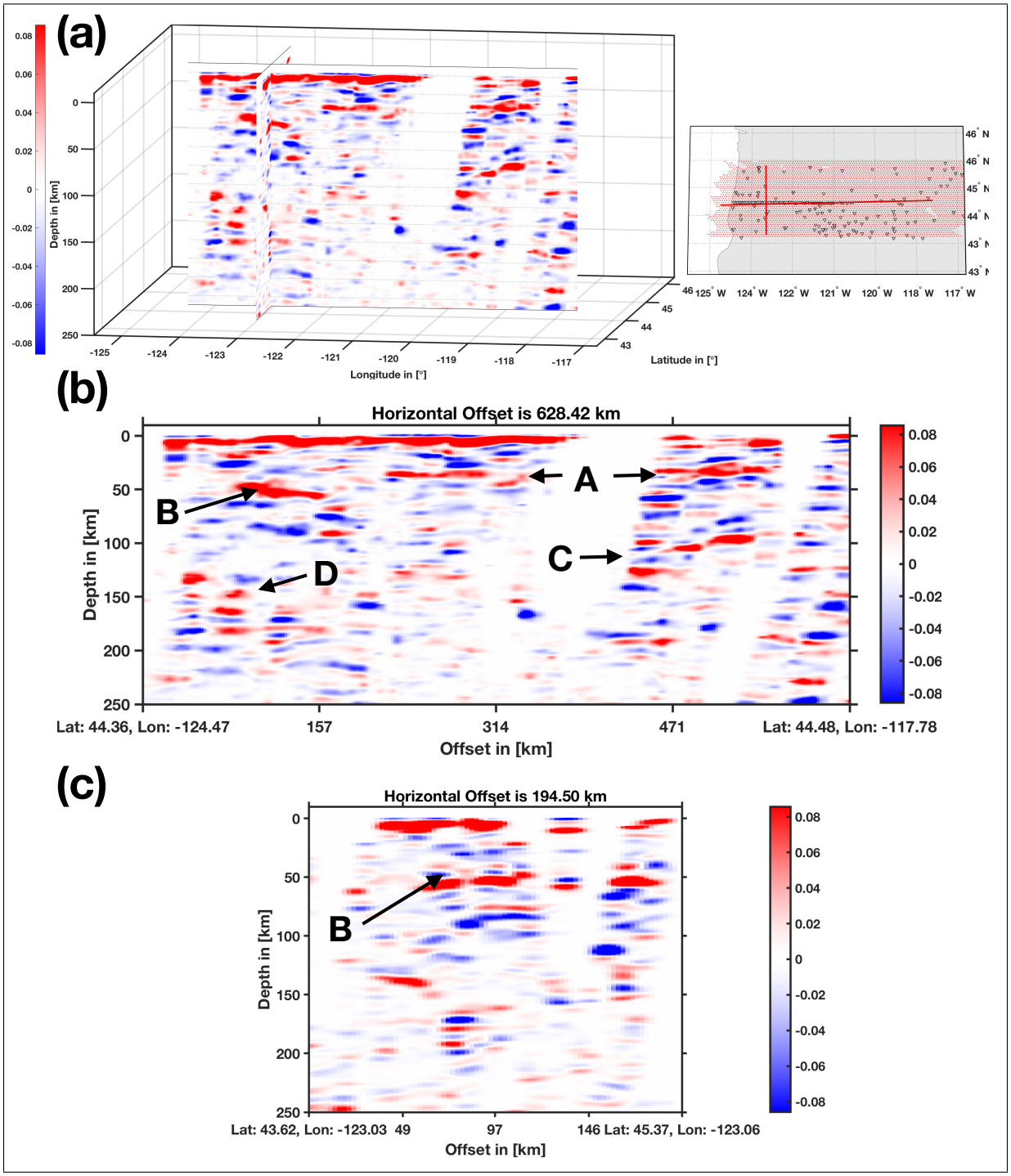

Figure 5.6: The volume and slices depicting the multi-mode stack. The colourbars in all three figures indicate the amplitude. **(a)** The calculated volume is shown on the left and on the map to the right, the slice locations are indicated. White triangles with black outline are seismic stations and red dots are CCP bin centres. **(b)** The latitude slice at a centre latitude of ca. 44.2°N. Location of the ending points indicated on the x-axis at the bottom on either end of the slice. **(c)** The longitude slice at a centre longitude of ca. 123.3°W. Location of the ending points indicated on the x-axis at the bottom on either end of the slice.

5.3 Discussion

The results from Section 5.2 will now be discussed. A brief presentation of each mode's identified signals is followed by a discussion of the geometry found in the interpretation of the cross sections. The focus lies on the latitude slices since they cut the subducting slab in the direction of subduction and provide the best overview.

In the *Pś* CCP stack (with interpretations in Figure 5.7 (a)), four dominant signals were found. The shallow flat signal that stretches almost along the whole cross section is identified as the Moho of the North American tectonic plate (Tauzin et al., 2016). Note that the line is solid where there is no data since the three dimensional view of the results revealed a continuous Moho. The shallow dipping signal is interpreted as the Moho of the Juan de Fuca (JdF) tectonic plate which is subducted under the North American west coast (Rondenay et al., 2001). It is preceded by the negative pulse (dotted line) indicating the top of the oceanic crust (Tauzin et al., 2016). Both of the Moho signals are followed by clear, deeper bands of positive signals and in the case of the Juan de Fuca tectonic plate also negative signals. These are the crustal multiples as indicated in the Figure 5.7.

The CCP stack of the *Pp̀ś* mode, shown with annotations in Figure 5.7 (b), is stacked with a different time correction. Hence, the *Pś* mode is imaged at a shallower depth as indicated in the figure, and the *Ps̀ś* is still imaged deeper. This is the inter-mode leakage described in Section 4.2.4. The correctly stacked *Pp̀ś* mode shows a clearly dipping, positive signal from the Juan de Fuca Moho as a well as a clear flat Moho for the North American plate. The dotted line indicates the top of the oceanic plate. What is interesting here is the clarity of both the *Pp̀ś* and *Ps̀ś* mode's signals that are imaging the subducted Juan de Fuca slab as well as the North American plate.

In Figure 5.7 (c), the CCP stack of the *Ps̀ś* is shown with the identified discontinuities annotated. Here, the *Pś* mode and the *Pp̀ś* mode are mapped shallower than their origin as a result of the inter-mode leakage. The *Ps̀ś* mode shows the same clear dip as the *Pp̀ś* mode. Unlike the previous two modes, in this cross section, a large signal can be seen at 119.5°W and approximately 120km depth. It is possible that it is a continuation of the subducting slab (Tauzin et al., 2016). With the given data gap however, this is hard to determine; more data coverage is necessary. Another possibility is a well-stacked 410km-discontinuity. Further research is necessary which is beyond the scope of this chapter and thesis. Compared to the previous two

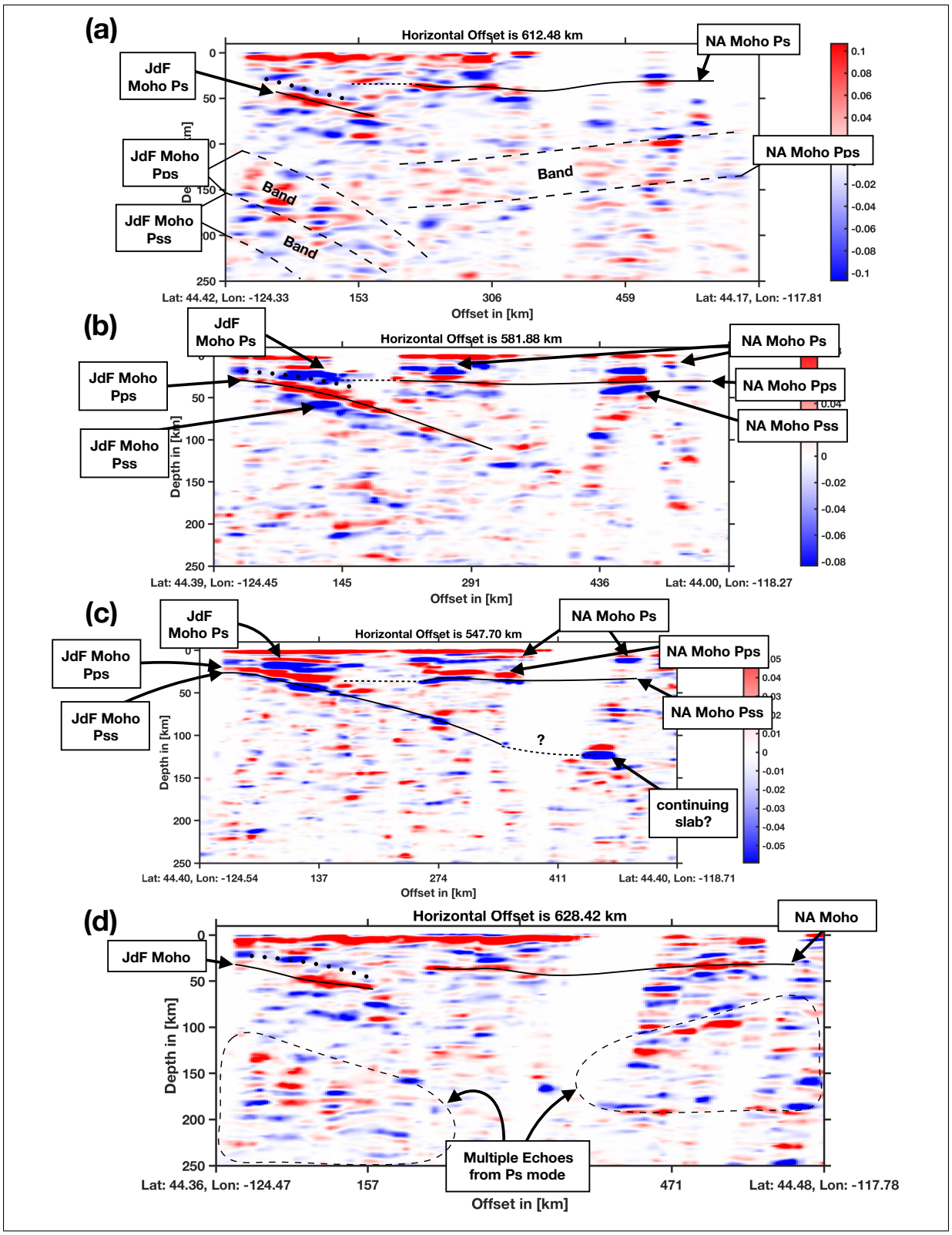

Figure 5.7: Interpretation of the Results of the Cascadia subduction zone. See text for more info. The respective pure results are found in image *(b)* of Figures 5.3 to 5.6. The dotted line in each cross section shows the top of the subducting Juan de Fuca plate (JdF). The dashed line continuing westwards from the North American plate (NA) indicates the gap in seismic impedance. **(a)** The *Pś* mode CCP stack with interpretations of the major signals. **(b)** The *Pp̀ś* mode CCP stack with interpretations of the major signals. **(c)** The *Ps̀ś* mode CCP stack with interpretations of the major signals. **(d)** The linear stack of the three modes.

modes, the top of the oceanic plate is not indicated in Figure 5.7. The reason for this is the fact that its signal is positive due to the reversed polarity of the *Pὶś* mode and most likely coincides with the positive signal of *Pὸś* mode. Hence, it is impossible to make a clear interpretation of its location.

The linear multi-mode stack (Figure 5.7 (d)) shows a clear, eastwards shallowing North American Moho from 122°W to 118.2°W with a data gap between 120.5°W and 119.8°W. Although there is a gap in the data, this discontinuity is seen in both horizontal dimensions. Large lateral changes in topography within the data gaps are not probable. The top of the subducting slab of the Juan de Fuca plate is indicated, again, with a dotted line. Echoes in the stack from the *Pś* mode are more clearly visible than desired. This could possibly be reduced by phase-weighted stacking of the modes, but from the synthetic testing in Section 4.2.5, it was found that phase-weighted stacking of the modes damages the resulting images more than it improves them.

Despite being seen very clearly in the *Pὸś* and the *Pὶś* mode, the dipping Juan de Fuca plate seems to be less pronounced in the stacked image. There are two reasons for this. First, the amplitudes in the *Pś* mode CCP stack are much higher than the amplitudes in the CCP stacks of the other two modes. Therefore, the structures seen in the *Pś* CCP stack dominate the multi-mode stack. Second, looking closely at each CCP stack, it can be observed that the Juan de Fuca plate and the North American plate are imaged deeper by the *Pś* mode than the *Pὸś* and *Pὶś* mode. A phase-weighted stack of the modes would, in this case, introduce a more destructive stacking than a linear stack since the modes are not in phase. Since the CCP stacking procedure was proven to work in a subduction-like environment in Section 4.2.5, this difference can be attributed to the difference between the actual crustal velocities in the subduction zone and the IASP-91 seismic velocities used for the ray tracing. The subcrustal velocities must average the crustal velocity errors because the location of the dipping crust in both *Pὸś* and *Pὶś* mode CCP stack is imaged in agreement with both Tauzin et al. (2016) and Rondenay et al. (2001).

Although the multi-mode stack could have provided better results with the choice of a better fitting velocity model, the resulting images do agree with previous receiver function studies. First, the negative seismic impedance contrast indicating the top of the basaltic crust is clearly imaged in the *Pś* and the *Pὸś* mode CCP stacks as well as the final stack. Furthermore, in all cross section, the seismic impedance gap between the Juan de Fuca plate and the North American plate is reproduced (see the dashed line in all images of 5.7, eastwards until it meets

the North American plate). Additionally, the Moho of the North American plate is also here imaged almost flat, shallowing eastwards into central Oregon to a depth of ca. 30 km.

What the other CCP studies in this area lack is the third dimension at local scale. Although not shown in this section, all longitude slices shown in Section 5.2 indicate a clear southwards dip of $\sim$4 degrees in the Moho of the subducting slab. A receiver function migration study by Cheng et al. (2017) revealed that the subduction of the Juan de Fuca and the Gorda plate might be imaged from a low subduction angle at 44°N to steep subduction below northern California due to a thermal anomaly causing a decrease in seismic velocities. This would also be in agreement with large scale tomographic images (Xue and Allen, 2007).

The results presented here cannot be of the same resolution as those of the detailed cross sections shown by Tauzin et al. (2016) or Rondenay et al. (2001). The reason for this is that the data stays spread in three dimensions instead of being projected into a two dimensional plane. As a consequence, the density of data along the cross section is smaller. This is acceptable, however, since the purpose of this chapter was merely to test the method and, if successful, demonstrate the global applicability of the method developed in Chapter 4.

It can be concluded that the global common conversion method and the multi-mode stacking can produce images of interpretable quality at small scale (in a teleseismic sense) as long as the velocity model does not diverge too far from the reality.

Chapter 6

Application II. - East Africa

The subsurface structure of the East African continent has been focus of a series of tomographic studies (Begg et al., 2009; Hansen and Nyblade, 2013; Hansen et al., 2012). The tomographic studies have discovered a large low velocity anomaly below large parts of the East African (Begg et al., 2009; Hansen et al., 2012), which is held responsible for the rift activity at the surface (Saria et al., 2014). Furthermore, these studies have revealed a cold, high velocity upper mantle below southern Africa.

In agreement with the tomography results, receiver function studies (Cornwell et al., 2011; Dugda, 2005; Julià et al., 2005; Last et al., 1997; Nair et al., 2006; Nguuri et al., 2001; Niu et al., 2004; Owens et al., 2000) have imaged not only the Moho topography, but also the topography of the mantle transition zone discontinuities. Until now however, each receiver function study has been restricted to a certain region on the East African continent.

The method developed in Chapter 4 will be used to overcome this issue. A cross section from Cape Town to the Afar region will be created to allow for an almost continuous view of the Moho and mantle transition zone across East Africa. To be able to discuss the results, a geological overview of East Africa is provided in Section 6.1. Then, the results obtained with this method are presented in Section 6.2 before discussing them in Section 6.3.

6.1 Geological Background

An overview over the complex basement geology of Africa is crucial to understand our geophysical data because of the strong link between surface geology and the subsurface (Begg

et al., 2009). The cross section presented in the following section spans several disparate, intracontinental, geological regions that differ markedly in their tectonic origin and age (Begg et al., 2009, see Figure 6.1). Although the map of Figure 6.1 shows the general surface geology of the complete African continent, the focus will lie on the regions that the cross section is imaging.

The African continent's basic building blocks are several Archean cratons and smaller cratonic regions connected by more recently developed foldbelts or mobile zones. The cratons differ significantly in their structure and evolution and vary in age from 3.6 to 2.5 Ga. The main continent was assembled during the late Neoproterozoic to the earliest Paleozoic Pan-African orogeny (Begg et al., 2009).

Archean Cratons

The *Tanzania Craton* (IV in Figure 6.1) is a small Archean block divided into two subterranes by the NW-oriented Dodoma Schist Belt (IVc), which is intruded by 2.6 to 2.5 Ga old granites (Begg et al., 2009). The northern terrane (IVa) consists of 2.8 to 2.66 Ga old basement rock overlain by 2.5 Ga old granitoid intruded molasse deposits. The southern subterrane (IVb) is composed of 2.93 to 2.85 Ga old gneisses and granitoids.

Large parts of the *Ugandan Craton* (III in figre 6.1) consist of Archean granulites as well as gneisses (Begg et al., 2009). Archean granulites in the North-West of the craton were subject to ultra-high pressure metamorphism 2.4 Ga ago. Hence, the Tanzanian Craton is easily distinguished from the Ugandan Craton in composition.

The *Kalahari Craton* is a composite craton made up of the *Kaapvaal Craton* (V in 6.1) in the South and the *Zimbabwe Craton* (VI in 6.1) in the North (Begg et al., 2009). These two cratons are separated by the *Limpopo Belt* (VII in 6.1). The Kaapvaal Craton is mainly composed of granitoids, some gneisses and some greenstone belts. Since most of the Kaapvaal Craton consist of Archean basins, the boundaries of the four terranes constituting the Craton were found using geophysical methods. The oldest rocks are found within the *Southeastern Terrane* (Va); the gneisses here are from 3.7 to 3.2 Ga ago. The narrow *Central Terrane* (Vb) consists of 2.6 Ga ago metamorphosed, 3.34 to 3.0 Ga old gneisses. In the North of the Kaapvaal Craton, 2.85 to 2.66 Ga old gneisses and greenstone belts constitute most of the *Pietersburg Terrane* (Vc). The *Western Terrane* (Vd) consists of 3.25 to 2.88 Ga old gneisses

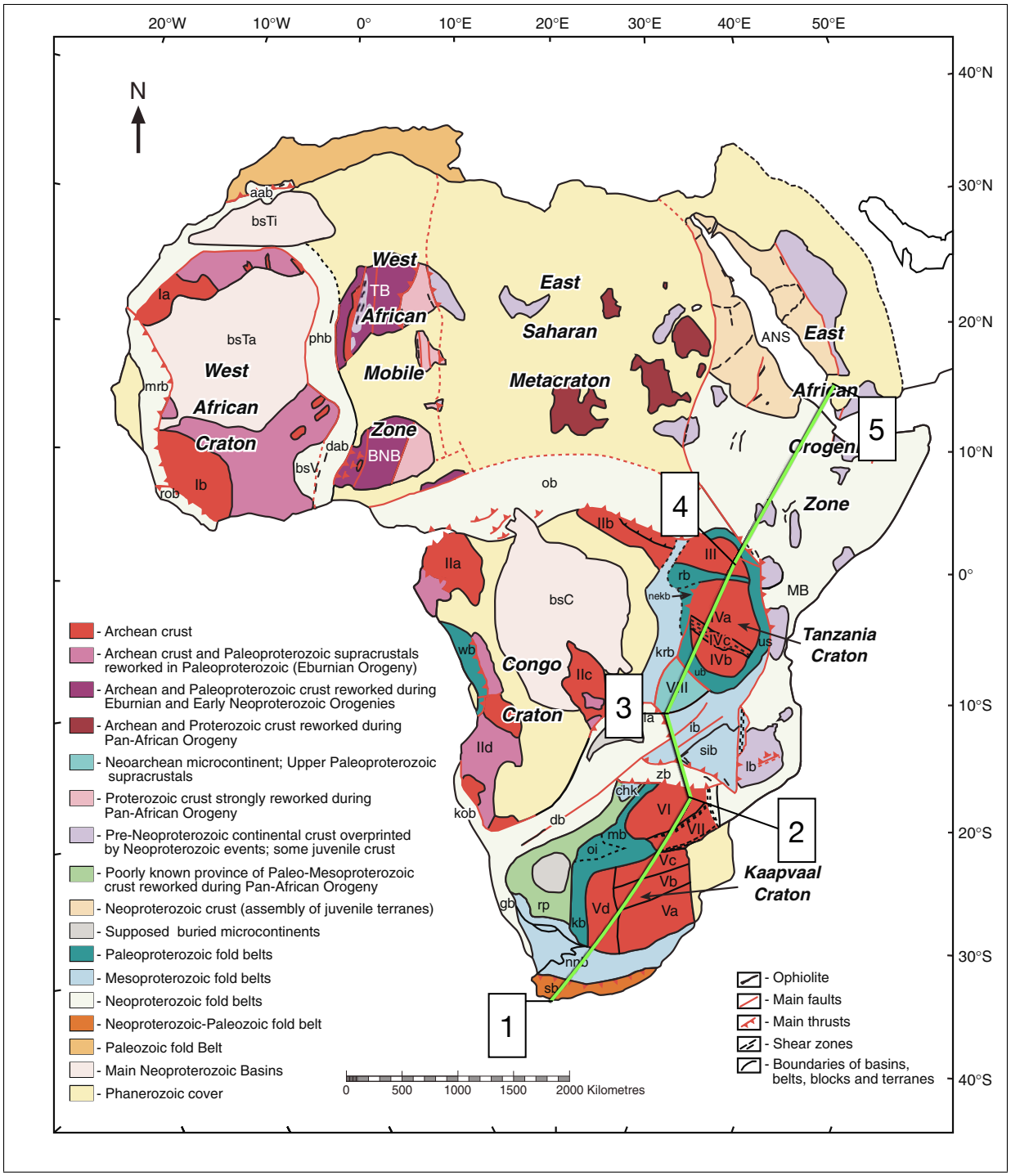

Figure 6.1: An overview of Africa's bedrock geology. The green line indicates the location of the cross section in Figures 6.3, 6.5, B.2, 6.4 and 6.6. The numbers indicate the waypoints. Regions cut by the cross section from South to North: **(1)** Saldania neoproterozoic belt (**sb**); **(2)** Namaqua-Natal mesoproterozoic belt (**nnb**); **(3)** Kaapvaal Craton (**Va**–Southern Terrane, **Vb**–Central Terrane, **Vc**–Pietersburg Terrane, **Vd**–Western Terrane); **(4)** Limpopo Block (**VII**); **(5)** Zimbabwe Craton (**VI**); **(6)** Zambezi neoproterozoic belt (**zb**); **(7)** Southern Irumide mesoproterozoic belt (**sib**); **(8)** Irumide mesoproterozoic belt (**ib**); **(9)** Bangweleu block (**VIII**); **(10)** Paleoproterozoic Ubendian belt (**ub**); **(11)** Tanzania Craton (**IVa**–Northern Terrane, **IVb**–Southern Terrane, **IVc**–Dodoma Zone); **(12)** Ruwenzori paleoproterozoic belt (**rb**); **(13)** Uganda Craton (**III**); **(14)** Usagaran paleoproterozoic belt (mesoproterozoic belt); **(15)** East African Orogenic Zone (**ANS**–Arabian-Nubian Shield, **MB**–Mozambique Orogenic belt). (figure from Begg et al. (2009))

and granitoids overlain by 3.0 to 2.78 Ga old greenstone belts. In the North, the Kaapvaal Craton is marked by 2.06 to 2.05 Ga old intrusions, commonly referred to as the Bushveld Igneous Complex. The Zimbabwe Craton accomodates a 3.5 to 2.8 Ga old gneiss complex which is covered by 2.8 to 2.7 Ga old flood basalts, komatiites and sediments. These, in turn, are overlain by 2.6 Ga old granitoids. The Limpopo belt, captured in between the Zimbabwe and the Kaapvaal Craton during their collision 2.7 to 2.6 Ga ago, consists of 3.3 to 3.1 Ga old gneiss which were affected by metamorphism and magmatism between 2.7 and 2.57 Ga ago. The boundaries to the adjacent cratons are strongly deformed.

The *Bangweleu Terrane* (VIII in Figure 6.1) is located South-West of the Tanzania Craton (Begg et al., 2009). It is described as an Archean microcontinent which has been strongly influenced by tectonic events in the neighbouring Paleoproterozoic belts. It consist of Archean granites and supracrustal rocks intruded by 2.73 Ga old granitic rocks. The terrane's northern half accommodates 1.87 Ga old arc-related metavolcanic rocks, 1.84 to 1.72 Ga old gneisses and 1.8 Ga old basins originating in rift-activity.

Paleoproterozoic fold belts

The *Ubendian Belt* (ub in Figure 6.1) is a fold belt bounding the southwestern Tanzanian Craton (Begg et al., 2009). Its main components are supracrustal rocks affected by metamorphism 2.03 to 1.97 Ga ago when the Tanzania Craton collided with the Bangweleu Terrane. The crust in the subsurface is Archean.

The *Usagaran Belt* (us in Figure 6.1) is located at the eastern boundary of the Tanzanian Craton (Begg et al., 2009). It mostly consists of granulite facies from 1.92 to 1.89 Ga ago, and 1.87 to 1.83 Ga old calc-alkaline granitoids with 2.0 Ga old eclogites in the central belt.

The *Ruwenzori Belt* (rb in Figure 6.1) in the North of the Tanzania Craton is composed of $>$2 Ga old metasedimentary rocks thrusted onto the craton (Begg et al., 2009).

Mesoproterozoic Mobile Belts

The *Irumide Belt* (ib in Figure 6.1) is located in the south of the Ubendian Belt (Begg et al., 2009). Here, 1.88 Ga old rhyolites and sediments cover Archean and Paleoproterozoic basement rocks. The belt is strongly affected by granotoid magmatism 1050 to 980 Ma ago

and metamorphism 1 Ga ago. The *Southern Irumide Belt* (sib in Figure 6.1) is viewed as separate from the main belt due to large regions of Mesoproterozoic gneisses.

The *Namaqua-Natal Belt* (nnb in Figure 6.1) surrounds the southern part of the Kaapvaal Craton (Begg et al., 2009). The Namaqua-Natal Belt joined with the southern Kaapvaal Craton 1.28 Ga ago. In turn, the Neoproterozoic-Paleozoic *Saldanian Fold Belt* (sb in Figure 6.1) wraps around the South of the Namaqua-Natal Belt.

Neoproterozoic Mobile Belts

The *Zambezi Belt* (zb in Figure 6.1) located between the Zimbabwe Craton and the Southern Irumide Belt mainly consists of Archean to Proterozoic gneisses covered by markedly deformed metasediments and granites (Begg et al., 2009).

The *East African Orogenic Zone* (same in Figure 6.1) is a broad suture zone between East and West Gondwana (the supercontinent predating the break-up of Africa and India) (Begg et al., 2009). The *Arabian-Nubian-Shield* (ANS in Figure 6.1) is composed by patches of island and back-arc terranes with some remaining fragments of younger oceanic crust. In the North, the *Mozambique Belt* (MB in Figure 6.1) located at Africa's East Coast and extending to the Arabian-Nubian Shield consists of young terranes and blocks of Archean to Mesoproterozoic continental crust. In the South, early Neoproterozoic sediments are inserted in interlayer spaces of Kenyan and Tanzanian, Archean gneisses. The basements of Mozambique's North, large parts of Malawi and Tanzania's South are composed of Paleoproterozoic to Neoproterozoic, 600 Ma old metamorphosed gneisses (Begg et al., 2009).

The East-African Rift

The East-African Rift (EAR) is one of the largest rift systems on Earth. It extents from the Afar region in the North of Ethiopia to the South of the Zambezi river. The rift is caused by the parting of the African and the Somalian plate as well as the Arabian plate in the North (Saria et al., 2014). The rift system is divided into two branches, the Western and the Eastern Rift. The Eastern Rift is divided into subbranches, which are the Afar Depression in the North, the Main Ethiopian Rift South of the Afar region, the Kenyan rift and a wide block faulting region in central Tanzania (Dugda, 2005). The Afar region in the North is depressed as a consequence

of the triple junction rifting of the three aforementioned plates and, hence, the extensional thinning in the region (Dugda, 2005). The Western Rift extents from the South of the Zambezi River, along the Ubendian Belt to the North of Lake Victoria. Studies of volcanism in the regions of continental rifting suggest that the rifting started 45 to 40 Ma ago in southern Ethiopia and propagated southwards into the North of Tanzania (Dugda, 2005). Similar investigations suggest that the rifting between the African and the Arabian plate started more recently, between 31 and 29 Ma ago. The formation of the Red Sea and Gulf of Aden, which is a consequence of the rifting, can be dated to 11 Ma ago; long after volcanic activity in the region had commenced (Dugda, 2005).

Previous Studies

The lithosphere and upper mantle of the East-African continent have been studied in some detail using various geophysical methods (Armitage et al., 2015; Begg et al., 2009; Cornwell et al., 2011; Dugda, 2005; Faccenna et al., 2013; Hansen et al., 2012; Julià et al., 2005; Last et al., 1997; Nair et al., 2006; Nguuri et al., 2001; Niu et al., 2004; Owens et al., 2000). Each study has provided new constraints on the different tectonic environments present in East Africa.

Lithosphere

Receiver function studies have confirmed that the crustal composition in southern Africa can be viewed as almost uniformly felsic (Nair et al., 2006). Furthermore, the crustal thickness varies marginally and the crust's thinnest regions ($\sim$38 km) are located below the oldest, undisturbed parts of the Zimbabwe and Kaapvaal Cratons (Nguuri et al., 2001). In these regions, high velocity contrasts observed between the lithospheric crust and mantle have provided a sharp image of the Moho (Nguuri et al., 2001). The crust below the Kaapvaal craton is thickening from South-West ($\sim$35 km) to North-East ($\sim$45 km) with the thickest region occurring in the Pietersburg Terrane which accomodates the Bushveld Complex. The Moho topography below the Limpopo belt was found to have a complex structure with depths of up to 50 km (Nguuri et al., 2001). A map of Africa's crustal thickness created with Data from the IRIS EARS automated receiver function survey (see Section 4.1) can be found in the Appendix B in Figure B.1.

The crust of the Tanzanian Craton has been found to be generally thinner than the crust in the Ubendian Belt (Last et al., 1997). Below the central craton, the crustal thickness is as low as 37 km (Dugda, 2005), whereas the Ubendian Belt has a crustal thickness of up to $\sim$ 44 km in the Central West of the Tanzanian Craton, likely thinning southwards (Dugda, 2005; Last et al., 1997).

Northwards within eastern Kenya, the crust was found to be systematically thinning through both refraction and receiver function studies (Dugda, 2005; Keller et al., 1994). The thinning is progressive from the border of Tanzania and Kenya, where the crust is 35 km thick, to the North of Kenya at 4°N, where the crust is 20 km thick. The shallowing Moho follows the Usagaran belt northwards between the Mozambique Belt in the East and the Tanzania and Ugandan Cratons in the West.

Receiver function studies of the Ethiopian Rift and the Afar Depression in northern Ethiopia and Djibouti have shown northward thinning within the main Ethiopian rift (from 36 to 27 km thickness) bounded by deep Moho recordings below both the Western Plateau and the Eastern Plateau, up to 44 and 42 km, respectively (Dugda, 2005). In the North, below the Afar Depression, the Moho shallows to values of $\sim$23 km (Dugda, 2005). Correlated with the thinning is an increase in Poisson's ratio from values as low as 0.27 to a maximum of 0.36 below the Afar Depression. This change in Poisson's ratio is attributed to the addition of large amounts of warm mafic rock (Dugda, 2005).

Mantle transition zone

Studies of the mantle transition zone below the Kalahari Craton and its vicinity have shown high v_p/v_s ratios in the upper mantle (Niu et al., 2004). This results in a shallower mapping of both MTZ discontinuities, the 410 and the 660, to $<$400 km and $<$640 km, respectively. Their topographies are rather flat, but they generally deepen southwards below the Namaqua-Natal Belt. The avarage thickness of MTZ lies at $\sim$250 km. (Niu et al., 2004).

As opposed to the Kahalari Craton, the Tanzanian Craton was found to have a variable mantle transition zone thickness introduced by the varying topography of the 410 discontinuity (Owens et al., 2000). The 660 is mostly flat at a depth of $\sim$670 km. The regions that have not been affected by the recent rift activity exhibit the thickest MTZ with a thickness of up to $\sim$280 km. The thinnest region ($\sim$240 km) is found in the area where the Eastern rift strikes the

craton's eastern boundary. The diameter of this region is up to 300km wide. The thinning is attributed to an increase in mantle temperature of between 200 and 300 K compared to regions in the southeastern craton. Furthermore, tomographic studies show clear low shear velocity anomalies below the Tanzanian craton.

Receiver function studies of the Afar regions have shown a largely flat 410 (Cornwell et al., 2011). The 410 is imaged 30 - 40 km deeper than global averages in the entire region. This depression is attributed to increasing temperatures and decreasing seismic velocities. The 660 was found to have a jump of $>$30 km which is located at the boundary between the Northern Main Ethiopian Rift and the Afar Depression. Below the Northern Main Ethiopian Rift, the depths of the 660 are depressed down to 700 km. Owens et al. (2000) interprets the cause to be a combination of both a hotter upper mantle and a difference in chemical composition; garnet-rich, where the 660 is deep, and olivine-rich, where the 660 is shallow. The jump in the 660's topography results in a thinning of the MTZ below the Afar Depression.

General Implications

The tomographic studies suggest that a mantle superplume originates from sub-asthenospheric depth below the South of the Tanzanian Craton with a flow northeastwards (Begg et al., 2009; Hansen and Nyblade, 2013; Hansen et al., 2012). The temperature anomaly is inferred to reach a maximum beneath the Afar region between 100 and 150 km (Begg et al., 2009; Hansen and Nyblade, 2013; Hansen et al., 2012) and that the northwards flow shallows to the same depths (Chang and Van der Lee, 2011). This is supported by geodynamic models, which suggest that the mantle plume shallows towards the sublithospheric depth beneath Arabia (Faccenna et al., 2013). From here, the mantle convection is modelled to flow northwards, curving almost 180° westwards underneath Anatolia to sink at the Hellenic subduction zone (Faccenna et al., 2013). The studies are in general agreement; that is, all studies show high temperatures beneath the Tanzanian Craton and the highest temperatures beneath Afar region. In Faccenna et al. (2013), the mantle flow of the plume northwards is shown to be abruptly thinning to a sublithospheric mantle flow below the Red Sea (see B.5). Furthermore, local tomographic images show a small, but localised low velocity anomaly beneath Yemen in the southern Arabian peninsula (Hansen and Nyblade, 2013). Northwards however, the high mantle temperatures seem to cease at asthenospheric depth.

The reason for the heavy thinning of the Afar region is attributed to the initial mantle-upwelling-induced decompression of the upper mantle (Armitage et al., 2015). Geochemical modelling suggests that initial melting of the lithosphere due to the mantle upwelling beneath Africa caused thinning of the lithosphere and rifting to start ∼23 Ma ago. Subsequently, the rising, high temperatures depressurised the upper asthenosphere which resulted in increased melting and thinning of the Afar region (Armitage et al., 2015).

6.2 Results

As in Chapter 5, the location and waypoints of the cross section seen in Figure 6.1 were chosen to maximise piercing points and imaging quality of the mantle transition zone. Maps of the stations in Africa and the piercing points for depths of the 410 and 660 are shown in Figures 6.2 (a) and (b). Furthermore, the cross section cuts two Archean cratons, the Kaapvaal and the Tanzanian Craton, and follows the mantle upwelling that is mapped to rises upwards from south of the Tanzania Craton to flow almost horizontally northeastwards in the upper asthenosphere (see Figures B.3 and B.5 in the Appendix B). Consequentially, the cross section should show a general thinning from South to North because of the transition from a cold upper mantle beneath the Kaapvaal Craton to a warmer one below the Tanzania Craton and a hot upper mantle below the Afar region. While the effect of the mantle upwelling on the mantle transition zone should be clearly visible, the effect on the Moho is expected to be very localised below the Afar region. In other parts of East Africa, the Moho is likely to be only affected by local changes in the tectonic setting or rifting associated with the East African Rift.

Lithosphere

The CCP stack for the lithosphere was calculated using a multi-mode stack in combination with phase-weighted stacking of the single modes. The gridcell size here is set to 0.5°-by-0.5° in size. Additionally, the bins were spatially averaged. While the spatial averaging does introduce lateral smoothing of the signal, it also enhances the signals in regions with poor data coverage, such as most parts of Africa.

A clear, positive signal ranging from 30 to 50 km depth is observed through all parts of East Africa except for the Afar region (see Figure 6.3). In the South, from ca. 530 to 1300 km

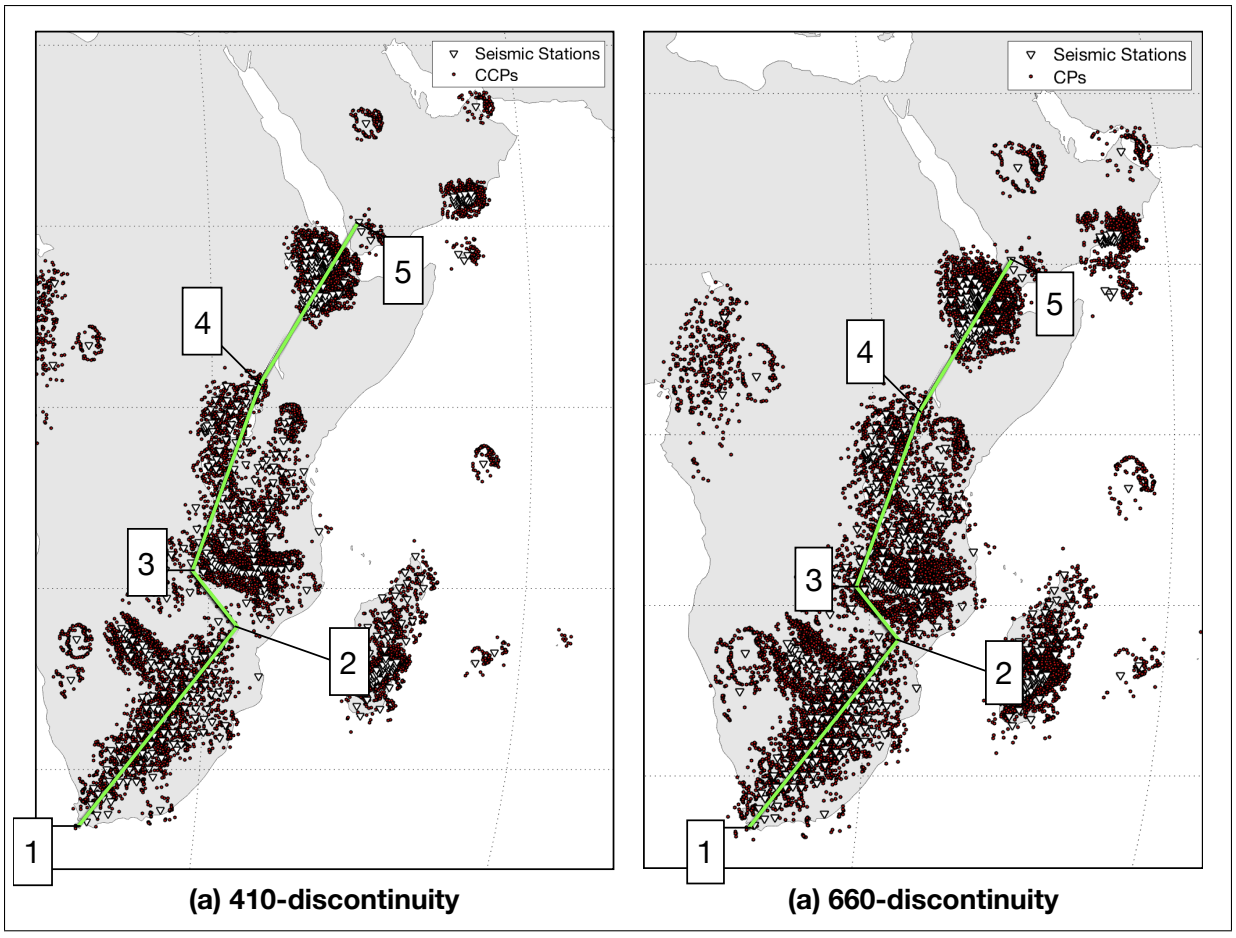

Figure 6.2: An overview of the piercing points at average mantle transition zone discontinuity depths. The white triangles are the stations used in our study and the dots are the **(a)** piercing points at 410 km depth and **(b)** piercing points at 660 km depth.

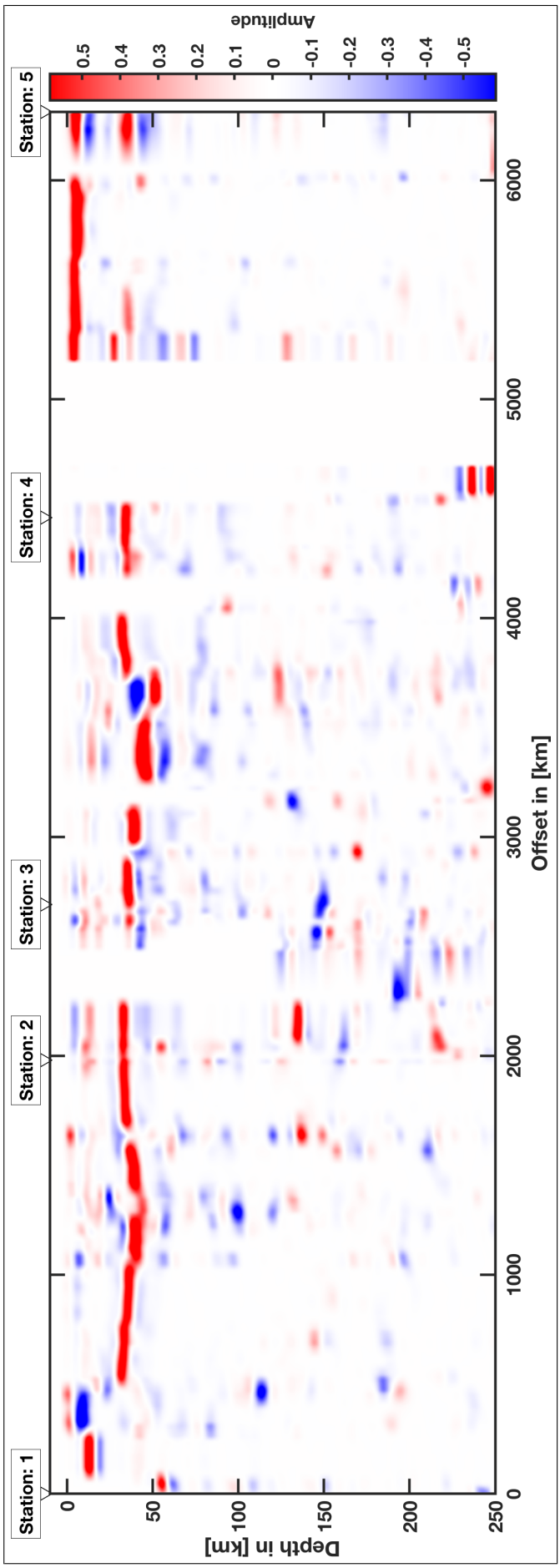

Figure 6.3: A reflectivity profile of East Africa's upper 250 km along the line shown in Figure 6.1. The cross section shows the Moho with a large, red, positive signal. See text for analysis and stacking procedures.

offset, the signal deepens from 31 to 42 km. Then, it shallows over the course of 700 km to a depth of 33 km and stays flat until 2200 km offset. Between 2200 and 2650 km offset, the data is interrupted due to the lack of stations in that area. Then, the signal shallows slightly from a depth of 36 km between 2650 and 2880 km offset. At 2900 km offset, the signal drops from 35 to 39 km depth; it continues flat to an offset of 3200 km where the signal drops again to 47 km depth. Also here, the signal stays flat for 300 km northwards. Between 3500 and 3750 km offset, the signal is flat and reaches its deepest point of 50 km depth. At 3750 km offset, the signal jumps to a depth of 35 km from where it shallows to 31 km depth at 4000 km offset. Between 4000 and 4200 km offset, there is no data and hence a white gap. From 4200 km, a flat signal stretches over 300 km northwards at a depth of 35 km. Between 0 and 530 km and between 5280 and 5800 km offset, the signals seem to disappear so that no contrast can be observed. However, the signals simply have much lower amplitude. Looking at Figure B.2 of Appendix B, a flat signal between 0 and 250 km offset at 40 km depth and a signal with a 4° updip from 250 to 530 km offset can be observed. Between 5280 and 5800 km offset, a clear shallowing of the signal can be observed from 35 to <30km depth.

Mantle Transition zone

The CCP stack for the MTZ was calculated using phase-weighted stacking of the *Pś* mode. The receiver functions were band-pass-filtered from 0.03 to 0.3 Hz to enhance the pulses of the 410 and 660. The gridcell size is set to 0.5°-by-0.5°. Additionally, the bins where spatially averaged. While the image clearly shows the Moho topography as well as bands of crustal reverberations between 100 and 200 km, the focus will be placed on the topography of the two mantle transition zone discontinuities, 410 and 660. Consequently, the distance between these two discontinuities, the thickness of the MTZ, will be presented as well. A reflectivity cross section of the upper 750 km is shown in Figure 6.4.

The 410 can be observed as a clear, positive signal throughout the whole cross section except for North-East Africa where it is weaker. In the South, from 0 to 500 km offset, the signal shallows from 410 to 400 km depth. From 400 to 2250 km, there is slight change in topography. In this range, the positive signal's deepest point is at 1500 km offset and 405 km depth. Between 2300 and 2600 km offset, there is a gap in the data, which correlates with the gap in station coverage between waypoints 2 and 3. From 2600 to 2950 km, the signal deepens

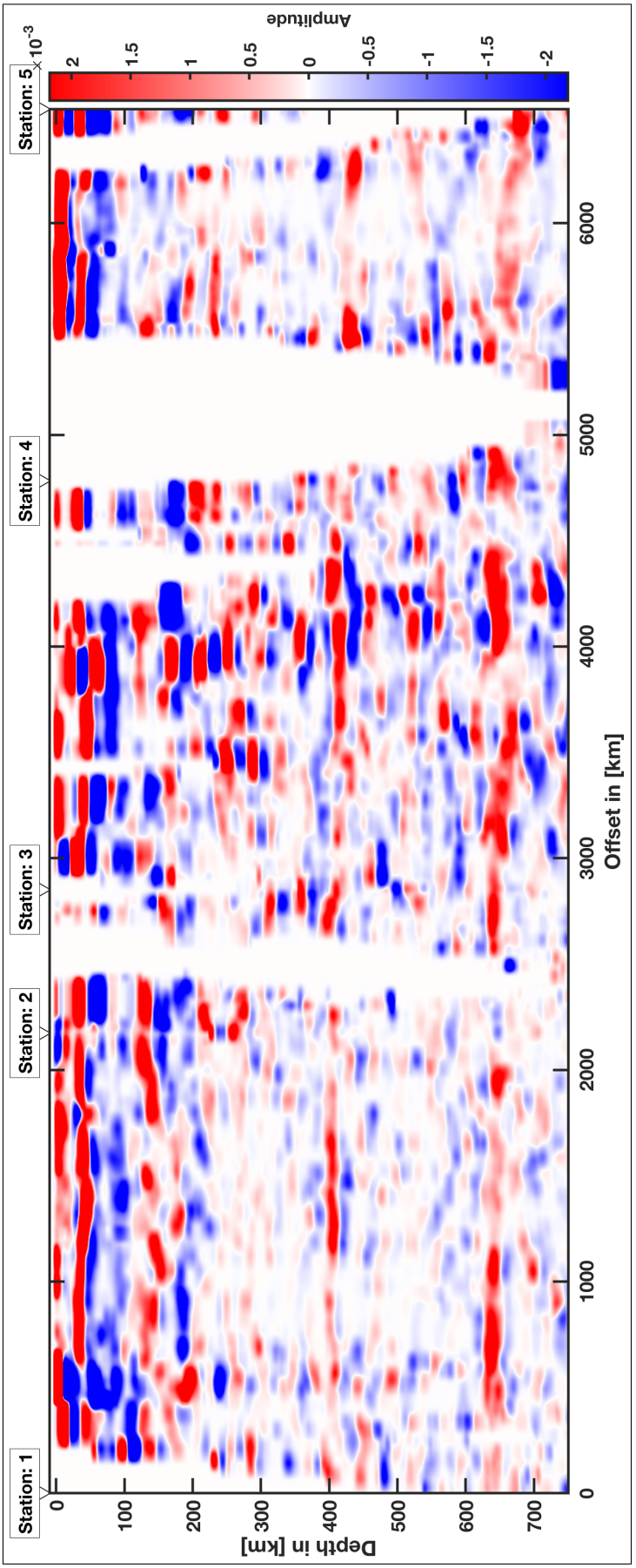

Figure 6.4: A reflectivity profile of East Africa's upper 750 km along the line shown in Figure 6.1. See text for details of the stacking procedures.

from 390 to 415 km. The signal deepens further to 430 km between 2950 and 3400 km offset. From this point it gradually shallows to a depth of 400 km at an offset of 4800 km. From 0 to 4800 km the signal is strong and relatively sharp. From 5400 to 6300 km however, the signal is weak compared to the rest of the cross section; visible, but weak and wide. Here, it ranges from between 415 to 435 km with the shallowest part at 5900 km.

The 660 can also be clearly observed as a positive signal along most of the profile. From 0 to 2000 km offset the signal deepens gradually from 635 to 645 km depth. The topography of the signal between 2500 and 5000 km changes gradually as well. From 2500 km offset towards 3600 km, the signal deepens from 640 to 660 km depth. From 3600 to 5000 km offset, the signal shallows again to a depth of 640 km. At 5300 km offset, the positive signal can be observed at a depth of 633 km. This signal drops to a depth of 655 km at 5550 km offset from where a wide, weak signal continues to deepen to 680 km depth.

Furthermore, two signals can be observed that have been seen at 520 km depth below other regions of the Earth. Between 3000 and 4200 km offset, a nearly flat signal can be seen that deepens from 515 to 520 km. A similar signal can be observed from 6000 to 6400 km, that shallows from 535 to 520 km.

The distance between the 410 and the 660 is generally decreasing from South to North with a sudden increase below waypoint 5 in the very North. While the distance between the two signals starts off rather small (230 km) compared to the global average of 250 km, it increases to 245 km from zero to 2300 km offset. Between waypoint 3 and 4, the distance between the 410 and the 660 varies from 230 to 250 km. Here, the thickness is at its lowest value at 3300 km offset due to a drop in 410 topography. On average, the signal is thinning towards waypoint 4 from 250 to 240 km. At an offset of 5400 km, the distance between the two signals is at its minimum of $\sim$205 km and jumps to a thickness of 220 km at 5550 km. From there, the distance gradually increases to its maximum of 265 km below waypoint 5.

6.3 Discussion

In this section, the results obtained in the previous section are discussed by first comparing the obtained results to previously found results for both the lithosphere and the mantle transition zone. Secondly, the general implications resulting from both lithospheric and mantle transition

zone investigations of East-Africa are discussed. The interpretation of the Moho depth results in Figure 6.3 are shown in Figure 6.5 and the interpretation of the MTZ results in Figure 6.4 are shown in Figure 6.6. The picked depths of the 410 and the 660 as well as an overview of the lateral changes in thickness can be seen in Figure 6.7.

Lithosphere

Below the Kalahari Craton, the Moho depth agrees with studies conducted by Nair et al. (2006) & Nguuri et al. (2001). The deepest point of the Moho is found below the Bushveld Igneous Complex located in the northern part of the Kaapvaal Craton in our results as well. From the Bushveld Complex southwards, the Moho shallows to the boundary of the Kaapvaal Craton, where the tectonic setting changes to the Namaqua-Natal Belt. Below, the Namaqua-Natal Belt, the Moho is rather deep (up to 45 km), which does not change below the Saldania Belt. In the North of the Kaapvaal Craton, the Limpopo Belt's Moho has a slight updip before it devolves to the flat Moho of the Zimbabwe Craton. The main differences between this study and the study of Nair et al. (2006) are the shallowness of the Moho below Cape Town and the >45 km deep Moho below parts of the Limpopo Belt, which is not observed in our study.

As opposed to the crustal thickness of the Kaapvaal Craton, crustal thickness of the Tanzanian Craton and its vicinity varies dramatically with several jumps in Moho depth. The change in tectonic environment introduces a significant change in Moho depth of 5 km from the the Bangweleu Block to the Ubendian Belt. Across the Ubendian belt, between the Bangweleu Block and the Tanzanian Craton, the same shallowing of the Moho from 39 to 40km depth can be observed, as it has been in the previous study of Hodgson et al. (2017). Below the southern Terrane of the Tanzanian craton, the Moho is shallowing slightly from 46 to 44 km before it jumps to its deepest signal of 51 km underneath the Dodoma zone. Station URAM of network XD (1994) is located at this point of the cross section. This is interesting because Last et al. (1997) did not see a clear Moho discontinuity below station URAM and Julià et al. (2005) could not find clear discontinuities in their S-velocity model below this station, either. After a jump in the signal due to the tectonic boundary between the Dodoma zone and the Northern Terrane, a thinning of the crust northwards can be observed below the Northern Terrane. The crust underneath the Ugandan Craton is generally flat at a depth of ca. 34 km.

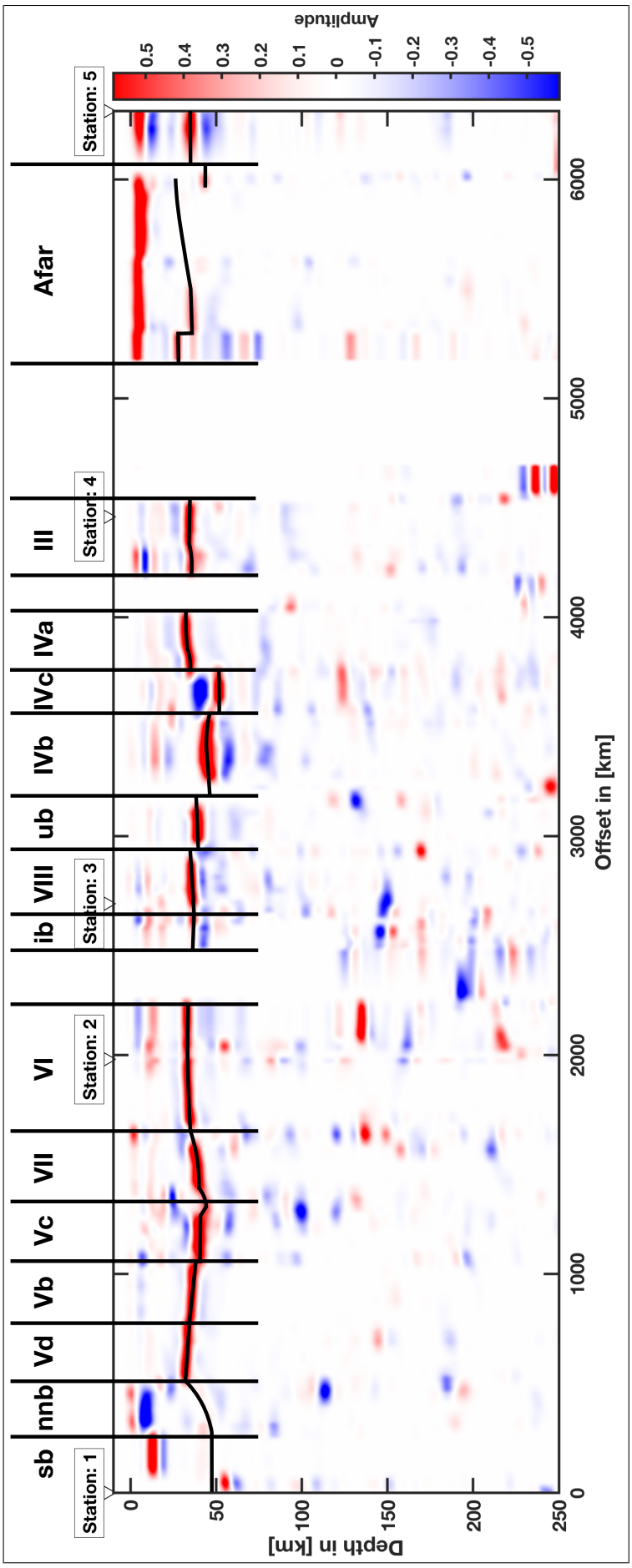

Figure 6.5: The cross section showing the Moho discontinuity along the line shown in 6.1 in form of a reflectivity profile with geological interpretation plotted on top. The vertical lines at the top of the figure indicate a change in tectonic environment. The abbreviations above the cross section and between the vertical lines are the respective tectonic environments found in Figure 6.1. The more or less horizontal lines mark the interpreted Moho depth.

Below the Afar region in Northern Ethiopia, the crust drops first from 29 to 35 km before it shallows northwards to a depth of 25 km. What is interesting here is how the signal of the Moho not only becomes shallower, but also weaker towards the North. The crust below the Arabian-Nubian Shield is flat and deeper again.

Mantle Transition Zone

As previous studies have shown (Niu et al., 2004), the 410 and the 660 are both flat below the Kalahari Craton with a slight depression of the 660 in the North of the Zimbabwe Craton. Here, the thickness of the MTZ varies only marginally; mostly due to interpreted depression of the 660 below the Zimbabwe Craton (see Figure 6.7). An alternative interpretation is indicated for the depth of the 660 below the Zimbabwe Craton. A splitting 660 has been observed in previous studies of North-East China's upper mantle and has been linked to lower temperatures in the MTZ caused by a subducted slab (Ai and Zheng, 2003). The double discontinuity associated with the 660 could be connected to the phase transformations of the non-olivine components, for example, garnet to perovskite, but it is still unclear whether these would be visible in the seismic images (Ai and Zheng, 2003). Furthermore, the split between the 660's here is up to 50 km in width, whereas Ai and Zheng (2003) found splits of a maximum of 15 km. Thus, the upper part of the discontinuity is interpreted as stacking anomaly.

The 410 and the 660 below the Tanzanian Craton are generally deeper below the centre of the craton than on the outskirts, but the thickness is relatively similar below the whole region with thinning at an offset of 2800km. This might be an indicator of low upper mantle velocities (Helffrich and Wood, 2001; Niu et al., 2004). From the southern border of the Iredium Belt to the southern parts of the Tanzania Craton's Southern Terrane, the 410 undulates significantly. These changes in 410 topography affect the thickness of the MTZ (see Figure 6.7 (a)). The mean thickness however stays around 240 km. The distinct flat signal below the centre of the craton, is interpreted as the 520-discontinuity. In the northern part of the Ugandan Craton, there appears to be a split of the 410. The 410 could either shallow or deepen northwards. The shallowing signal is chosen due to its higher amplitude.

The topography of the discontinuities below the Afar region is more complex than in the other regions. The 410 shows a shallowing in the centre of the Afar region and the 660 deepens to its deepest point underneath the Arabian-Nubian Shield. A jump in the 660 could

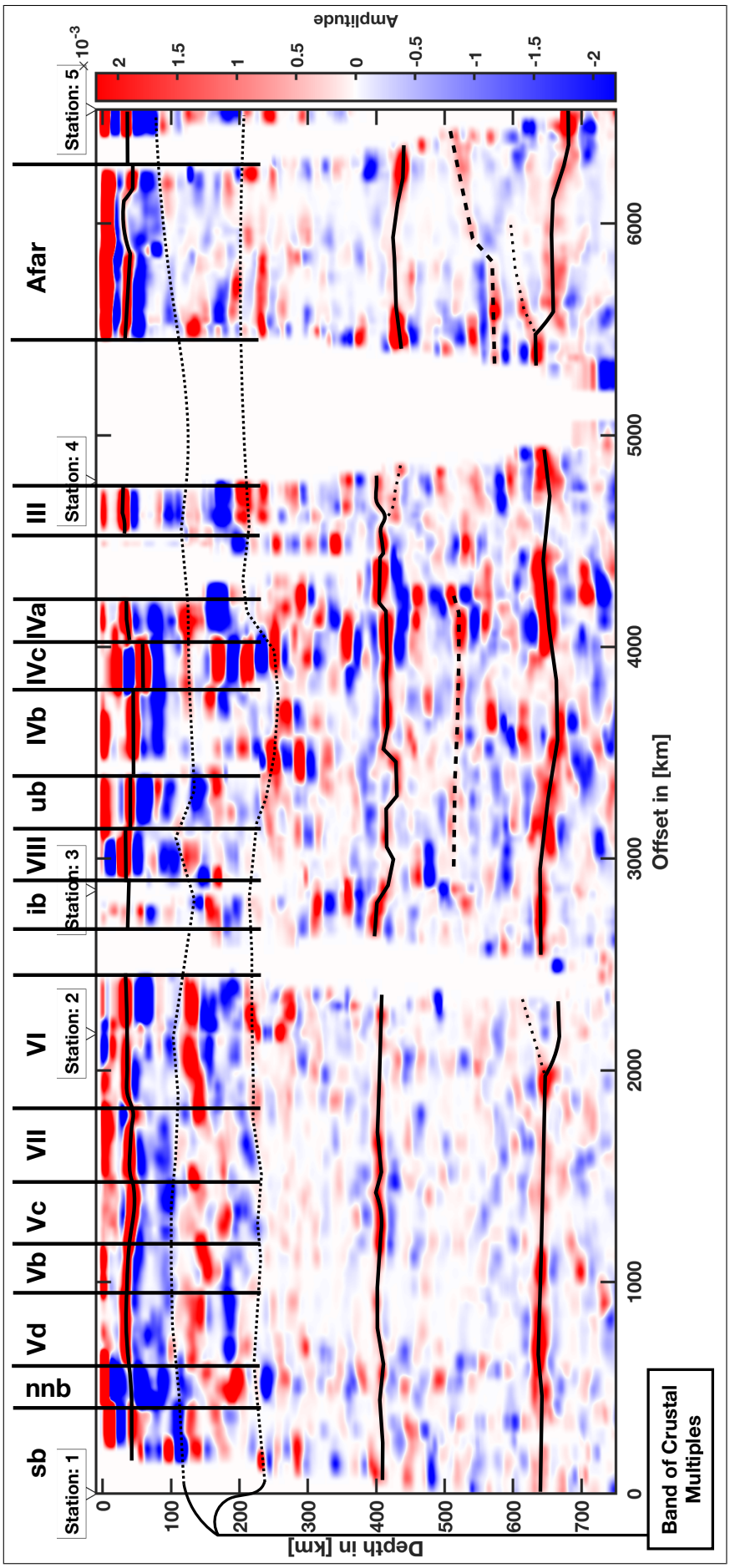

Figure 6.6: The cross section showing the Moho discontinuity as well as the mantle transition zone along the line shown in 6.1 in form of a reflectivity profile with geological interpretation plotted on top. The vertical lines at the top of the figure indicate a change in tectonic environment. The abbreviations above the cross section and between the vertical lines are the respective tectonic environments found in Figure 6.1. The more or less horizontal lines mark the interpreted Moho depth (between ca. 20 and 70 km), the 410-discontinuity (between ca. 380 and 440 km) and the 660-discontinuity (between ca. 600 and 700 km). The thin dotted lines show possible other solutions to the interpretations of 410 and 660. The dashed line at ca. 520 km marks interpretations for the 520-discontinuity.

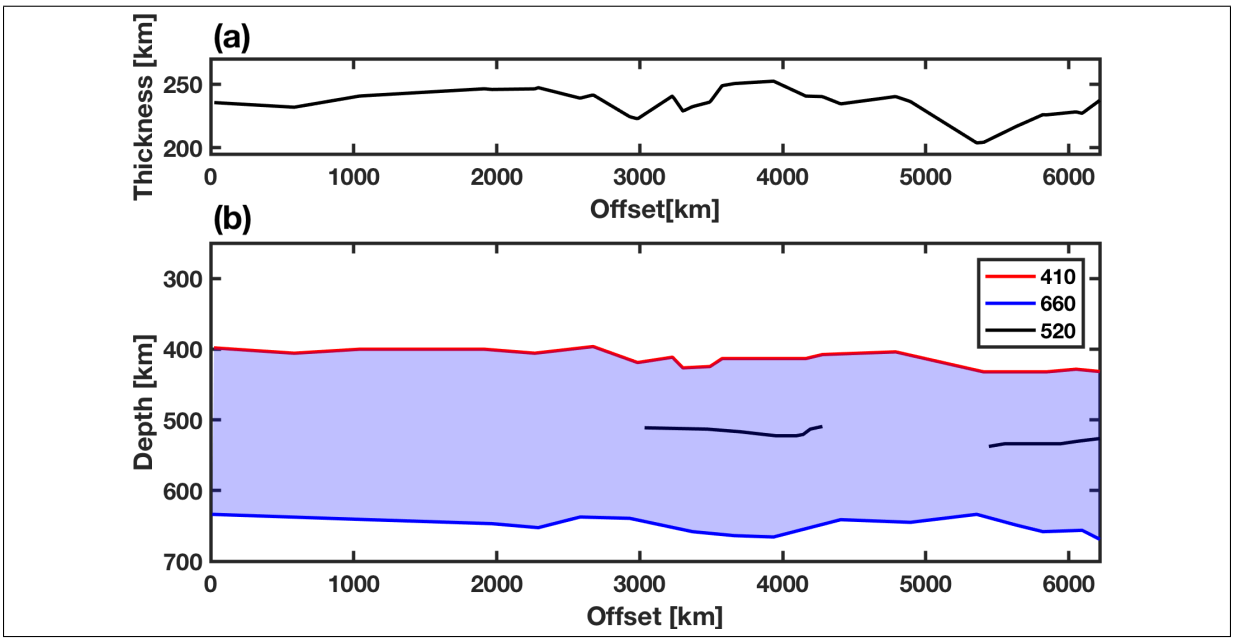

Figure 6.7: Thickness of the mantle transition zone as picked from the geological interpretation of Figure 6.6. **(a)** Shows lateral changes in MTZ thickness. **(b)** Shows changes in topography of the 410 and the 660 as well as the 520.

be observed (indicated by the dotted line) as in a previous study (Cornwell et al., 2011), but the results obtained here show a more coherent signal deepening towards the Arabian peninsula. What is most striking here is the development of the 520-discontinuity in relation to the 410 and 660. While the 410 stays relatively flat at its lowest regional average, the 520 shallows at average angle of 3° and the 660 deepens with an average angle of 1.9°. Looking back at Figure 2.3 of the introduction, this development indicates a hot MTZ in the South of the Afar region with a large, negative temperature gradient towards the Arabian Peninsula (Bina and Helffrich, 1994; Helffrich and Bina, 1994; Helffrich and Wood, 2001).

In our cross section, the 410 and 660 are imaged generally shallower or deeper than in previous CCP studies depending on the region. For example, Niu et al. (2004) found a 410 that is up to 15 km shallower than the one observed here before applying the traveltime residual method. Furthermore, Cornwell et al. (2011) sees the 410 and 660 much deeper than imaged here. The reason for this is that the other methods have used the IASP91 model for the ray tracing which is based on a global average in arrival times. Owing to the Kalahari Craton's colder temperatures and resulting high v_p/v_s ratio, the 410 is mapped much shallower than the global average. In case of the Afar region, the temperatures are high and the v_p/v_s ration low. Thus, the 410 is mapped deeper. In this study, to avoid the issue, the global tomographic GyPSuM model was used as shown in Section 4.2.2 to correct for upper mantle velocity

anomalies. Hence, the discontinuities are imaged at a more accurate depth than if a one dimensional velocity model would have been used (see Figure A.2).

Implications

The Moho's topography along the cross section is heavily influenced by the tectonic history of Africa which is an assemblage of ancient continents and microcontinents. The different tectonic regions are distinguishable by jumps introduced by their tectonic boundaries (Begg et al., 2009). Within the cratons, the shallowest Mohos are found below the oldest, undisturbed parts, whereas the deepest Mohos are found beneath the 'most disturbed' parts of the cratons; that is, the Moho below the Bushveld Complex within the Kaapvaal Craton and the Moho below the Dodoma zone in the centre of the Tanzanian Craton. In the vicinity of the Bushveld complex, this is attributed to the added overburden of high density mafic basalt (Nair et al., 2006). The Dodoma zone, as well, has been intruded by granites, which results in added load and could be the reason for a depressed Moho. Since granite is felsic however, and, therefore, not as dense as basalt, it is difficult to make an assumption whether it is, in fact, the added load causing the Moho to be so deep.

The thinning of the mantle transition zone beneath the Bangweleu block coincides with the location where the mantle upwelling penetrates the MTZ from the lower mantle (Hansen et al., 2012). This was also revealed by Bastow et al. (2018). Our approximate interpretation of the MTZ thickness is plotted on top of a tomographic image by Bastow et al. (2018) in Figure B.4. Below the central Tanzanian Craton, the depression of the 410 suggests low velocities in the upper asthenosphere (Helffrich and Wood, 2001), while the thickness of the MTZ does not provide a clear indication of high temperatures within the MTZ. Hence, after piercing the MTZ, high mantle temperatures could be restricted to $<$410 km depth (Helffrich and Bina, 1994).

Below the Afar region, the observed results agree with studies of Hansen and Nyblade (2013) and Faccenna et al. (2013). The MTZ's thinnest point below the Afar region indicates that the temperatures of the asthenosphere, especially within the mantle transition zone, are the highest. The thickening of the MTZ towards Arabia as well as the thinning crust below the Afar region suggest that mantle convection and thus, the hot temperatures of the African plume are restricted to sub-lithospheric depths below the Arabian peninsula. The localised low velocity anomaly below Yemen is only in the vicinity of the cross section.

In the previous paragraphs, four indicators were found for the development of the African plume below East Africa:
(1) a thin MTZ beneath the Bangweleu Terrane and the Ubendian belt suggests a possible piercing of the mantle plume due to high temperatures within the MTZ (Bastow et al., 2018; Hansen et al., 2012; Helffrich and Wood, 2001).
(2) a depressed 410 below the central Tanzanian Craton suggests low upper asthenosphere velocities and, hence, high temperatures (Helffrich and Wood, 2001; Niu et al., 2004);
(3) a weak and thinning Moho below the Afar region suggests extensional thinning of the crust below the Afar region (Dugda, 2005; Saria et al., 2014) as well as decompression melting (Armitage et al., 2015);
(4) the thinnest part of the MTZ located below the Afar region suggests the hottest temperatures across all of East-Africa (Begg et al., 2009; Chang and Van der Lee, 2011; Hansen and Nyblade, 2013); (5) the thickening of the MTZ from below the Afar region to the Arabian-Nubian Shield indicates a negative temperature gradient (Helffrich and Wood, 2001), while the unchanging depth of 410 in the upper asthenosphere suggests low velocities and, hence, high temperatures.

In Figure 6.8, these results are summarised in agreement with previously found constraints. Note that this model is a very rough schematic and does, for example, not explain the local uplift of the 660 beneath Afar found by (Cornwell et al., 2011). It does however explain the four points above and agrees with the general geometry of the low velocity anomalies found by Begg et al. (2009); Hansen et al. (2012) and the geodynamically modelled flow of the upper mantle (Faccenna et al., 2013).

Future Outlook

Concerning Africa's subsurface, the region between the Ugandan Craton and the Afar region is lacking coverage in seismic stations. A deployment of seismic stations could shed a light on the development of the Moho and MTZ between the two regions. Especially intriguing would be the change in MTZ thickness . Since the largest thinning gradient seems to be located there, a study could provide better constraints on the MTZ temperature and, hence, the plume's temperature compared to its asthenospheric surroundings. A seismic study would, however, not only be interesting for mapping sharp discontinuities. Tomography results have already imaged

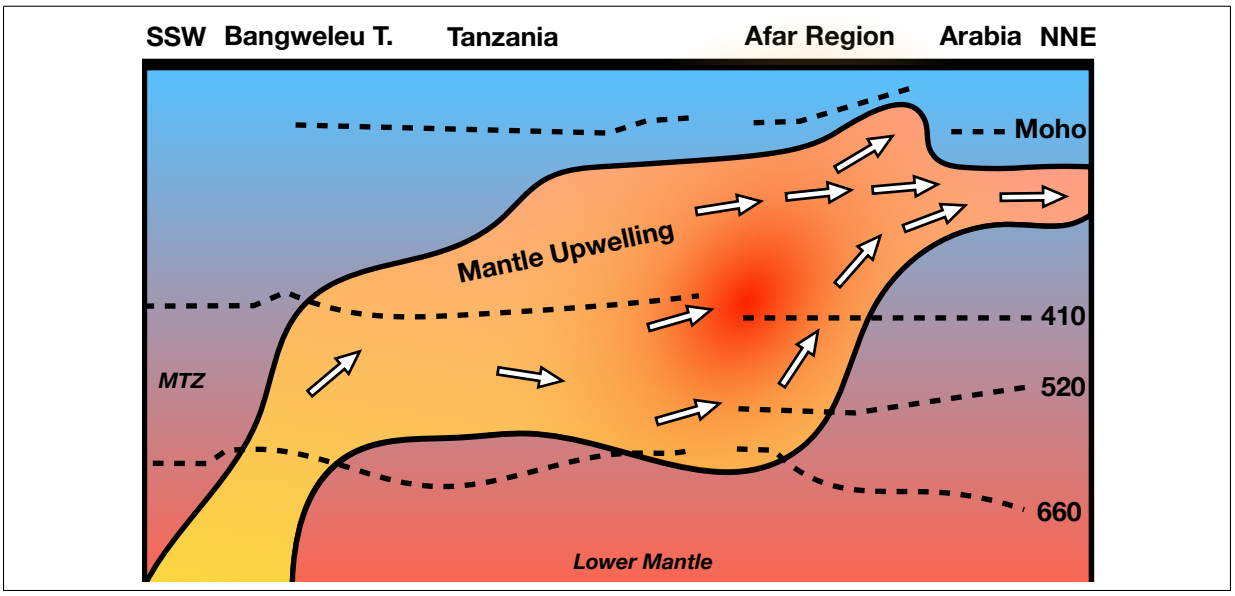

Figure 6.8: Schematic model of the mantle upwelling below the Eastern Africa from the Bangweleu Terrane South-Southwest to the Arabian peninsula North-Northeast. Red indicates warmer temperatures within the mantle upwelling as well as the surroundings. However, surrounding temperatures and mantle upwelling temperature do not necessarily correlate. The blue colour indicates colder temperatures in the surroundings, and yellow colour within the plume. The white arrows indicate plume-induced mantle flow direction in agreement with (Faccenna et al., 2013). This schematic is only meant to be a rough sketch rather than a complete explanation. It merely explains our data in agreement with previous studies.

the lateral dimensions of the high temperature anomaly below the Afar depression (Hansen and Nyblade, 2013). A seismic tomography study between the two regions could further constrain the lateral extent of the temperature anomaly northwards from below the Ugandan Craton. In conclusion, deploying seismic stations would be most interesting.

Chapter 7

Discussion

A brief discussion of the in Chapter 4 developed method's functionality, advantages and disadvantages was already given as a part of section 4.2.5. This chapter will serve as a short discussion of the method in the light of the results obtained in Chapters 5 and 6.

As already mentioned in Section 3.4, the common conversion point stacking has certain disadvantages compared to other methods. One of these was clearly observed in the results of Chapter 5. As soon as the velocity model is not clearly adapted to the geology of the near-subsurface, structures are imaged at the wrong depth. This is especially counterproductive in the case of multi-mode stacking. Since each mode is wrongly mapped, the multi-mode stack attenuates the signals due to their incoherence. In case of the mantle transition zone, Niu et al. (2004) used S-P traveltime residuals to correct for discrepancies in the velocity model of the lower lithosphere and upper asthenosphere. This, however, is not an efficient method for a global dataset of receiver functions. Here instead, a global tomographic velocity model was chosen due to its simple implementation and because such a model originates in one study which ensures that all data are treated equally – something that cannot be done in composite velocity models.

Another disadvantage of this method is the issue of not being able to image dipping layers correctly due to the assumption of horizontal layers. As shown in Section 4.2.5 however, all dips up to a dip angle of 20° can be imaged smoothly. The only condition is that the velocities of the subsurface do not diverge too much from the ones used to stack, something that is often difficult to achieve. Thus, for more complex structures, other methods, such as the migration of

receiver functions (Cheng et al., 2017) or full waveform inversion (Tong et al., 2014), are better suited.

When CCP studies focus on a certain area, the results will generally be better than those obtained by the method developed here. One of the reasons for this is a usually better suited data selection in each individual study; something that this method is not concerned with. Furthermore, arrival times of the P-wave were not picked by hand, but a theoretical P-arrival time is found since hand-picking arrivals of such an extensive catalogue is simply too inefficient (Rondenay et al., 2017). Additionally, variable bin sizes to accommodate more data are not implemented here, which can increase the quality of the results (see Cornwell et al. (2011); Niu et al. (2004) for comparison). However, the variable bin size introduces not only a variable spatial averaging as done on the method developed here, but also an uneven distribution of data, which can result in biased images of the subsurface. Furthermore, better local velocity models can be used to produce better results in the stacking. The method developed here is, in fact, variable in terms of velocity model. It can use any three-dimensional, geo-located velocity model for the raytracing to provide better results than using a non-local velocity model. The disadvantage is that most regions that have not been studied extensively yet do not have a better local velocity model.

The clear benefit of this CCP procedure developed here is its versatility. It can be used globally and at different scales as seen in Chapters 5 and 6 and provide similar results as methods that have investigated the same areas, without heavy data-selection procedures. That is, the resolution of the area investigated can be matched with the density in seismic stations and provide good results at either end of the scale. Furthermore, the stacking procedure can be chosen as shown in Section 4.2.5. As aforementioned, a consequence of three-dimensional CCP stacking is the spreading of the data in three dimensions. This results in smaller data densities, especially when one compares our results to two-dimensional studies. However, an advantage of stacking in three dimensions is that it reveals structures, such as the ones seen in Section 5.2, that cannot be observed by two-dimensional stacking procedures. Additionally, the plotting tools developed as a part of this thesis and project GLImER can display the calculated data as three-dimensional volumes in form slices. The slices can then be moved in both horizontal directions and be rotated to make the CCP stacks explorable in three dimensions as seen in 5.

In Section 4.2.5, it was shown that the multi-mode stack provides clearly better images than a single mode stack. As observed in Sections 6.2 and 6.3, the method was able to image a clear signal from the Moho and attenuate all other incoherent signals. Especially the usually strong multiples are not detectable. As opposed to a study by Tauzin et al. (2016), the phase-weighted stacking was done here on the single-modes followed by a linear multi-mode stack, instead of the other way around, because we found that stacking in this order generally provides better results (see Section 4.2.5).

Lastly, it is worth mentioning that the computational efficiency has improved significantly throughout the development. CCP stacks for a bin grid with 0.25°-by-0.25° cell size can now be calculated for Africa in less than 2.5h (on a machine with 16 cores and moderate clock speed); this includes the raytracing, binning and stacking. In the beginning of the development, the same calculation would have taken more than a week due to a lack of optimisation. This speed allows for fast recalculation of the stacks and quick testing of different parameters, such as the velocity model.

Future Outlook

With a more extensive time frame several aspects of this method could be further developed. First of all, the 3D volumes obtained by using the plotting tool in combination with the CCP stacks could be imported to a professional seismic interpretation program such as Schlumberger's Petrel Software. Petrel would provide a better means to pick surfaces such as the Moho, the 410 or the 660 discontinuities. Furthermore, a better bin grid setup could potentially provide better stacking results and improve the performance of the calculation. The possibly best solution is to create a mesh of triangles (Persson and Strang, 2004) at the surface of the Earth, where the triangles vertices define the bin centres as explained Section 4.2.3. From these bin centres, all piercing points within a certain epicentral distance (calculated with Vincenty's formula for the distance on an ellipse (Vincenty, 1975)) are stacked. This way the spatial averaging can be controlled in ratio of overlap between two circles.

Chapter 8

Conclusion

In this thesis, a method was developed that enables the calculation of global common conversion stacks using the receiver functions of project GLImER. It was shown that the method has certain advantages and disadvantages, but proves itself to be a suitable tool to study the local, regional and global variations in crustal as well as upper mantle structure. Especially the method's versatility is to be highlighted. Depending on the depth of investigation and density of seismic data, the data can be filtered and the bin size can be adjusted. For shallow discontinuities, the CCPs may additionally be constructed using multiple conversion/reflection modes, which further enhances the results of the subsurface images.

The method was applied to two tectonically different regions to provide a real-data test and provide some new constraints in crustal and upper mantle structure. The results of the Cascadia subduction zone were shown to match the previous CCP studies of the same region (Tauzin et al., 2016). The method was not only able to reproduce the horizontal North American Moho but also the dipping discontinuities associated with the subducting slab of the Juan de Fuca plate. Furthermore, the subducting slab was shown to have a slight dip southwards perpendicular to the subducting slab's dip. The crustal structure of Africa was found to be predominantly influenced by its tectonic history, showing jumps at almost every tectonic boundary. Furthermore, East Africa's upper mantle was shown to be significantly affected by previously investigated plume activity from Tanzania to the Afar region, which manifests in a general thinning of the MTZ from Cape Town to Northern Ethiopia. Additionally, a negative temperature gradient at mantle transition zone depth was detected from the centre of the Afar region, across the Red Sea towards the Arabian-Nubian Shield.

In conclusion, the method developed here is an excellent tool to not only quickly but also thoroughly obtain an overview of local, regional and global changes in topography of sharp subsurface discontinuities, which is superior to single station stacking and does not relie on dense seismic arrays.

References

Ai, Y. and T. Zheng (2003). The upper mantle discontinuity structure beneath eastern China. *Geophysical Research Letters 30*(21), 1–5.

Aki, K. and P. G. Richards (2002). *Quantitative Seismology* (2 ed.). Sausalito, CA: University Science Books.

Armitage, J. J., D. J. Ferguson, S. Goes, J. O. Hammond, E. Calais, C. A. Rychert, and N. Harmon (2015). Upper mantle temperature and the onset of extension and break-up in Afar, Africa. *Earth and Planetary Science Letters 418*, 78–90.

Audet, P. (2013). Seismic anisotropy of subducting oceanic uppermost mantle from fossil spreading. *Geophysical Research Letters 40*, 173–177.

Bastow, I., C. Ogden, N. Hodson, C. Venereau, and S. Pilidou (2018). The TROODOS Experiment : Tomography and Receiver function Observations of an Ophiolite using Data Obtained from Seismology. In *Geophysical Research Abstracts*, Volume 20.

Begg, G., W. Griffin, L. Natapov, S. Y. O'Reilly, S. Grand, C. O'Neill, J. Hronsky, Y. P. Djomani, C. Swain, T. Deen, and P. Bowden (2009). The lithospheric architecture of Africa: Seismic tomography, mantle petrology, and tectonic evolution. *Geosphere 5*(1), 23–50.

Bina, C. R. and G. Helffrich (1994). Phase transition Clapeyron slopes and transition zone seismic discontinuity topography. *Journal of Geophysical Research 99*(B8), 15,853–15,860.

Bostock, M. G., R. D. Hyndman, S. Rondenay, and S. M. Peacock (2002). An inverted continental moho and serpentinization of the forearc mantle. *Nature 417*(6888), 536–538.

Bostock, M. G. and S. Rondenay (1999). Migration of scattered body waves. *Geophysical Journal International 137*(March), 732–746.

Bostock, M. G., S. Rondenay, and J. Shragge (2001). Multiparameter two-dimensional inversion of scattered teleseismic body waves 1. Theory for oblique incidence. *Journal of Geophysical Research: Solid Earth 106*(B12), 30771–30782.

Chang, S. J. and S. Van der Lee (2011). Mantle plumes and associated flow beneath Arabia and East Africa. *Earth and Planetary Science Letters 302*(3-4), 448–454.

Cheng, C., T. Bodin, B. Tauzin, and R. M. Allen (2017). Cascadia subduction slab heterogeneity revealed by three-dimensional receiver function Kirchhoff migration. *Geophysical Research Letters 44*(2), 694–701.

Connolly, P. (1999). Elastic impedance. *The Leading Edge 18*(4), 438–452.

Cornwell, D. G., G. Hetényi, and T. D. Blanchard (2011). Mantle transition zone variations beneath the Ethiopian Rift and Afar: Chemical heterogeneity within a hot mantle? *Geophysical Research Letters 38*(16), 1–6.

Crotwell, H. P. and T. J. Owens (2005). Automated Receiver Function Processing. *Seismological Research Letters 76*(6), 702–709.

Crotwell, H. P., T. J. Owens, and J. Ritsema (1999). The TauP Toolkit: Flexible Seismic Travel-time and Ray-path Utilities. *Seismological Research Letters 70*(2), 154–160.

Drottning, A. (2017). *Inversion of Teleseismic Polarization Data for Crustal Velocities in Norway*. Master's thesis, University of Bergen.

Dueker, K. G. and A. F. Sheehan (1997). Mantle discontinuity structure from midpoint stacks of converted P to S waves across the Yellowstone hotspot track. *Journal of Geophysical Research: Solid Earth 102*(B4), 8313–8327.

Dugda, M. T. (2005). Crustal structure in Ethiopia and Kenya from receiver function analysis: Implications for rift development in eastern Africa. *Journal of Geophysical Research 110*(B1), B01303.

Faccenna, C., T. W. Becker, L. Jolivet, and M. Keskin (2013). Mantle convection in the Middle East: Reconciling Afar upwelling, Arabia indentation and Aegean trench rollback. *Earth and Planetary Science Letters 375*, 254–269.

Farestveit, M. (2017). *Anisotropic Properties of a Mid-Lithospheric Discontinuity in Eastern North America*. Master's thesis, University of Bergen.

Frassetto, A., G. Zandt, H. Gilbert, T. J. Owens, and C. H. Jones (2010). Improved imaging with phase-weighted common conversion point stacks of receiver functions. *Geophysical Journal International 182*(1), 368–374.

Frederiksen, A. W. and M. G. Bostock (2000). Modelling teleseismic waves in dipping anisotropic structures. *Geophysical Journal International 141*(2), 401–412.

Ganguly, J., A. M. Freed, and S. K. Saxena (2009). Density profiles of oceanic slabs and surrounding mantle: Integrated thermodynamic and thermal modeling, and implications for the fate of slabs at the 660 km discontinuity. *Physics of the Earth and Planetary Interiors 172*(3-4), 257–267.

Gurrola, H., J. B. Minster, and T. J. Owens (1994). The Use of Velocity Spectrum For Stacking Receiver Functions and Imaging Upper Mantle Discontinuities. *Geophysical Journal International 117*(2), 427–440.

Hansen, S. E. and A. A. Nyblade (2013). The deep seismic structure of the Ethiopia/Afar hotspot and the African superplume. *Geophysical Journal International 194*(1), 118–124.

Hansen, S. E., A. A. Nyblade, and M. H. Benoit (2012). Mantle structure beneath Africa and Arabia from adaptively parameterized P-wave tomography: Implications for the origin of Cenozoic Afro-Arabian tectonism. *Earth and Planetary Science Letters 319-320*, 23–34.

Havskov, J. and L. Ottemoller (2010). *Routine Data Processing in Earthquake Seismology*. Dordrecht: Springer Netherlands.

Helffrich, G. and C. R. Bina (1994). Frequency dependence of the visibility and depths of mantle seismic discontinuities. *Geophysical Research Letters 21*(24), 2613–2616.

Helffrich, G. R. and B. J. Wood (2001). The Earth's mantle. *Nature 412*(6846), 501–507.

Hodgson, I., F. Illsley-Kemp, R. J. Gallacher, D. Keir, C. J. Ebinger, and K. Mtelela (2017). Crustal Structure at a Young Continental Rift: A Receiver Function Study From the Tanganyika Rift. *Tectonics 36*(12), 2806–2822.

Julià, J., C. J. Ammon, and A. A. Nyblade (2005). Evidence for mafic lower crust in Tanzania, East Africa, from joint inversion of receiver functions and Rayleigh wave dispersion velocities. *Geophysical Journal International 162*(2), 555–569.

Keller, G. R., C. Prodehl, J. Mechie, K. Fuchs, M. A. Khan, P. K. Maguire, W. D. Mooney, U. Achauer, P. M. Davis, R. P. Meyer, L. W. Braile, I. O. Nyambok, and G. A. Thompson (1994). The East African rift system in the light of KRISP 90. *Tectonophysics 236*(1-4), 465–483.

Kennett, B. L. N. (1991). The Removal of Free Surface Interactions From Three-Component Seismograms. *Geophysical Journal International 104*(1), 153–154.

Kennett, B. L. N. and E. R. Engdahl (1991). Traveltimes for global earthquake location and phase identification. *Geophysical Journal International 105*, 429–465.

Langston, C. A. (1979). Structure under Mount Rainier, Washington, inferred from teleseismic body waves. *Journal of Geophysical Research 84*(B9), 4749.

Last, R. J., A. A. Nyblade, C. A. Langston, and T. J. Owens (1997). Crustal structure of the East African Plateau from receiver functions and Rayleigh wave phase velocities. *Journal of Geophysical Research: Solid Earth 102*(B11), 469–483.

Marshak, S. (2015). *Earth: Portrait of a Planet* (5th ed.). New York: W.W. Norton & Company.

McCrory, P. A., J. L. Blair, F. Waldhauser, and D. H. Oppenheimer (2012). Juan de Fuca slab geometry and its relation to Wadati-Benioff zone seismicity. *Journal of Geophysical Research: Solid Earth 117*(9), 1–24.

Mussett, A. E. and M. A. Khan (2000). *Looking into the Earth: An Introduction to Geological Geophysics* (1 ed.). Cambridge: Cambridge University Press.

Nair, S. K., S. S. Gao, K. H. Liu, and P. G. Silver (2006). Southern African crustal evolution and composition: Constraints from receiver function studies. *Journal of Geophysical Research: Solid Earth 111*(2), 1–17.

Nguuri, T. K., J. Gore, D. E. James, S. J. Webb, C. Wright, T. G. Zengeni, O. Gwavava, and J. A. Snoke (2001). Crustal structure beneath southern Africa and its implications for the formation and evolution of the Kaapvaal and Zimbabwe cratons. *Geophysical Research Letters 28*(13), 2501–2504.

Niu, F., A. Levander, C. M. Cooper, C. T. A. Lee, A. Lenardic, and D. E. James (2004). Seismic constraints on the depth and composition of the mantle keel beneath the Kaapvaal craton. *Earth and Planetary Science Letters 224*(3-4), 337–346.

Osborne, P. (2013). The Mercator Projections. Technical report, Edinburgh.

Owens, T. J., A. A. Nyblade, H. Gurrola, and C. A. Langston (2000). Mantle transition zone structure beneath Tanzania, East Africa. *Geophysical Research Letters 27*(6), 827–830.

Owens, T. J., G. Zandt, and S. R. Taylor (1984). Seismic Evidence for an Ancient Rift Beneath the Cumberland Plateau, Tennessee: A Detailed Analysis of Broadband P Waveforms. *Journal of Geophysical Research 89*, 7783–7795.

Persson, P.-O. and G. Strang (2004). A Simple Mesh Generator in MATLAB. *SIAM Review 46*(2), 329–345.

Rondenay, S. (2009). Upper mantle imaging with array recordings of converted and scattered teleseismic waves. *Surveys in Geophysics 30*(4-5), 377–405.

Rondenay, S., G. A. Abers, and P. E. van Keken (2008). Seismic imaging of subduction zone metamorphism. *Geology 36*(4), 275–278.

Rondenay, S., M. G. Bostock, and J. Shragge (2001). Multiparameter two-dimensional inversion of scattered teleseismic body waves 3. Application to the Cascadia 1993 data set. *Journal of Geophysical Research 106*(12), 30795–30807.

Rondenay, S., K. Spieker, L. Sawade, F. Halpaap, and M. Farestveit (2017). GLImER: A New Global Database of Teleseismic Receiver Functions for Imaging Earth Structure. *Seismological Research Letters 88*(1), 39–48.

Saria, E., E. Calais, D. S. Stamps, D. Delvaux, and C. J. H. Hartnady (2014). Solid Earth Present-day kinematics of the East African Rift. *Journal of Geophysical Research: Solid Earth 119*(4), 3584–3600.

Schimmel, M. and H. Paulssen (1997). Noise reduction and detection of weak, coherent signals through phase weighted stacks. *Geophysical Journal International 130*, 497–505.

Shearer, P. M. (2009). *Introduction to Seismology* (2 ed.). New York: Cambridge University Press.

Simmons, N. A., A. M. Forte, L. Boschi, and S. P. Grand (2010). GyPSuM: A joint tomographic model of mantle density and seismic wave speeds. *Journal of Geophysical Research: Solid Earth 115*(12), 1–24.

Stein, S. and M. E. Wysession (2003). *An Introduction to Seismology, Earthquakes and Earth Structure* (1 ed.). Oxford: Blackwell Science.

Tauzin, B., T. Bodin, E. Debayle, J. P. Perrillat, and B. Reynard (2016). Multi-mode conversion imaging of the subducted Gorda and Juan de Fuca plates below the North American continent. *Earth and Planetary Science Letters 440*, 135–146.

Tong, P., D. Komatitsch, T.-l. Tseng, S.-h. Hung, P. Basini, Q. Liu, and C. Marseille (2014). A 3D spectral-element and frequency-wavenumber (SEM-FK) hybrid method for high-resolution seismic array imaging. *Geophysical Research Letters 41*, 7025–7034.

Trabant, C., A. R. Hutko, M. Bahavar, R. Karstens, T. Ahern, and R. Aster (2012). Data Products at the IRIS DMC: Stepping Stones for Research and Other Applications. *Seismological Research Letters 83*(5), 846–854.

Vincenty, T. (1975). Direct and Inverse Solutions of Geodesics on the Ellipsoid With Application of Nested Equations. *Survey Review 23*(176), 88–93.

Vinnik, L. P. (1977). Detection of waves converted from P to SV in the mantle. *Physics of the Earth and Planetary Interiors 15*(1), 39–45.

Xue, M. and R. M. Allen (2007). The fate of the Juan de Fuca plate: Implications for a Yellowstone plume head. *Earth and Planetary Science Letters 264*(1-2), 266–276.

Zhu, L. and H. Kanamori (2000). Moho depth variation in southern California from teleseismic receiver functions. *Journal of Geophysical Research 105*, 2969–2980.

Appendix A

Additional Information

A.1 Hilbert Transform

The Hilbert transform is used to transform a real time-signal into a complex-valued one. That is, if $s(t)$ is a real time-signal, then

$$s_A(t) = s(t) + i\mathscr{H}[s](t)$$

is its analytical counter-part, where $i^2 = -1$ and $\mathscr{H}$ is a linear operator called Hilbert transform. The Hilbert transform is defined as

$$\mathscr{H}[s](t) = \frac{1}{\pi}\int_{-\infty}^{\infty}\frac{s(\tau)}{t-\tau}d\tau.$$

Note that the Hilbert transform itself produces real values.
Since the analytical signal can also be expressed as

$$s_{analytical}(t) = A(t)e^{i\psi(t)},$$

the instantaneous amplitude $A(t)$ (also referred to as the envelope) and instantaneous phase $\psi(t)$ can be extracted. $\psi(t)$ is used in Chapter 4 to find the similarity in phase between different time-signals.

A.2 IASP91 vs. GyPSuM

A quick comparison of the two velocity models to show the advantage of using a three-dimensional one. Through the images of Figure A.2, it becomes clear that receiver function traveltimes are heavily affected by their location. While traveltimes to a certain depth in northern East Africa are longer than the global average, the traveltimes in southern Africa are generally shorter. Figure A.1 shows the difference in traveltime calculated with the GyPSuM velocity model between the Afar Depression and the Kaapvaal Craton. At the 660 discontinuity the traveltime differs as much as $\sim$5.2 seconds.

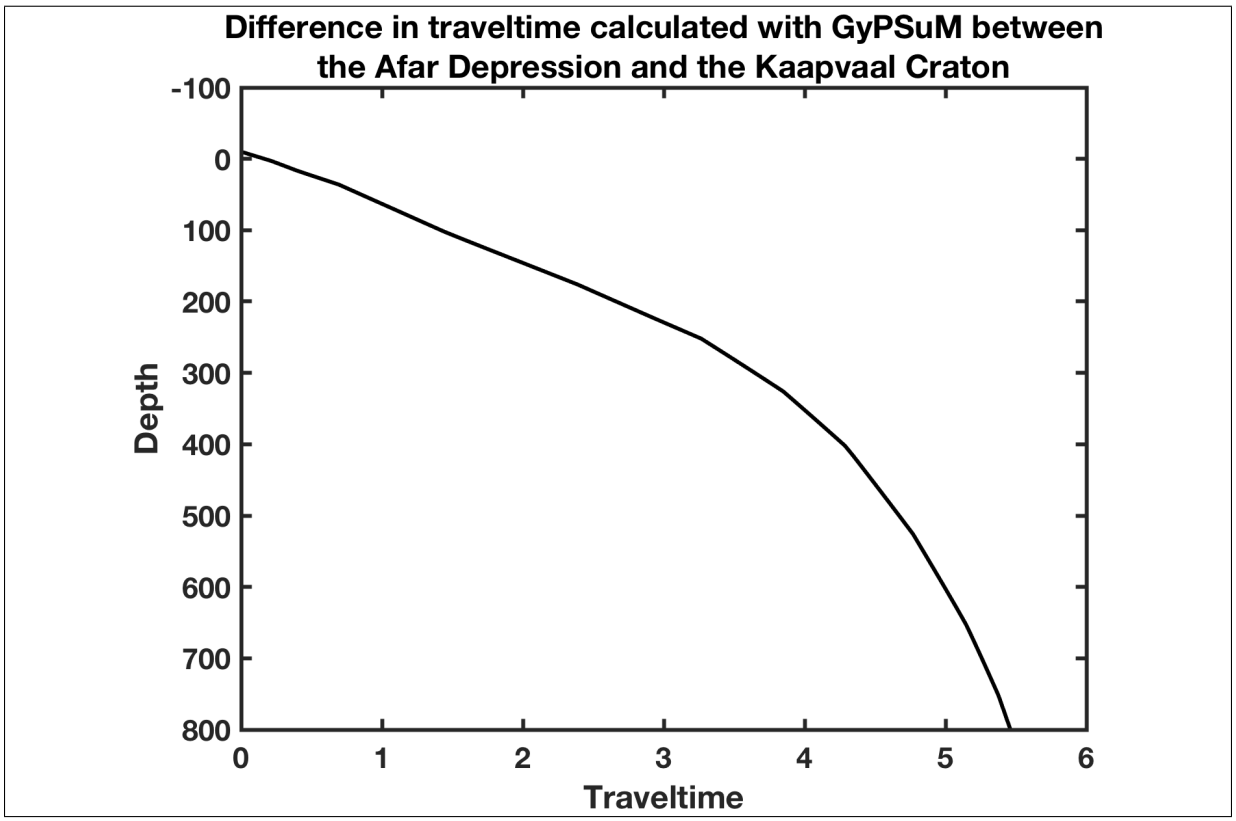

Figure A.1: A comparison of calculated traveltimes with GyPSuM model between the Afar region and the Kaapvaal Craton. Depth is in kilometres and traveltime is in seconds.

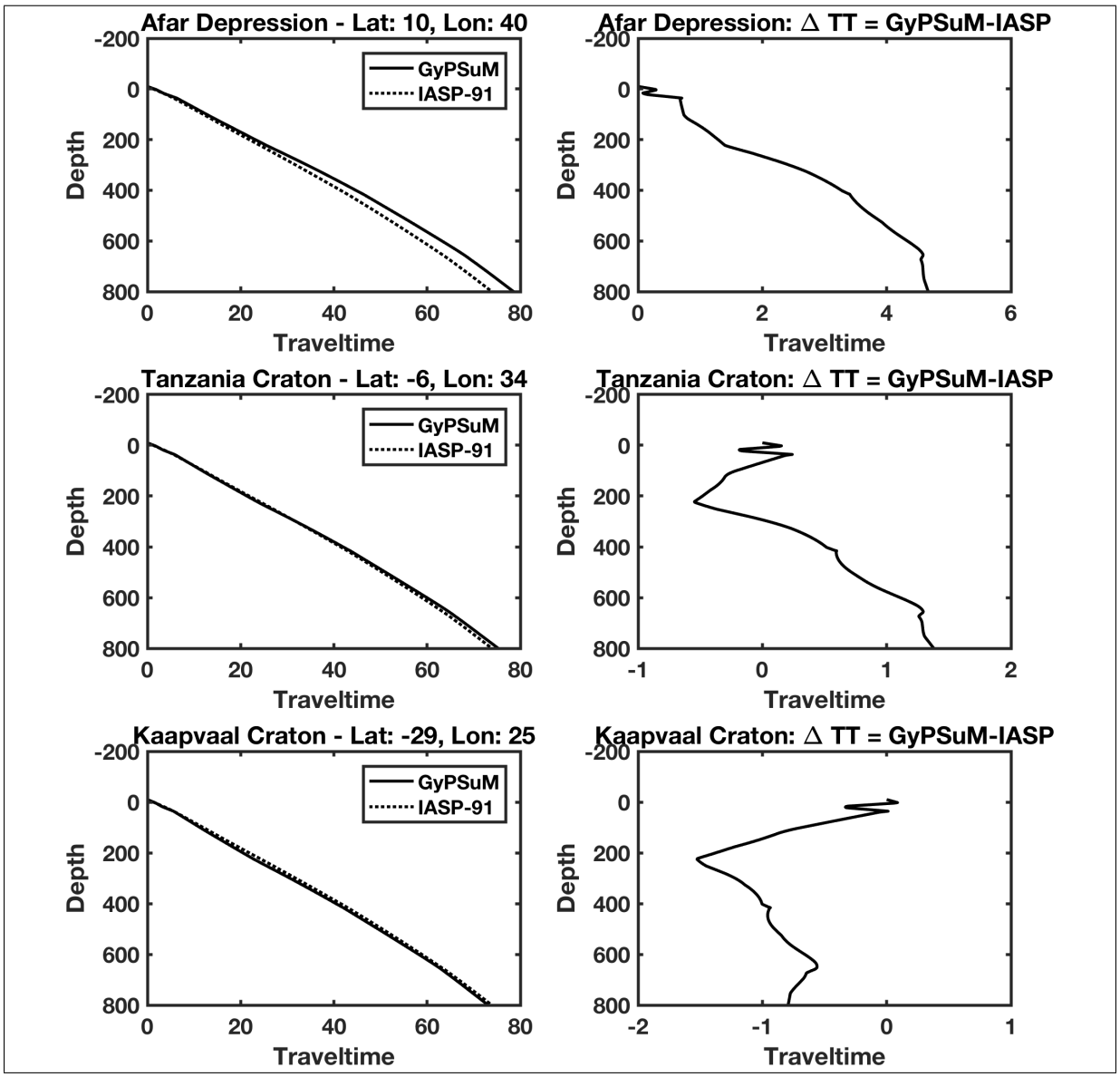

Figure A.2: A comparison of calculated traveltimes with the IASP91 model and the GyPSuM model at three different locations. Depth is in kilometres and traveltime is in seconds. To the **left**, vertical traveltimes calculated with the indicated velocity models. To the **right**, the difference in traveltime between the two models. **Top row** Afar Depression. **Middle row:** Tanzania Craton. **Bottom row:** Kaapvaal Craton.

Appendix B

Additional Images for East Africa

B.1 Lithosphere

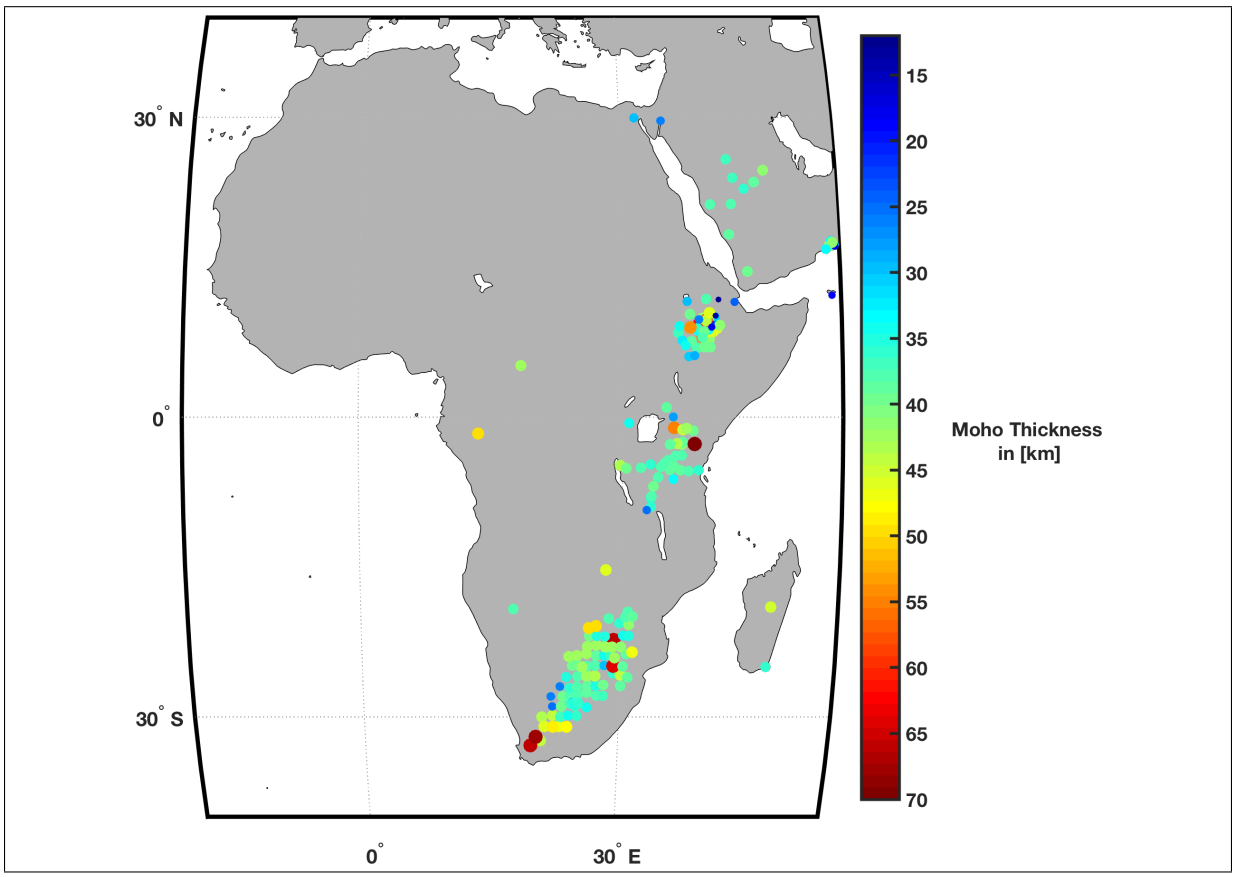

Figure B.1: A map of crustal thickness created from crustal thickness data of the IRIS EARS global receiver function survey (see Section 4.1).

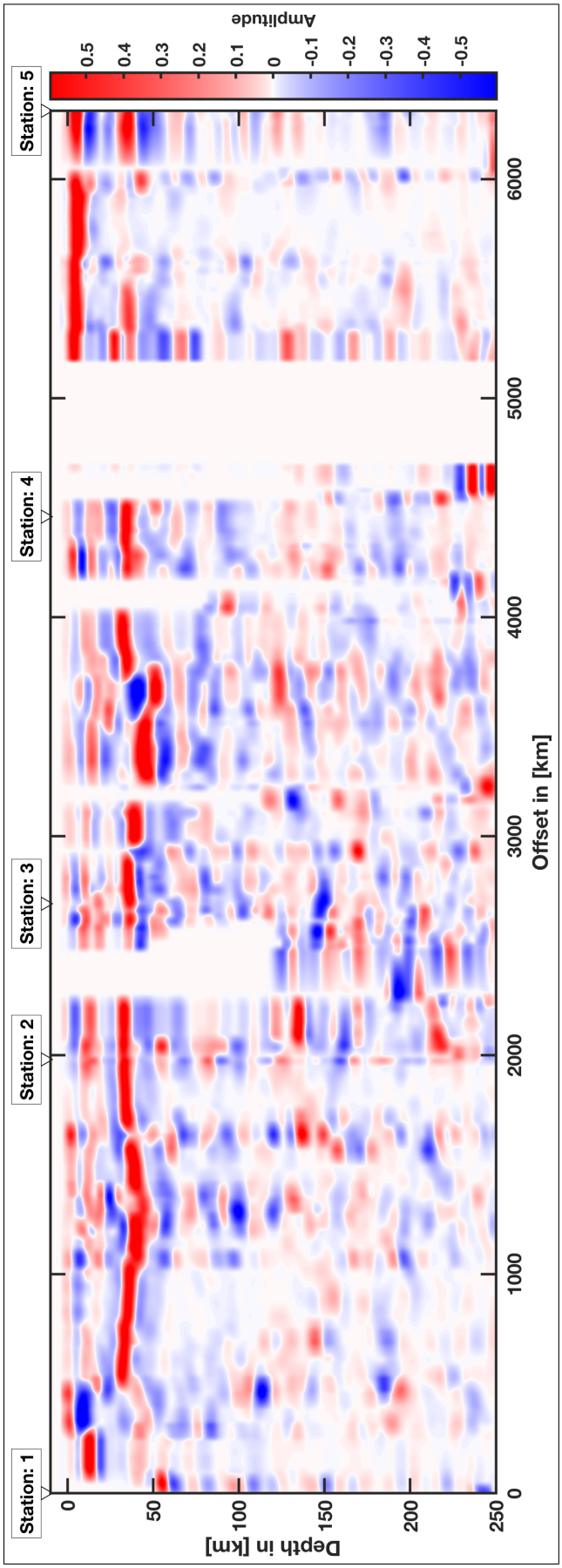

Figure B.2: The cross section showing the Moho discontinuity along the line shown in Figure 6.1 in form of a reflectivity profile. It is the same profile as seen in Figure 6.3. Here, the Moho below the Afar region and below the Saldania Belt are visible due to the colour scale. See text for analysis and stacking procedures.

B.2 Mantle Transition Zone

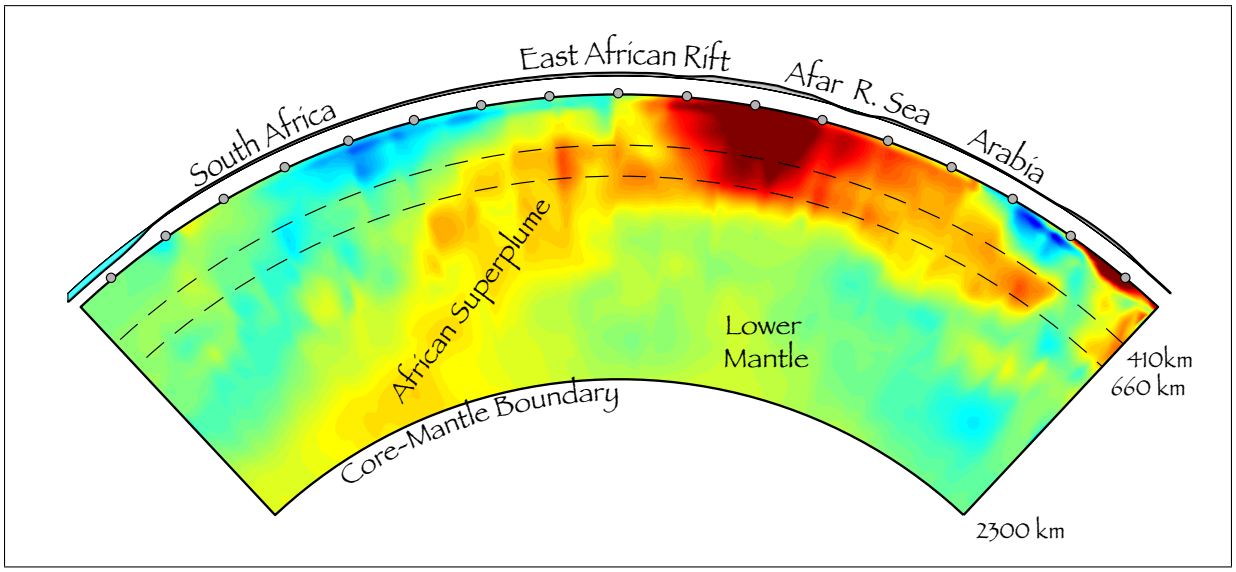

Figure B.3: A tomographic image of the the first 2300km below the surface across East Africa and the Arabian peninsula (Bastow et al., 2018). The study has not been published yet.

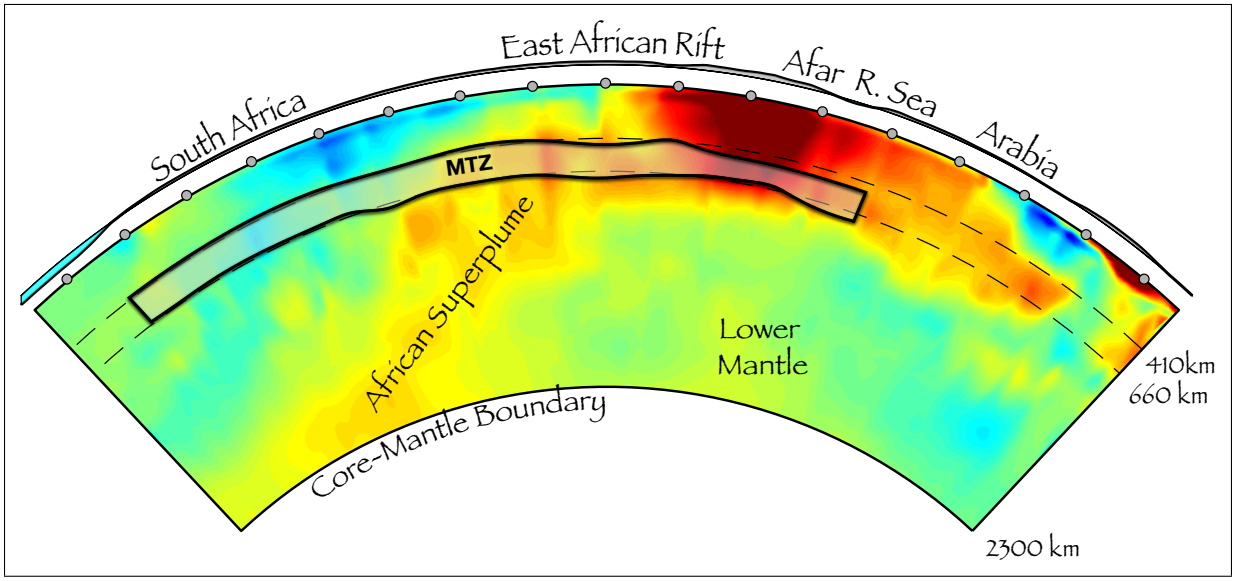

Figure B.4: The same tomographic image as shown in Figure B.3, but the results of the mantle transition zone thickness obtained here (see Figure 6.7) are plotted on top.

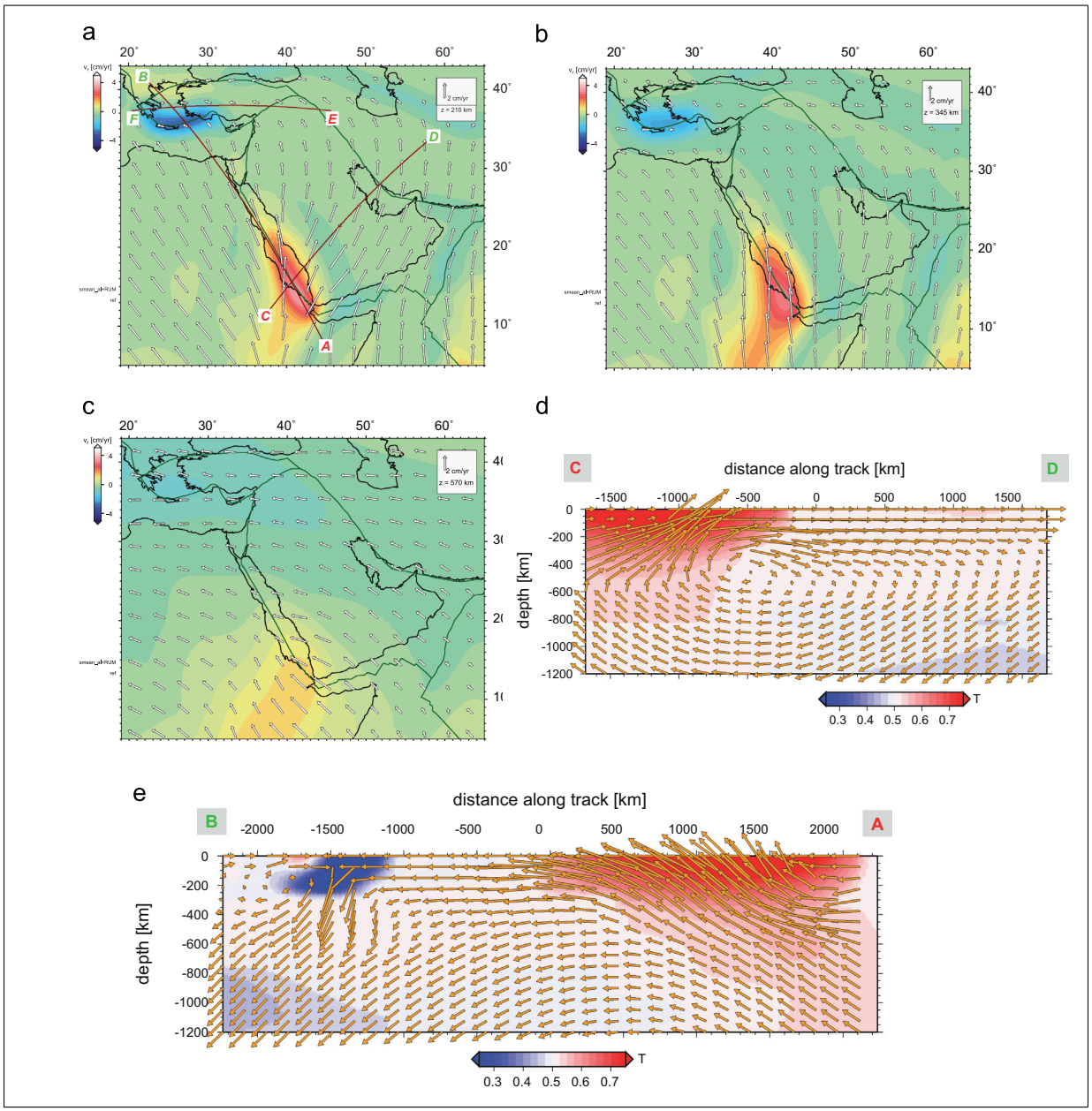

Figure B.5: Images of geodynamically modelled mantle flow below the Afar region and northwards. Figure from Faccenna et al. (2013). The mantle flow is modelled for three different depths: (a) 210 km, (b) 345 km, and, (c) 570 km. Vectors show the horizontal velocities and background shading represents radial velocities. The velocities within three cross sections (d)–(e) are the same as shown in the legend on (a), with the background showing non-dimensional temperature. For this thesis, most interesting are the abrupt stop in high temperatures and change to upwards flow North-East of the Red Sea as seen in cross section (d).

Appendix C

Synthetic Tests

This section gives a selection of figures that provide an overview and quantitative comparison of the different options that the CCP stacks can be calculated with including a subducting slab with increasing dipping angle. The figures in this chapter are given as a function of both order of the phase-weighted stack (0 which is linear or 2 which is quadratic) and dip angle α in the base model shown in 4.10. An overview of the following figures and their corresponding data is given in table C.1. The data is always given as the computed SV receiver function trace from an incoming P-wave. For more detail on how the data is created, see Section 4.2.5. For each data set and stacking option, a figure of the different traveltime corrected modes [*Pś*, *Pp̀ś* and *Ps̀ś*] is shown as well as a figure showing the multi-mode stacks. The top multi-mode stack is a simple linear stack of the three modes, the centre stack is the Zhu and Kanamori inspired stack (see Section 4.2.5) and the bottom one is a phase-weighted stack of the three modes. This means that if the table states phase-weighted stack (as opposed to linear), the bottom multi-mode stack is stacked twice with a phase weight – first in the traveltime correction and stacking procedure and then as a multi-mode stack.

Testdata	Stacking type	Spatial averaging	Fig.
Dip of 5°	.....		C.1
	linear	no	C.2-C.3
	PWS: order 2	no	C.4-C.5
	linear	yes	C.6-C.7
	PWS: order 2	yes	C.8-C.9
Dip of 10°	.....		C.10
	linear	no	C.15-C.16
	PWS: order 2	no	C.17-C.18
	linear	yes	C.15-C.16
	PWS: order 2	yes	C.17-C.18
Dip of 20°	.....		C.19
	linear	no	C.20-C.21
	PWS: order 2	no	C.22-C.23
	linear	yes	C.24-C.25
	PWS: order 2	yes	C.26-C.27
Dip of 40°	.....		C.28
	linear	no	C.29-C.30
	PWS: order 2	no	C.31-C.32
	linear	yes	C.33-C.34
	PWS: order 2	yes	C.35-C.36
Dip comparison	linear	no	C.37-C.38
Dip comparison	PWS: order 2	no	C.39-C.40
Dip comparison	linear	yes	C.41-C.42
Dip comparison	PWS: order 2	yes	C.43-C.44

Table C.1: Overview over the tests shown in Appendix C and its corresponding figures. All tests are based on the model shown in Figure 4.10.

C.1 5°Dip

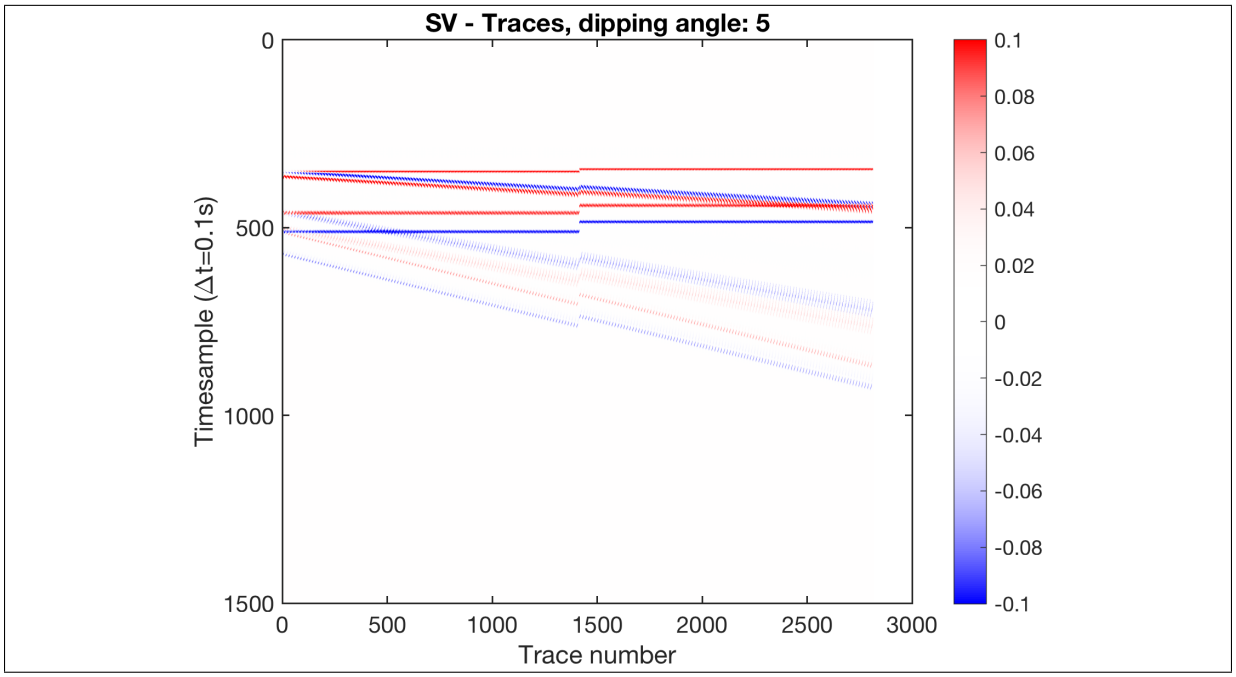

Figure C.1: Receiver function data for a 5°dipping angle. See text for sorting of the traces.

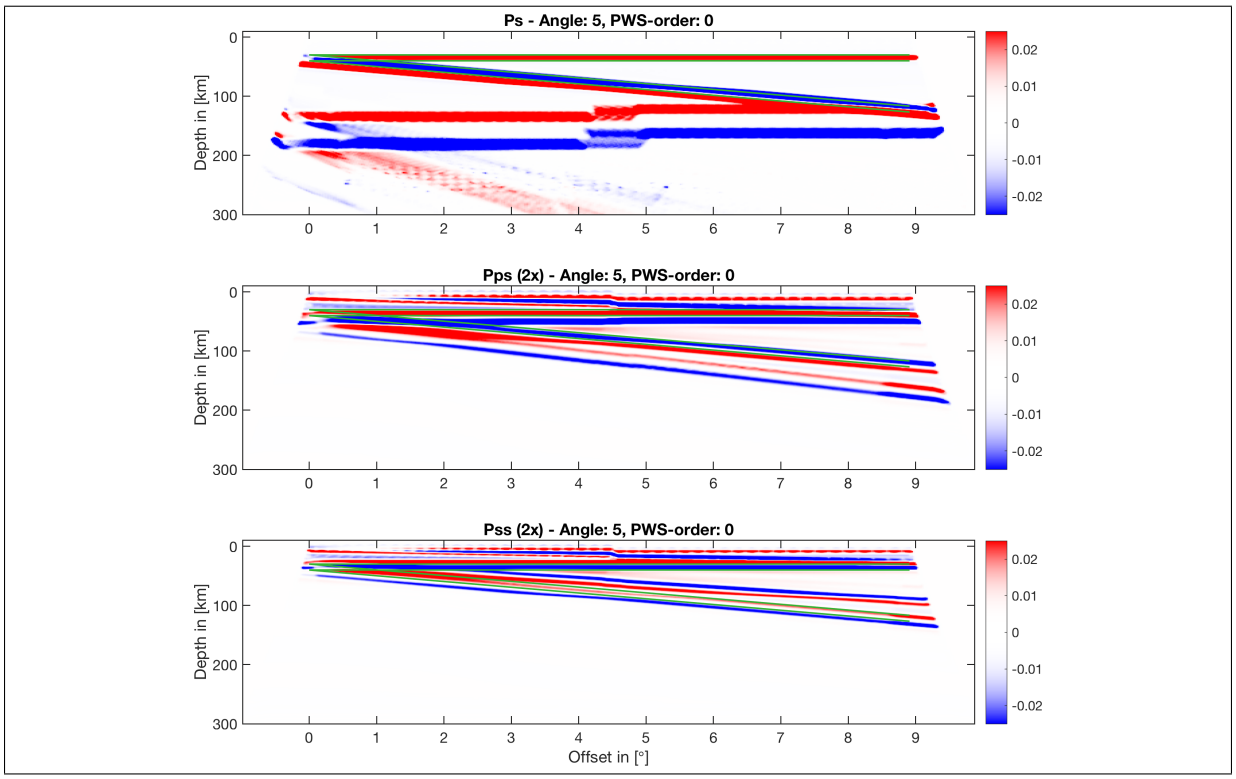

Figure C.2: CCP stacked receiver functions.

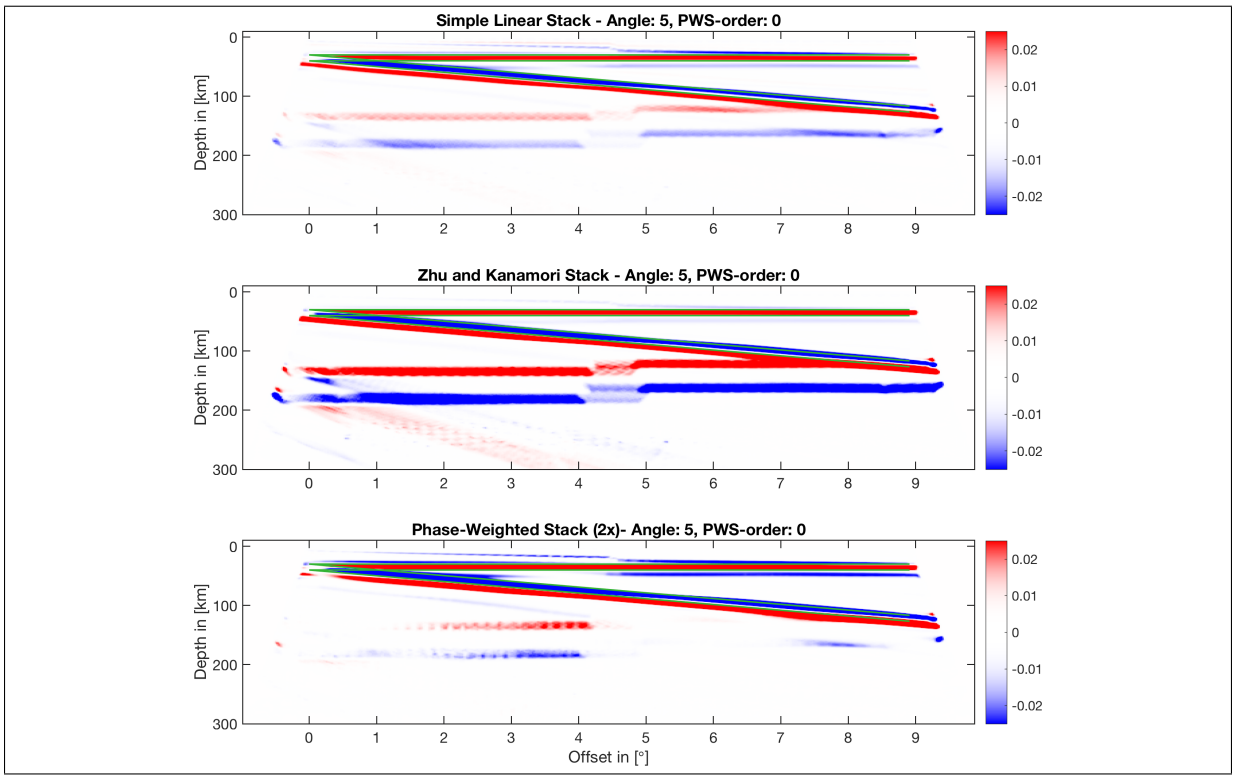

Figure C.3: Multi-mode stacked CCP stacks.

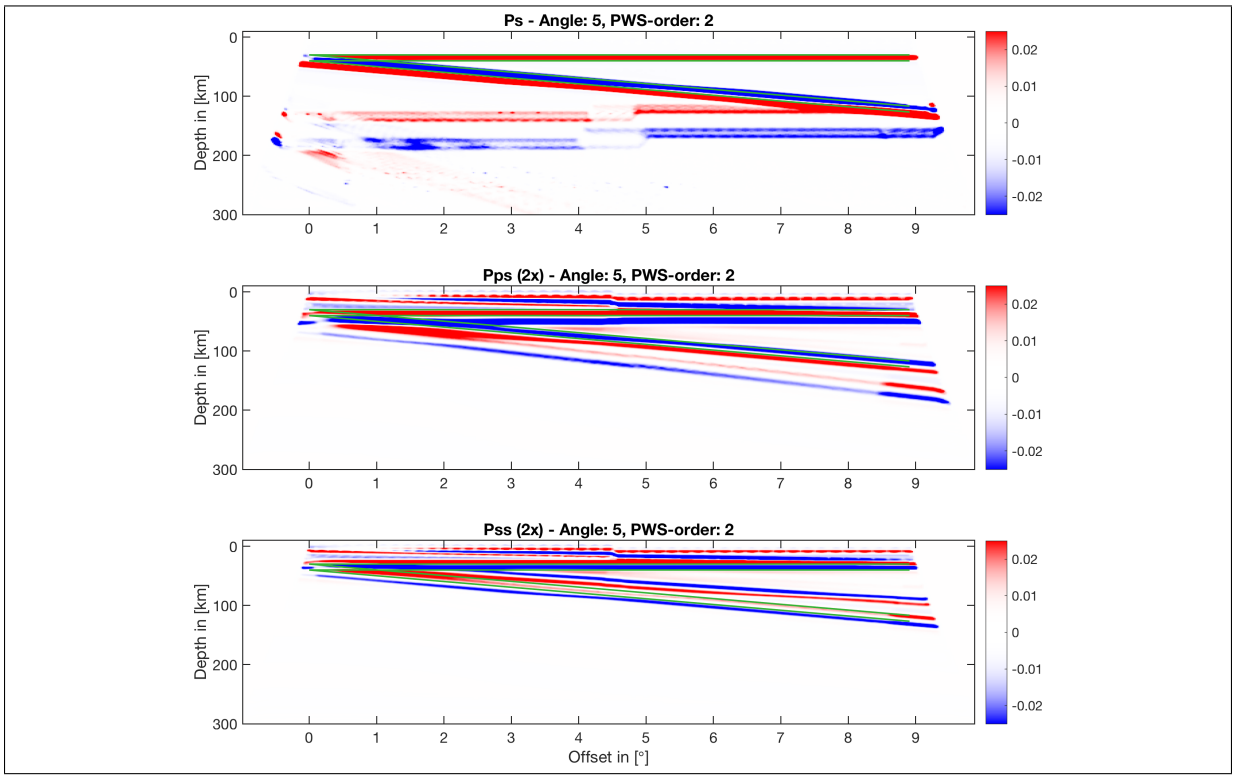

Figure C.4: CCP stacked receiver functions.

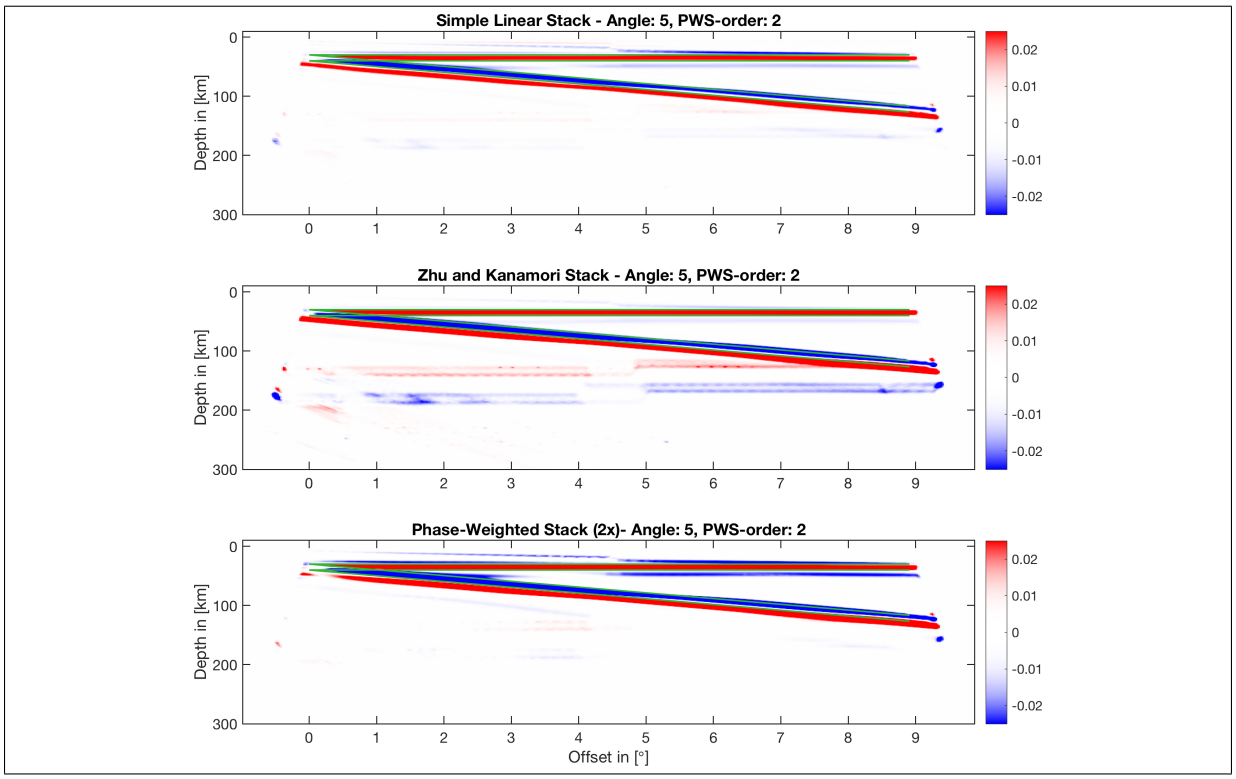

Figure C.5: Multi-mode stacked CCP stacks

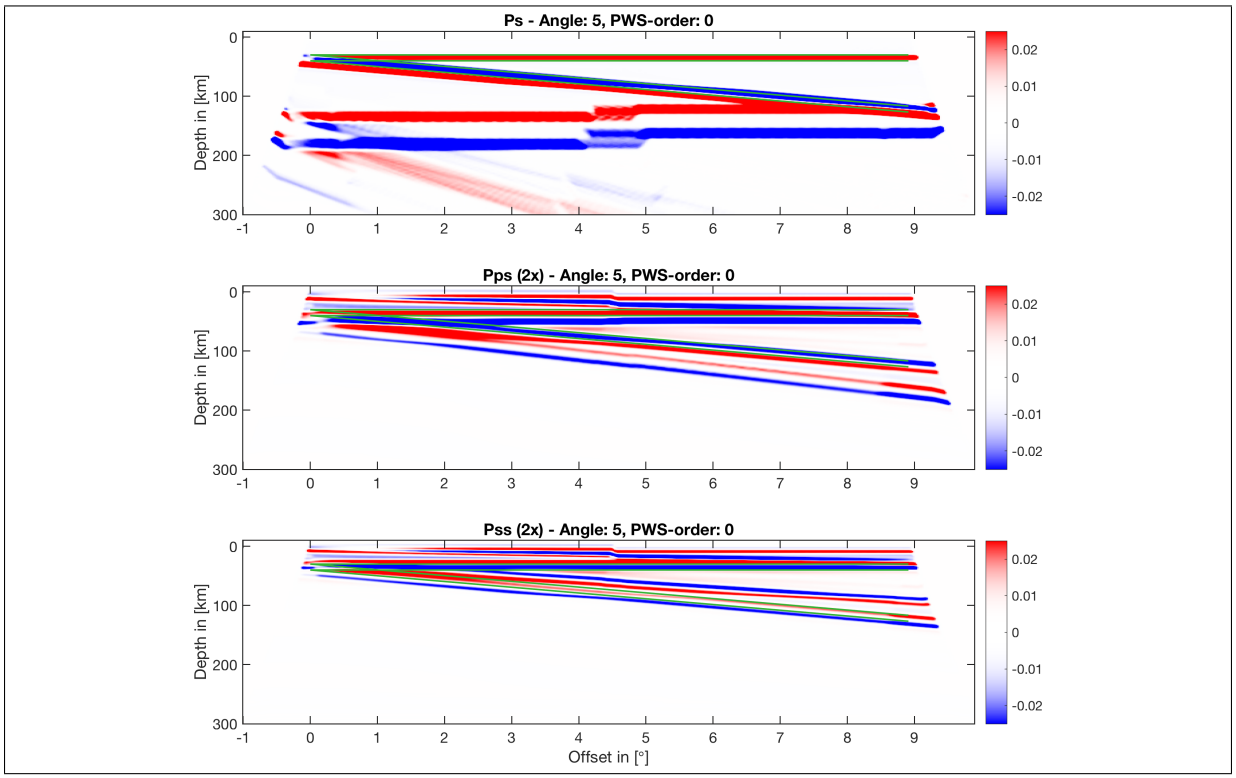

Figure C.6: Spatially averaged, CCP stacked receiver functions.

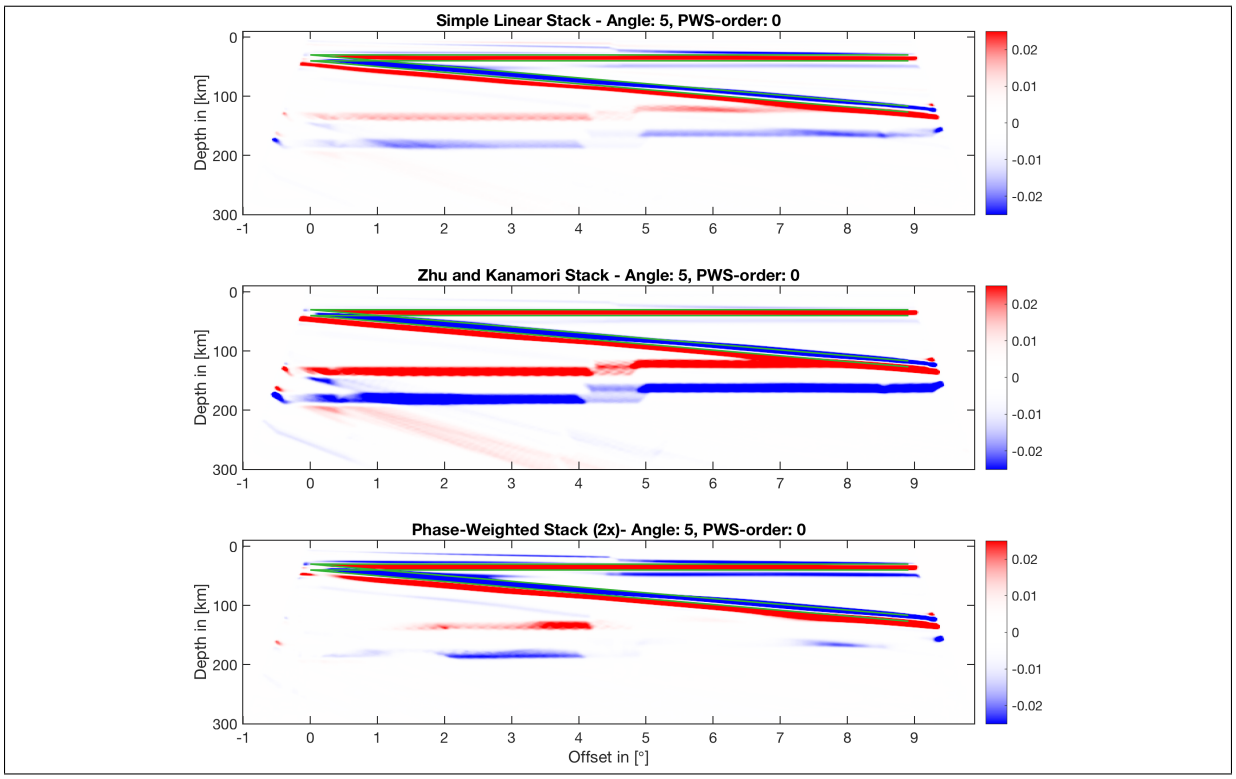

Figure C.7: Spatially averaged, multi-mode stacked CCP stacks.

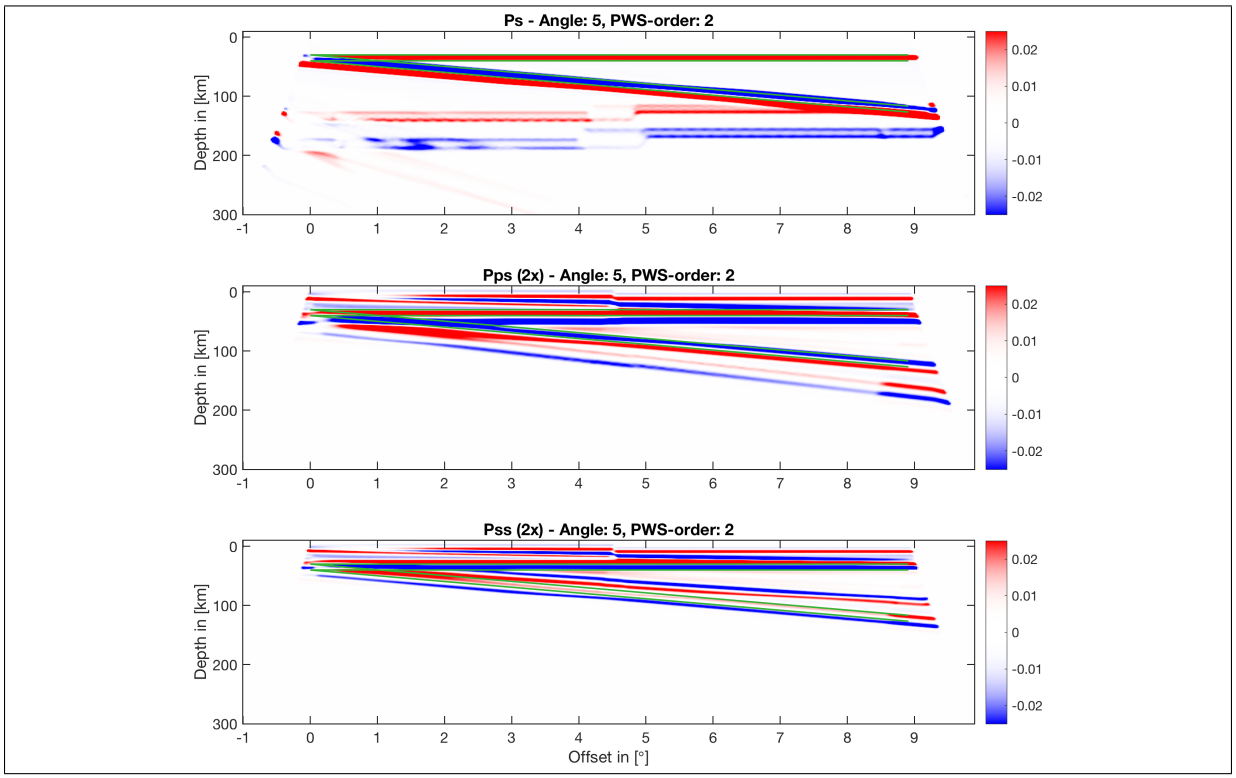

Figure C.8: Spatially averaged, CCP stacked receiver functions.

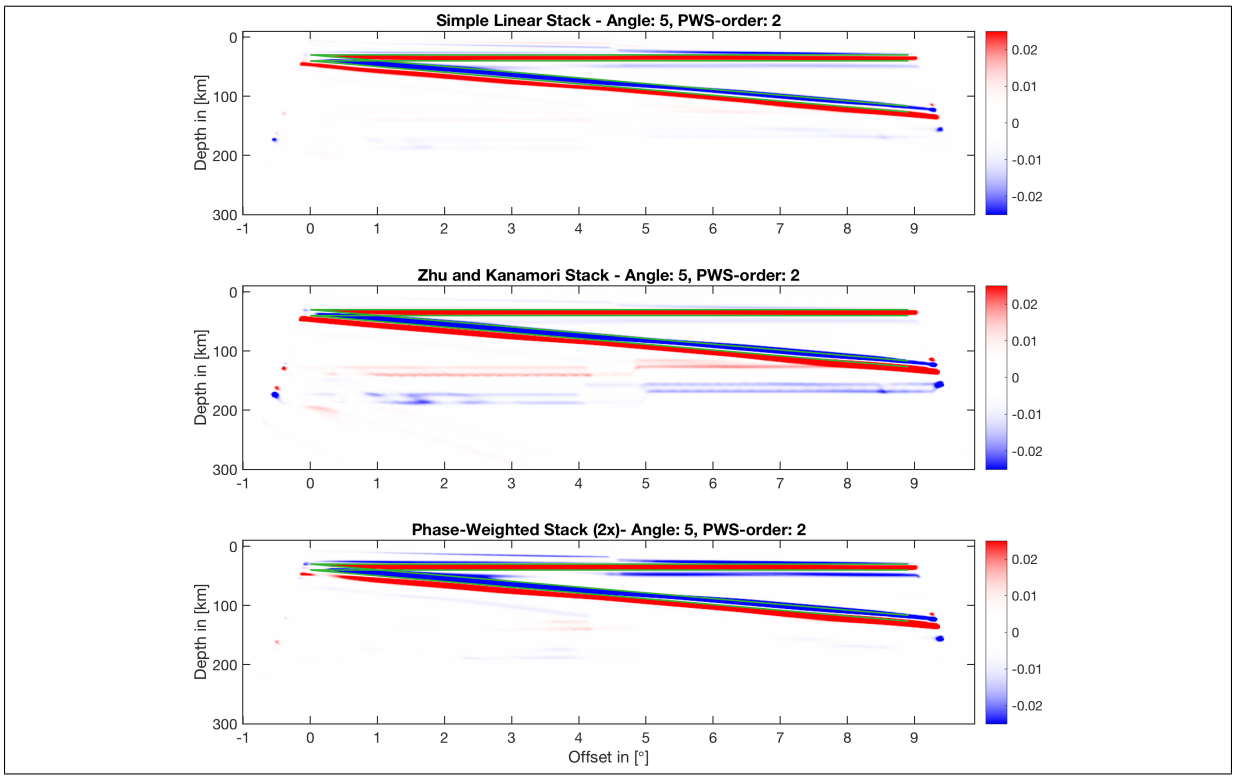

Figure C.9: Spatially averaged, multi-mode stacked CCP stacks

C.2 10°Dip

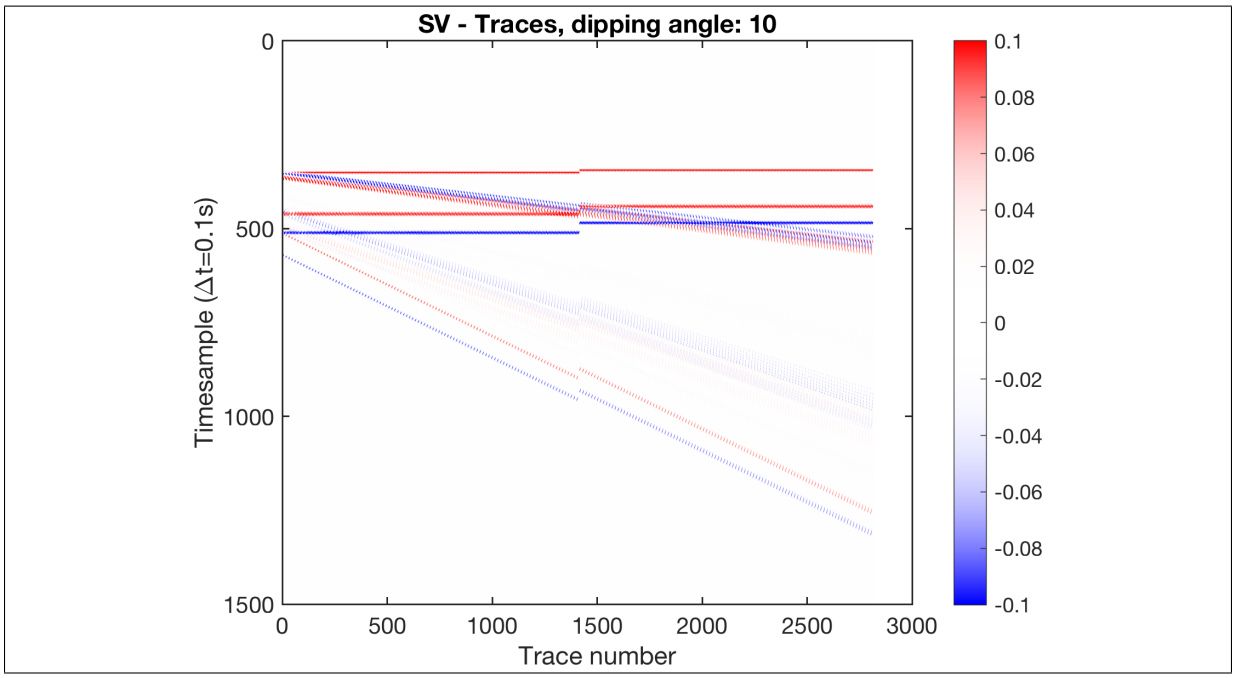

Figure C.10: Receiver function data for a 10°dipping angle. See text for sorting of the traces.

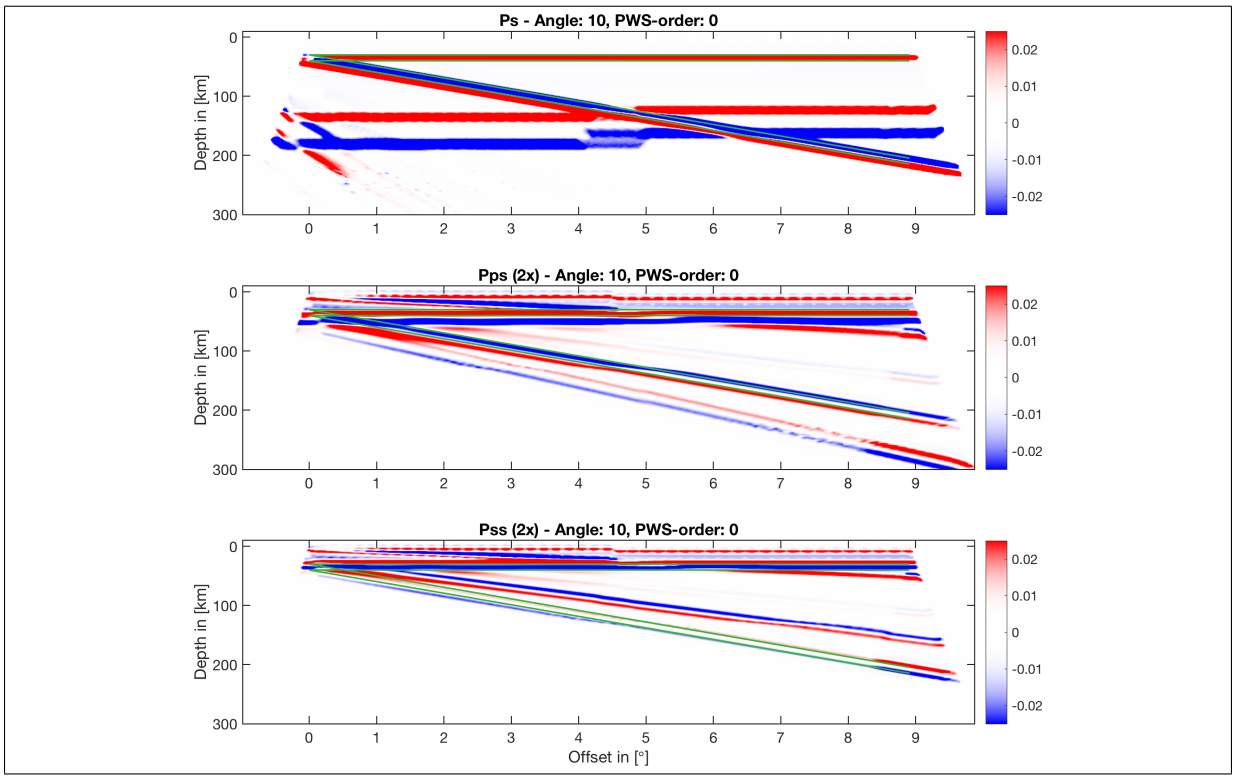

Figure C.11: CCP stacked receiver functions.

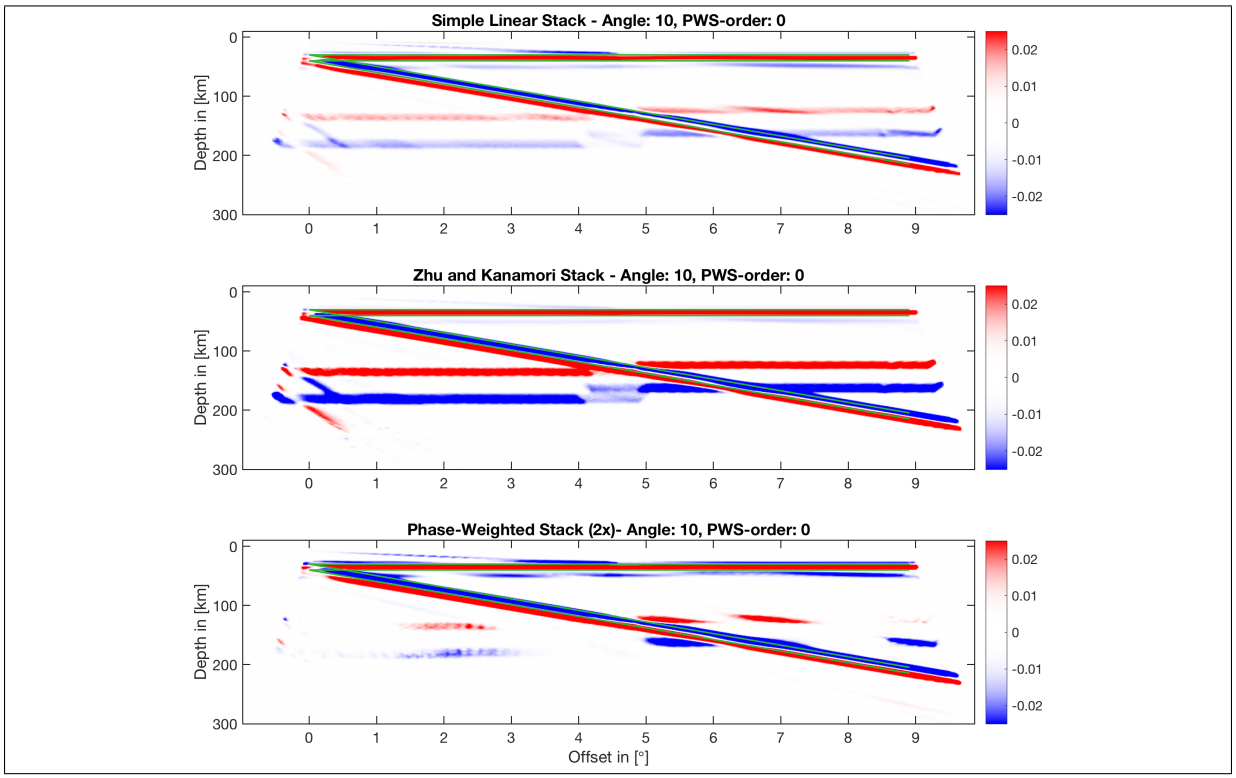

Figure C.12: Multi-mode stacked CCP stacks

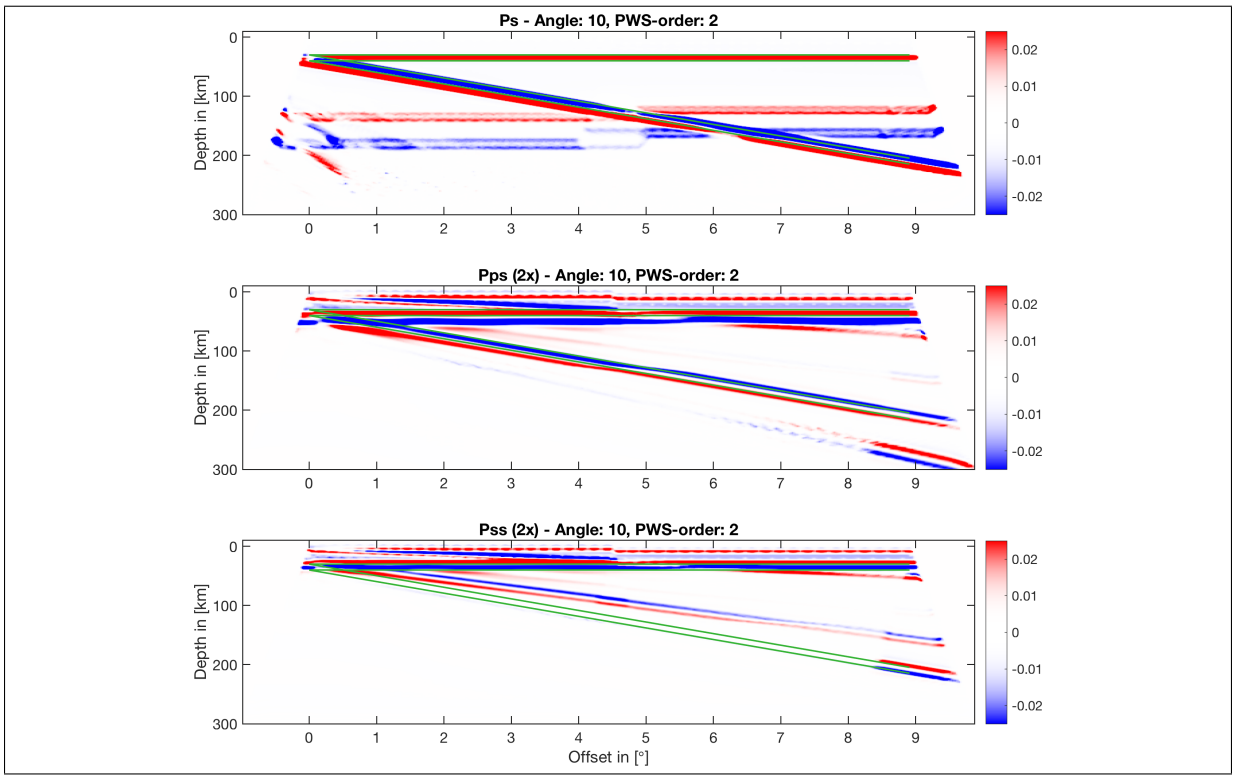

Figure C.13: Phase-weighted, CCP stacked receiver functions.

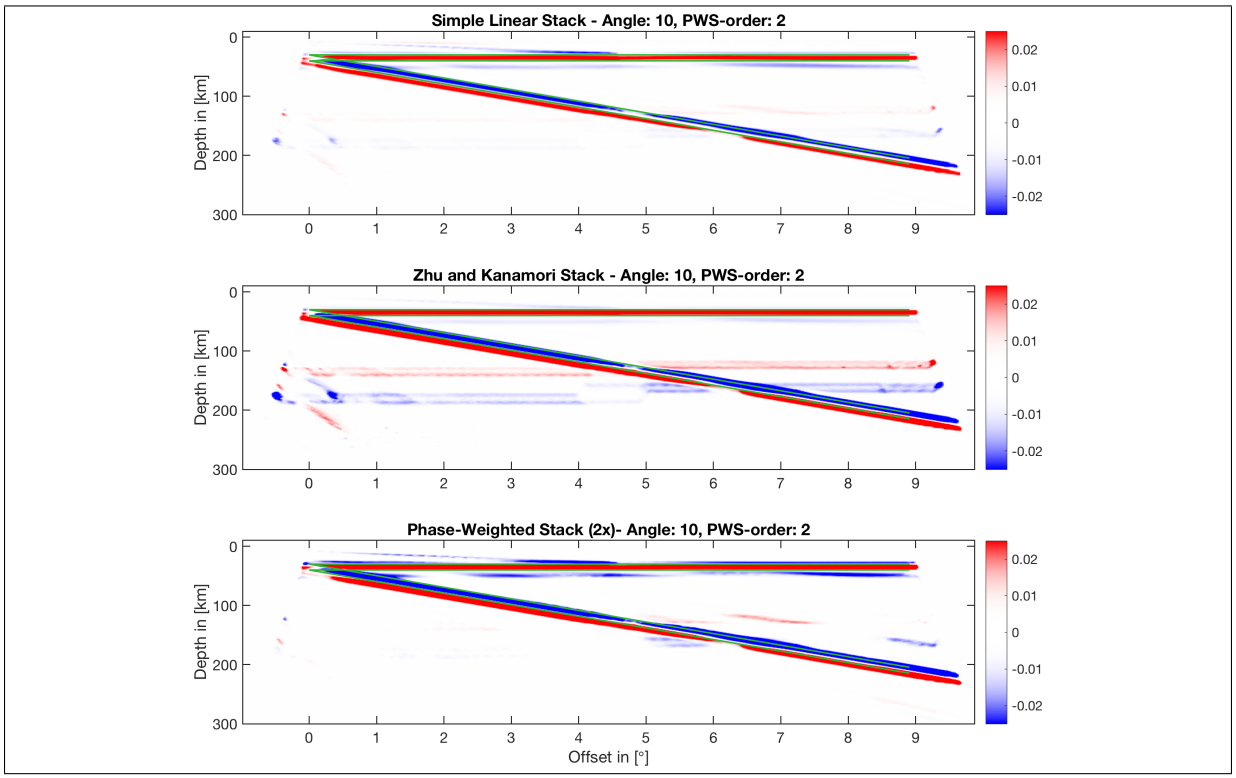

Figure C.14: Multi-mode stacked CCP stacks

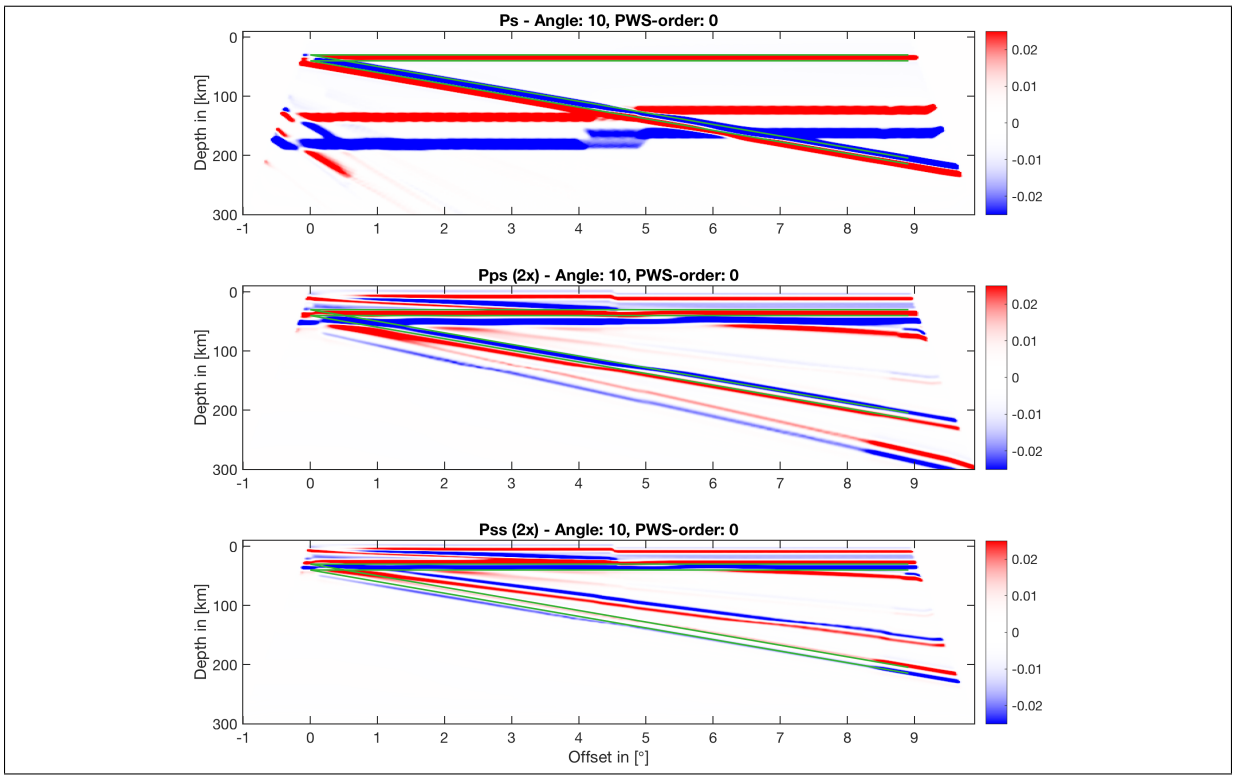

Figure C.15: Spatially averaged, CCP stacked receiver functions.

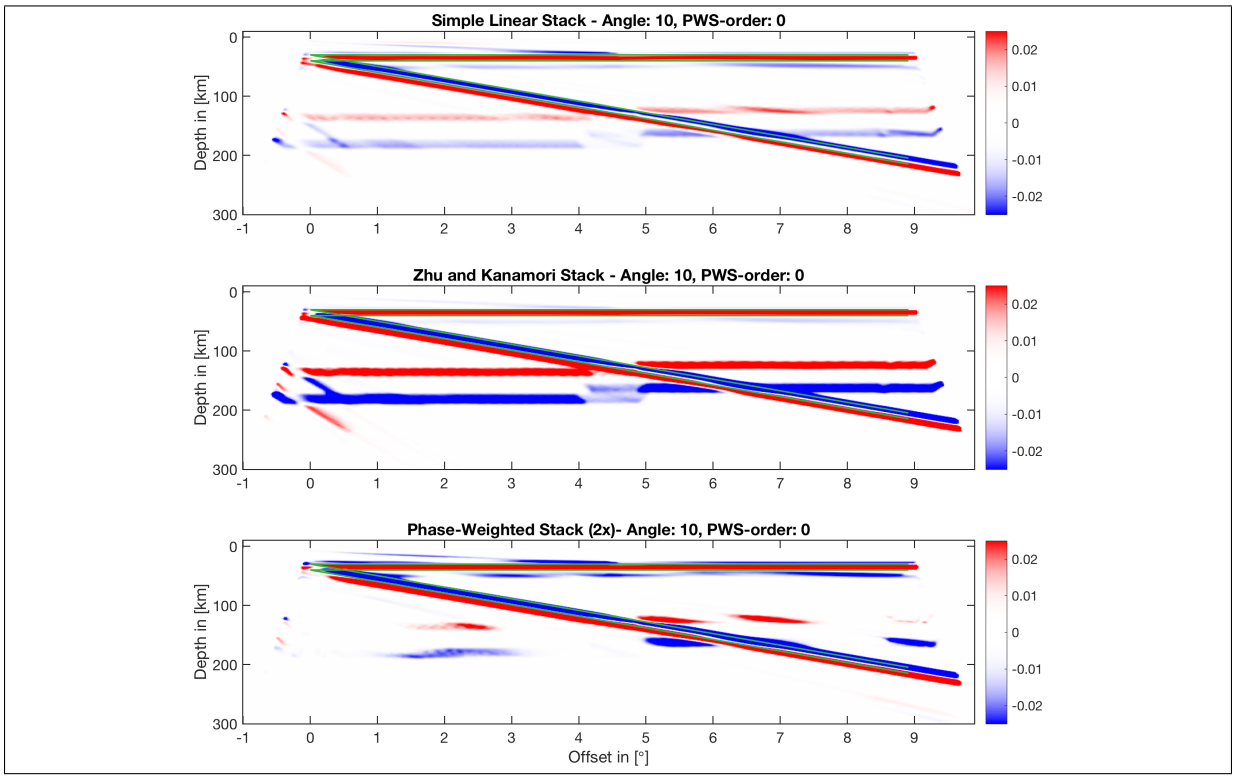

Figure C.16: Spatially averaged, multi-mode stacked CCP stacks.

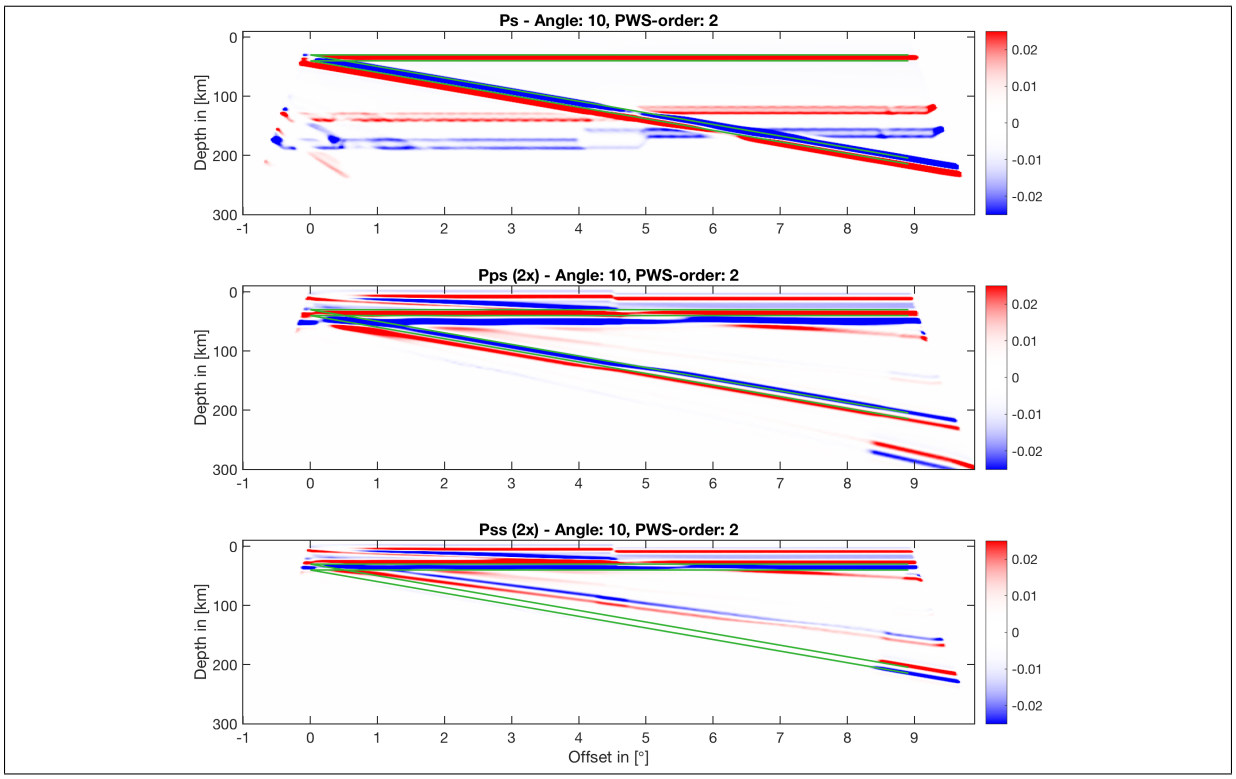

Figure C.17: Spatially averaged, CCP stacked receiver functions.

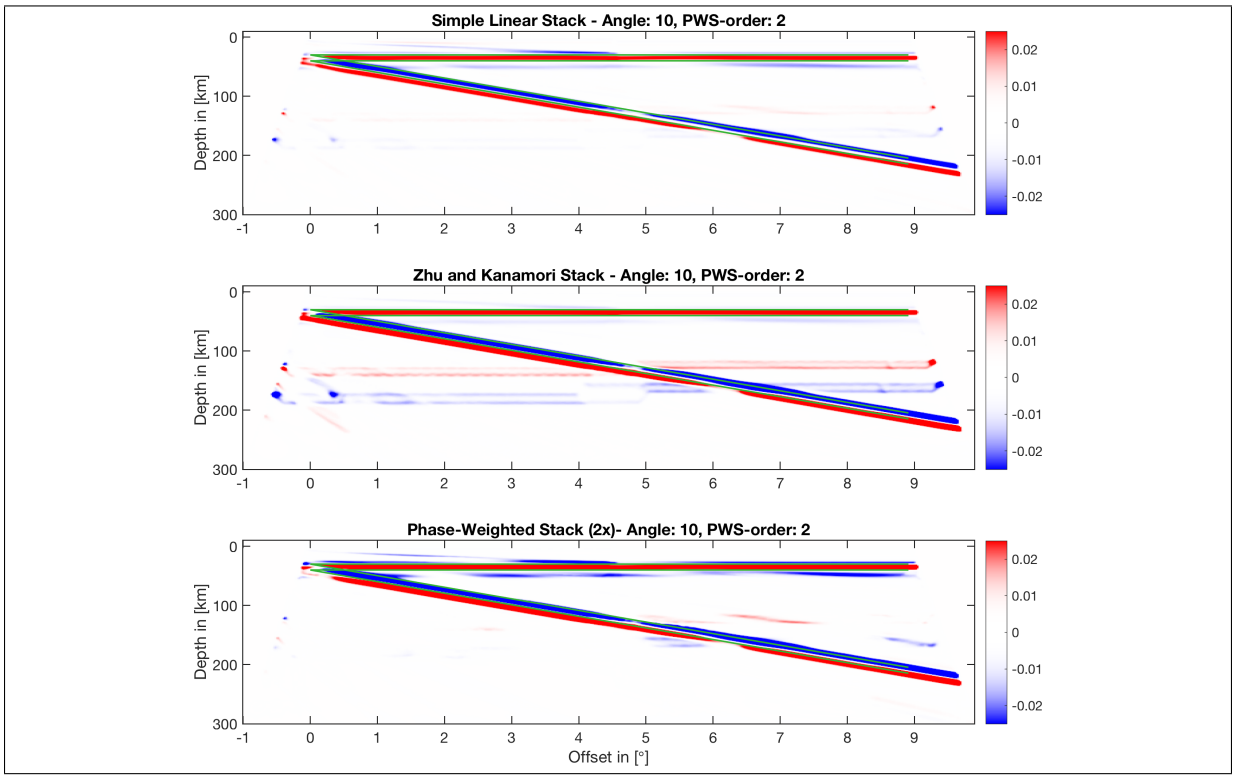

Figure C.18: Spatially averaged, multi-mode stacked CCP stacks

C.3 20°Dip

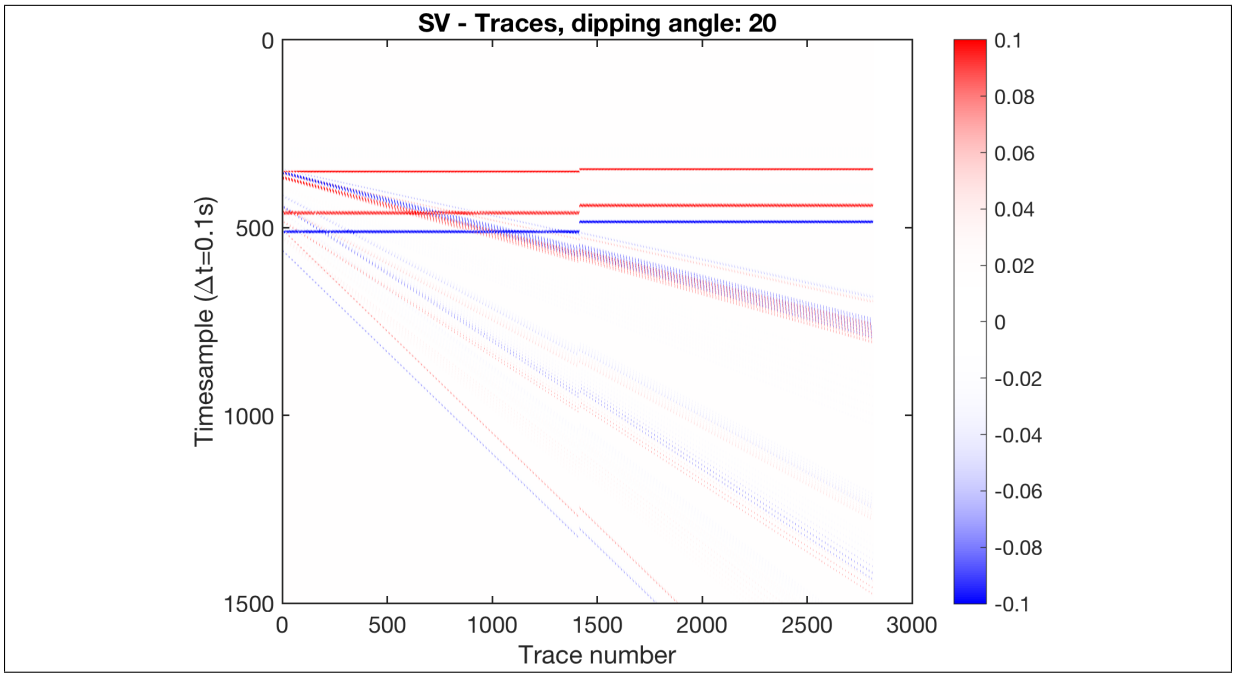

Figure C.19: Receiver function data for a 20°dipping angle. See text for sorting of the traces.

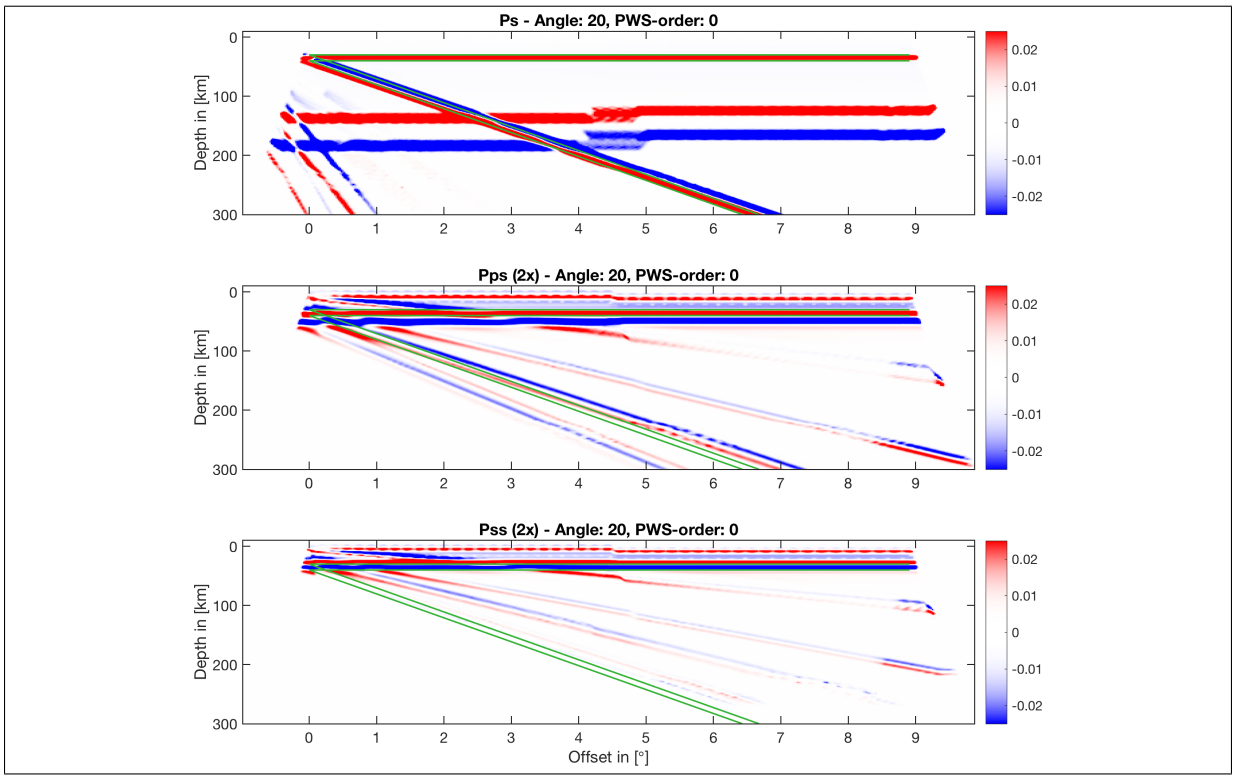

Figure C.20: Linearly, CCP stacked receiver functions.

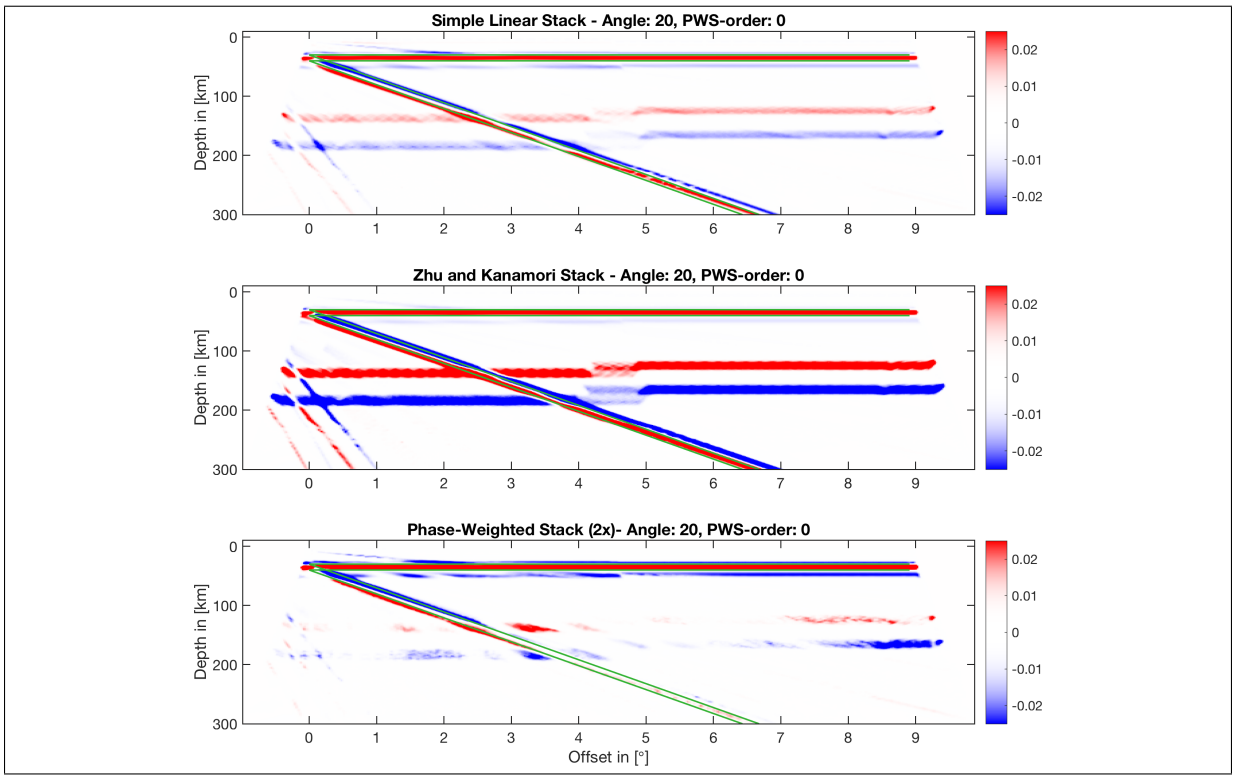

Figure C.21: Multi-mode stacked CCP stacks

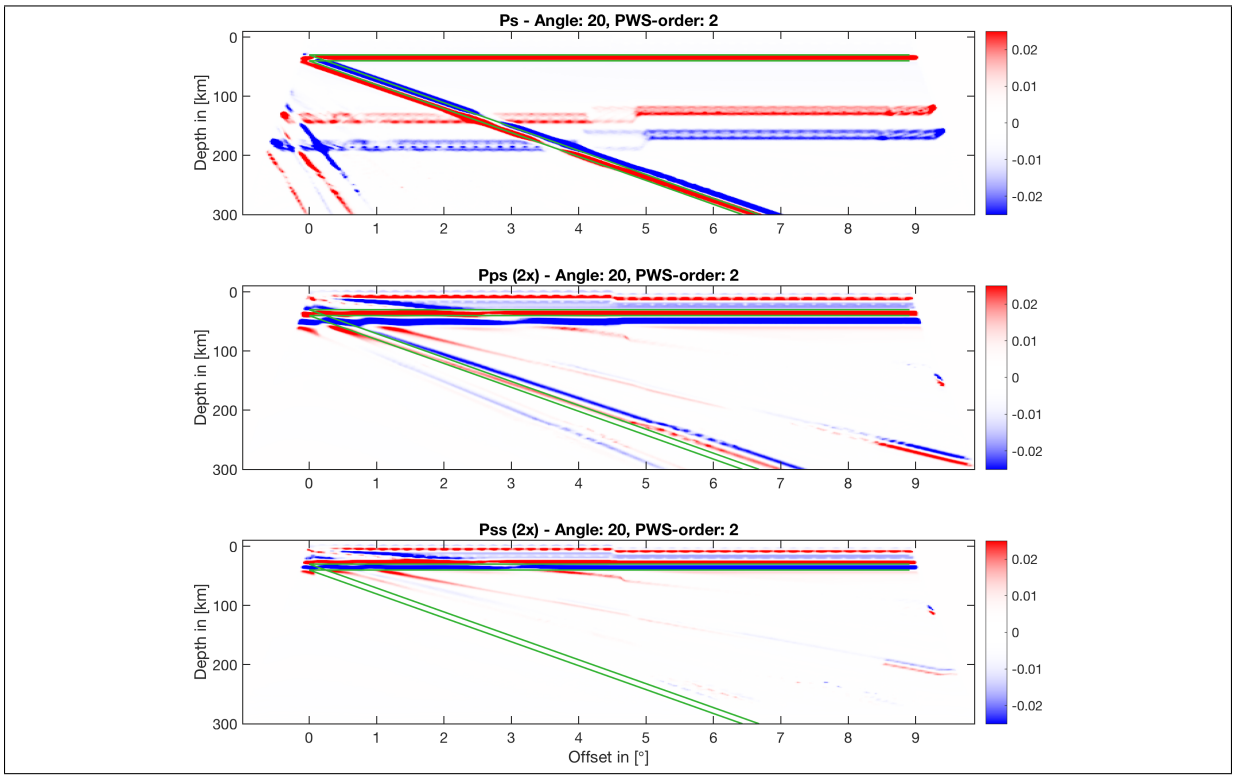

Figure C.22: Phase-weighted, CCP stacked receiver functions.

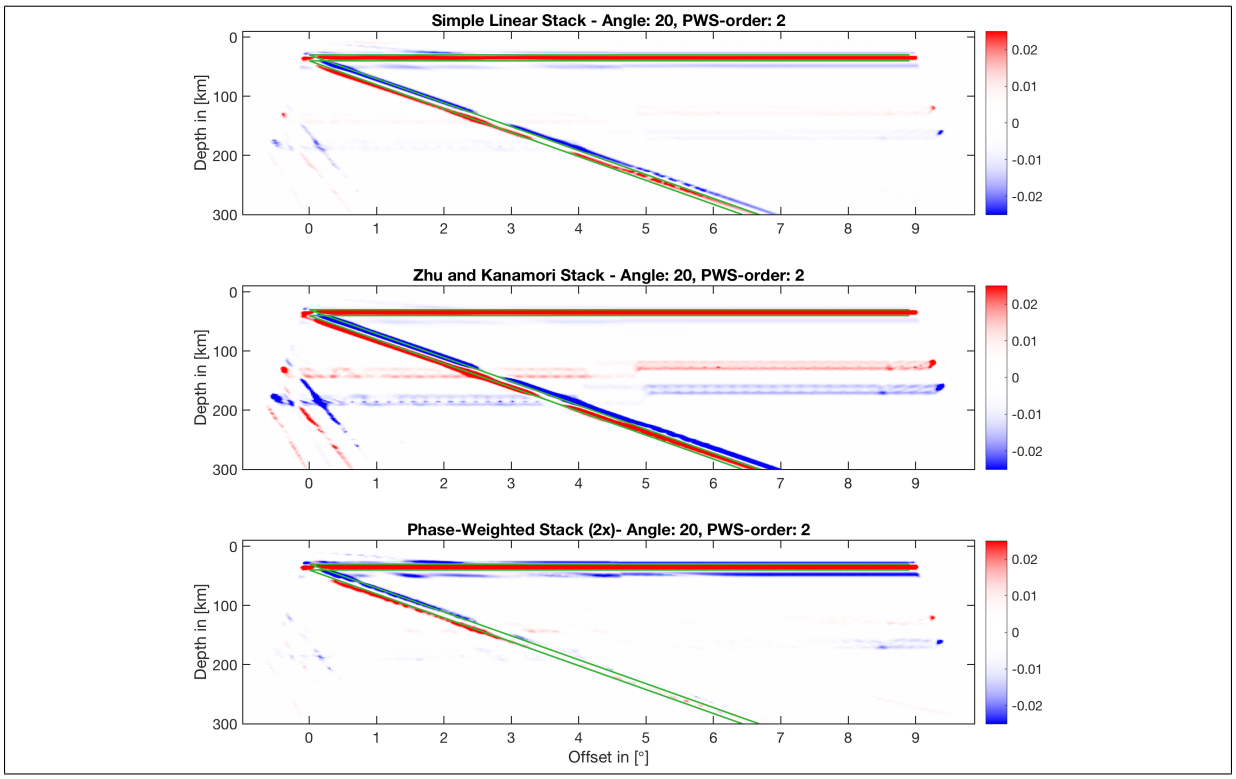

Figure C.23: Multi-mode stacked CCP stacks

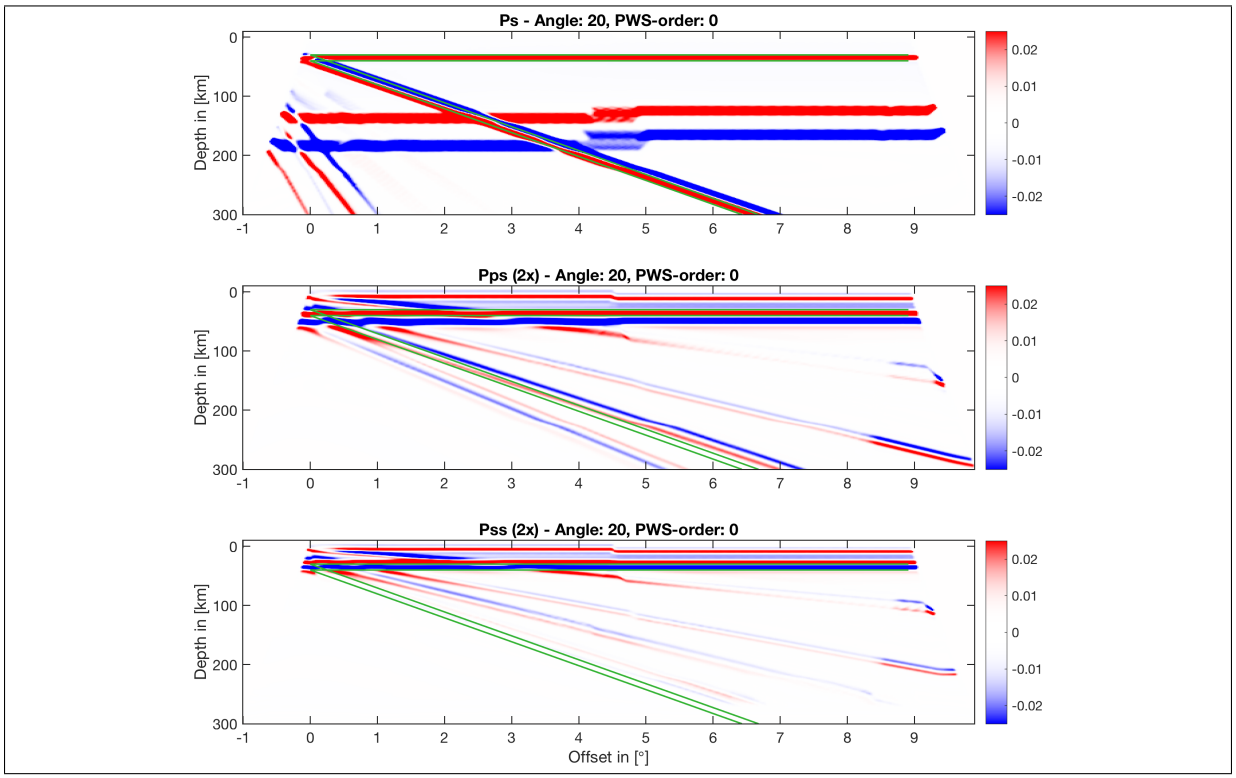

Figure C.24: Spatially averaged, CCP stacked receiver functions.

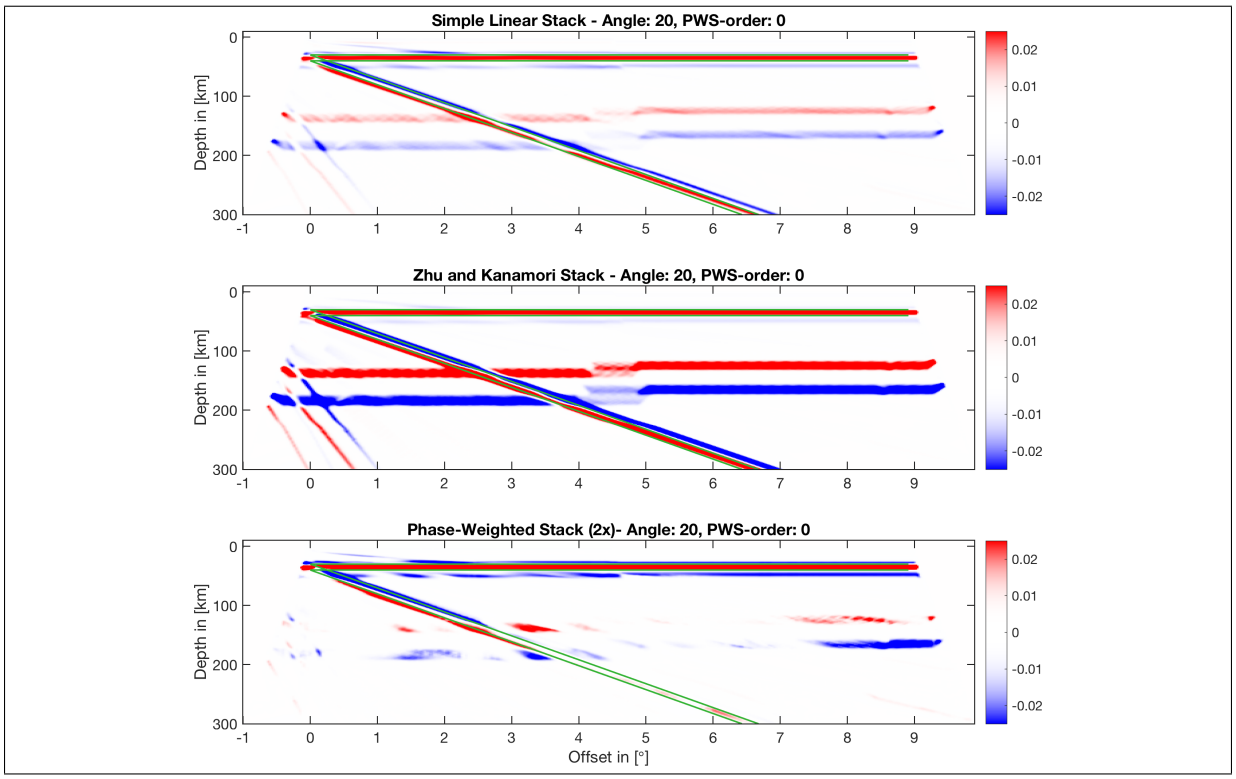

Figure C.25: Spatially averaged, multi-mode stacked CCP stacks.

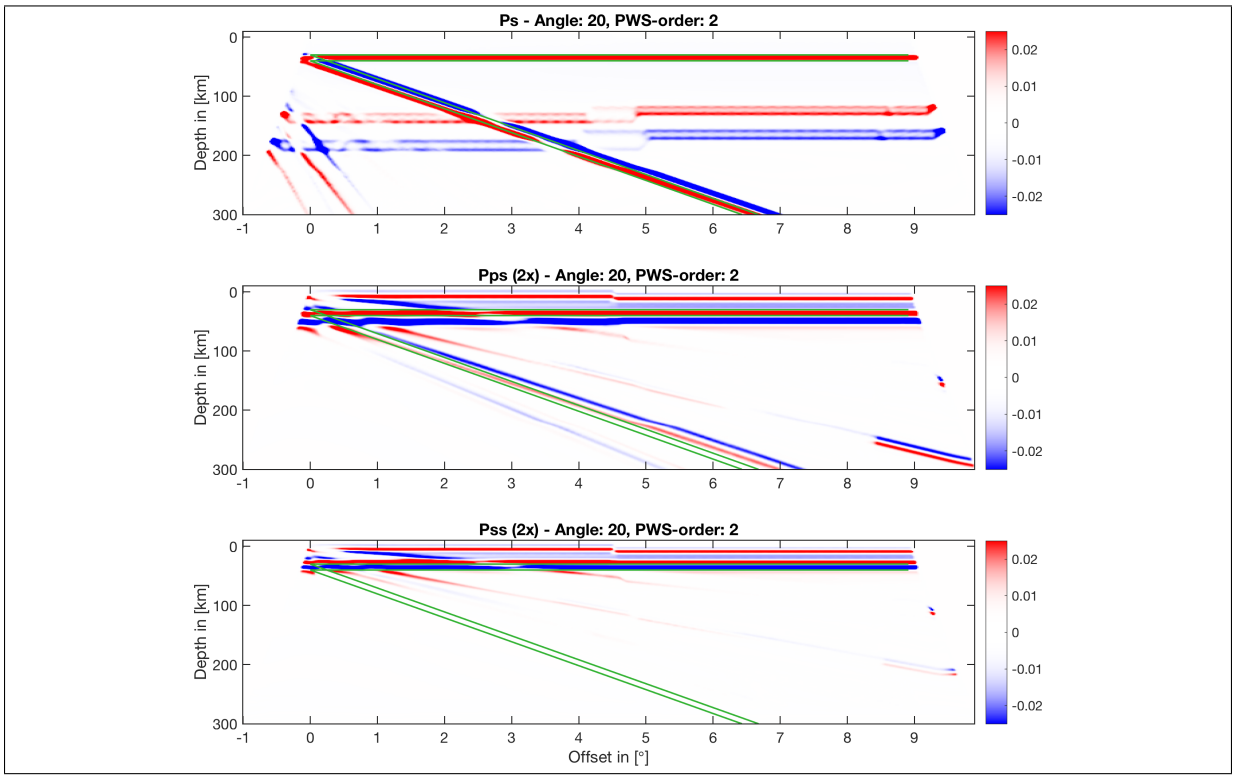

Figure C.26: Spatially averaged, CCP stacked receiver functions.

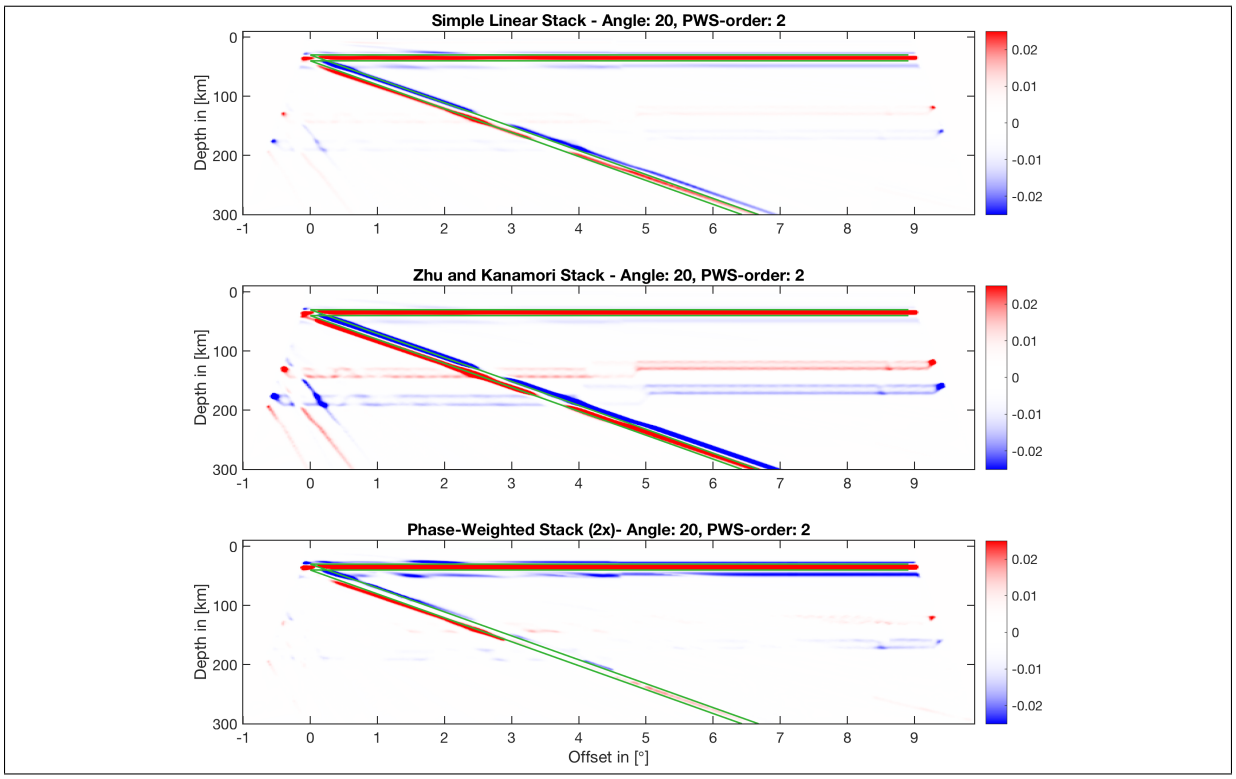

Figure C.27: Spatially averaged, multi-mode stacked CCP stacks

C.4 40°Dip

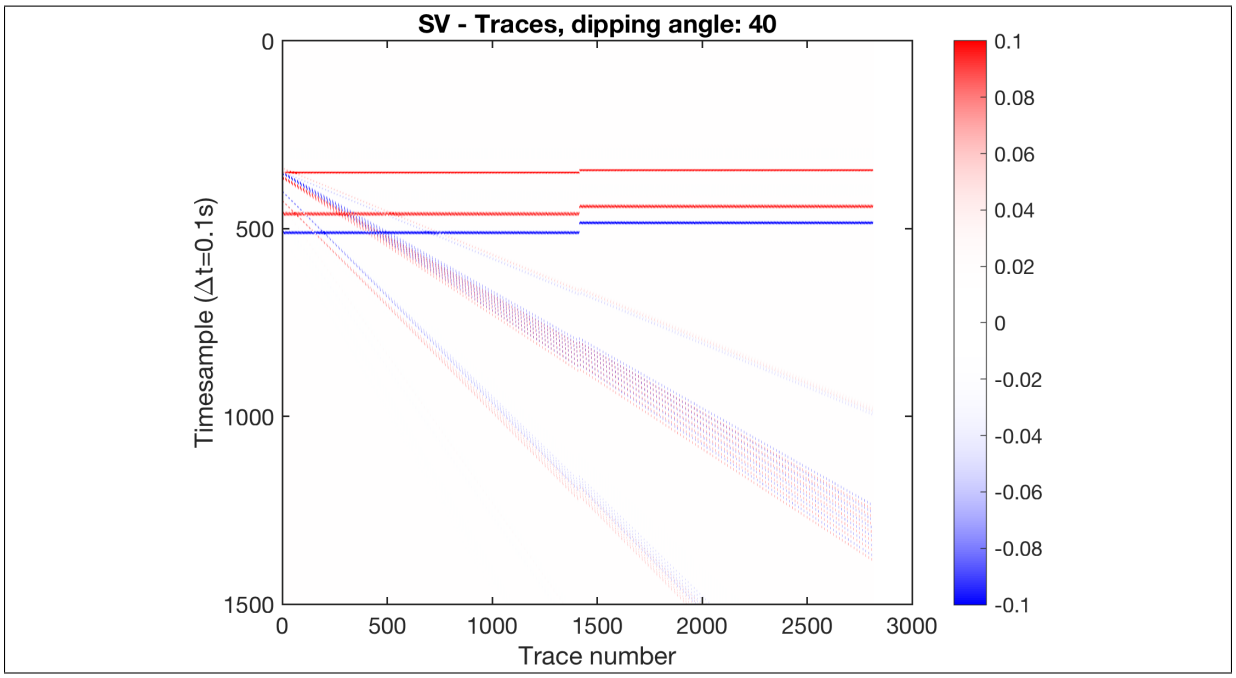

Figure C.28: Receiver function data for a 40°dipping angle. See text for sorting of the traces.

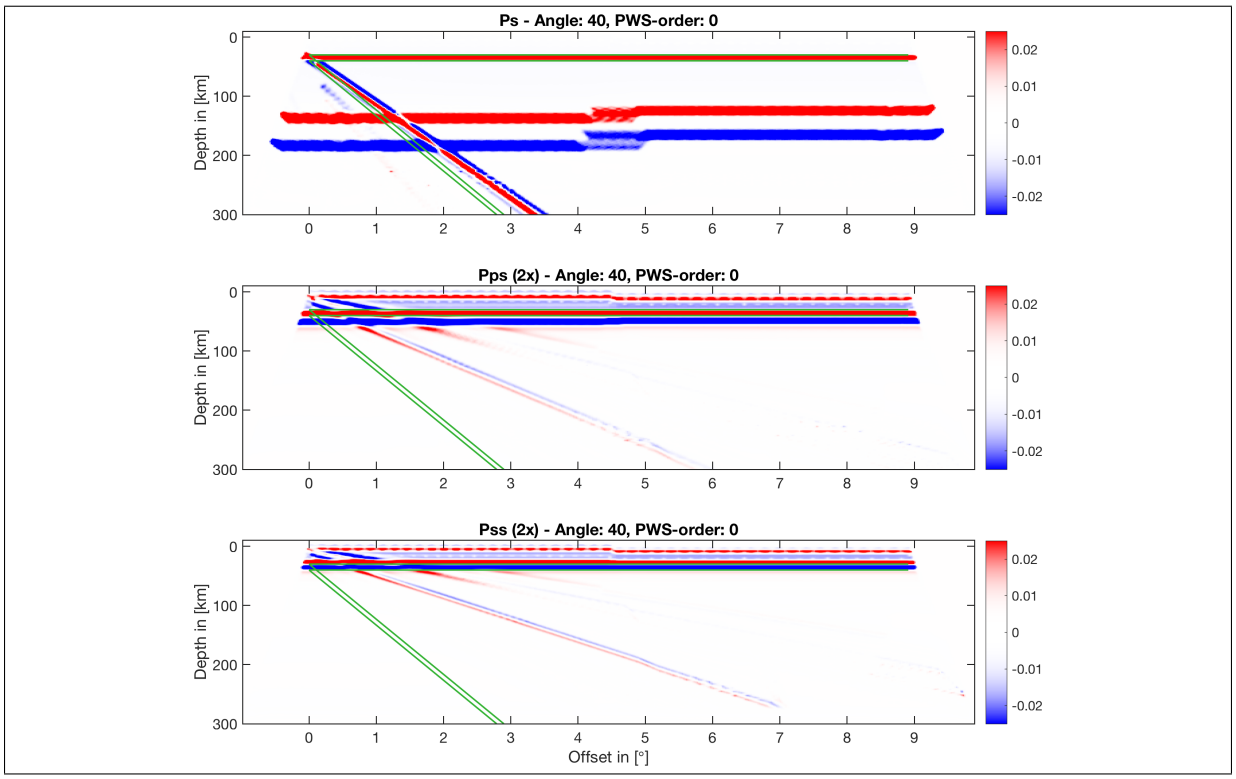

Figure C.29: Linearly, CCP stacked receiver functions.

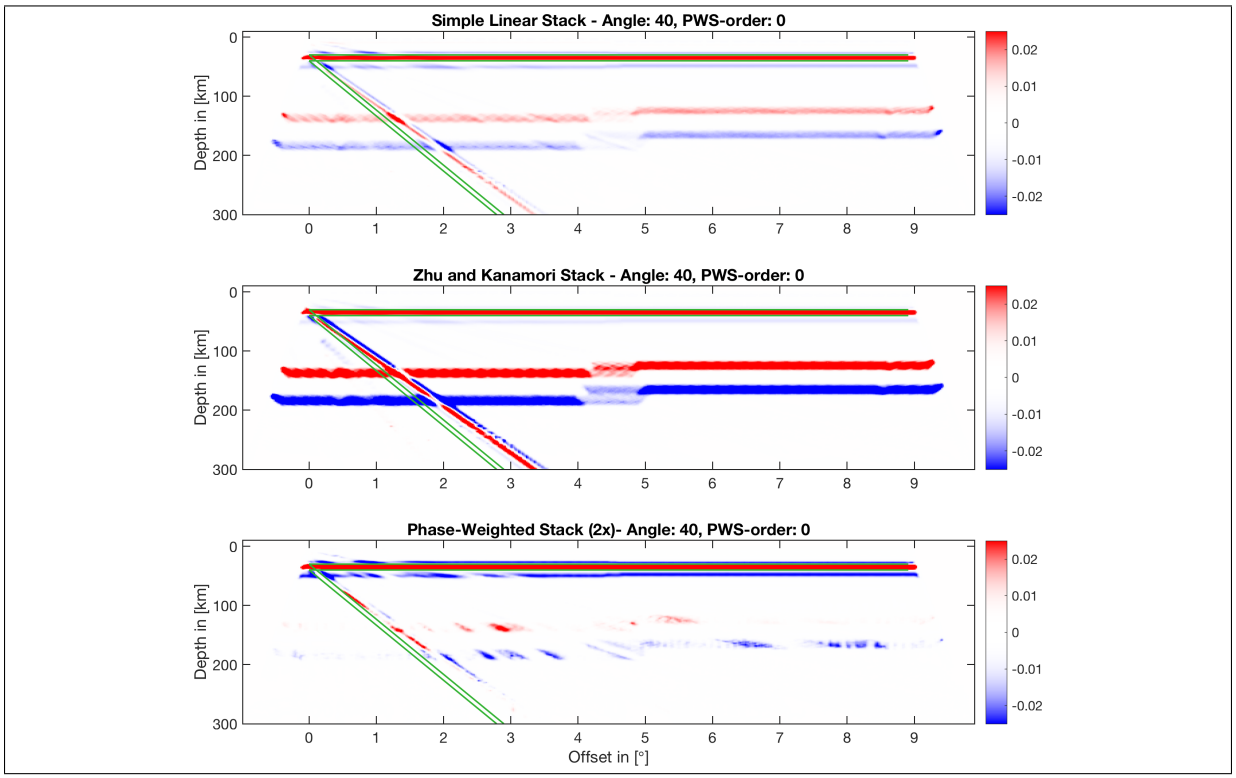

Figure C.30: Multi-mode stacked CCP stacks

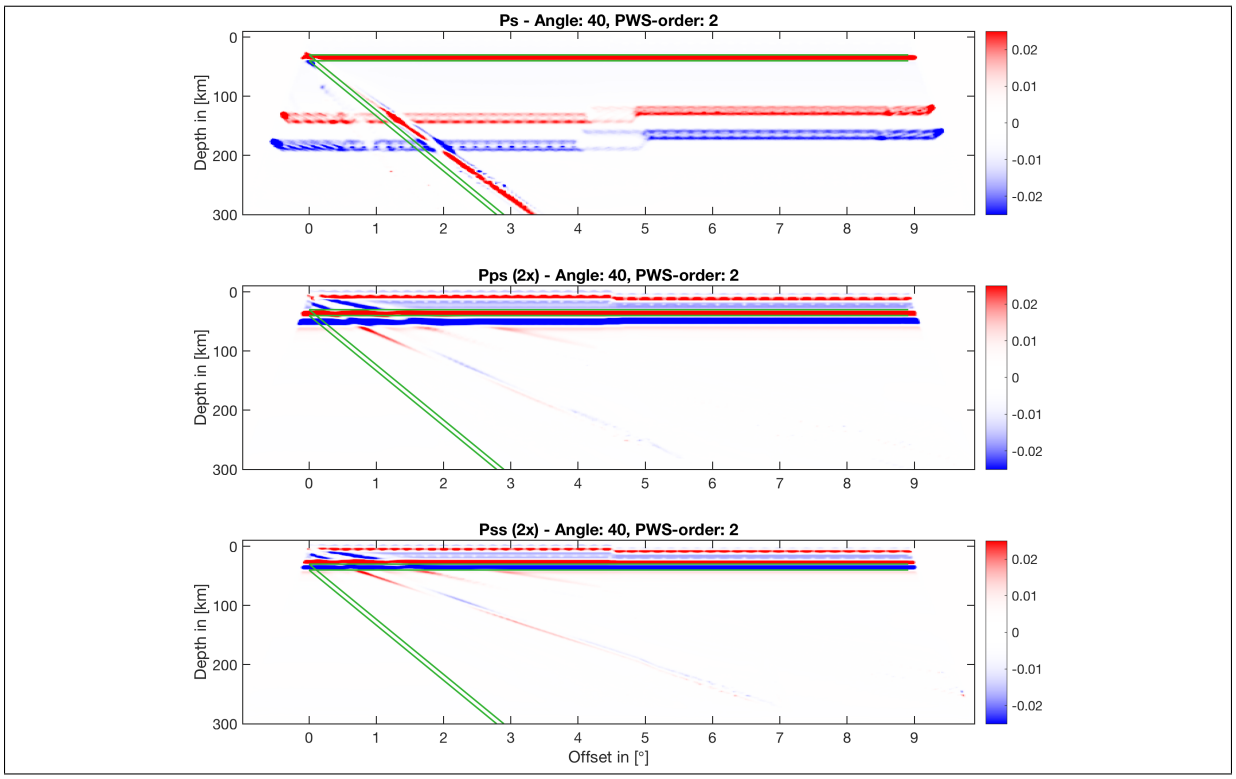

Figure C.31: Phase-weighted, CCP stacked receiver functions.

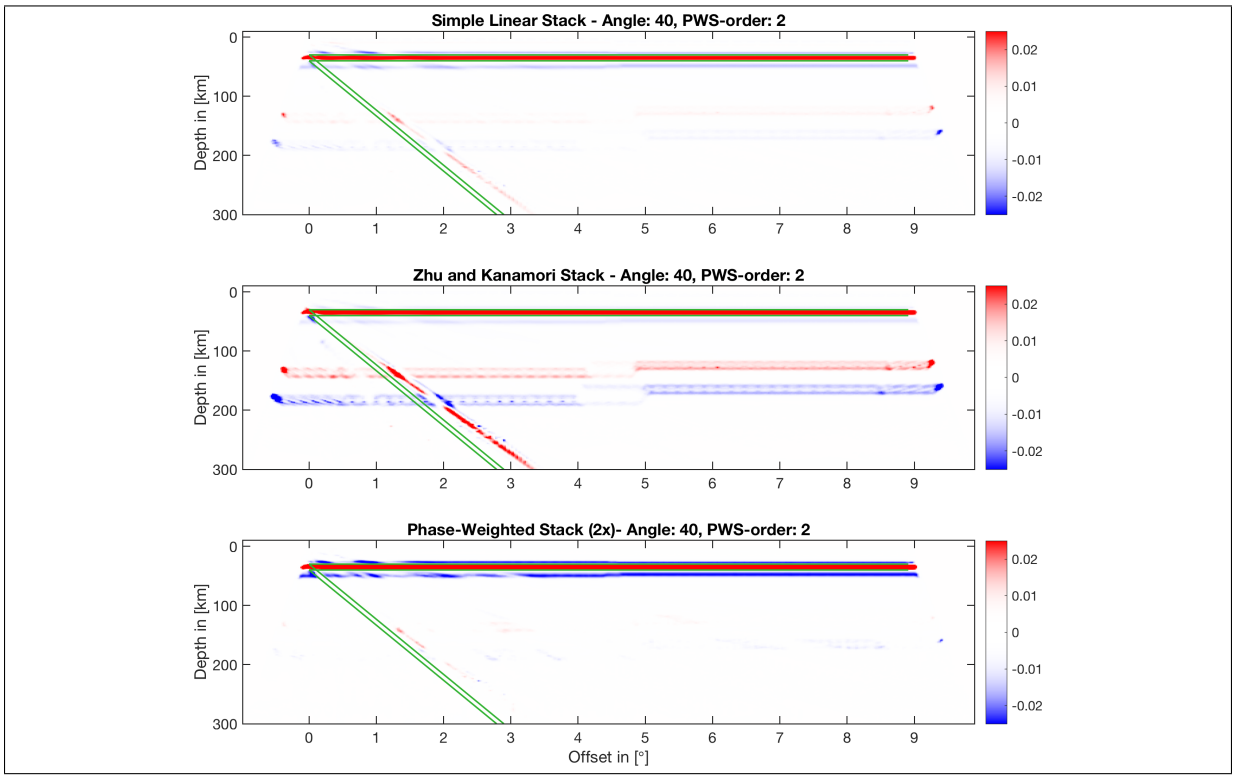

Figure C.32: Multi-mode CCP stacks

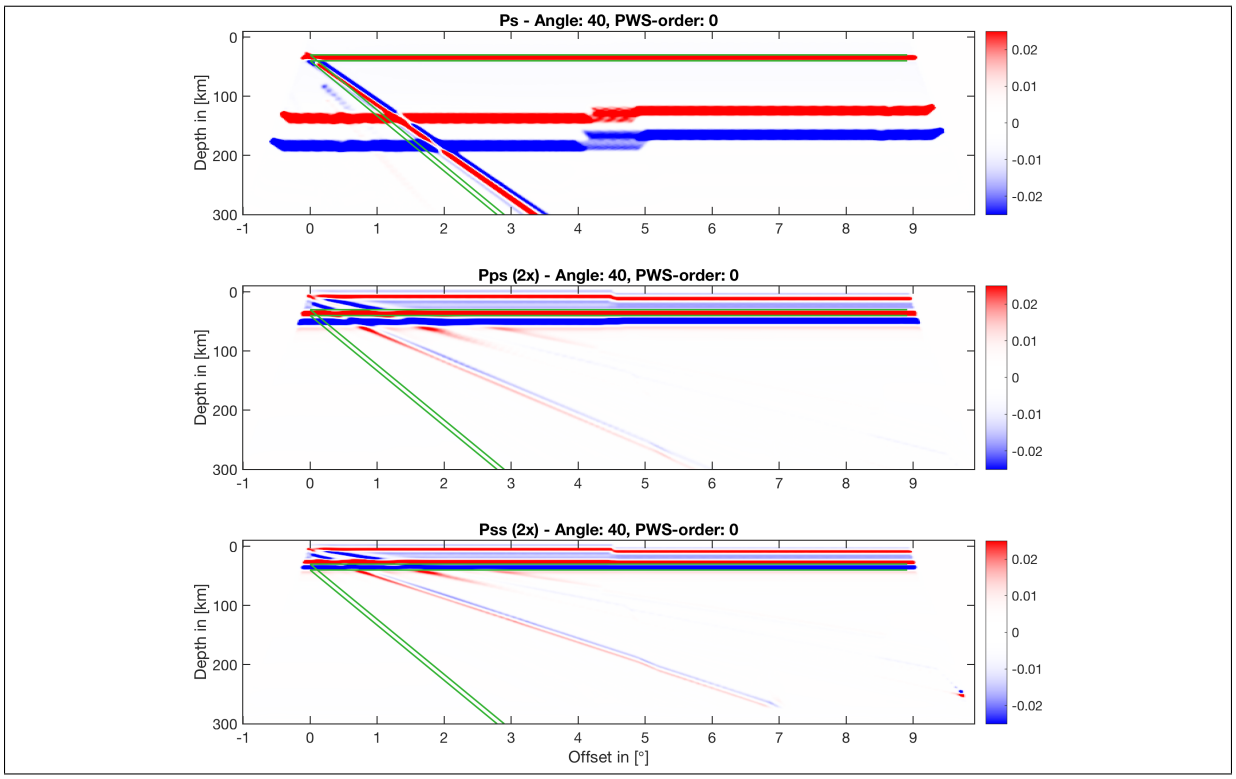

Figure C.33: Spatially averaged, CCP stacked receiver functions.

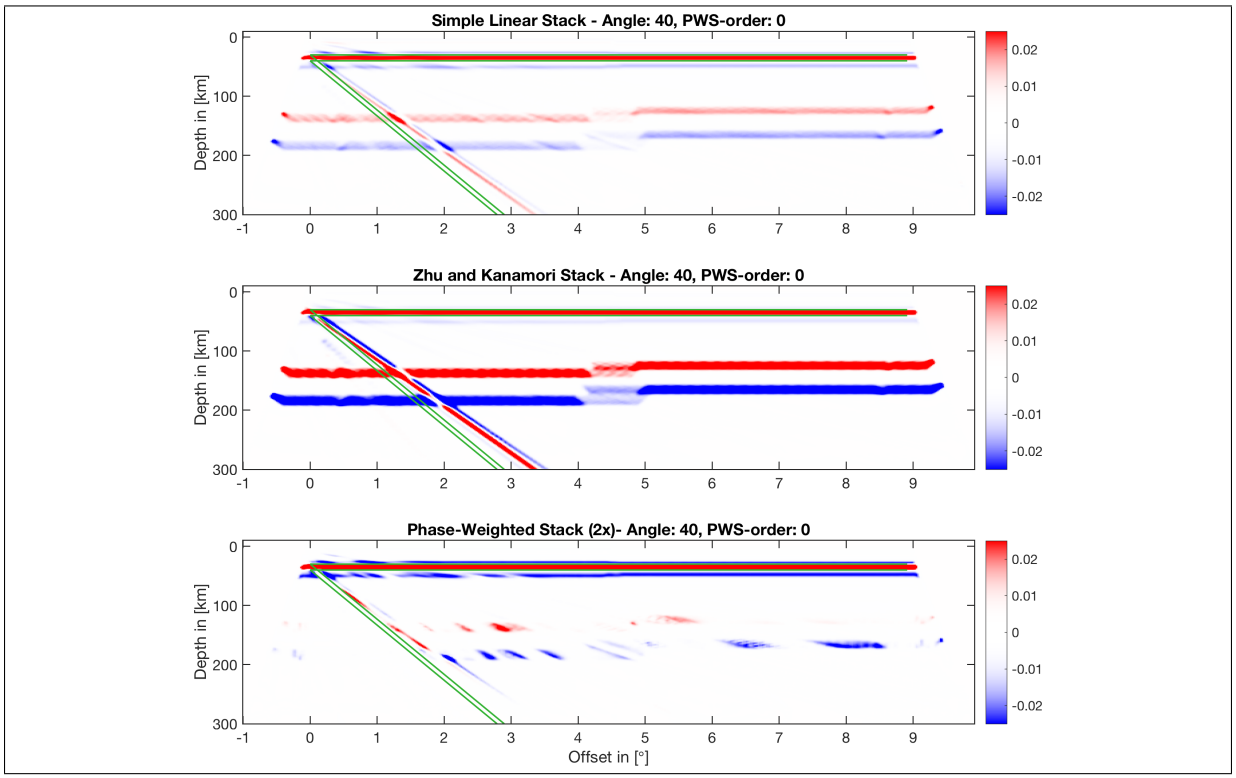

Figure C.34: Spatially averaged, multi-mode stacked CCP stacks.

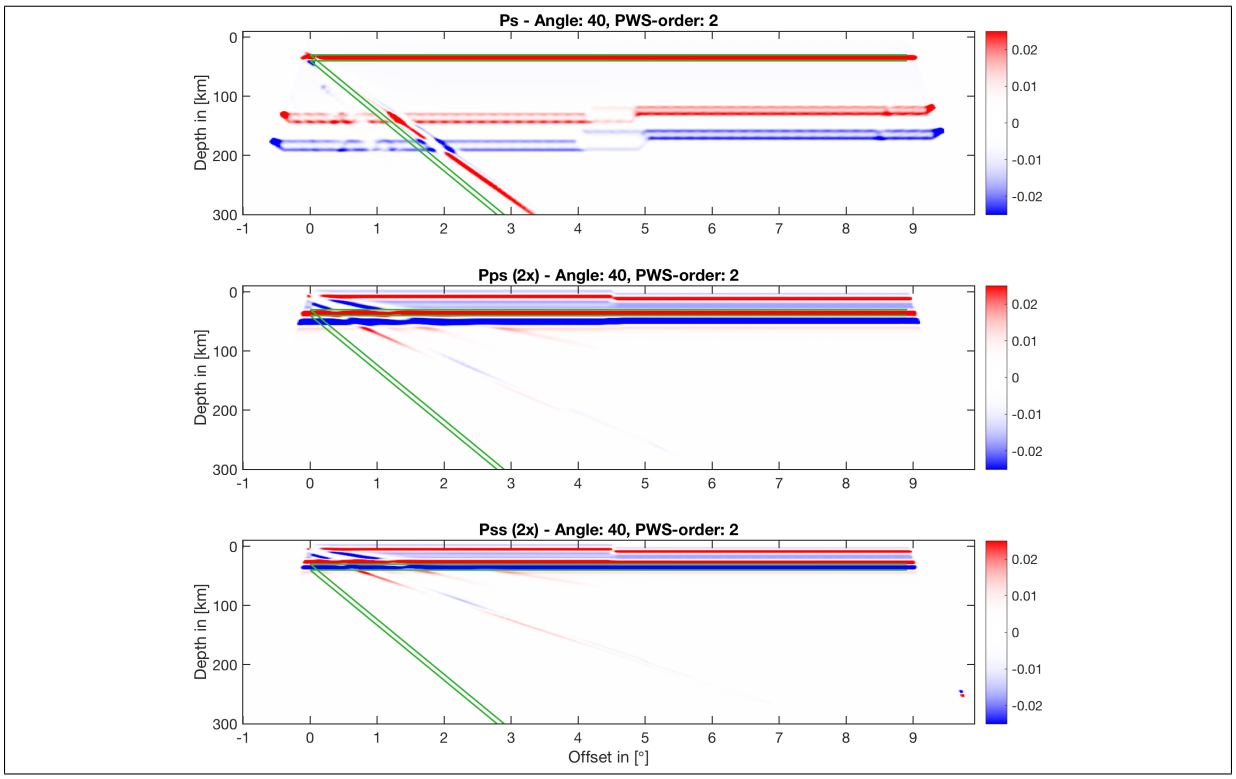

Figure C.35: Spatially averaged, CCP stacked receiver functions.

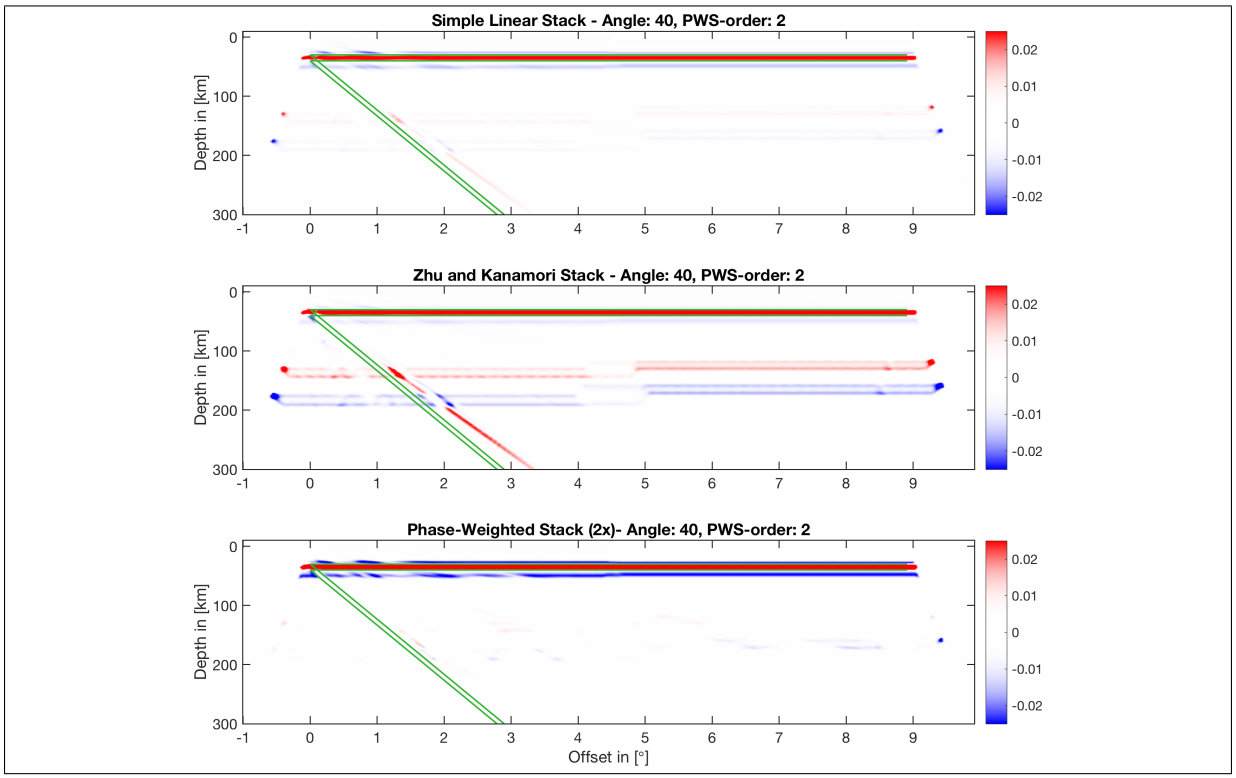

Figure C.36: Spatially averaged, multi-mode stacked CCP stacks

C.5 Comparison of the Multi-Mode Stacks

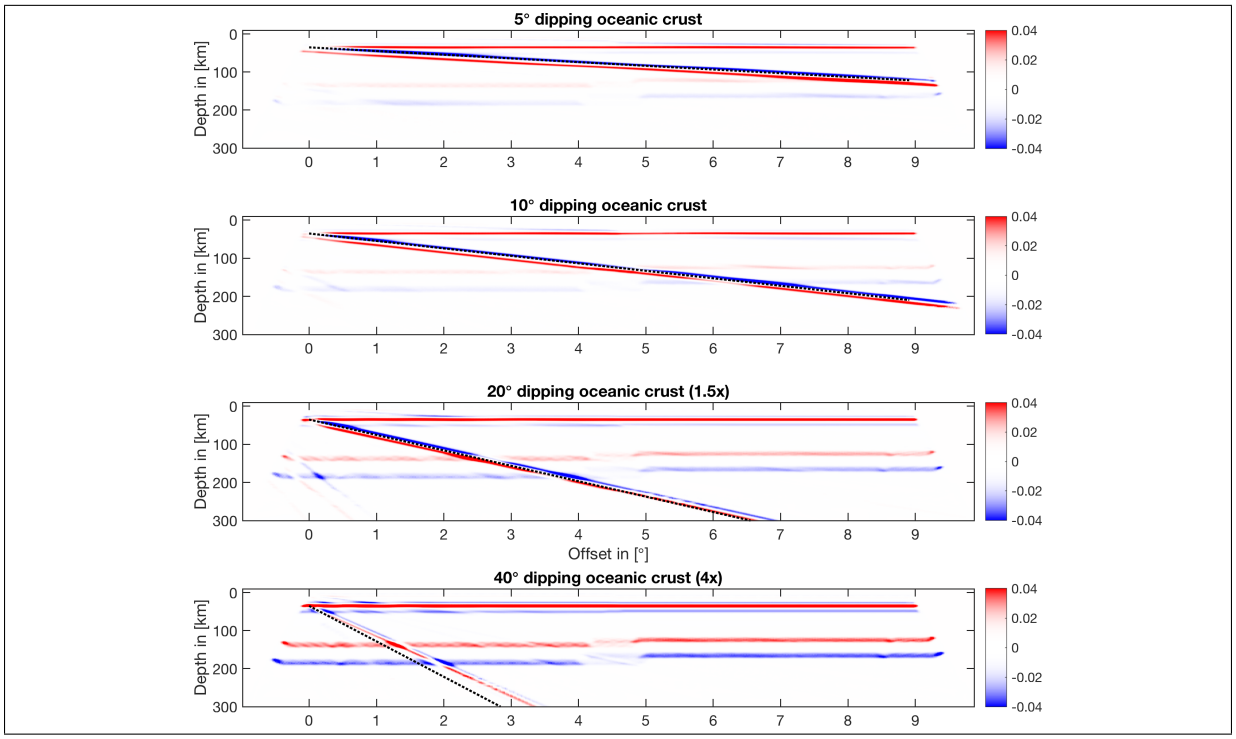

Figure C.37: Multi-mode simple CCP stacks. Pure linear stacking.

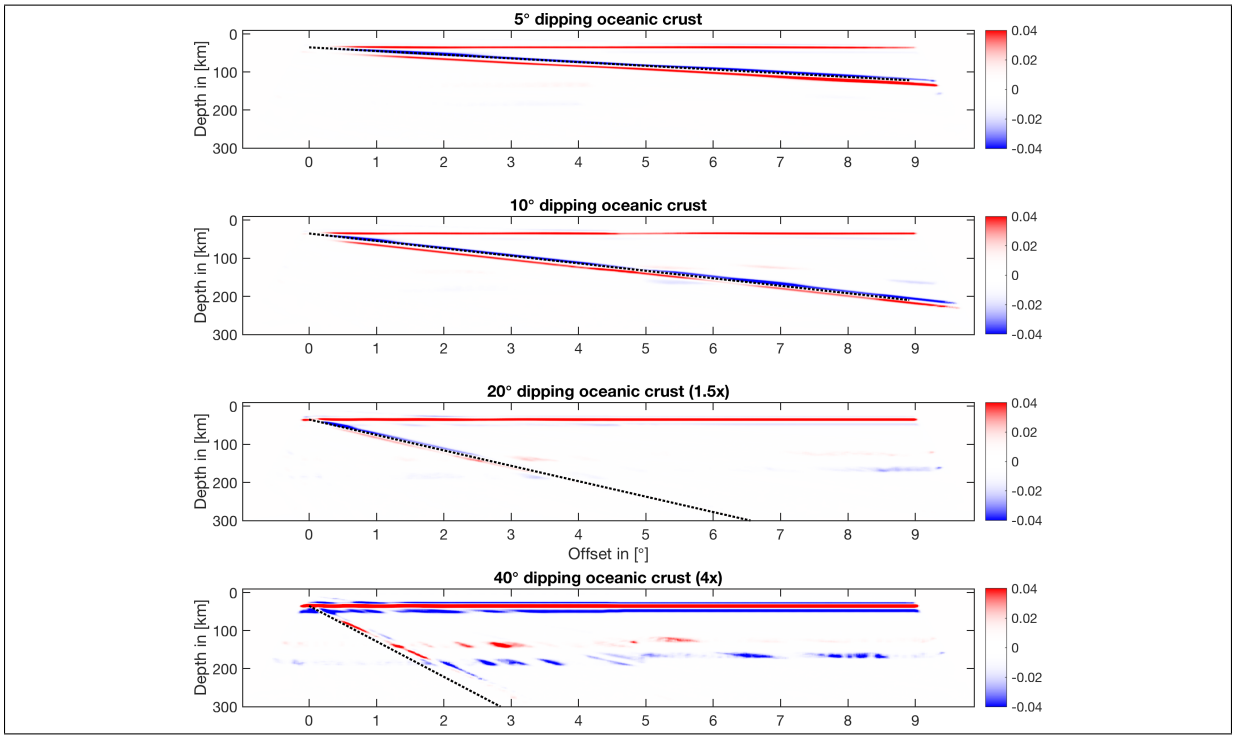

Figure C.38: Multi-mode phase-weighted CCP stacks. The single modes are stacked linearly. In the multi-mode stacking process the stacks are phase-weighted.

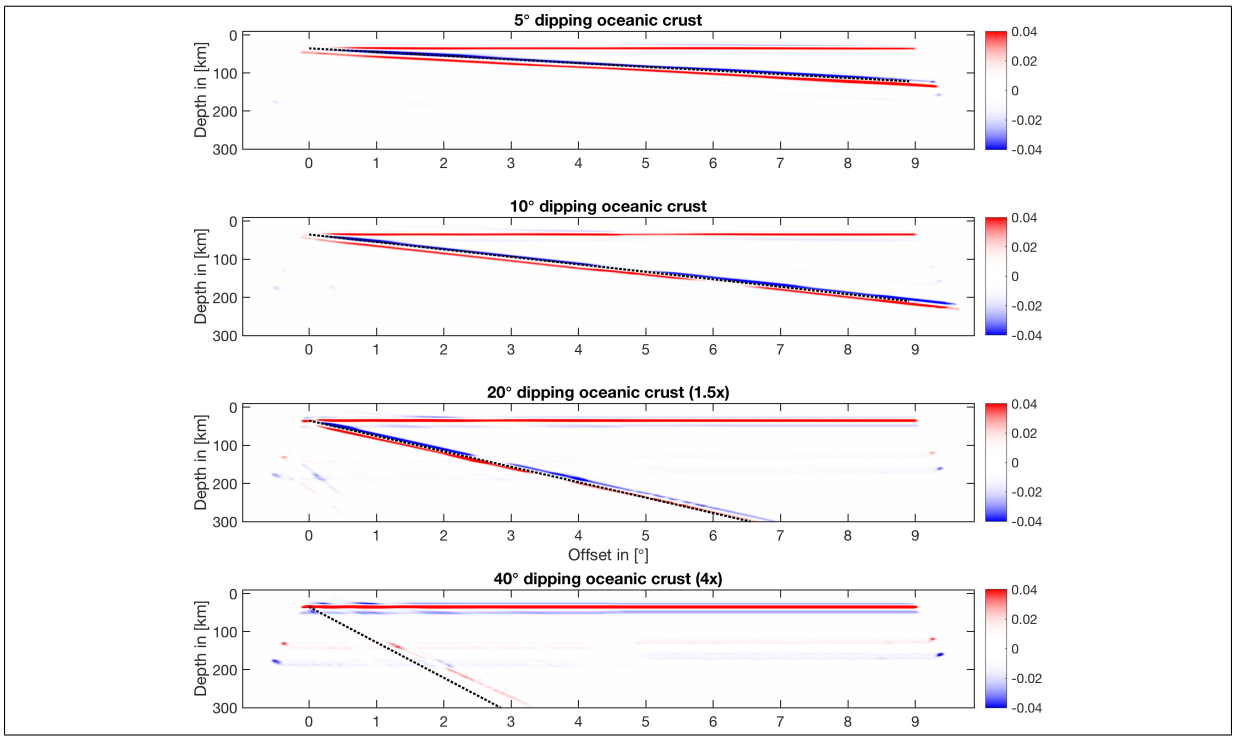

Figure C.39: Multi-mode linear CCP stacks of phase-weighted single modes. Here, phase weighting is applied when stacking the single modes into CCP-stacks. The three mode stacks are then linearly stacked on top of each other.

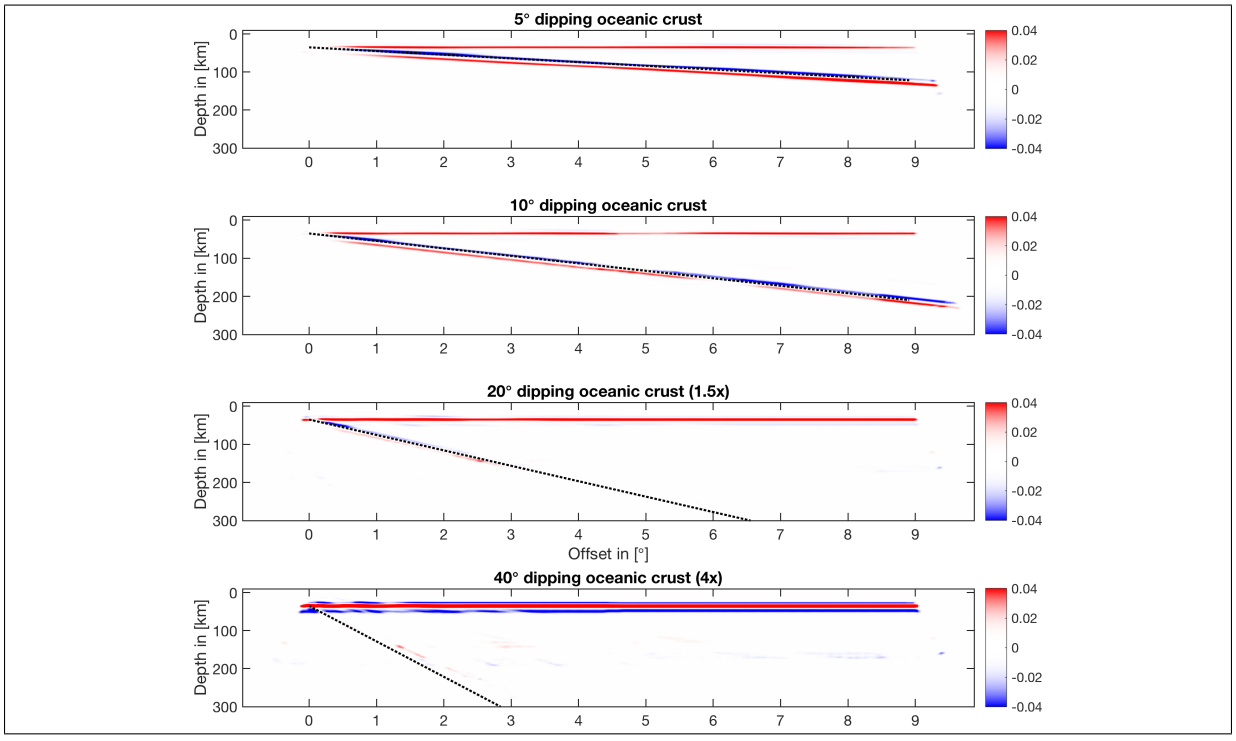

Figure C.40: Multi-mode twice phase-weighted CCP stacks. Here, phase weighting is applied when stacking the single modes into CCP-stacks and when the mode stacks are stacked.

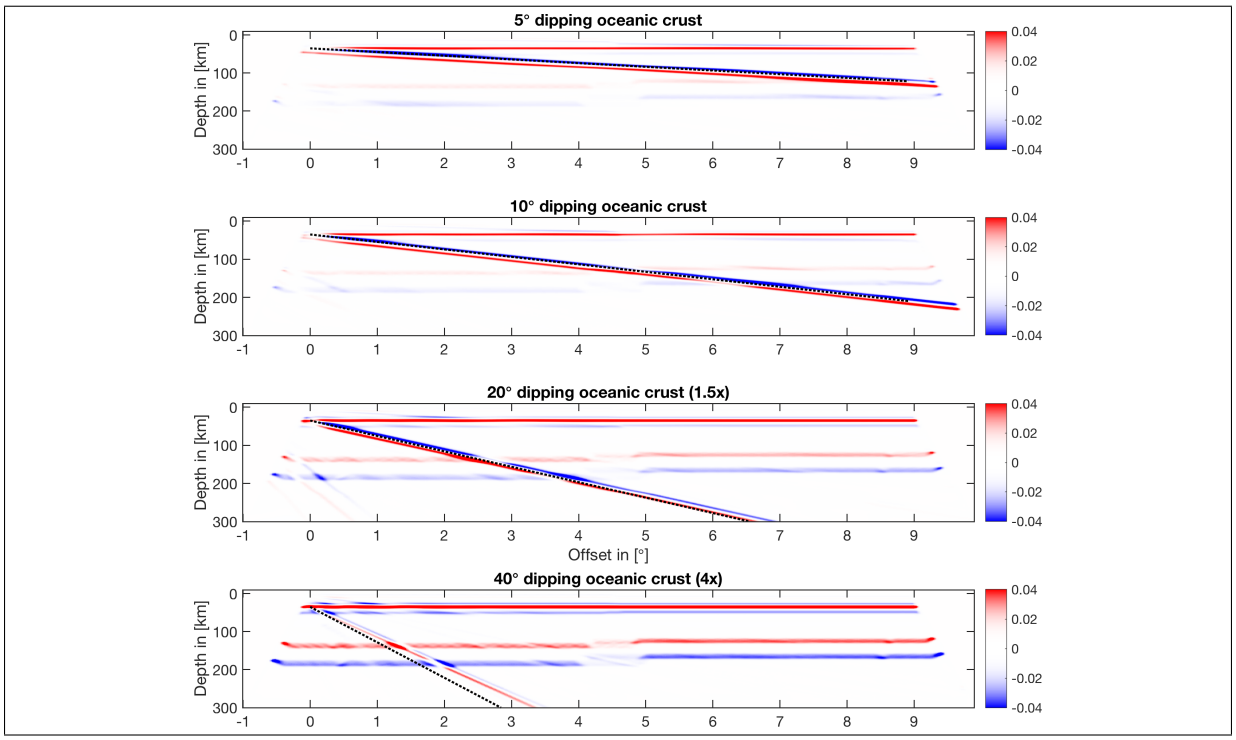

Figure C.41: Spatially averaged, multi-mode simple CCP stacks. Pure linear stacking.

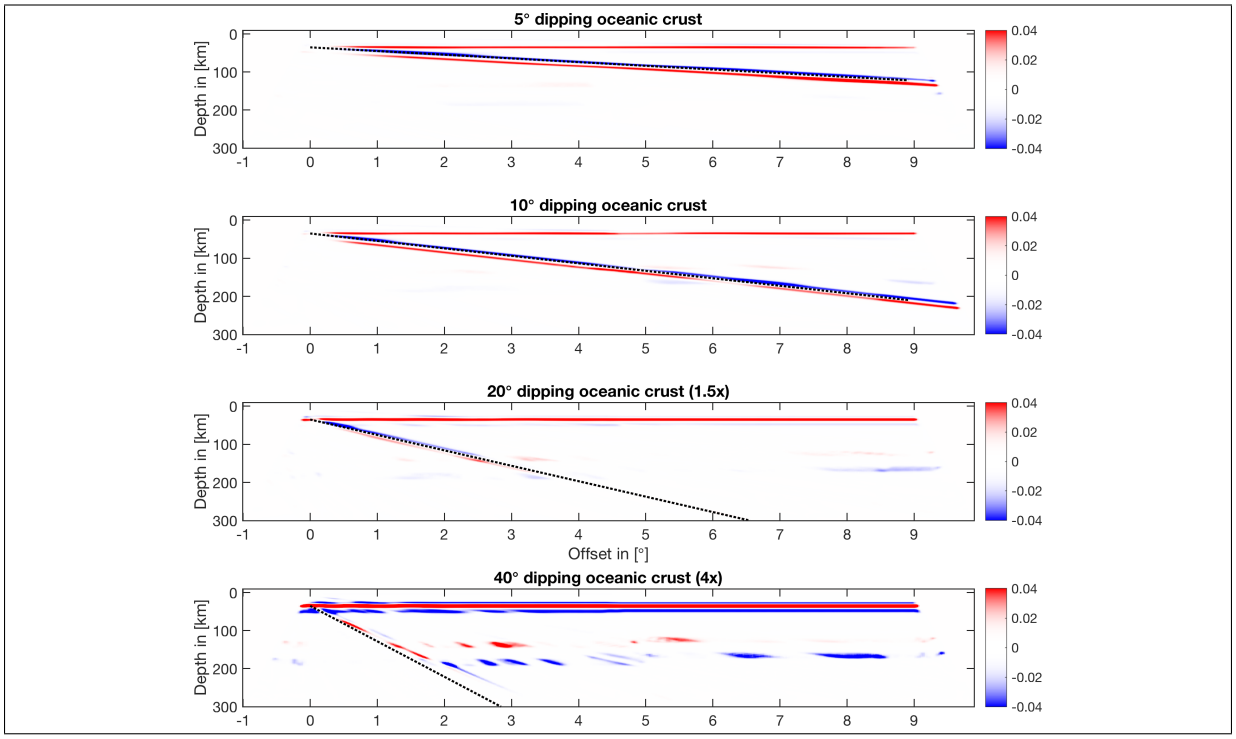

Figure C.42: Spatially averaged, multi-mode phase-weighted CCP stacks. The single modes are stacked linearly. In the multi-mode stacking process the stacks are phase-weighted.

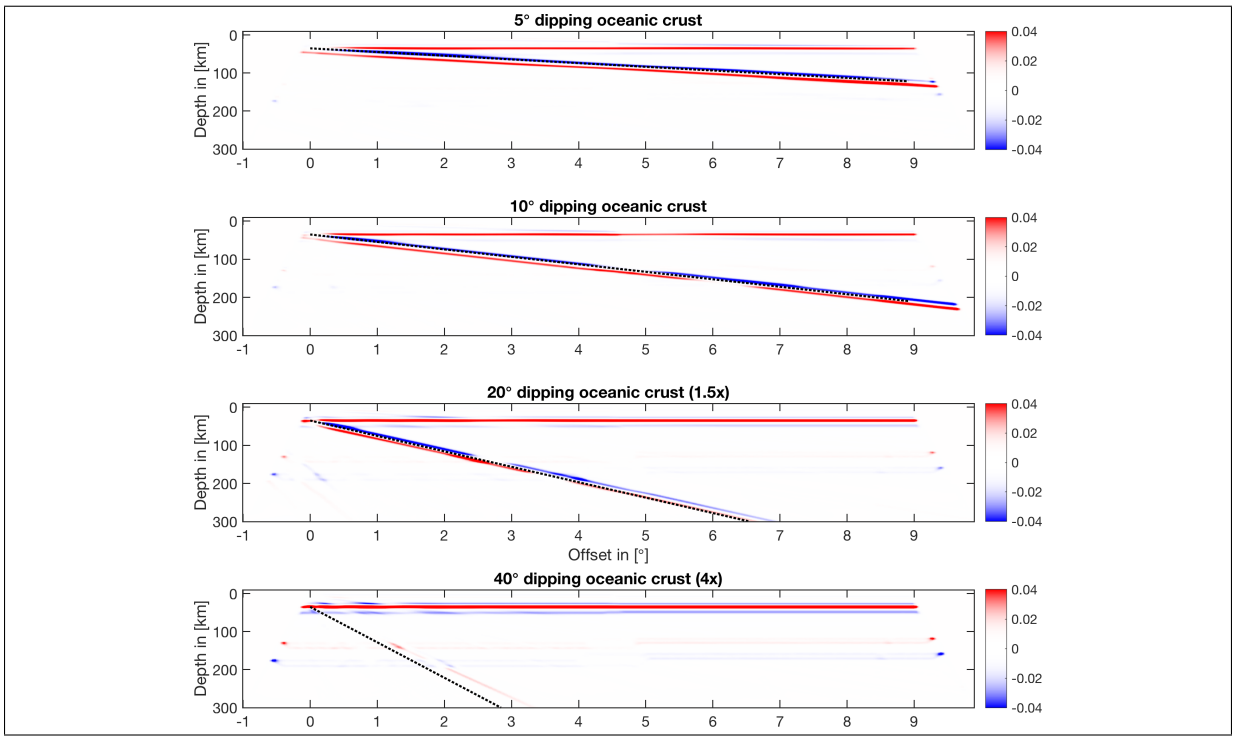

Figure C.43: Spatially averaged, multi-mode linear CCP stacks of phase-weighted single modes. Here, phase weighting is applied when stacking the single modes into CCP-stacks. The three mode stacks are then linearly stacked on top of each other.

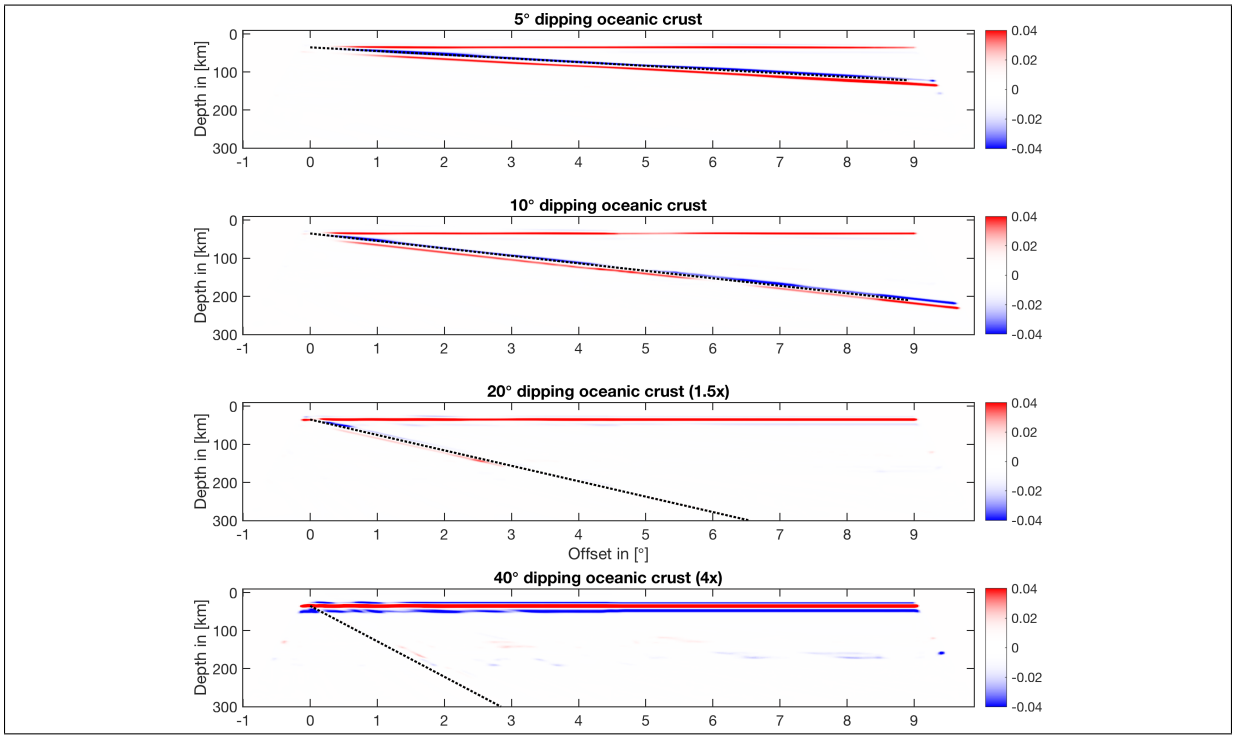

Figure C.44: Spatially averaged, multi-mode twice phase-weighted CCP stacks. Here, phase weighting is applied when stacking the single modes into CCP-stacks and when the mode stacks are stacked.